UNIVERSITAT DE BARCELONA

Transparent nanostructured metal oxides for chemical biosensors: towards point-of-care environments

Raquel Pruna Morales

UNIVERSITAT DE BARCELONA

Transparent nanostructured metal oxides for chemical biosensors: towards point-of-care environments

Autor:
Raquel Pruna Morales

Director y tutor:
Dr. Manuel López de Miguel

Memoria presentada para optar al grado de doctor por la Universidad de Barcelona

Programa de doctorado en Ingeniería y Ciencias Aplicadas

Departamento de Ingeniería Electrónica y Biomédica
Facultad de Física
Universidad de Barcelona

Barcelona, junio de 2019

"*All you need is faith, trust and a little bit of pixie dust.*"

Peter Pan

Acknowledgements

En primer lugar no podría estar otro que el director, tutor y gran responsable de esta tesis, Manel López: me engañó al empezar, siguió engañándome durante los años de máster y tesis y finalmente parece que hemos sacado algo de verdad. Muchas gracias por aguantarme, ayudarme y empujarme hasta llegar al final.

Al resto del equipo, Fran Palacio y Fernando Arreza. Sin vosotros (y vuestra paciencia), todo esto no hubiera sido posible.

Part del temps que ha durat aquesta tesi l'he passat a l'ICMAB, així que gràcies als professors Francesc Teixidor i Clara Viñas (i equip) per obrir-me les portes de casa seva i tractar-me com a una més del grup. Val a dir que no tot el temps l'hem dedicat a treballar, ja és mala sort haver coincidit en una època tan convulsa... (o no? Ho hem passat molt bé!).

Muchas gracias al mayor *pecador de la pradera* que he conocido, el profesor Abdelhamid Errachid. Thanks as well to the rest of the ISA team; it was a pleasure to stay at Lyon those months. Special thanks to the *jamoncito* Abdel: all your knowledge, ideas and comments were also very helpful, and without them this work wouldn't have been possible. You manage!

Gracias al resto de compañeros de estos años, en especial a Mauri por su apoyo y ayuda, cafés, charletas... A Ángel Diéguez, por prestarme su firma. A Oriol Monereo, por todas las horas de cafés y tertulia, y por revisar este manuscrito. A todos los que de algún modo habéis contribuido a esta tesis o me habéis acompañado estos años: Catalina, Juan Pablo, Miriam, Mònica Martínez, Oriol Blázquez, Romén... Gracias a todos.

A les *nenes* del Masnou, per ser-hi sempre i des de sempre. Manel Bosch, tu també hi ets des de (gairebé) sempre, *bien qu'on ne se voie pas souvent...*

Por el apoyo incondicional a lo largo de los años quiero agradecer a mis padres, Jordi y Feli; a mi hermano, Aitor; als avis i tieta Eli; a todos los que están un poquín más lejos, y a los que ya no están. A mi segunda familia, Montse y Jose. Gracias por tanto.

A Urf, mi paz y mi equilibrio (a veces... otras veces me das la vida mártir, *salao* ☺). Qué años te he dado con esto, ¿eh? Y ahí has estado, haciendo de cada día una aventura, en todos los lugares donde hemos estado, siempre sonriendo. Y lo que queda. "Tú tan sólo ilumíname con tu presencia cada día".

Contents

Chapter 1

Introduction

1.1 Motivation: towards a very early-stage detection using smart biosensors

The term *biosensor* is relatively new and it refers to a device for the detection of analytes that combines a biological recognition element with a physicochemical signal transducer [1]. Specific biochemical reactions mediated by isolated enzymes, immunosystems, tissues, organelles or whole cells are used to detect biochemical compounds by triggering electrical, thermal or optical signals [2].

Over the past years, the dynamization of research and development of biosensors has been enormous. Amongst others, these devices have been key for early diagnosis of several diseases, which is crucial for their successful treatment. With all, a proper development of biosensors requires multidisciplinary technology. Among the different disciplines involved, molecular biology has led to a much understanding of potential biomarkers for diagnosis. In this sense, the implementation of point-of-care (POC) diagnosis requires proper attention to the major challenge of multitarget detection. This trend, together with rapidity, cheapness and reliability must be conjured up for a successful disease diagnosis in a decentralized setting.

The first part of this chapter consists of a historical revision of the origins of medical biosensing, from ancient civilizations to our days. Furthermore, some notes on the application of biosensing to food and environmental analysis are provided. The second part of this chapter contains details on this work: a presentation of the dissertation, the hypothesis and objectives and an account of the scientific articles composing the main body of the thesis.

1.1.1 Medical diagnosis along history: a brief overview

Medical diagnosis is not at all a modern concept. Medicine is an old discipline, and the first documented diagnosis practices date of Ancient civilizations; however, these have indeed changed over time. The discipline was initially focused on treating (and eventually healing) diseases confirmed by physiological evidences, but still an extremely high mortality rate was usual. In the present, the concept has evolved towards "early diagnosis", which evidently tries to prevent the advent of diseases in patients, thus lowering mortality rates. All in all, the history of medicine can be divided into three distinct periods associated to different diagnosis methods: bedside medicine was prevalent from Middle Ages to the 18th century; hospital medicine became popular from 1794 to 1848; finally, laboratory medicine took over from then and up to our days [3]. Let us devote

the following lines to summarizing what is known about the origins of medical diagnosis.

The first documented reference to diagnosis as a medical practice dates around 3000 BC in Ancient Egypt (Figure 1.1a). It is supposed to have been practiced by Imhotep, who would have been the founder of Ancient Egyptian medicine [4, 5]. The practice of diagnosis was further rationalized by physicians in Babylonia (around 2000 BC, Figure 1.1b). The Babylonian "Diagnostic Handbook" (by Sakikku) documented the application of diagnosis and prognosis to many variations of epilepsy, intestinal and urinary disorders, respiratory issues and several mental disorders [6]. References to Babylonian medicine were also found in the Laws of Hammurabi. Further East, diagnosis was also a relevant practice, and still has particular features in the present days. Indeed, inspection, listening and smelling, inquiry and palpation are diagnosis practices that outlived modern times until today, but were first reported in an ancient Chinese book, the "Inner Canon of the Yellow Emperor" (Huangdi Neijing), dating around 300 BC [7].

Two renowned personalities of Ancient Greece (Figure 1.2a), the "father of medicine" Hippocrates of Kos (c. 460–c. 370 BC) and surprisingly the philosopher and mathematician Pythagoras of Samos (c. 570–c. 495 BC), are known to have had a say in the topic. Regarding the practice of diagnosis, Hippocrates was known for tasting his patients' urine and smelling their sweat, for he was the first to boost the doctrine of humoral pathology. Pythagoras included this humour-based diagnosis doctrine into his four elements (earth, air, fire and water) theory. Moreover, physicians in Ancient Greece postulated heredity as the potential cause of some diseases, although no complete description or examples were provided. The latter was pursued by specialists in the Islamic world (Figure 1.2b). As an example, Arabian physician Abu al-Qasim al-Zahrawi first categorised haemophilia as an hereditary disease, whereas Persian physician Ibn Sina introduced the concept of syndrome as a group of symptoms consistently occurring together as the basis of diagnosis.

During the medieval period, medicine experimented a major setback as Christian culture became more widespread, and both diagnosis and therapy were superfluous and based, basically, on religious preaching (Figure 1.3a). However, it would be greatly unfair

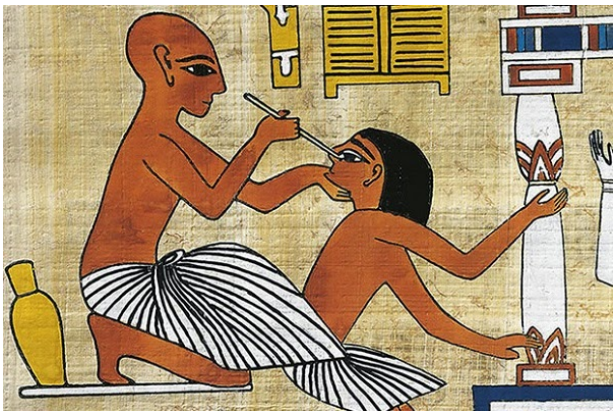

(A)

(B)

FIGURE 1.1: (A) Diagnostics procedure in Ancient Egypt; (B) Babylonian stone inscribed with details on diagnosis of medical conditions and prognostics of the outcome (1900–1700 BC).

(A) (B)

FIGURE 1.2: (A) Greek mug with images of medical procedures; (B) diagnosis in the Islam.

to obviate pagan medicine during that time, which did consider diagnosis by analysing symptoms, pulse palpitation (rate, tempo and arterial power helped determining the origin of fevers) and even human secretions. Ancient Greek theories of humour imbalances prevailed until Middle Ages, becoming the analysis of urine the most important source of information for medical diagnosis. As an example, a flask called "matula" was employed for collecting urine, and four differentiated regions were associated with different parts of the human body. Analysis of the properties of the liquid in each region was supposed to reveal the source of injury. Certainly, during that time, astrology and interpretation of dreams also had a role in diagnosis.

It was not until the 17th century that medical diagnosis experimented a new impulse, and it was due to the invention of the microscope, opening the door to the micro-world. Microscopy in diagnosis was first employed by German Jesuit priest Athanasius Kircher (1602–1680). Parallelly, the analysis of urine was still in widespread use at that time. Urine was first reported to contain proteins in 1694, probably becoming a primitive mention to biomarkers, which will be defined and discussed in the following sections. Unlike the 17th, the 18th was not very prolific century in terms of advances in diagnosis. Few attempts to employ precision instruments for practicing clinical diagnostic methods of percussion, temperature, blood pressure and heart rate measurements were reported. More relevant to our topic were observations of sediments in the urine of febrile patients by J. W. Tichy in 1774, and the studies on the sweetness of urine and blood serum caused by presence of sugar in diabetic patients (around 1780). With the 19th century came a new wave of diagnostic tools: refined microscopes, X-rays, electrocardiographs and the first chemical and bacteriological tests. Indeed, the breakthroughs in bacteriology made by Robert Koch and Louis Pasteur (Figure 1.3b) during the second half of the century permitted the isolation of organisms responsible for major infectious diseases. Simultaneously, laboratory tests were introduced to detect a number of illnesses, and advances in the analysis of urine and blood improved diagnostic tools.

(A) (B)

FIGURE 1.3: (A) "The Extraction of the Stone of Madness" by Hyeronymus van Aken *Bosch*, dating from around 1494 and parodying the popular beliefs during the medieval period; (B) picture of French microbiologist and chemist Louis Pasteur (1822–1895).

1.1.2 Medical diagnosis today: the concept of biomarker and early detection

It was in the early 1900s that Archibald Garrod postulated that deoxyribonucleic acid (DNA) encoded genes that in turn carried the information for encoding proteins responsible for body structure and functionalities. However, this was not fully appreciated in diagnosis until the sequencing of the human genome (the full set of genes encoded by DNA in human cells) in 2003 (Human Genome Project, HGP [8]), which finally confirmed Garrod's hypothesis of biological individuality. The HGP revealed that biological individuality, inheritance and the environment are closely related at the level of DNA and gene expression, and this accounts for how the body of an individual will be modified and which diseases will develop throughout life. Thus, the sequencing of the human genome is actually helping in preventing a number of diseases of hereditary causes, raising the traditional medical attention level of individualization (in terms of risk prevention) up to unprecedented standards. Moreover, this technology provides knowledge about physiological features of diseases, their genetic causes and the factors that induce genetic disposition for the disease to actually manifest.

On the other hand, it was previously pointed out that genes are further processed into encoding proteins in a mechanism called translation, carried out inside the cells by complex molecular machines called ribosomes. Each protein is encoded at a certain time, at certain types of cells and under determined conditions. The full set of proteins expressed by the genome, in the case of humans, at determined locations, cells, organs and at certain times is called the proteome. As can be deduced, the encoding of proteins is a highly delicate process that can be easily altered. Too high or too low protein levels or even a switch in the type of protein can occur, and the measurement of this phenomena is becoming of increased importance in diagnosis. What is more, the alteration in a patient's proteome usually occurs before symptoms manifest. Thus, the detection and eventual quantification of specific proteins will become of capital importance for early diagnosis of many hereditary and also acquired diseases, and will eventually severely increase probabilities of survival.

With all, prevention but especially early-stage disease diagnosis is of utmost importance for appropriate prognosis but also for patient wellness during treatment (for example saving the patient eventual awful operations and treatments). In this framework, science and technology have become key pillars in the way of developing new strategies

for early-stage detection of diseases. Advances in biomedical science, as recently experienced with genome and proteome mapping and also the search and determination of biomarkers, sets new paradigms in medical diagnosis. On the other hand, technological progress, in the present case manifested as the development of miniaturized, low-cost and easy-to-use diagnostic kit systems, is crucial in actually materializing medical diagnosis paradigms postulated by biomedical science.

Up to this point, the need for defining the previously mentioned term "biomarker" comes up inevitably. It is understood by biomarker a detectable and quantifiable (biological or chemical) indicator of presence and severity of a physiological condition, risk of progression of a disease or response of disease to a treatment. Such indicators may be specific cells, simple or complex molecules, proteins, hormones, genes and gene derivatives. Some experts even consider temperature and blood pressure to be biomarkers for fever and stroke, respectively. Examples of biomarkers could be antibodies indicating infections or autoantibodies present in blood as a sign of autoimmune disease. In the field of oncology, where biomarkers have gained increased interest lately, the KRAS gene and its role in colorectal cancer can be highlighted [9], as well as prostate specific antigen (PSA) for prostate cancer [10], amongst others. Early-stage biomarker detection has become of capital importance to pursue effective treatment on cancer patients, but also on other chronic and degenerative diseases such as Alzheimer's disease and rheumatoid arthritis, which both often begin with an early symptom-free stage, being beta amyloid (Aβ) and the anti-cyclic citrullinated peptide (anti-CCP) [11, 12] the most paradigmatic biomarkers, respectively. Besides, individualized treatment plans are becoming more and more popular due to the widespread use of biomarkers in, for example, tailoring specific drugs addressed to each type of tumour and the particular stage of its development.

A classification of biomarkers may essentially be done regarding their application as diagnosis, prognosis or predictive biomarkers. Diagnosis biomarkers help detecting and identifying risk of a determined disease; prognosis biomarkers reveal how the disease will progress (regardless of the existence and type of treatment), and predictive biomarkers help monitoring the clinical response to a treatment. The transversal utility of biomarkers can be observed: indeed, they are a tool for helping the doctor make decisions on diagnosis or treatment at any stage of the disease. Another classification of biomarkers could be based on their characteristics and physicochemical properties [13].

1.1.3 Towards point-of-care assistance: biosensors and lab-on-a-chip

From a clinical point of view, biomarkers must be easy to obtain and process by the clinician. Biomarkers may be obtained from blood, urine or saliva samples. Classical tests are performed on specialized laboratories, where the clinicians send the biofluids for further processing by complex machines. However, there is an increasing interest in the development of integrated tools for *in situ* analysis of biofluids without the need for sending the samples to an external clinical laboratory, with the high costs this implies, as well as the time spent between the moment of sample extraction and diagnostic communication to the patient. A paradigmatic case in this respect is the blood sugar test kit, used in screening for diabetes. The latter is a compact pen-sized instrument that basically consists of a layered strip with a microfluidic channel and a reaction zone where the glucose oxidase enzyme is present. The enzyme reacts with the glucose present in the blood sample, producing gluconic acid and hydrogen peroxide. The latter reacts with a new reagent to produce either a current flow or a colour change, which are measured

by amperometry or colorimetry, respectively. The intensity of the signal is correlated with the amount of glucose present in the blood sample. This test may take between few seconds to few minutes, so it fulfils the requirements of tiny sized, easy-to-use and quick analysis.

The latter example takes us to two new concepts: biosensors and point-of-care (POC) testing. Biosensors are devices consisting of a detection layer, where a reaction between the target analyte and a biological element occurs; and a transduction layer, where the energy released from the latter interaction is transformed into a measurable electrical signal, either a difference of potential or a small current. Ideally, the electrical signal is proportional to the amount of analyte measured in the detection layer. On the other hand, POC testing uses biosensors and other devices for performing medical testing at the site of patient care (bedside care), ideally at home or at the doctor's office.

The evolution and refinement of biosensor kits has occurred simultaneously with the improvement of computers. For example, let us highlight, out of all types of biosensors (which will be detailed in subsequent chapters), electrochemical biosensors. Electrochemical biosensors' transduction stage transforms the energy released from a biochemical event into a measurable quantity in an electrochemical system. Around 1960s, computer-controlled systems were introduced in the field of electrochemistry in order to control the potential and current on electrodes and simultaneously record and represent these quantities, to graphically visualize reactions occurring at the electrodes. Before, several huge electronic systems were needed to excite the electrodes, and also big oscilloscopes to monitor the responses and eventually to save the curves for subsequent analysis. For this, obviously, an expert in electronics was required to work side by side with the chemist in order to support the whole measurement process. With the advent of improved personal computers, a new era of commercial computer-interfaced electrochemical devices began, which are each time more accessible to doctors and untrained personnel.

Currently, miniaturized POC systems based on biosensors are becoming popular in the biomedical field, and a number of diagnostic kits are actually available. Beyond the aforementioned blood sugar test, another famous kit is the pregnancy test, which is based on a lateral flow assay for the detection of human chorionic gonadotropin (hCG), a glycoprotein that can be found in urine [14, 15]. Similarly, tests for blood gas and electrolytes, rapid cardiac markers, haemoglobin diagnostics and cholesterol screening, amongst others, are in widespread use in POC environments. However, there is still a long way to go towards a well-established network of portable and stable POC systems covering a wide palette of diseases. Research in this scope must include three action lines: (1) development of new materials with enhanced transduction properties; (2) refinement of existing immunoassays and innovation for increasing biomolecule detectiveness, and decreasing the time needed for conducting the immunodetection; (3) development of rapid, portable, low-cost and low-power electronic devices for testing biosensors at POC environments.

1.1.4 New horizons in biosensing: environmental care and food analysis

Although biomedicine is the field where biosensors have had major impact during the past years, these do have also a great future projection in food industry as well as environmental applications [16]. In the case of food industry, food processing operators and safety authorities have long needed immobilization platforms and novel food detection strategies to effectively detect potential contaminants and pathogens in a rapid, specific, inexpensive and sensitive way. Biosensors have been employed in the food industry for detection of contaminants, monitoring of product freshness, verification of product content and even beverage analysis. The latter is of special interest in the particular case of assessing the quality of drinking water, for one of the most studied microorganisms in the field is *Escherichia Coli*, responsible for diarrhoeas, urinary tract infections, inflammation and peritonitis in risk groups such as immunosuppressed patients [17]. Other microorganisms such as *Salmonella* and *Listeria* monocytogenes have also received much attention in the food analysis field, as well as pesticides, sugars and other analytes [18, 19].

On the other hand, the use of biosensors in environmental analysis can provide fast and specific data of contaminant sites in a reliable, low-cost and sensitive way [20]. Even though high accuracy data with a low limit of detection has already been accomplished by conventional methods, still these imply the need for highly trained personnel and are time consuming, for samples must be sent to a laboratory for testing. In environmental applications, the need for biosensors in order to perform field monitoring in a sensitive, rapid and low-cost way becomes evident. Moreover, these permit the measurement of pollutants in complex matrices with minimal sample preparation, offering the possibility of detecting specific chemicals and also determining their biological implications. Environmental monitoring has become a priority for the European Research Council, as has been demonstrated in the last H2020 calls. The main reason for this concern is the clear relationship between environmental pollution and human health and socioeconomic development. The need for portable, rapid and smart biosensing devices is crucial to explain the development in the past years of biosensors based on new transduction materials for the detection on environmental contaminants.

1.2 About this work

1.2.1 Hypothesis and objectives

The importance of developing qualified point-of-care systems in medical environments but also for monitoring a number of natural parameters of utmost importance (e.g. quality of air and water) is forcing researchers towards investigating (1) smart ways of miniaturizing and developing integrated electronic circuitry and compact sensors into portable devices and (2) new sensing materials in order to facilitate the stated miniaturization and integration and yet guaranteeing a reasonable sensitivity.

In this work, we propose nanostructured indium tin oxide (ITO) as a suitable material for developing working electrodes for electrochemical biosensing. In first place, the combination of interesting features such as electrical conductivity and optical transparency may make ITO suitable not only for electrochemical sensing but also for optical biosensors, or for developing a sensor based on the combination of both principles. Furthermore, the nanostructuration of the material may help increasing the sensor sensitivity, especially when miniaturizing the whole device and thus reducing the total geometric sensing area.

On the other hand, this work also includes some contributions to readout electronics for electrochemical biosensors. Some potentiostat prototypes were developed and tested in collaboration with other european institutions in the frame of the 7th Framework Programme project "Real time monitoring of SEA contaminants by an autonomous Lab-on-a-CHIP biosensor" ("SEA-on-a-CHIP", grant agreement number 614168). The description of the most relevant aspects of these prototypes, as well as the results obtained with adapted versions employed for measuring ITO-based electrochemical sensors, are presented in this work. With all, the main objectives of this thesis project can be itemized as follows:

- to develop nanostructured ITO electrodes by electron beam evaporation and to test their performance in an electrochemical environment, benchamarking these results agains those obtained with thin ITO films;
- to optimize the fabrication parameters in order to obtain good-quality nanostructured ITO electrodes offering maximum electrochemical sensitivity;
- to prove that nanostructured ITO electrodes can be successfully derivatized with crosslinkers of interest such as organosilanes or diazonium salts, and to characterize such derivatization by standard spectroscopic methods such as X-ray photoelectron spectroscopy (XPS) or Fourier transform infrared spectroscopy (FTIR);
- to develop a full immunoassay on nanostructured ITO used as working electrode, in order to detect biomolecules of interest by standard electrochemical procedures with commercial potentiostats;
- to design an appropriate electronic circuitry for miniaturizing potentiostats, focusing on the measurement of electrochemical impedance spectroscopy, potentiometry and amperometry;
- to design and develop a flexible and open-source graphical user interface to facilitate the operation of the developed portable potentiostats and

- to integrate electronics, hardware and software into a compact device with commercial or self-developed ITO-based electrodes for point-of-care testing.

1.2.2 Dissertation summary

As detailed along the previous sections, there is an increasing need for developing innovative, versatile and low-cost point-of-care (POC) systems capable of screening for diseases before severe symptoms appear, i.e. at early stages of development. POC systems usually consist of a biosensor part integrated in an electronic circuit and eventually a microfluidic system to manage the body fluid samples [21, 22]. The aim of this doctoral thesis is to investigate several ways of improving POC technology.

On the one hand, biosensors currently integrated into POC systems have limitations. Let us consider one of the most popular POC systems: the blood glucose detector. This is based on a lateral flow immunoassay, which consists in a set of capillary beds (e.g. porous paper or microstructured polymer) capable of carrying the sample fluid through them. Thus, the sample moves along the different capillary beds hosting several molecules with affinity for the target analyte that may be contained within the sample (exhaustive descriptions of how lateral flow assays work can be found in [23–25]). This way, precise qualitative indicators of the presence or not of the target analyte (such as glucose) in a sample (e.g. blood) are obtained. Home pregnancy tests work very similarly, and, as a matter of fact, these and blood glucose monitoring devices commercialized nowadays provide precise quantitative results [26, 27]. However, a wide variety of important analytes cannot be properly detected and quantified by means of a lateral flow immunoassay, and other methods supported by a powerful electronic systems that supply the necessary energy to trigger a measurable event that can be monitored are required. For this, adequate sensing substrates are required that allow the coupling of analytes and other biomolecules and enable the detection of chemical reactions occurring at their surfaces. Besides, the complex electronic circuitry capable of simultaneously exciting the sensor and monitoring its response must be redesigned into a low-cost and miniaturized format to be integrated into POC systems.

Leaving lateral flow assays aside, electrochemical and optical biosensors have become relevant in point of care technology due to the versatility of POC systems based on such transducing principles [28–30], which provide the sensors with high sensitivities and specificities. In particular, sensitivity may become badly affected by the miniaturization of sensors and devices. During the past years, gold [31–33], some polymers [34, 35] and some oxides [36, 37] have been widely used as sensing materials in electrochemical biosensors for providing high sensitivities. However, the need for reducing the surface of sensing electrodes and yet maintaining the sensitivity has boosted the research and development of nanostructures such as gold nanoparticles and gold or oxide-based nanostructured surfaces [38–44]. The high surface-to-volume ratio (SVR) presented by nanostructures makes them extremely interesting for the detection of biomolecules, since an increase of surface enables the interaction with a big amount of small-sized molecules and this implies an increase of sensitivity and the possibility to reduce the sensor size [45].

Nevertheless, the attention paid to transparent materials in the field of biodetection is limited and can be reduced to optical biosensors, with some exceptions [42, 46]. In this thesis, nanostructured indium tin oxide (ITO), a transparent conducting oxide, is

proposed as working electrode (WE) for electrochemical biosensors. Indeed, the transparency of ITO to optical and infrared wavelengths makes it a good candidate for optical sensors. Moreover, its electrical conductivity suggests it could also be employed in electrochemical sensors, and its nanostructuration would allow the reduction of the effective size of ITO-based devices so that they could be integrated into POC systems.

With all, the first part of this thesis consists in a study of ITO properties and its electrical, optical, electrochemical and structural characterization both as a thin film and as nanostructured electrodes prepared by electron beam evaporation onto silicon (R. Pruna *et al.*, 2016, Electrochemical characterization of organosilane-functionalized nanostructured ITO surfaces) and glass (R. Pruna *et al.*, 2019, Tuning the deposition parameters for optimizing the faradaic and non-faradaic electrochemical performance of nanowire array-shaped ITO electrodes prepared by electron beam evaporation) substrates. Moreover, the interaction of nanostructured ITO with some molecules known as crosslinkers, which allow subsequent functionalization of surfaces with biomolecules, has also been studied in the frame of this thesis (R. Pruna *et al.*, 2016, Organosilane-functionalization of nanostructured indium tin oxide films). Finally, several immunoassays were performed using nanostructured ITO as substrate, from the classical ones (involving bovine serum albumin –BSA– or the interaction between biotin and streptavidin) usually employed for testing the suitability of the substrates for biosensing, to the detection of several concentrations of tumour necrosis factor α (TNF–α), a heart failure biomarker extensively studied in the context of POC (Pruna *et al.*, 2018, Novel nanostructured indium tin oxide electrode for electrochemical immunosensors: Suitability for the detection of TNF–α).

On the other hand, we have also paid attention to the electronics integrating POC systems and complementing the biosensor. Several electrochemical sensor mechanisms were studied. These were based upon different ways of electrically attacking the sensor and processing its response, and included potentiometry, amperometry and electrochemical impedance spectroscopy. Potentiometry consists in measuring the open circuit voltage difference between two electrodes immersed in aqueous media, which will account for the amount of free ions in solution (the pH). Amperometry consists in applying a constant voltage level between the sensor and a reference electrode and measuring the current flow. This way it can be detected whether the target analyte is present in solution by observing its effects on the behaviour of the current as long as the system presents some redox activity at such level of voltage. Regarding the practical implementation of amperometry, this technique may be performed with two or three electrodes, just as electrochemical impedance spectroscopy, although the use of three leads is highly recommended. Concerning electrochemical impedance spectroscopy, a small AC voltage is applied between the sensor and the reference electrode whose frequency is varied with time, and the current level and phase shift are monitored between the sensor and an auxiliary electrode, thus obtaining a numerical value for the sensor impedance at each frequency. This way, the sensor behaviour may be fitted into an electronic model regarding the biochemical species interacting with its surface.

A low-cost and miniaturized device implementing electrochemical impedance spectroscopy measurements was designed and developed for the detection of several concentrations of TNF–α biomarker with an array of eight parallel gold-based microelectrodes (R. Pruna *et al.*, 2018, A low-cost and miniaturized potentiostat for sensing of biomolecular species such as TNF–α by electrochemical impedance spectroscopy). Besides, we

also designed the electronics for performing two-electrode amperometry and potentiometry. The latter was tested on nanostructured ITO electrodes covered with a doped conducting polymer, which was sensitive to pH changes in aqueous media.

To synthesize, this thesis gathers several proposals for improving current POC systems, regarding both the biosensor and the electronic parts, employing an important biomarker in the biomedical area for the measurements and proofs of concept, and being such approaches extensible to the environmental field.

1.2.2.1 Specific contributions

First, the contribution of ITO nanowires to the electrochemically active surface area was tested by cyclic voltammetry and benchmarked against the active surface area presented by thin ITO films. This was done with as-deposited as well as with annealed ITO electrodes prepared by electron beam evaporation, proving that there is indeed an increase in electroactive surface area provided by nanostructured ITO surfaces at a constant geometrical projection regardless of the crystallinity of the substrate.

Second, the fabrication of nanostructured ITO electrodes by electron beam evaporation was optimized in order to maximize the exposed electroactive surface area and hence its sensitivity to electrochemical reactions occurring at its surface. This was achieved by studying the influence of the configuration parameters during the evaporation process, especially the substrate temperature, on the electrical, optical and electrochemical performance of the resulting electrodes.

Third, a model for the formation of ITO nanowires on fused silica by electron beam evaporation based on the Stranski-Krastanov paradigm of epitaxial growth was proposed for the first time to our knowledge. This is suggested as a complement to the widely reported self-catalyzed vapour-liquid-solid (VLS) growth method, which we believe helps understanding not only the geometry of single nanowires but also the cross-sectional appearance of the resulting electrodes.

Fourth, transparent nanostructured ITO was employed for the first time to the best of our knowledge as a working electrode for the electrochemical detection of an important cardiac biomarker, tumour necrosis factor α (TNF–α). The processes of derivatization and functionalization of nanostructured ITO with electroaddressed reduction of diazonium salt and anti–TNF–α, respectively, were checked with spectroscopic techniques (FTIR) and also with fluorescence microscopy. Detection of several concentrations of TNF–α cytokine was performed by electrochemical impedance spectroscopy (EIS) with a commercial potentiostat.

Fifth, a low-power miniaturized potentiostat for electrochemical impedance spectroscopy analysis was designed and interfaced with a micropatterned gold working electrode array with integrated reference and auxiliary leads. Subsequent detection of TNF–α at increasing concentrations was performed and the results were benchmarked against those obtained with a commercial potentiostat, obtaining a straight correlation between the signal levels and species concentrations, as well as a good signal-to-noise ratio.

Finally, alternative potentiostat architectures for monitoring amperometry and potentiometry were designed and implemented. An open-source software-based graphical

user interface (GUI) was developed to interface the miniaturized device, which was tested on a nanostructured ITO electrode working as potentiometric sensor.

1.2.3 Organisation of the thesis

Chapter 1 includes the motivation of this thesis, with a historical overview on the origins and evolution of medical diagnosis. The chapter also includes some notes on the application of biosensors to food analysis and environmental care. Then, a summary of the present dissertation, together with an outline of the specific contributions of this thesis is provided.

An extensive background overview is provided in Chapter 2. The main topics discussed are three: (1) in-depth description of ITO from a solid-state physics point of view; (2) review on the basic principles of electrochemistry and electronics applied to potentiostatic measurements used along the thesis and (3) introduction of generalities about biosensors and immunochemistry, and description of the basic immunoassays studied during the thesis.

In Chapter 3, a thorough description on the ITO-based electrode fabrication and physicochemical characterization is provided. A comparison between thin films and nanostructured films regarding electrochemical surface area available for detection is presented, as well as the study of the influence of substrate temperature during material deposition on nanostructure features.

Chapter 4 includes the results of the experiments performed using nanostructured ITO as electrochemical biosensor. Specifically, the efforts were concentrated in carefully describing the necessary steps for preparation of the immunosensor, providing for that extensive characterization by a number of microscopy and electrochemistry techniques, and finally, performing immunodetection of several biomolecules as proof-of-concept.

In Chapter 5, two low-cost and miniaturized electronic devices for electrochemical biosensor testing are presented. Description of the electronic circuitry and software is exhaustively provided, as well as pros and cons of both systems. Furthermore, results on immunodetection performed with the manufactured electronic devices are provided and analysed, with a well-established gold-based biochip and with a nanostructured ITO-based prototype electrode.

Chapter 6 concludes this dissertation highlighting the most relevant aspects presented in the thesis.

1.2.4 List of publications

The publications itemized below are gathered as the main body of this dissertation. Each one is reproduced in the indicated pages with permission of the corresponding Journal.

Article I. R. Pruna, F. Palacio, M. López, J. Pérez, M. Mir, O. Blázquez, S. Hernández and B. Garrido, *Electrochemical characterization of organosilane-functionalized nanostructured ITO surfaces*, Applied Physics Letters 109 (2016) 063109. DOI: 10.1063/1.4960734.
The full article is reproduced on **page 69**.

Article II. R. Pruna, F. Teixidor and M. López, *Tuning the deposition parameters for optimizing the faradaic and non-faradaic electrochemical performance of nanowire array-shaped ITO electrodes prepared by electron beam evaporation*, Nanoscale 11 (2019) 276 – 284. DOI: 10.1039/C8NR07908K.
The full article is reproduced on **page 79**.

Article III. R. Pruna, F. Palacio, M. Martínez, O. Blázquez, S. Hernández, B. Garrido and M. López, *Organosilane functionalization of nanostructured indium tin oxide films*, Interface Focus 6.6 (2016) 20160056. DOI: 10.1098/rsfs2016.0056.
The full article is reproduced on **page 107**.

Article IV. R. Pruna, A. Baraket, A. Bonhommé, N. Zine, A. Errachid and M. López, *Novel nanostructured indium tin oxide electrode for electrochemical immunosensors: Suitability for the detection of TNF-α*, Electrochimica Acta 283 (2018) 1632 – 1639. DOI: 10.1016/j.electacta.2018.07.066.
The full article is reproduced on **page 120**.

Article V. R. Pruna, F. Palacio, A. Baraket, N. Zine, A. Streklas, J. Bausells, A. Errachid and M. López, *A low-cost and miniaturized potentiostat for sensing of biomolecular species such as TNF-α by electrochemical impedance spectroscopy*, Biosensors and Bioelectronics 100 (2018) 533 – 540. DOI: 10.1016/j.bios.2017.09.049.
The full article is reproduced on **page 143**.

Chapter 2

Theoretical background

The aim of this dissertation is to investigate all the parts composing a biosensing device, from the nature and shape of the material in the sensing element (coloured in pale red in Figure 2.1), to the transduction mechanism of the biosensor (pale green in Figure 2.1) and the signal conditioning and readout electronics (pale orange in Figure 2.1) interfacing the biosensor.

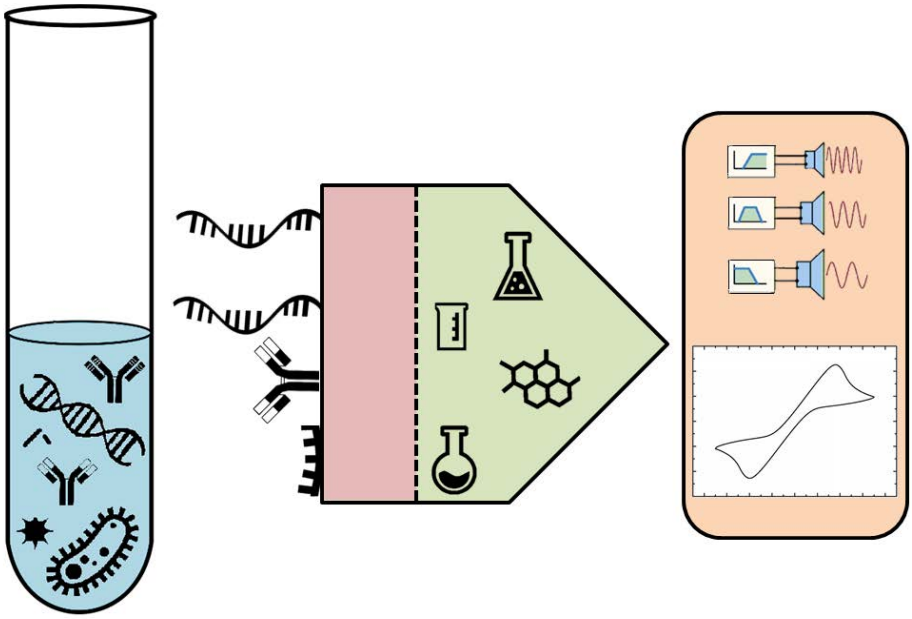

FIGURE 2.1: Schematic representation of a biosensing device, with three differentiated parts corresponding to sensing material (red), transduction mechanism (green) and signal conditioning and readout electronics (orange).

This chapter gathers some theoretical background on concepts employed along the thesis; for this, it is divided into three parts attending to the schematic shown in Figure 2.1: in Part I, an in-depth study of the physical nature of the sensing material (indium tin oxide in our case) is presented. In Part II, a detailed description of concepts of electrochemistry is provided, since this is the main transduction principle on which the developed biosensor is based. Moreover, Part II also compiles the main readout electronics configurations for electrochemical devices. Finally, Part III consists of a compendium of concepts on biosensors and the description of the immunoassays studied in this work.

2.1 Part I: The sensing material. Indium tin oxide

As previously highlighted in Chapter 1, this thesis orbits around indium tin oxide (ITO) as principal material used in almost all experiments. Indium tin oxide is a degenerate n-type semiconductor that, due to its structural features, combines high optical and near infrared (NIR) transparency and electrical conductivity, together with a high reflectance of the infrared (IR), being thus classified as a transparent conducting oxide (TCO). Other TCOs are zinc-doped oxide (ZnO), aluminium-doped zinc oxide (AZO) or fluorine-doped tin oxide (FTO) [47–49]. The interest in transparent conductors can be traced back to the beginnings of the 20th century, and these have been gold standards in optoelectronics, display devices and some mechanical applications. Among the wide range of metal oxides and alloys exhibiting high transmittance and electrical conductivity, ITO has always been one of the most employed and studied. Due to its rare and yet excellent electrical and optical properties, as well as a wide electrochemical window, ITO may provide high efficient ways for signal transduction as compared to traditional methods. Let us now revise some of the fundamental physical properties of this material, as well as the applications where it has been employed and the most used preparation techniques, each providing unique electrical and optical features and structure.

2.1.1 Properties of indium tin oxide

2.1.1.1 Physical and structural properties

ITO is usually referred to as "tin-doped indium oxide", which suggests that it consists of a large lattice of indium oxide with a small tin doping level. Let us then first understand the crystal structure of bare indium oxide (In_2O_3), whose formula in a lattice structure is $In_2O_{3-x}\,(V_O)_x$ [50]. Here, x accounts for the atomic portion of oxygen vacancies (generally $x < 0.01$), and V_O represents the donor-like oxygen vacancy. As reported by Mryason and Freeman [51], defect-free indium oxide presents a structure based on the superposition of two basic atomic distributions (Figure 2.2a): the first one (In_1 sublattice in Figure 2.2a) contains an indium atom at the centre of the cube and two missing oxygen atoms in the body diagonal, and all other corners occupied with oxygen atoms, being the medium atomic distance between them and indium of 2.18 Å; the second distribution (In_2 sublattice in Figure 2.2a) also contains the indium atom in the centre of the cube, but the missing atoms lie on the diagonal of one face, and other oxygens between 2.13 Å and 2.23 Å away from the central indium atom. Both incomplete body centred cubic structures are anion-deficient, and this oxygen vacancy population regulates the electron concentration and thus the oxide conductivity, with a free carrier concentration between 10^{19}–10^{20} cm^{-3} [52]. This atomic distribution (Figure 2.2b) is the basis to build the unit cell, which is defined as the smallest group of atoms containing the overall symmetry of a crystal and the three-dimensional translation of which results in the entire crystal lattice [53]. The In_2O_3 unit cell is shown in Figure 2.2c.

Soft external tin doping does not affect the crystal structure and yet enhances the properties of the material. For example, in the case of electrical conductivity, two mechanisms are possible when tin is doping the indium oxide structure: (1) if SnO is formed, Sn^{+2} acts as acceptor (in a In^{+3} lattice), it takes an electron; and (2) if SnO_2 is formed, this Sn^{+4} acts as donor and loses an electron. The latter is the dominating mechanism in ITO, and this is why tin-doping increases the carrier density in the material up to 10^{20}–10^{21} cm^{-3} [54] and thus the conductivity, provided there is no saturation (the carrier

density and other properties are summarized in Table 2.1). A strong doping can damage the lattice structure, for tin could interstitially replace indium, and the performance of the material would become hindered. To go further into the conduction mechanism, some basic concepts on solid state physics and electronic bands theory were gathered in Appendix A.

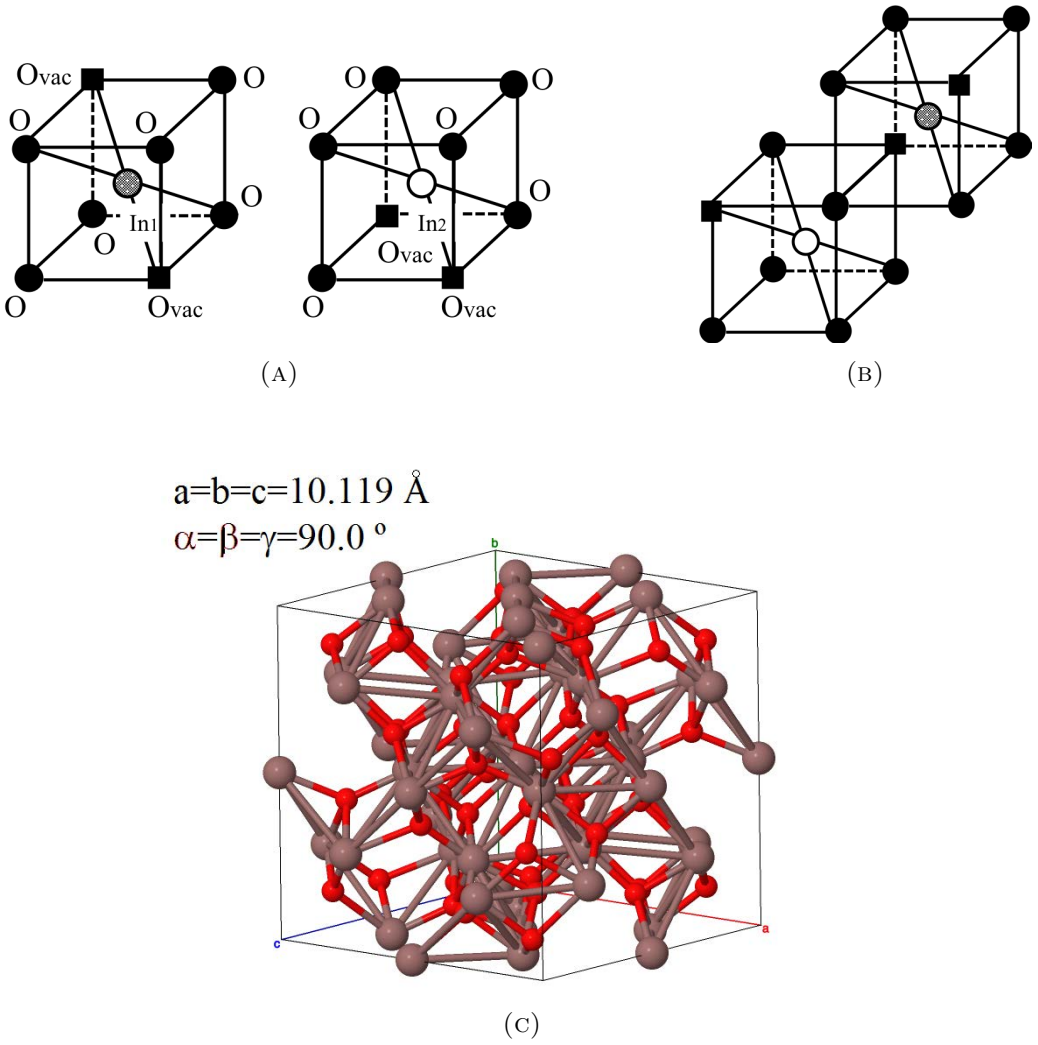

(A) (B)

(C)

FIGURE 2.2: (A) Schematic illustration extracted from [51] showing the atomic arrangements in In-O octahedra corresponding to In_1 and In_2 sublattices of the In_2O_3 lattice. Solid circles and squares correspond to oxygen atoms and oxygen vacancies, respectively. Shaded circles correspond to In_1 atoms, whereas open circles correspond to In_2 atoms. The merging of both sublattices is shown in (B), which was adapted from [55]. The adequate replication and positioning of such structure originates the unit cell, shown in (C) and extracted from [56]. Here, the red small spheres correspond to indium atoms whereas the brown bigger ones correspond to oxygen atoms.

As expected, the level of tin doping modulates the carrier density in the crystal structure and hence its electrical (and optical) properties. Theoretical and experimental dependence of carrier density with tin doping level can be observed in Figure 2.3. Clearly, a tin doping level around 10 % (atomic weight) is optimal in terms of carrier

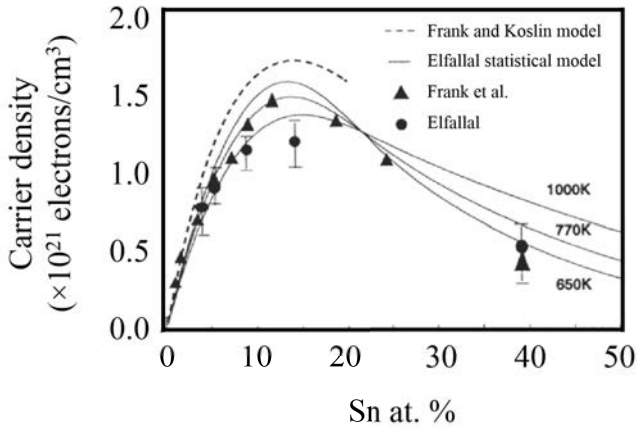

FIGURE 2.3: Several models and real data of carrier density as a function of the percentage of tin present in ITO. Extracted from [57].

density, with a value between 10^{21}–2×10^{21} cm^{-3} [58], at least an order of magnitude above bare indium oxide. This optimal degeneracy is believed to be caused by both oxygen vacancies and substitutional tin dopants created during the deposition of the film. Below 8 % tin doping, the carrier concentration decreases due to a distortion of the lattice structure by tin oxide [59]. Above 20 % tin doping, the probability of two or more tin atoms occupying adjacent cation positions increases (this means that part of the defective donor levels are being compensated), diminishing the conducting properties of the crystal structure [60].

TABLE 2.1: Electrical and optical properties of ITO electrodes typically reported in the literature, extracted from [61], who in turn adapted them from [58].

Sheet resistance R_s ($\Omega\square^{-1}$)	4–10^{-4}
Electrical conductivity σ (Ω^{-1} cm^{-1})	30–2.3×10^4
Carrier concentration N (cm^{-3})	10^{20}–10^{21}
Hall mobility N (cm^{-3})	10–70
Transmission (visible region) T	80–95
Reflection (infrared region) R	80–90
Band-gap E_g (eV)	3.0–4.6
Refractive index n	1.8–2.1
Effective mass m^*/m_o	0.30–0.35

As can also be observed in Figure 2.3 and Figure 2.4c, the film conductivity of thin ITO films also depends on substrate temperature and post annealing processes. It can be appreciated that an increase in substrate and annealing temperatures tends to decrease the sheet resistance of the films (Figure 2.5a) as a result of a reorganisation of the crystal lattice, achieving a maximum in conductivity around 300 °C. This can be attributed to the generation of oxygen-deficient films at these temperatures, which in turn contributes to reducing the interplanar spacing after annealing (Figure 2.5b) [62]. The X-ray diffraction (XRD) technique has been employed to characterize the crystal structure of most of the surfaces developed up to now, including ITO films. Commercial

ITO substrates show a polycrystalline structure with the (222) as the dominant crystallographic plane (Figure 2.5). Regarding home-made ITO, the temperature of deposition is fundamental to modulate the degree of crystallinity of the resulting films. In the particular case of this work, the ITO films were deposited by electron beam evaporation and experiments were conducted at a substrate temperature ranging from 100 °C to 600 °C. Only samples grown at 100 °C showed a completely amorphous structure, yet after a process of annealing at high temperature in a controlled atmosphere the atoms in the lattice reorganize in a crystalline fashion, dramatically increasing both the transparency and conductivity, as expected. Samples grown at substrate temperatures higher than 200 °C presented a nanostructured morphology,

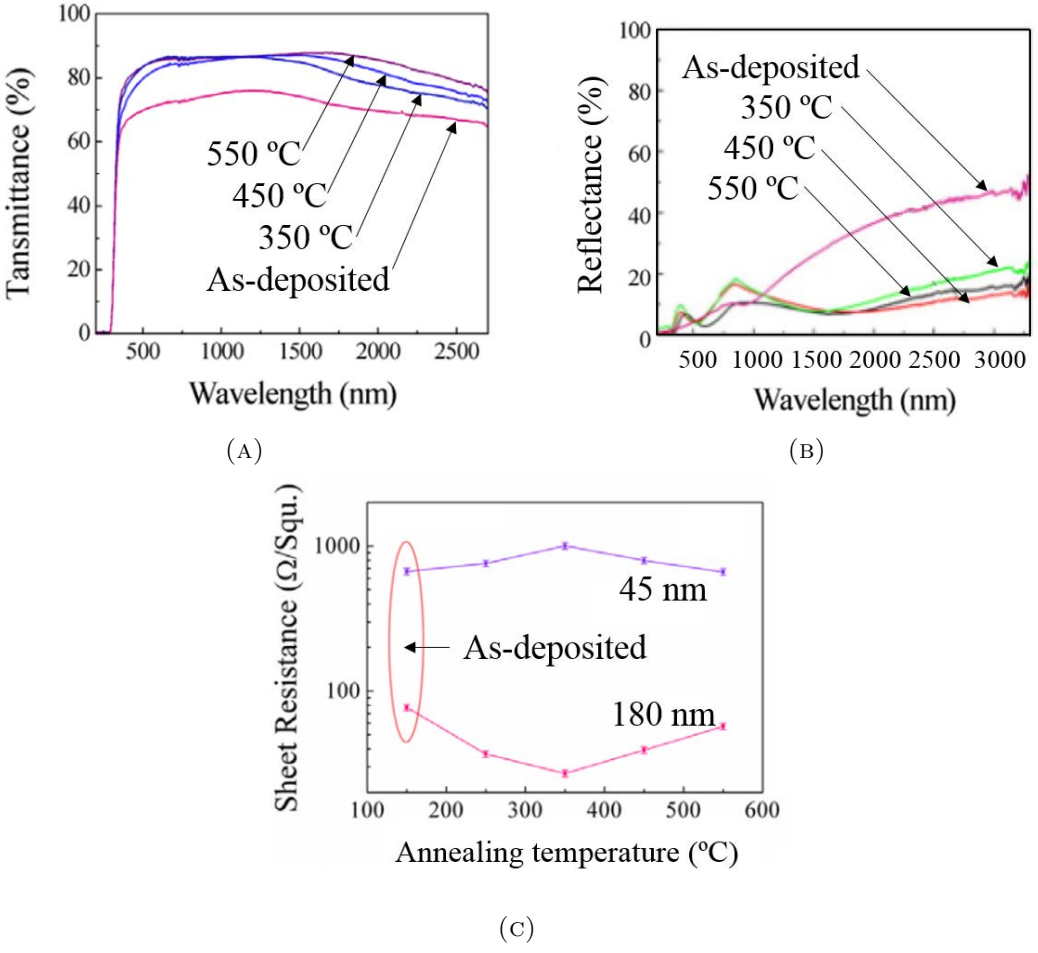

FIGURE 2.4: (A) Transmission spectra for 45 nm thick ITO films prepared by electron beam evaporation and annealed at several temperatures in N_2 atmosphere. (B) Reflection spectra for ITO films deposited without oxygen and anneled at several temperatures. (C) Dependence of sheet resistance with annealing temperatures for 45 nm and 180 nm thick ITO films prepared by electron beam evaporation. All subfigures were extracted from [63].

The different behaviours of optical properties of ITO films with post-annealing temperature are also shown in Figure 2.4. The kind of substrate and thickness of deposit are also very influent in the degree of optical transparency of the films, as well as the level of impurities and microstructures in the film. The mechanism of optical transparency again depends on the band gap width. In the case of *n*-type semiconductor

TCOs, the promotion of an electron from the valence to the conduction band requires more energy than that of visible radiation photons, and so the absorption of radiation by the TCO begins at higher energies (below 500 nm in Figure 2.4b) than the typical energy of undoped oxides. Dopants take free levels closer to the conduction band, where the electron can be easily promoted, hence causing a high reflectance and a degree of absorption at low energies (infrared radiation) modulated by the dopant and oxygen vacancy percentage. Eventually, high energy photons (ultraviolet radiation) are able to provide the energy required to excite electrons to the conduction band, thus involving a high absorption level. It has been shown that tin-doping increases both transmittance and reflection [59].

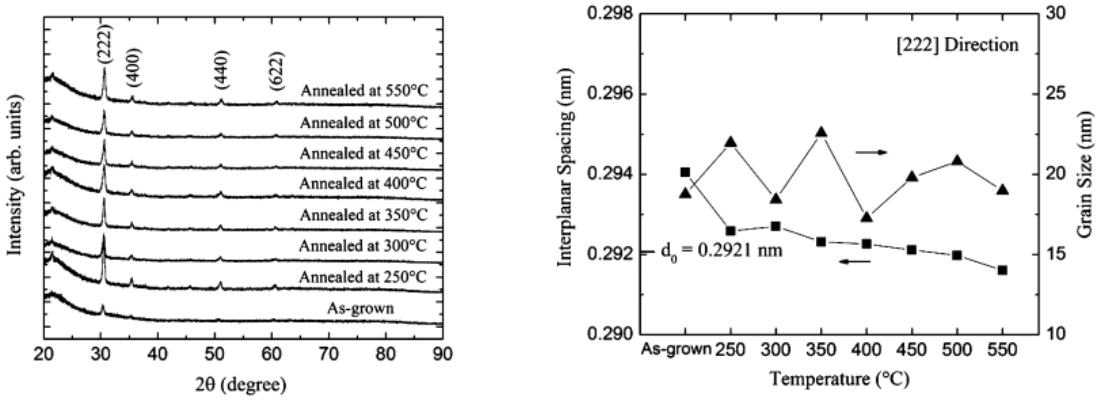

(A) (B)

FIGURE 2.5: (A) X-ray diffraction patterns of as-deposited and annealed ITO films. (B) Graing size and interplanar spacing along the (222) crystal direction as a function of post-annealing temperature for ITO films. Both subfigures were extracted from [62].

2.1.1.2 Chemical properties

In this subsection we provide some chemical features of indium tin oxide films, related to their bulk and surface compositions, and also to the kind and degree of reactivity in determined media.

The deposition technique introduces changes in the bulk composition and other properties of the films, as well as in the properties and shape of other structures which are of interest in this thesis (i.e. nanowires, as will be explained in Section 2.1.3). On the other hand, the post-deposition treatments introduce changes in the surface features. Such post-deposition treatments can be mechanical (e.g. scrubbing with cleaning solution followed by ultrasonication for removing surface contamination), wet (e.g. *piranha*, *aqua regia*[1] or acid or alkaline solutions) and dry (e.g. air, hydrogen, argon or oxygen plasma treatment for cleaning and also for modifying surface morphology and chemical or electrical properties). In particular, piranha treatment and air plasma have been shown to increase significantly the level of surface hydroxyde coverage [64]. This is of

[1] *Piranha* solution is a mixture of sulfuric acid (H_2SO_4) and hydrogen peroxide (H_2O_2), typically at a proportion of 3 parts of the former and 1 part of 30 % hydrogen peroxide, although this may vary regarding the cleaning protocol being followed; *aqua regia* is a mixture of nitric acid (HNO_3) and hydrochloric acid (HCl), typically at a molar ratio of 1:3.

utmost importance for surface derivatization and functionalization, for the attachment of organic molecules onto metallic and oxide surfaces needs reactive radicals to interact with them [65, 66].

Surface chracterization of ITO films has been basically accomplished by techniques such as X-ray photoelectron spectroscopy (XPS), which has proved useful in providing details on surface chemical states and element composition [67–69]. An exhaustive description of surface composition of thin film and nanostructured ITO electrodes prepared by electron beam evaporation measured by XPS is provided in Article 4.1.1 [70] presented in this dissertation. Briefly, from the O1s peak we can obtain most of the information on the surface composition of the films; it can be typically adjusted by three gaussian-lorentzian curves, accounting for In_2O_3-like and Sn-bound oxygen (529.8 eV), oxygen adjacent to oxygen-deficiency sites (521.0 eV), oxygen from hydroxyde and oxy-hydroxide (532.1 eV) and oxygen from adventitious contaminants [64, 70, 71]. The $Sn3d_{5/2}$ and $In3d_{5/2}$ peaks are fitted to SnO_2-like, SnOH-like and In_2O_3-like, $In(OH)_3$-like species, respectively.

With all, the hydrolysis of indium oxides is generally more favoured than for tin oxides at any pH, and can occur in a complete (Equation 2.1) or incomplete (Equation 2.2) way:

$$In_2O_3 + 3H_2O \longrightarrow 2In(OH)_3 \tag{2.1}$$

$$In_2O_3 + H_2O \longrightarrow 2InOOH \tag{2.2}$$

Concerning the behaviour of ITO molecules in solution, it is worth having a look at the isoelectric point (IEP) concept. The IEP is the pH at which a molecule (understood as the average molecule out of a set of molecules) is electrically neutral, i.e., it carries no net electrical charge. This is directly affected by the pH of the surrounding environment; indeed, the molecules can become positively (negatively) charged due to the gain (loss) of protons.[2] ITO has a IEP of 6 [72], which means it can be easily dissolved either in strong acids or in strong alkaline solutions. Besides, its chemical structure is not affected when stored for a long period in atmospheric conditions, since it is inert to most atmospheric gases.

2.1.2 Common preparation methods

Several deposition methods have been reported for preparing ITO films, and these can be divided into physical [73–78] or chemical [79–82] techniques. In this section, the most popular of them are briefly described. Table 2.2 gathers some general features of some of the most popular material deposition techniques, and details on the characteristics of ITO films prepared by each method are provided along the following subsections.

It is worth mentioning that nanostructured ITO surfaces cannot be prepared by all of the techniques described below. Information on the suitability of each technique for the preparation of nanostructured ITO electrodes will be provided at each corresponding subsection. Moreover, Section 2.1.3 is devoted to ITO nanostructuration, and details on the physical processes leading to the formation of nanostructures are provided there.

[2] `https://en.wikipedia.org/wiki/Isoelectric_point`.

2.1.2.1 Chemical vapour deposition (CVD)

Chemical vapour deposition consists in the reaction of one or more gaseous reactive species on a solid substrate; in the case of ITO, such species use to be organometallic compounds, e.g. indium 2-ethyl hexanoate, indium and tin acetyl acetonates and tin chloride [83, 84]. An inert gas (such as Argon) carries the vapour containing the condensate material from the evaporation zone to the reaction zone, where it reacts with the substrate. Plasma-enhance and low-pressure CVD are the most popular CVD variations.

In plasma-enhanced chemical vapour deposition (PECVD), a reacting plasma[3] is created out of the gases by alternating current (AC) or direct current (DC). In low-pressure chemical vapour deposition (LPCVD), the diffusion of the gases decreses proportionally to the reciprocal of the pressure, thus decreasing the velocity of mass transport; this results in highly uniform and homogeneous films. Variations in pressure maintaining low temperatures can be achieved by working with non-thermal plasmas. On the other hand, LPCVD can only be performed at high temperatures.

The morphology of the resulting films is highly dependent on deposition parameters (e.g. difference of temperature between reaction and evaporation zones, gas flow rate) and on the nature of the chemical reaction [83]. Advantages of preparing ITO films by CVD include reproducibility and (relative) cheapness, and the possibility to do it without the need for high vacuum and for large-scale applications.

2.1.2.2 Spray pyrolysis

This technique consists in spraying a metallic compound dissolved in a liquid mixture with a spray nozzle onto a preheated surface, where it experiences pyrolytic decomposition. Reproducible and homogeneous films may be produced by finely controlling parameters such as the thickness and substrate temperature, the distance between the nozzle and the substrate and total deposition time [58, 85–87]. Concretely, the substrate surface temperature is the most critical parameter, since it influences the film roughness, crystallinity and cracking degree, amongst others.

2.1.2.3 Sputtering

Here, the target and substrate holders are used as cathode and anode, respectively, and the chamber is filled with an inert gas with a pressure between 10^{-2}–10^{-3} Torr. A voltage applied between the cathode and the anode induces the formation of a plasma, and the target material (contained in the target holder) is intensely bombarded by plasma ions and eventually ejected from the cathode towads the anode, where it becomes uniformly deposited. The sputtering system may be powered either in direct current (DC) or in radio frequency (RF) mode, both useful for conducting targets and only the latter apropriate for non-conducting ones. Both DC and RF sputtering have been reported as methods for ITO growth [89–92]. Parameters such as the sputtering rate, substrate temperature and gas composition and pressure have a strong influence on the quality of the resulting films [58].

[3] A plasma is a partially ionized gas with a high content (around 50 %) of free electorns; plasmas can be cold (non-thermal) or thermal. In the latter, electrons and gas particles are at the same temperature, whereas in cold plasmas the electrons present a much higher temperature than that of the ions and neutral atoms.

2.1.2.4 Atomic layer deposition (ALD)

Atomic layer deposition is similar to CVD in that a thin film deposit is achieved by gas phase chemical processes. However, ALD typically uses two chemicals or precursors that are alternately presented to the reacting surface. The film is slowly deposited through the repeated exposure to separate precursors. Advantages presented by the ALD method include high control and precision in film thickness and thermodynamics. However, ALD is an expensive, slow and material-limited method [93].

2.1.2.5 Electron beam (vacuum) evaporation

The electron beam is generated by resistively heating a tungsten or tantalum source under high vacuum (typically between 10^{-4}–10^{-5} Torr), and it is deflected by a magnetic field towards the target material (usually in the form of pellets) contained in a crucible, which is sublimated into the gaseous phase. The material can be evaporated directly or rather in the presence of oxygen [88] onto a substrate which can be heated up to high temperatures. The substrate on which the material is deposited rotates during the whole process in order to get a uniformly deposited film. A schematic of the experimental setup for electron beam evaporation is shown in Figure 2.6. Film roughness may be achieved by mounting the substrate at a steep angle with respect to the material flux in the so-called glancing-angle deposition (GLAD) method.

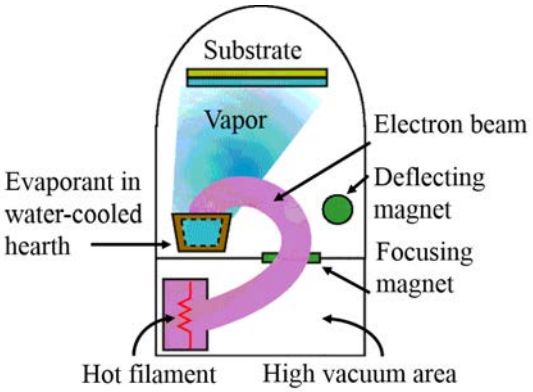

FIGURE 2.6: Electron beam evaporation system.[4]

Compared to other deposition processes, electron beam evaporation provides a high material utilization efficiency. Moreover, a deposition rate as low as 1 nm per minute can be achieved, allowing a very precise control on the thermodynamics and geometry of the films. On the other hand, some disadvantages of electron beam evaporation include a potential degradation of the electron gun filament that could result in a non-uniform evaporation rate; moreover, the rotational motion of the substrate holder is useless for coating the inner surfaces of complex geometries. Due to a positive balance between the pros and cons and due to the previous experience of some members in the research group in which this thesis was conducted, electron beam evaporation was chosen as the method for preparing the ITO samples employed in the experimental part of this work.

2.1.2.6 Others

Some other techniques have also been reported for preparing ITO films of relatively good quality and/or cost-effective. For instance, electroless chemical growth and the sol-gel technique consist in dipping a substrate into a solution of metal hydroxides, and then heating the coated surface for yielding the desired metal oxides [95, 96].

[4] `https://www.tungsten.com/how-does-electron-beam-evaporation-work/`.

TABLE 2.2: Qualitative features of some thin film deposition methods. Extracted from [94].

Process	**Material**	**Substrate temperature (°C)**	**Deposition rate (Å s^{-1})**	**Directionality**	**Uniformity**	**Film density**	**Grain size (nm)**	**Impurity level**	**Cost**
Thermal evaporation	Metal or low-melting point materials	50-100	1-20	Yes	Poor	Poor	10-100	High	Very low
E-beam evaporation	Both metal and dielectric	50-100	10-100	Yes	Poor	Poor	10-100	Low	High
Sputtering	Both metal and dielectric	-200	Metal -200, Dielectrics 1-10	Some degree	Very good	Good	-20	Low	High
PECVD	Mainly dielectrics	200-300	10-100	Some degree	Good	Good	10-100	Very low	Very high
LPCVD	Mainly dielectrics	600-1200	Metal -100, Dielectrics 1-10	Isotropic	Very good	Excellent	1-10	Very low	Very high
Thermal ALD	Mainly dielectrics	50-300	0.1-1	Isotropic step conformal	Superior	Superior	1-10	Very low	Very high
Plasma ALD	Mainly dielectrics	20-200	0.1-1	Isotropic	Superior	Superior	1-10	Very low	Very high
Spatial ALD	Mainly dielectrics	20-200	1-10	Isotropic step conformal	Superior	Superior	1-10	Very low	High

2.1.3 ITO nanowire growth by vapour-liquid-solid (VLS) mechanisms

Thin ITO films have found many applications (as will be detailed in the following section), and research was focused on the film properties as deposited by various methods. However, during the last few years, the growth of ITO nanostructures has gained much attention due to the improvement in the performance of many applications (further developed in Section 2.1.4). This is mainly due to an increased surface offered as a result of nanostructuration, and also due to an enhanced mechanical flexibility over thin film electrodes, which usually form cracks when employed in flexible device applications [100–103].

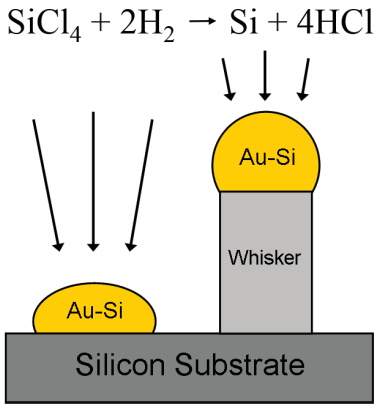

FIGURE 2.7: Growth mechanism of a silicon nanowhisker from the reaction of the vapor phases of $SiCl_4$ and H_2.[5]

Many of the previously described methods are suitable for growing ITO nanostructures, although physical ones have been reported more frequently: electron beam evaporation [76, 77, 104, 105], sputtering [74, 75] and pulse laser deposition [78], amongst others. Of these, electron beam evaporation provides nanostructured ITO electrodes of a high quality and in a relatively easy way. In this frame, mainly two mechanisms for ITO nanowire growth exist: vapour-liquid-solid (VLS) and self-catalytic VLS, which require relatively high growth temperatures between 700 °C–1000 °C and 250 °C–600 °C, respectively [77, 106].

2.1.3.1 The VLS method

The VLS method is a mechanism by which the growth of a crystal by adsorption of a gas phase on a solid surface is achieved in a quick way thanks to liquid alloy catalyzers. These act as nucleated seeds at the substrate surface, absorbing vapour at supersaturation levels and inducing the crystal growth. The method was first proposed to explain silicon whisker growth from silicon gas in presence of liquid gold droplets on silicon substrates [107]. ITO nanowhiskers have also been prepared by the VLS method, also using gold as catalyzer [106]. In this case a thin gold layer (< 5 nm) is sputtered or evaporated onto a silicon or quartz substrate. Then, the wafer is annealed at a temperature above the gold-silicon eutectic point,[6] thus creating gold-silicon alloy droplets, which will catalyze the chemical or physical growth of nanowires in the presence of ITO in vapour phase. Thermodynamically, the presence of alloy droplets on the substrate surface lowers the activation energy of traditional vapour-solid growth. Finally, ITO vaporized atoms adsorbed on the silicon-gold seed precipitate out of the droplet at the liquid-alloy/solid-silicon interface, thus rising the droplet from the surface (as observed in Figure 2.7).

[5] By Brandon Howe in Wikipedia (Vapor–liquid–solid method), `https://en.wikipedia.org/wiki/Vapor$%$E2$%$80$%$93liquid$%$E2$%$80$%$93solid_method`.

[6] The eutectic point of an homogeneous mixture is the unique temperature at which it solidifies or melts, and it is lower than the melting or solidifying temperature of the separate constituents.

2.1.3.2 The self-catalyzed VLS method

The self-catalyzed VLS method is similar to the previously described one, except for that no external catalyzer atoms or molecules are introduced now, but the same electrode material acts as catalyzer. A quick look at the binary phase diagram of the In–Sn system (Figure 2.8) reveals that its the eutectic point is located around 125 °C. Some studies [77, 108] have demonstrated that at substrate temperatures around 100 °C, indium and tin are in the solid state, and hence no In–Sn alloy is formed because the temperature is below the melting points of indium and tin and the eutectic point of the alloy. This non-catalytic activity of the material compounds results in the absence of nanowire growth.

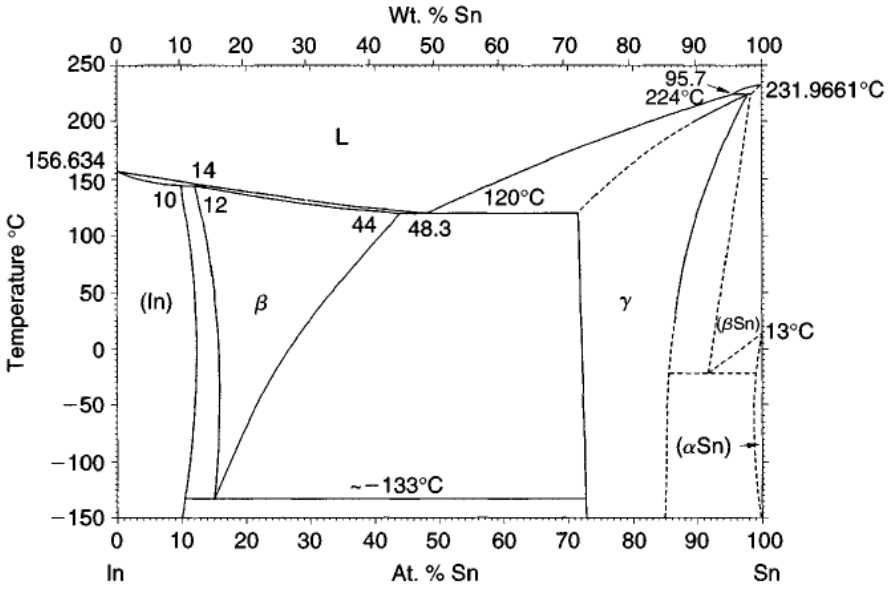

FIGURE 2.8: In–Sn phase diagram. Extracted from [109].

At higher temperatures, branched nanowhisker growth is observed. Similar to those growth by the VLS method, the self-catalyzed nanowhiskers present the catalyst particle at their tips, which has been confirmed to be made of the same material as the nanowire by micrograph techniques [108], thus adding evidence to the self-catalytic VLS hypothesis. With all, the self-catalytic VLS growth occurs due to the formation of a In–Sn liquid alloy above its eutectic point which promotes the growth of the nanowhiskers by collecting vapour atoms; this occurs because the sticking coefficient of the catalyst particle is higher than that of the surface [107, 110, 111]. The morphology of ITO nanowhiskers depends largely on the substrate temperature, deposition rate, presence or absence of oxygen during deposition and vapour incident angle, amongst others, and their electrical properties can be tuned in order to optimize the desired outputs [108].

2.1.4 Applications of ITO films

- **Touch panels (TP)**. TPs are input devices that are generally layered on top of an electronic display and enable the user to control information processing systems through simple or multi-touch gestures. They can be found in smartphones, personal digital assistants (PDAs), tablets and point-of-sale (POS) systems, amongst others. Several technologies have provided different methods for sensing touch,

including resistive, surface acoustic wave, capacitive, infrared and optical based approaches, amongst others. Of these, capacitive based touch panels can be found in most of the devices implementing this technology. Capacitive sensing is based on detecting and measuring a dielectric different from air (e.g. a fingertip). For this, an insulator (typically glass) is coated with a transparent conductor (e.g. ITO) and is integrated in an electrical design such that a touch on its surface results in a distortion of the screen's electrostatic field. Such distortion is measured as a change in capacitance. Since the transparent conductor coating is pixel-wise distributed, the location of the touch can be easily determined and sent to a microcontorller for processing.

- **Electrochromic devices (ECD)**. ECDs reversibly control the optical properties (transmission, reflectance, absorption, emittance) of a material on application of voltage, including smart glasses, electrochromic mirrors and electrochromic displays. The structure of ECDs is based on two transparent conducting electrodes sandwiching an ion storage layer, an electrolyte and an electrochromic layer. The former is a pure ion conductor (niquel oxide has been very popular recently [118–120]), whereas the latter requires a material that changes colour upon electrochemical reduction and oxidation (e.g. Prussian blue or tungsten oxide). Thus,

Table 2.3: Summary of the role of ITO in several electrooptical applications, as well as the improvement introduced by the replacement of thin films by nanostructured ITO electrodes. No relevant information was found on nanostructured ITO-based LCDs and HRCs.

Applic.	**Role of ITO**	**NW improvement**	**Refs.**
TP	First or second piezoelectric transparent electrode	Nanostructured surfaces present a higher piezoelectric constant and improve the performance of non-contact TP	[112]
ECD	Working electrode for charge transfer	Increase in contrast ratio between On-Off states by having large surface area electrodes	[113]
ELD	Transparent top contacts to light-emitting devices	The nanostructured geometry maximizes the spectral emission and there is no need for multistep deposition of defect-free layers for reducing refractive indexes (which would hinder the film conductivity)	[114, 115]
GS	Surface for electronic charge transfer in the presence of reducing gas	More than 7 times response to acetone increase of nanowires compared to thick wires at 400 °C	[116]
PV	Transparent top contact for heterojunction solar cells	Large surfaces for increased light absorption and short charge extraction distances for the full relevant wavelength and incident angle ranges, improving the efficiency and short-circuit current	[73, 117]

electrons move from the transparent conductor into the electrochromic material whereas charge balancing ions enter from the electrolyte at a determined voltage, enabling the adequate redox reactions. Two operation modes are available for these devices: the transmittance mode for smart glasses and the reflection mode for electrochromic mirrors and displays (the latter can also operate in transmittance mode). When operating in reflection mode, one of the transparent conducting layers is replaced with a reflective surface in order to gain control over the intensity of the reflective light.

- **Electroluminescent displays (ELD)**. These also consist in a sandwich-like structure with an electroluminescent material (e.g. gallium arsenide) between two conducting electrodes (an opaque one and a transparent one to let light out). The inner material emits light at current passing through it (as a result of a voltage difference between the external electrodes) due to atoms excitement.

- **Liquid crystal displays (LCD)**. LCDs are a very popular type of flat panel displays that can be found in televisions, computer monitors, instrument panels, digital cameras and watches, amongst others, and whose operation principle is based on the light-modulating properties of liquid crystals. Liquid crystals are materials that combine some properties of conventional liquids and some of solid crystals: they flow like liquids but keep an order degree in the arrangement of their molecules. Regarding the orientation of the molecules, which can be modulated by an applied voltage, these liquid crystals can act either as light polarizers or as repolarizers (i.e. they can change the polarization of light). The typical configuration of a LCD consists of a liquid crystal sandwiched by two transparent conducting electrodes (one of them patterned with what ought to be displayed), and these in turn sandwiched by two perpendicular polarizing filters. Finally, either a light source or a reflective surface is placed at the back of the pixel (regarding the viewer). A full display is composed of several of such pixels, and can be employed to display images (from seven segments displays, preset words or digits or even television images).

- **Heat reflective coatings (HRC)**. These are also called insulative or insulating paints, and consist of some specific micro-spheres coated with a broad spectrum thermally reflective material able to reducing heat transfer through the coating in around 90 % [121].

- **Gas sensors (GS)**. Gas sensors can detect and quantify the presence of specific gases; as usual, they are classified according to the mechanism on which they are based: oxidation, semiconductors, infrared, catalytic, etc. In particular, the operation principle of a semiconductor gas sensor consists in a change in its electrical conductance as a result of a chemical reaction between the surface and the target gas. Tin oxide has been a very popular semiconductor material with gas sensing applications, and its electrical properties have been tuned by doping with several elements in order to improve the sensitivity and selectivity to specific gases. ITO has been reported as carbon dioxide, carbon tetrachloride, nitric oxide, nitrogen dioxide, methanol and chlorine gas sensor [122–127], amongst others.

- **Photovoltaics (PV)**. The photovoltaic effect is a physicochemical phenomenon that experiences a material creating a voltage difference and a current flow at the exposure to light. Such materials typically are semiconductors, and in general terms, photovoltaics consists in transforming ligth into electricity. This occurs at

solar (or photovoltaic) cells, which can be made of a single layer of light-absorbing materials and called single-junction cells; or can be made of several physical configurations to take advantage of the maximum number of absorption mechanisms, and are called multi-junction cells. Traditionally, ITO has been employed in the past as a transparent conducting electrode for multi-junction solar cells [128, 129], although it has been lately replaced by cheaper conducting polymers and other metals [130–132].

The use of transparent conducting ITO electrodes for biosensing applications has only been popular recently, and the most striking examples reported in the literature will be provided in Section 2.3.1.2.

2.2 Part II: The methodology. Electrochemistry

Along Part I in the present chapter, physicochemical aspects of the material (ITO) employed in the fabrication of electrodes were studied. The purpose of Part II is to revise the main aspects in the theory of electrochemistry and potentiostatic electronics, since the main objective of this thesis is to utilise ITO as working electrode for electrochemical biosensing. purposes.

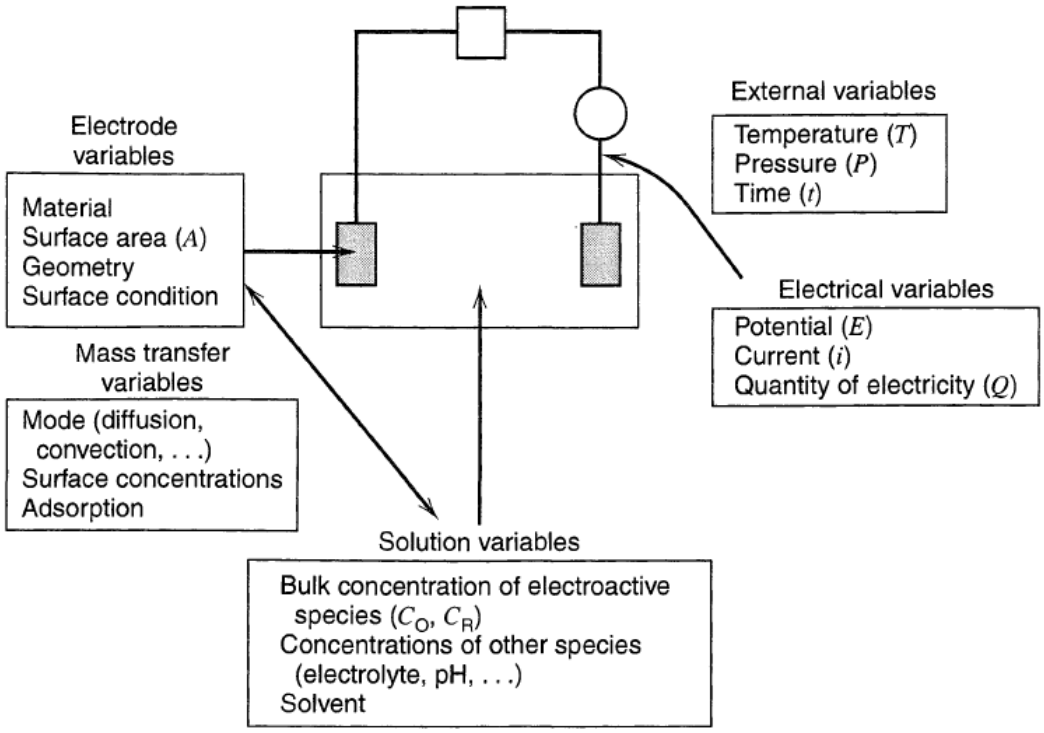

FIGURE 2.9: Schematic arranging the variables that affect the rate of electrode reactions. Extracted from [133].

Figure 2.9 shows a schematic where several groups of variables affecting the rate of electrode reactions are highlighted. These are discussed in Section 2.2.1, together with the description of the electrode-solution interface and the electrical equivalent circuits used to model this interface in the two possible working regimes: faradaic and non-faradaic current modes. In Section 2.2.2, a brushstroke of the kinetics of electrode reactions is presented. A complementary electrochemical impedance technique, the Mott-Schottky analysis, which is used to study semiconductor electrode-solution interfaces, is presented in Section 2.2.3 due to its importance along Chapter 3. Finally, the electrochemical measurement techniques employed in this work are described in Section 2.2.4 together with the suitable potentiostat electronic configuration in each case.

2.2.1 Variables affecting the rate of electrode reactions

2.2.1.1 Mass transfer

Mass transfer is described as the transport of material from one location in solution to another as a result of differences in intensive properties of the system at both locations [133]. The three known mass transfer modes are:

Migration Motion of charged species as a consequence of a potential gradient, i.e. an electrical field.

Diffusion Motion of charged or uncharged species as a consequence of a concentration gradient, i.e. a chemical potential.

Convection Motion of species as a consequence of density gradients (natural convection) or external fluid stirring (forced convection).

Such mass transfer modes and their influence in electrode reactions are gathered in the Nernst-Planck equation (Equation 2.3), whose one-dimensional version is written as

$$J_i(\boldsymbol{r}) = -D_i \boldsymbol{\nabla} C_i(\boldsymbol{r}) - \frac{D_i z_i F}{RT} D_i C_i \boldsymbol{\nabla}\phi(\boldsymbol{r}) + C_i \boldsymbol{v}(\boldsymbol{r}). \tag{2.3}$$

In the Nernst-Planck equation, the three mass transfer modes can be clearly identified. In the first term of the equation, the gradient of the species concentration, $\boldsymbol{\nabla} C_i(\boldsymbol{r})$, appears weighted by the species' diffusion coefficient (D_i); it corresponds to diffusion. The second term consists in the contribution of migration, for the gradient of the electrical potential, $\boldsymbol{\nabla}\phi(\boldsymbol{r})$, appears weighted by the species' concentration and diffusion coefficient, as well as other thermodynamical factors. Finally, the third part of the equation consists in the advection term accounting for convection; this is represented as the velocity $\boldsymbol{v}(\boldsymbol{r})$ of a volume element in solution (at position $\boldsymbol{r}$) by the concentration C_i of species i at that position. In Equation 2.3, J_i is the flux of the ith species at $\boldsymbol{r}$ measured with respect to the coordinates origin at the electrode surface, and z_i is the charge of species i.

A minimisation of the effects of mass transfer processes is important for the study of real electrochemical systems. The convection efffect is easiliy avoidable if no vibrations or stirring occur in the system, in other words, if the solution is in static equilibrium. On the other hand, the influence of eventual electrical fields can be minimized by adding to the redox species of interest an inert supporting electrolyte at much (generally ten times) higher concentrations than the former species.

2.2.1.2 External variables: thermodynamics of electrochemical cells

The usage and evaluation of any physicochemical system and the theoretical description of its behaviour needs to be done assuming some more or less severe stability conditions. Usually, the most important condition to be met is *reversibility*. Reversibility is essential for achieving a thermodynamic description of the physicochemical system.

In the case of electrochemical systems, prior to thermodynamic reversibility, chemical reversibility must be accomplished. Only if the latter exists, thermodynamic reversibility can occur, although not necessarily:

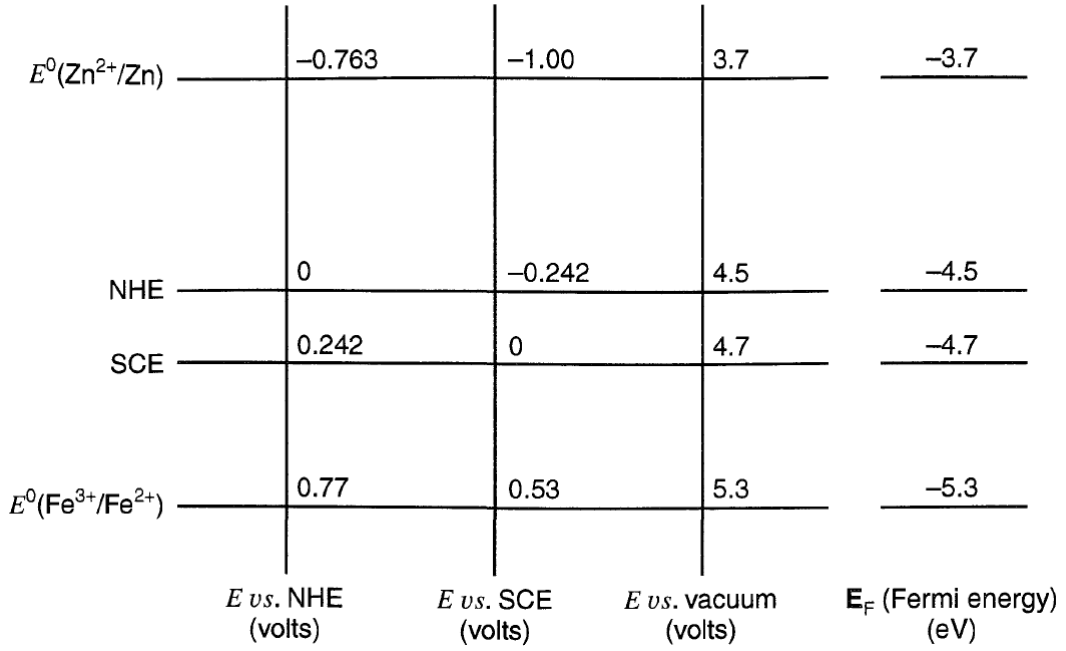

FIGURE 2.10: Schematic relating the potentials on the NHE, SCE and "absolute" scales. Extracted from [133].

$$\text{Thermodynamic stability} \longrightarrow \text{Chemical stability},$$
$$\neg\text{Chemical stability} \longrightarrow \neg\text{Thermodynamic stability}.$$

But, what is understood by *chemical reversibility*? In electrochemistry, the object of study are reduction-oxidation (redox) reactions taking place at an electrode, which implies the exchange of electrons between the electrode surface and the species undergoing reaction. The oxidant agent (O) is itself reduced by capturing an electron, and on the contrary the reducing agent (R) is oxidized by giving an electron, as summarized in Equation 2.4:

$$\mathrm{O}^{n+} + n\mathrm{e} \rightleftharpoons \mathrm{R}^{n-}. \tag{2.4}$$

Each redox reaction occurs at a characteristic potential (needs an exact energy), and thus the current flows from the electrode to the species in solution or *viceversa*. A chemically reversible system undergoes the reversed reaction (and thus the current is also reversed, e.g. from the species in solution to the electrode) in the absence of additional reactions. Moreover, if this process is done in the absence of energy losses, then it is said to be *thermodynamically reversible*. A more precise definition for thermodynamic reversibility is found in [134], where the author claims that a reversible process reverses its direction when infinitesimal driving forces are applied to its surroundings and with a zero entropy balance, which implies that the system must be in equilibrium. As usual, this entelechy can be overcome by considering actual quasireversible processes, which are realized at very low rates (small enough perturbations applied to the system).

Thermodynamically reversible electrochemical systems can be partially described by the Nernst equation (2.5) [135]:

$$E = E^{0'} + \frac{RT}{nF} \ln \frac{C_{\mathrm{O}}}{C_{\mathrm{R}}}, \tag{2.5}$$

which relates the actual reduction potential at which a reaction takes place (E) with the standard electrode potential ($E^{0'}$), concentrations (as an approximation of the chemical activities) of the chemical species undergoing the reaction and the system temperature.

It is worth mentioning that the standard electrode potential, $E^{0'}$, is the measure of the potential of a reversible electrode in standard conditions (i.e. solutes at an effective concentration of 1 mol dm^{-3} and gas pressures of 1 atm), generally tabulated at 25 °C and referenced to a standard hydrogen electrode (SHE). The SHE is a platinum electrode in a theoretical ideal solution at which the hydrogen's standard electrode potential is zero volts at all temperatures [1]. Actually, this was implemented as the normal hydrogen electrode (NHE), consisting of a platinum electrode in a 1 N strong acid solution. Other common reference electrodes used in electrochemistry are the standard calomel electrode (SCE) or the silver-silver chloride Ag/AgCl/KCl electrode. Figure 2.10 shows a schematic relationship between potentials on the NHE, SCE and "absolute" scales [133].

Generally, strong experimental reasons lead the choice for one or other reference electrode. For example, whether the electrochemical system is built upon aqueous or nonaqueous solvents may determine that a Ag/AgCl/KCl electrode in aqueous solution or a Ag/Ag^{+} in CH_3CN is used [136, 137].

2.2.1.3 Electrical variables

When metal electrodes are used in electrochemical applications and they are brought in contact with an appropriate ionic solution, the particular zone where electrochemical phenomena take place, i.e. the electrode-solution interface or electrical double layer (EDL), acquires special importance. The capacitance of this interface quantifies its ability to store charge as a response to a perturbation in potential. In this sense, the differential capacitance relates a small change in charge density to a small alteration in potential. Thermodynamically, this has its origins in what are called surface excess quantities (in a two-phase interface), surface tension and its implication in surface structure [133]. It is important to take into account that, contrary to ideal capacitors, the interface capacitance is not constant with the applied potential, as will be explained hereafter.

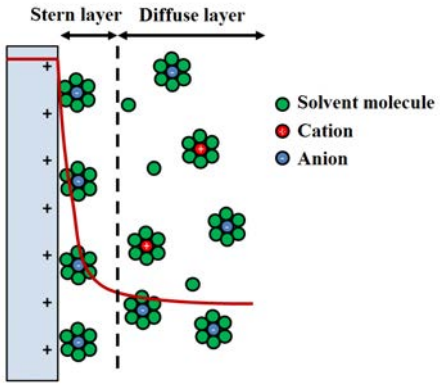

FIGURE 2.11: Guoy-Chapman-Stern model of the EDL at an electrode-solution interface. Adapted from Wang *et al.* [138].

Many theoretical models were proposed in the past to describe the EDL. A very complete one is the Gouy-Chapman-Stern model [138–140], which is represented schematically in Figure 2.11. An anode in physical contact with a ionic solution can be observed. When a potential difference is applied to the electrode, if the latter is conductive enough, its charges accumulate at the surface. Solvated ions of the opposite charge arrange in solution at a finite distance from the electrode by electrostatic interaction. This structure is known as the Stern (or classical Helmholtz) layer, and is analogous to a parallel-plate capacitor, with the ability to accumulate (non-faradaic) charge. Moreover, the potential drop across this layer (represented as a red line in Figure 2.11) is almost linear, which accounts for a constant differential capacitance. The remaining voltage difference drops in a non-linear fashion along the so-called diffuse layer, thus implying a potential-dependent capacitance in this region. The Stern and diffuse layers contribute serially to the double layer capacitance, and the prevalence of one or another will depend on the concentration of electrolyte and applied potential [133].

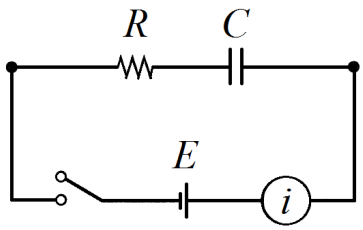

FIGURE 2.12: Equivalent RC circuit for non-faradaic processes occuring at an electrode-solution interface.

In order to illustrate how electrical variables affect the rate of electrode reactions, let us consider that no electron exchange is occurring at the electrode-solution interface (non-faradaic process). In this situation, let us assume that the electrode-solution system can be modelled as an electrical circuit consisting of the series addition of a resistor (of resistance R) and a capacitor (of capacitance C). These assumptions will be further discussed and developed in forthcoming sections. Now, with the described electrochemical system, let us study how the applied voltage will affect the current flowing through the system in several examples. The equivalent electrical circuit in Figure 2.12 shows the general configuration for electrode excitation with a potential step.

2.2.1.3.1 Voltage step

Let us consider that a constant voltage is applied as a step function to the RC equivalent circuit (modelling the electrode-solution system). Considering that the applied voltage must divide up between the resistor (E_{R}) and the capacitor (E_{C}), as shown in Equation 2.6, taking into account that the current flowing through the resistor and through the capacitor is the same and the necessary for the capacitor to charge $\left(i = \frac{\mathrm{d}q}{\mathrm{d}t}\right)$, and knowing the Ohm's law by which $E = iZ_{\mathrm{tot}}$ and knowing that $Z_{\mathrm{tot}} = Z_{\mathrm{R}} + Z_{\mathrm{C}}$, where $Z_{\mathrm{R}} = R$ and the $C = \frac{\mathrm{d}Q}{\mathrm{d}V}$ relation for capacitors, then the current flowing through the system is a decreasing exponential as shown in Equation 2.7 and in Figure 2.13a.

$$E = E_{\mathrm{R}} + E_{\mathrm{C}} \tag{2.6}$$

$$i = \frac{E}{R} \exp\left(\frac{-t}{RC}\right) \tag{2.7}$$

2.2.1.3.2 Voltage sweep

When a voltage ramp instead of a voltage step is applied, the potential varies linearly with time at a rate ν (Equation 2.8). Taking the previous expressions and the one in

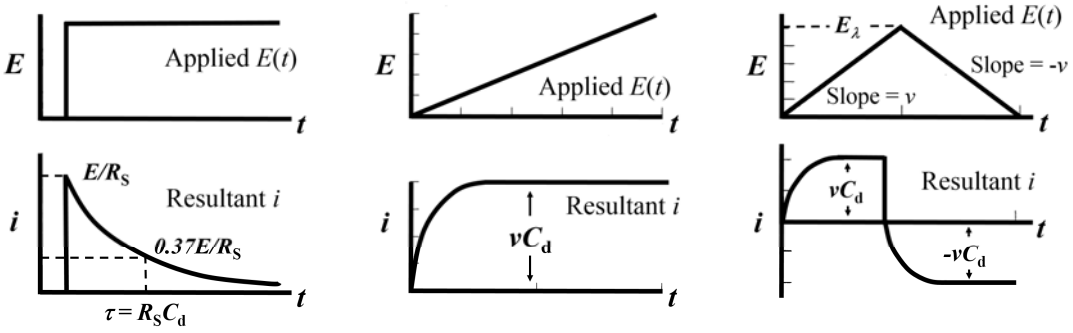

(A) (B) (C)

FIGURE 2.13: Time-dependent voltage and current flowing through the equivalent RC circuit with applied (A) voltage step, (B) one-direction voltage sweep and (C) cyclic voltage sweep.

Equation 2.8, now the current flowing through the system (Equation 2.9) is an increasing function that stabilizes at $i_{\max} = \nu C$, when the capacitor is fully charged (please see Figure 2.13b). As will be explained in subsequent sections, cyclic voltammetry (CV) experiments consist in linearly sweeping the voltage up to a certain value and back towards the initial value, as shown in Figure 2.13c. In this case, the current stabilizes at $i_{\max} = \nu C$ and starts falling with decreasing voltage down to $i_{\min} = -\nu C$.

$$E = \nu t \tag{2.8}$$

$$i = \nu C \left[1 - \exp\left(\frac{-t}{RC}\right)\right] \tag{2.9}$$

The equations shown here were taken as examples of the influence of electrical variables in the rates of non-faradaic simple systems. The introduction of the effect of redox reactions at the electrode-solution interface in faradaic systems is tackled in Section 2.2.2.

2.2.1.4 Electrode and solution variables

The double layer capacitance introduced in Section 2.2.1.3 is represented as Q_{CPE} (CPE stands for constant phase element, which accounts for non-idealities in the electrode surface) in the equivalent circuits shown in Figures 2.14a and 2.14b. Figure 2.14a corresponds to a system with ionic solution consisting of an electrolyte and a redox probe, whereas the system's ionic solution in Figure 2.14b consists of the electrolyte alone (without any redox probe). In the former case, an additional path is available for charge at the electrode-solution interface. Indeed, the accumulation of solvated ions at the electrode surface offers a resistive barrier to potential charge transfer between redox species in solution and the electrode (faradaic current), which corresponds to a charge transfer resistance R_{CT} as alternative path to (in parallel with) the Q_{CPE}. Additionally, the diffusion of ions occurs at the surroundings of the double layer, phenomenon that contributes to the total impedance as a Warburg element (Z_{W}). The equivalent impedance model is schematically represented in Figure 2.14a as a Nyquist plot. The charge transfer process is modulated by the applied potential difference, as can also be observed in the schematic CV, shown in Figure 2.14a. Indeed, maximum reduction and

oxidation currents occur at determined potentials, as predicted by the Nernst equation.

On the contrary, and as expected, the charge transfer phenomenon cannot be appreciated in Nyquist and CV plots in Figure 2.14b, for there is no redox species in solution accounting for it in this case, and all the current has capacitive (non-faradaic) origin. In the Nyquist plot representation, the effect of the charge transfer resistance dominating in the previous case is here screened by the impedance associated to the double layer capacitance ($Z_{C\mathrm{DL}}$), which in turn is overlapping the contribution of diffusion (or Warburg effect). As expected, no redox peaks appear in the CV representation, and the current level is directly proportional to the non-faradaic capacitance of the interface. In both cases, a solution resistance (R_{S}) is added serially to the equivalent circuit.

A study of conductive electrode electrochemical features can be done by CV analysis of faradaic current, as described by the Randles-Sevcik equation [133, 141, 142]:

$$I_{\mathrm{f}} = \kappa n \mathrm{F} A C \sqrt{\frac{n \mathrm{F} \nu D}{RT}}. \tag{2.10}$$

Here, $\kappa = 0.4463$ is a non-dimensional proportionality constant; n is the number of electrons for the redox couple (1 in the case of $\mathrm{Fe(CN)}_6^{-3/-4}$, which is the one used in this thesis); F and R are Faraday's (96 485 C mol^{-1}) and universal gas (8.314 J mol^{-1} K^{-}1) constants, respectively; A is the electrode area in cm^2; ν is the rate at which the potential is swept, in V s^{-1}; D is the analyte's diffusion coefficient in cm^2 s^{-1}; C is the analyte's concentration in mol cm^{-3} and T is the solution temperature in K. This process was thoroughly described elsewhere [143], but briefly, all parameters were known except for the area of the nanostructured electrode. In order then to retrieve this area, successive

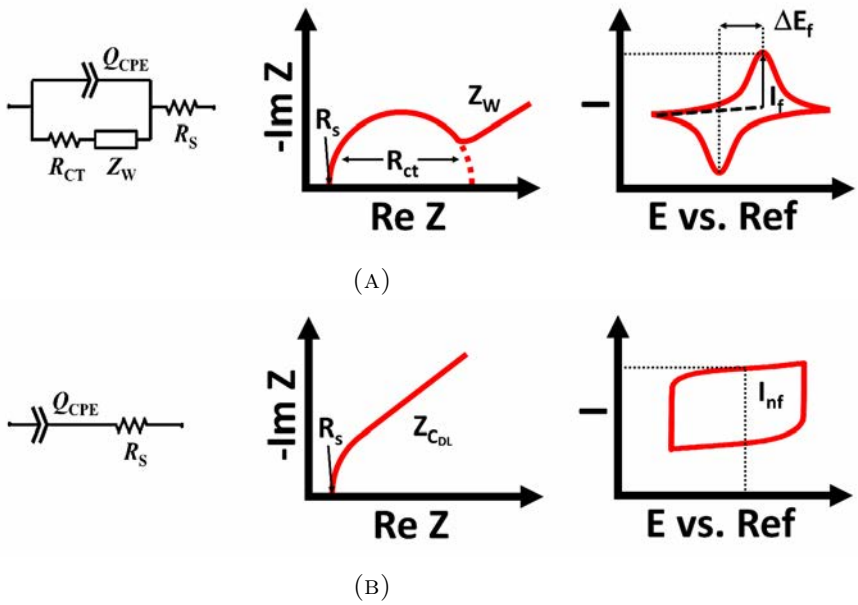

FIGURE 2.14: (A) Faradaic electrochemical analysis: the Randles equivalent electrical circuit of the EDL includes R_{CT}, R_{S}, Z_{W} and Q_{CPE}. Typical EIS and CV representations for faradaic systems are shown. (B) Non-faradaic electrochemical analysis: the equivalent electrical circuit consists of single Q_{CPE} in series with R_{S}. Typical EIS and CV representations for non-faradaic systems are shown.

CVs at different scan rates must be performed and the oxidation current against the square rooted scan rate should be plotted. The slope of this plot is directly proportional to the electroactive surface area of the electrode. This, as can be deduced from Equation 2.10, is only dependent on the electrolyte solution and redox probe composition, providing the electrode is conductive enough. The electrode features are not affecting the intensity of the peak, but its position. Indeed, the more resistive the electrode, the wider the separation between reduction and oxidation peaks. This is because redox reactions occur reversibly at the ideal electrode surface, but this reversibility is hindered by non-ideal conducting properties of the electrode.

On the contrary, when no redox probe is present in the aqueous medium, interactions are assumed to be non-faradaic. As there is no redox species, no charge transfer occurs at the electrode surface, as shown in Figure 2.14b. Moreover, in cyclic voltammetry, all the current becomes capacitive; no faradaic peaks appear. In this case the current height (assumed constant) is proportional to the scan rate, and the differential capacitance becomes the proportionality constant, as shown in the following expression:

$$I_{\mathrm{nf}} = C_{\mathrm{d}}\nu. \tag{2.11}$$

The differential capacitance is directly proportional to the area of the electrode, as will be developed in the following sections. This is a faster and more precise method than the classical one, which consists in calculating the integral of the voltammogram and dividing this by the potential scan rate to find the capacitance [144].

2.2.2 Kinetics of electrode reactions. Processes occurring at the electrode-solution interface

Along the previous section, some variables affecting the rate of electrode reactions were mentioned, amongst which the electrodynamics of electrochemical cells was introduced. This is the basis for achieving a theoretical model for the kinetics of reactions at an electrode's surface. In this section, the Nernst equation (2.5) will be gathered together with some classical thermodynamics concepts to present the Butler-Volmer model of electrode kinetics, which is used in the treatment of almost any problem involving heterogeneous kinetics [133].

2.2.2.1 Preliminary considerations

Let us assume that substance A is transformed into substance B in a discrete chemical event:

$$\mathrm{A} \underset{k_{\mathrm{f}}}{\overset{k_{\mathrm{b}}}{\rightleftharpoons}} \mathrm{B}. \tag{2.12}$$

The rates of forward and backward reactions can be expressed as:

$$\nu_{\mathrm{f}} = k_{\mathrm{f}} C_{\mathrm{A}}, \tag{2.13}$$

$$\nu_{\mathrm{b}} = k_{\mathrm{b}} C_{\mathrm{B}}. \tag{2.14}$$

Regarding Equations 2.12, 2.13 and 2.14, some considerations may be drawn:

- The rate constants k_f and k_b are defined as the reciprocals of the mean lifetimes of substances A and B. This is, the lower the lifetime of a substance, the quicker its transformation.
- The higher the concentration of a substance, the quicker its transformation into the other substance.
- At equilibrium, $\nu_\mathrm{f} = \nu_\mathrm{b} \equiv \nu_0$, where ν_0 is the exchange velocity.

Experimentally, most solution-phase reactions are characterized by temperature-dependent rate constants where $\ln k \sim \frac{1}{T}$; such experimental behaviour was formulated by Arrhenius as

$$k = Ae^{-E_\mathrm{A}/RT}. \tag{2.15}$$

Some more considerations:

- R is the universal gas constant.
- The pre-exponential (also known as *frequency*) factor A is constant and characteristic of each chemical reaction, accounting for the number of collisions or "attempts" for the reaction to occur.
- The activation energy E_A determines the energy barrier the system must surmount for the reaction to occur.
- The exponential shape expresses a probability (for the system to overcome the energy barrier), which is enhanced by an increase in temperature. With all, the "number of attemps" to react by the probability of surmounting the energy barrier of the reaction ($e^{-E_\mathrm{A}/RT}$) accounts for "how fast" (k, the *kinetics*) the reaction occurs.

All the independent variables affecting the state of a system can be considered as "reaction coordinate", and each posible state has its own potential energy. This describes a multidimensional surface in the system energy space, and reaction "paths" may be "drawn" describing system reactions. These ideas are pictured in Figure 2.15, where

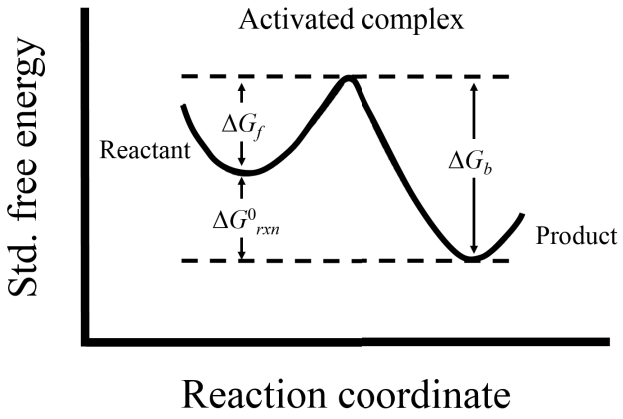

FIGURE 2.15: Representation of potential or standard free energy changes during a reaction.

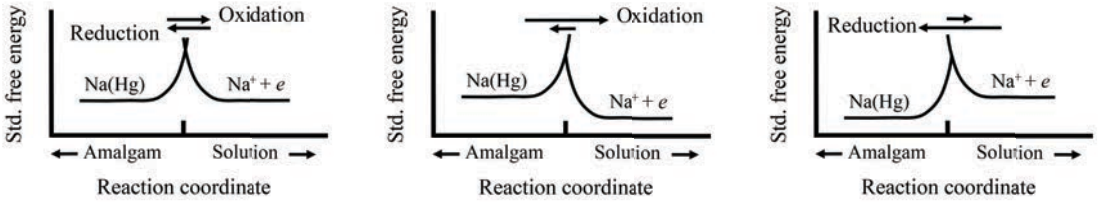

(A) (B) (C)

FIGURE 2.16: Representation of the standard free energy changes during faradaic processes (A) at the equilibrium potential; (B) at a potential higher (more positive) than the equilibrium potential and (C) at a potential lower (more negative) than the equilibrium one.

the standard free energy[7] along a reaction coordinate shows two minima at which the system is stable. The most stable state is that with the lowest free energy (the product in Figure 2.15, or substance B in Equation 2.12).

The standard free energy changes in faradaic processes as a function of the electrode potential are shown in Figure 2.16. In Figure 2.16a the applied potential is the standard one, for which the reaction is at equilibrium. It is equally favorable for the reaction to occur in one or another direction (reduction and oxidation), and thus the standard free energy has the same value both for reactant and product. When a potential more positive than the one in equilibrium is applied to the system (Figure 2.16b), the oxidation reaction is favoured because this way the system minimizes the free energy. On the contrary, when a potential more negative than the equilibrium potential is applied (Figure 2.16c) the system moves spontaneously towards reduction to minimize the standard free energy.

2.2.2.2 The Butler-Volmer model of electrode kinetics: one-step, one-electron processes

Let us have a look at expression 2.4 arranged for one-electron redox reactions,

$$\mathrm{O}^{+} + \mathrm{e} \underset{k_\mathrm{a}}{\overset{k_\mathrm{c}}{\rightleftharpoons}} \mathrm{R}^{-},$$

and consider the forward ($\rightharpoonup$) as the *cathodic* reaction and the backward ($\leftharpoondown$) as the *anodic* reaction. These are characterized by reaction rate constants k_c and k_a, respectively, as shown as follows:

$$k_\mathrm{c} = k^\mathrm{o} \exp\left[-\alpha_\mathrm{c} \frac{nF\left(E - E^\mathrm{o}\right)}{RT}\right], \tag{2.16}$$

$$k_\mathrm{a} = k^\mathrm{o} \exp\left[\alpha_\mathrm{a} \frac{nF\left(E - E^\mathrm{o}\right)}{RT}\right]. \tag{2.17}$$

[7] Along the text, *potential energy* and *standard free energy* are used indistinctively. Let us define ΔE_A as the standard activation energy, then the standard enthalpy of activation, according to thermodynamics, is $\Delta H_\mathrm{A} = \Delta E_\mathrm{A} + \Delta\left(PV\right)_\mathrm{A}$. Since $\Delta\left(PV\right)_\mathrm{A}$ is usually negligible in the described reactions, then $\Delta H_\mathrm{A} \approx \Delta E_\mathrm{A}$.

Equations 2.16 and 2.17 define the rate constants of reduction and oxidation of a species as a multiple of the standard heterogeneous rate constant k^{o}, which is characteristic of the reaction between the reactant and the electrode material, same as the electron transfer coefficient, $\alpha \equiv \alpha_{\mathrm{a}} = 1 - \alpha_{\mathrm{c}}$. Attention should be paid to the signs inside the exponentials, which show that positive and negative potentials (E) favour the oxidation and reduction processes, respectively. Defining the cathodic and anodic currents at the electrode surface ($x = 0$) as $i_{\mathrm{c}} = k_{\mathrm{c}} nFAC_{\mathrm{O}}(0,t)$ and $i_{\mathrm{a}} = k_{\mathrm{a}} nFAC_{\mathrm{R}}(0,t)$, the total current through the electrode at its surface with respect of time is known as the Butler-Volmer equation (2.18):

$$i = FAk^0 \left[C_{\mathrm{O}}(0,t)\, e^{-\alpha f\left(E-E^{0'}\right)} - C_{\mathrm{R}}(0,t)\, e^{(1-\alpha) f\left(E-E^{0'}\right)} \right]. \tag{2.18}$$

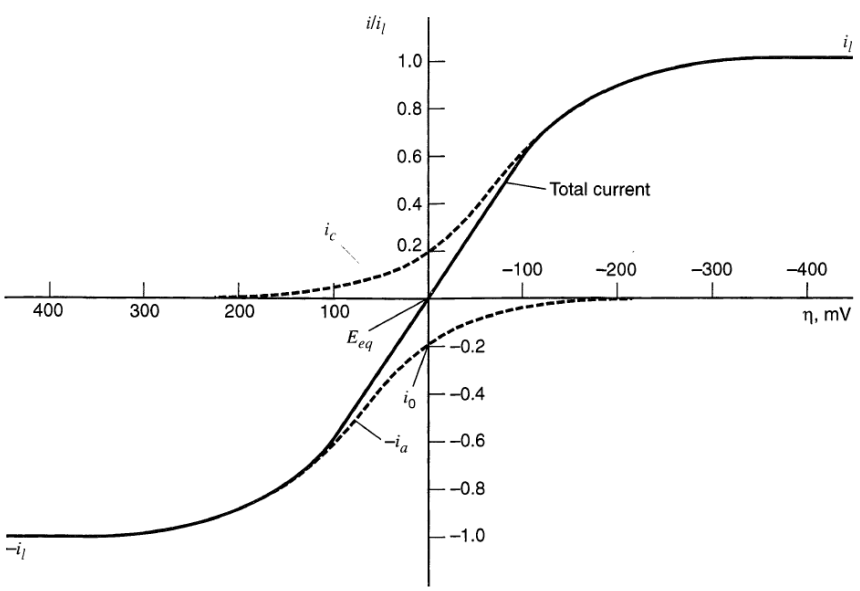

FIGURE 2.17: Current-overpotential curve simulation of the one-electron redox system $O^- + \mathrm{e} \rightleftharpoons R^+$ with $\alpha = 0.5$, $T = 298$ K, and dashed lines corresponding to i_{c} and i_{a}. Extracted from [133].

Figure 2.17 shows the current-overpotential simulation of the one-electron redox system as predicted by the Butler-Volmer equation. Of course, the solution to *real* systems can only be approximated to what is described in this section. Advanced studies of the kinetics of electrode reaction must include mass transfer effects, multistep mechanisms (the ferrocyanide reaction, $\mathrm{Fe(CN)}_6^{3-} + \mathrm{e} \rightleftharpoons \mathrm{Fe(CN)}_6^{4-}$ –which is the one studied in this thesis– is a one-step reaction) and quasireversible and irreversible electrode processes.

2.2.3 Mott-Schottky analysis of the semiconductor electrode

Another measurement of the capacitance of semiconducting electrodes can be obtained from non-faradaic Mott-Schottky analysis. This is a much more precise method than the ones mentioned before, for it allows distinguishing between the double layer capacitance and the capacitance associated to a semiconductor electrode (which was not contemplated before).

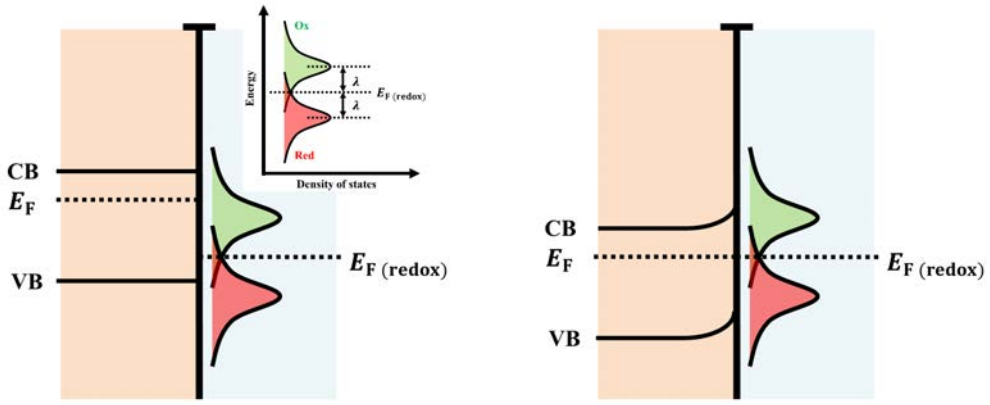

(A) (B)

FIGURE 2.18: Electronic band diagram of a *n*-type semiconductor electrode-solution system (A) before and (B) after thermodynamic equilibrium. The density distribution of redox energy states in solution is shown as inset in (A). Adapted from Gelderman *et al.* [145].

When the working electrode is not based on a metal but on a semiconductor material (such as ITO), additional phenomena is occurring at the edge of the semiconductor. Indeed, if the electrolyte solution is conductive enough, then the system can be regarded as analogous to the classical metal-oxide-semiconductor (MOS) capacitor in transistor electronics [146]. With no aim of entering into further details, it is worth bearing in mind that in MOS capacitors, the capacitance value is modulated by the voltage applied to the metallic gate and referred to the bulk semiconductor. Now the total capacitance of the system becomes the series sum of the capacitances of the semiconductor (because of internal charge distribution due to differences in the energy bands) and the double layer (exhaustively detailed in the previous section). Figure 2.18 intents to summarize this physical phenomenon. The *n*-type semiconductor electrode is shown as the orange area, whereas the blue area corresponds to the electrolyte solution. The electrolyte solution can be parametrized in this analysis by a Fermi energy level associated to the species in solution, $E_{F\ (redox)}$, which typically stays at the equilibrium between reduction (red Gaussian) and oxidation (green Gaussian) quantum states. $E_{F\ (redox)}$ typically stays below the Fermi level of *n*-type semiconductors until the systems are brought into thermodynamic equilibrium, when they both leverage, inducing a bending of the semiconductor valence and conduction bands and an internal electrical field that empties the region of charge carriers. This spatial charge region entails the semiconductor capacitance, and the band bending can only be overcome by the so-called (external) flat band potential.

In this context, electrochemical impedance spectroscopy (EIS) and Mott-Schottky analysis are electrochemical techniques that can help understand the phenomena occurring at the (semiconductor) electrode-solution interface. EIS consists in submitting the working electrode at an alternating voltage and measuring the current to retrieve the electrode's complex impedance. For this, a small sinusoidal signal is added to the working voltage, and the frequency is scanned between the desired limits. The resulting impedance spectrum is fitted to the equivalent circuit shown in Figure 2.14b and described before. At a determined polarization voltage, the evolution of the charge transfer

resistance with subsequent functionalization steps provides a qualitative and pseudo-quantitative measurement of the nature of the insulating layer between the electrode and the solution. On the other hand, the evolution of the electrode's capacitance with the polarization voltage accounts for physical properties of the semiconductor electrode (e.g. the flat band potential of the semiconductor and the density of charge dopants). The latter is gathered in the Mott-Schottky equation, which in turn is derived from the Poisson's equation, i.e. the assumption of charge neutrality inside the semiconductor and Boltzmann's statistics. The Mott-Schottky equation for n-type semiconductor electrodes (which is the case of ITO) can be written as [145]

$$\frac{1}{{C_{\mathrm{sc}}}^2} = \frac{2}{\epsilon\epsilon_0 A^2 \mathrm{e} N_{\mathrm{D}}} \left(V - V_{\mathrm{FB}} - \frac{k_{\mathrm{B}} T}{\mathrm{e}} \right), \tag{2.19}$$

where C_{sc} is the capacitance of the semiconductor electrode; ϵ and ϵ_0 are the relative and absolute dielectric constants of the semiconductor and vacuum, respectively; A is the area of the electrode in contact with the electrolyte solution; e is the unitary charge; N_{D} is the density of donors (doping atoms) in the n-type semiconductor; V and V_{FB} are the polarization potential and the semiconductor's flat band potential, respectively; T is the temperature of the electrochemical system and k_{B} is the Boltzmann's constant.

Capacitance values can be retrieved by data adjustment of subsequent EIS measurements at several DC polarization voltages in the frequency range of interest (Figure 2.14b). Representation of $\frac{1}{C^2}$ against DC polarization voltage at a determined frequency value may present several regions of different behavior [147]. Linear fitting of the data points in the region attributable to C_{sc} to Equation 2.19 eventually leads to determination of semiconductor electrode's flat band voltage and carrier density.

2.2.4 Electrochemical techniques and potentiostatic configurations

A potentiostat is an electronic device interfaced with an appropriate software for controlling two or three-electrode cells and performing a variety of electrochemical measurements. In general terms, a voltage wave (which can be DC, AC or a combination of both depending on the measurement technique) is applied between working and reference electrodes in the electrochemical cell, and the current flowing through the cell is measured between the working and counter leads. A general schematic of configuration of an electrochemical cell interfaced by a potentiostat is shown in Figure 2.19.

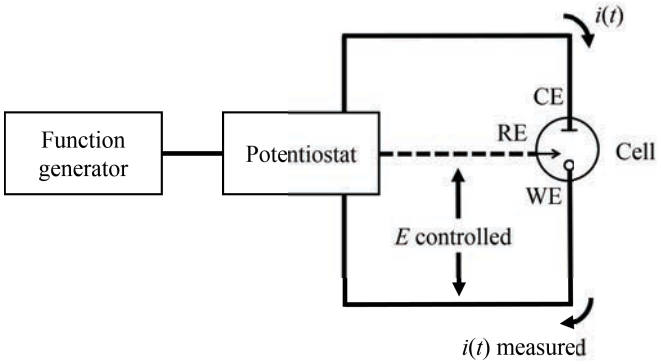

FIGURE 2.19: Schematic of electrodes configuration for controlled-potential experiments. Based on [133].

In this section, the most popular electrochemical techniques, i.e. potentiometry, voltammetry (or amperometry if the voltage is kept constant at a DC value) and electrochemical impedance spectroscopy, are described and details on their practical implementation are provided. The mentioned techniques are also those employed in the experimental part of this thesis to characterize the developed electrodes.

2.2.4.1 Potentiometry

Potentiometry is the simplest of the available potentiometric techniques, and it basically consists in passively measuring the potential at open circuit between two electrodes in solution. As usual, one is called the reference electrode, which is nonpolarizable (i.e. it maintains a constant potential); the other one is the indicator electrode. The difference of potential between these two electrodes is the potential of the solution, and it accounts for the composition of the medium. The indicator leads usually are ion selective electrodes (ISEs), which are selectively sensitive to an ion of interest present in solution. This way, the measured potential accounts for the activity of the studied ion. If the indicator electrode is sensitive to protons (H^+), then the open source voltage gives a measure of the solution pH.

2.2.4.2 Linear sweep voltammetry

To determine the electrochemical behaviour of a system it would "suffice" to measure the time-dependence of the current at a determined excitation potential, and to explore several potentials, generating a three-dimensional surface in the $i - E - t$ domain as shown in Figure 2.20a. However, some obvious issues arise from this approach:

- the accumulation of a huge amount of data hinders a rapid and/or proper analysis;
- single $i - t$ curves alone are not optimal for recognizing the presence of different species and
- the representation of well-resolved $i - E$ curves requires very closely spaced potential steps.

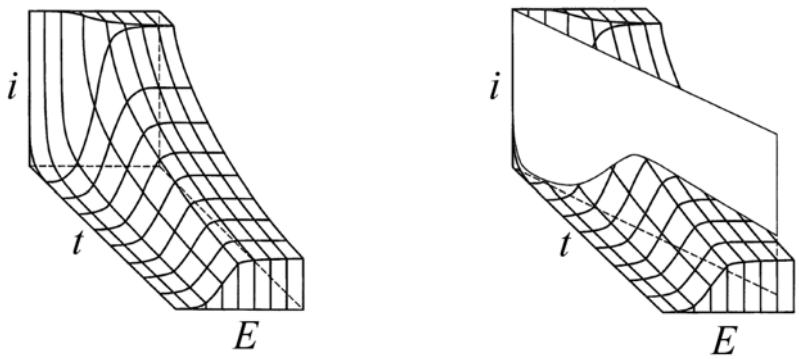

(A) (B)

FIGURE 2.20: (A) Representation of the $i - E - t$ space for a nernstian reaction, and (B) linear potential sweep across the surface. Reproduced from [148].

A solution to this is to perform a single experiment in which the $i - E$ is recorded at once by sweeping the voltage at a constant rate. In the $i - E - t$ space this would be equivalent to intersecting the three-dimensional surface with a plane representing the voltage variation with time, as shown in Figure 2.20b. This is called *linear potential sweep chronoamperometry* or *linear sweep voltammetry* (LSV). If, at a certain time (switching time or potential), the voltage sweep is reversed, then this reversal technique is called *cyclic voltammetry* (CV).

The electron transfer rate must be rapid at the electrode surface, so that the ratio of concentrations of species O and R is the one predicted by the Nernst equation (2.5). In this case, the system is said to be *reversible*, and the half-wave peak separation is only dependent on the number of electrons echanged in the redox reaction:

$$\left|E_{\mathrm{p}} - E_{\mathrm{p}/2}\right| = \frac{56.5}{n} \text{ mV at } 25\ ^{\circ}\text{C}. \tag{2.20}$$

The notation $\left|E_{\mathrm{p}} - E_{\mathrm{p}/2}\right|$ refers to half the distance between reduction and oxidation peaks in a faradaic cyclic voltammetry, being p referred to the current peak, as shown in Figure 2.14a.

2.2.4.3 Electrochemical impedance spectroscopy

An interesting way of studying electrode reactions by large system perturbation is to apply a small-amplitude alternating signal to the cell and observing how the system follows the perturbation at a steady state. These techniques based on impedimetric principles permit high-precision measurements at a wide frequency range, and thus are very useful in providing knowledge of the system at the microscopic level. Electrochemical impedance spectroscopy (EIS) consists in sweeping the frequency of the small-amplitude sinusoidal voltage and measuring the resulting current to retrieve the system's impedance at each frequency. This was first presented by Sluyters [149] and developed by others [150–153].

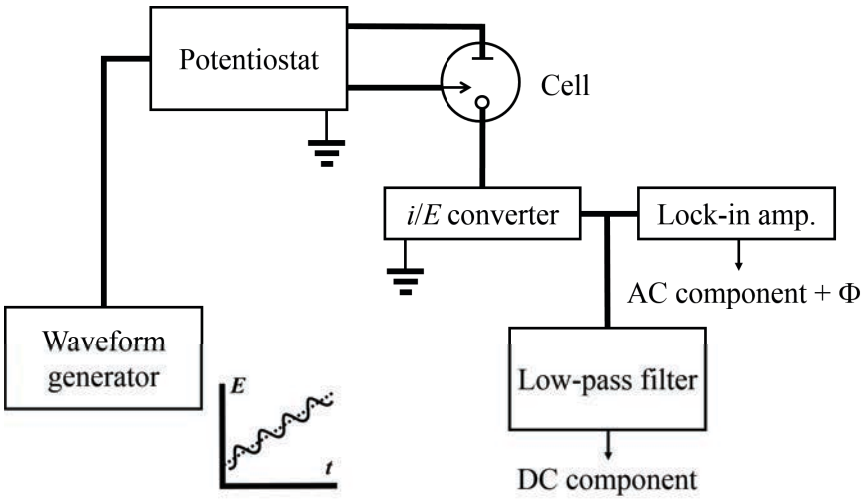

FIGURE 2.21: Schematic of apparatus for impedance spectroscopy measurement. Adapted from [133].

A general schematic of the electronics in an electrochemical impedance system is shown in Figure 2.21. Here, a (either digital or analogue) waveform generator provides the potentiostat with the potential signal to attack the electrochemical system, represented in the figure as a three-electrode cell. The system current response to the excitation signal is measured in the working electrode and converted to a measurable potential, which is then processed by a low-pass filter to extract the DC component and by a lock-in amplifier to extract the AC component and phase shift with respect to the reference signal. In the following lines, the basics of the lock-in amplifier are provided.

To understand how EIS works, one must bear in mind that an electrochemical system can be modelled as a more or less complex electrical circuit (which is called the *equivalent circuit*). By definition, the equivalent circuit must be such that a small-amplitude sinusoidal voltage induces in it a current of the same amplitude and phase that the current through the real cell under the same excitation. The Randles equivalent circuit (Figure 2.22) is the most representative one and facilitates both the calculations and the interpretation of the results as chemical information.

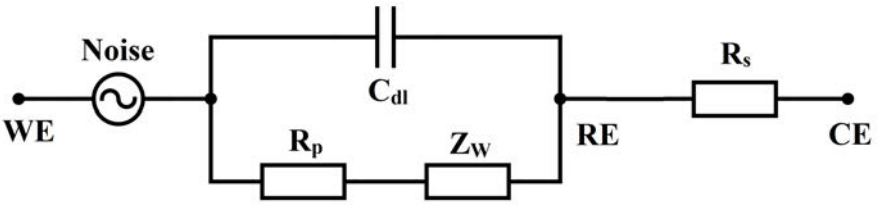

FIGURE 2.22: Equivalent Randles circuit for an electrochemical cell.

The *lock-in amplifier* is a mathematical tool very useful to retrieve the interesting parameters from an EIS measurement. Henceforth, the methodology of the lock-in amplifier will be illustrated with some basic equations to show the power of this tool (a summarized version of the mathematics can also be found in Article V). Let us suppose the sensor is excited with a periodic signal (called V_{ref}^0, Equation 2.21) of amplitude, frequency and phase V_r, f_r and ϕ_r, respectively:

$$V_{\text{ref}}^0(t) = V_\text{r} \sin(2\pi f_\text{r} t + \phi_\text{r}) . \tag{2.21}$$

Now, the sensor response to the excitation signal (V_{out}), attending to the circuit shown in Figure 2.22 is a result of the contribution of the resistive and the capacitive parts, as well as an added noisy signal due to random interferences. As shown in Equation 2.22, the contribution of the resistive-capacitive part to the sensor response is a periodic signal of the same frequency as the excitation signal ($f_\text{s} = f_\text{r}$) and generally phase-shifted and of different amplitude ($V_\text{s} \neq V_\text{r}$, $\phi_\text{s} \neq \phi_\text{r}$). Other periodic interferences from undesired sources (the 50–60 Hz from the electrical network, electromagnetic couplings) are added to the output signal:

$$V_{\text{out}}(t) = V_\text{s} \sin(2\pi f_\text{s} t + \phi_\text{s}) + \sum_{i \neq \text{s}} V_i \sin(2\pi f_i t + \phi_i) + N(t) . \tag{2.22}$$

A digital lock-in filter consists in generating a $\frac{\pi}{2}$ shifted reference signal $\left(V_{\text{ref}}^{\frac{\pi}{2}}\right)$ from the original one (V_{ref}) and multiplying both by the output signal:

$$\left.\begin{aligned} V_{\mathrm{ref}}^{0}(t) &= V_{\mathrm{r}} \sin\left(2\pi f_{\mathrm{r}} t + \phi_{\mathrm{r}}\right) \\ V_{\mathrm{ref}}^{\frac{\pi}{2}}(t) &= V_{\mathrm{r}} \sin\left(2\pi f_{\mathrm{r}} t + \phi_{\mathrm{r}} + \frac{\pi}{2}\right) \end{aligned}\right\} \times V_{\mathrm{out}}(t), \tag{2.23}$$

and integrating the resulting terms for a time period $\left(\tau_{\mathrm{r}} = \frac{1}{f_{\mathrm{r}}}\right)$, assuming $f_{\mathrm{r}} = f_{\mathrm{s}}$):

$$\alpha = \int_{0}^{\tau_{\mathrm{r}}=1/f_{\mathrm{r}}} V_{\mathrm{out}}(t)\, V_{\mathrm{ref}}^{0}(t)\, \mathrm{d}t = \frac{1}{2} V_{\mathrm{r}} V_{\mathrm{s}} \tau_{\mathrm{r}} \cos\left(\phi_{\mathrm{s}} - \phi_{\mathrm{r}}\right), \tag{2.24}$$

$$\beta = \int_{0}^{\tau_{\mathrm{r}}=1/f_{\mathrm{r}}} V_{\mathrm{out}}(t)\, V_{\mathrm{ref}}^{\pi/2}(t)\, \mathrm{d}t = \frac{1}{2} V_{\mathrm{r}} V_{\mathrm{s}} \tau_{\mathrm{r}} \sin\left(\phi_{\mathrm{s}} - \phi_{\mathrm{r}}\right). \tag{2.25}$$

Simple manipulation of the resulting terms (defined as α and β) lead to the expressions for the absolute amplitude (Equation 2.26) of the output signal and its phase shift (Equation 2.27) with respect to the reference signal.

$$\Delta\phi = \arctan\left(\frac{\beta}{\alpha}\right) \tag{2.26}$$

$$V_{\mathrm{s}} = \frac{2}{V_{\mathrm{r}} \tau_{\mathrm{r}}} \sqrt{\alpha^2 + \beta^2} \tag{2.27}$$

2.3 Part III: The application. Biosensors

A biosensor is an analytical tool, consisting of a bioreceptor component and a transductor mechanism (which is based on a determined principle of operation), used for the detection of chemical substances. The bioreceptor is a sensitive biological element capable of recognizing, binding or interacting with the target analyte, and it can be either an enzyme, a nucleic acid sequence, cellular structures, an antibody, etc. Bioreceptors are required a high selectivity for the target analyte among a matrix of interfering biochemical components.

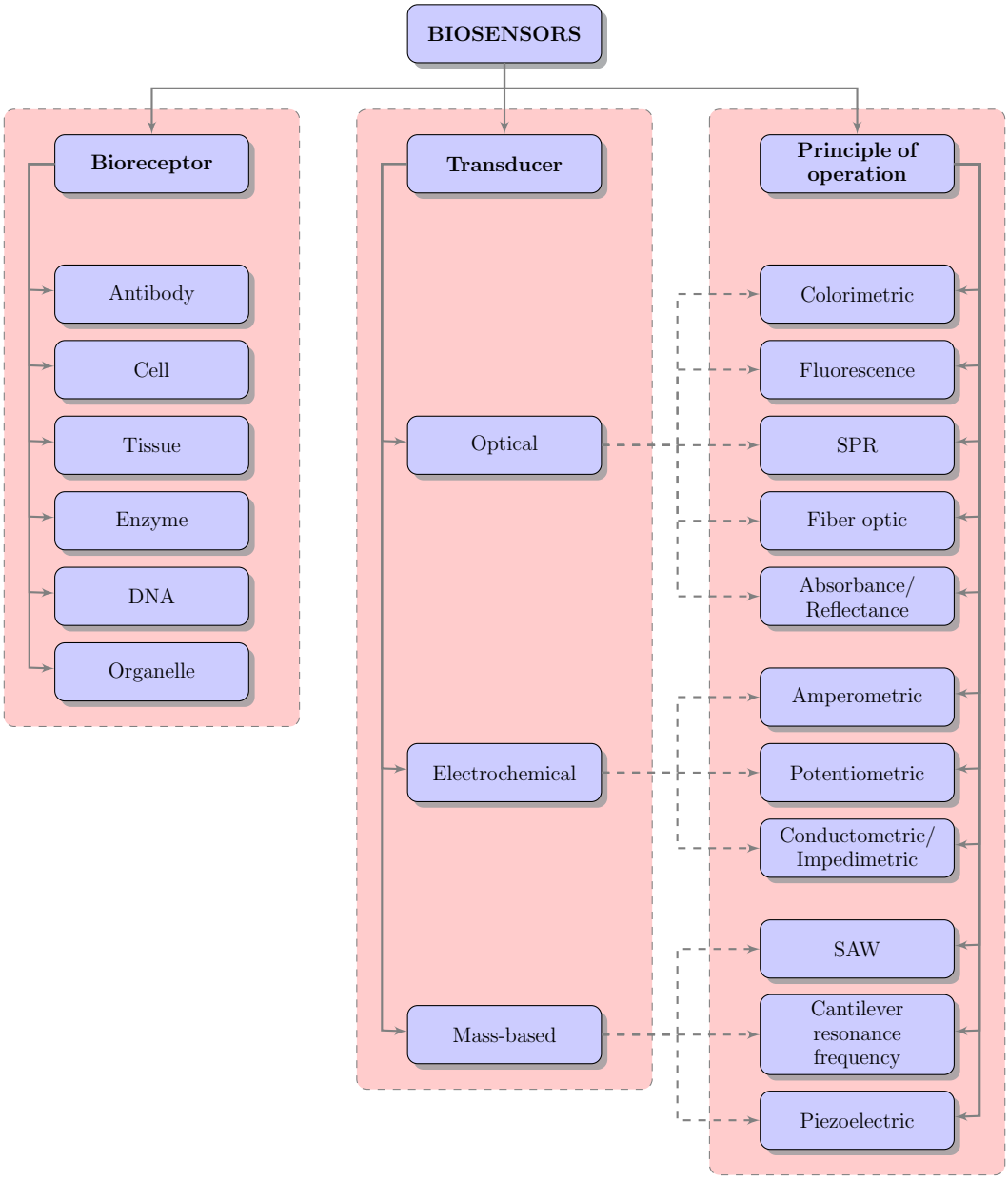

FIGURE 2.23: Block diagram for the classification of biosensors regarding the bioreceptor, biotransducer and principle of operation (please note that this classification is not exhaustive, the interested reader is referred to the IUPAC reports and others [13, 154, 155] for further details).

On the other hand, the transducer transforms the physicochemical signal derived from the interaction between the target analyte and the bioreceptor into a measurable signal that can be optical, electrical or of any other kind. Optical, electrochemical and mass-based detector elements are the most typical transducers, and these can be in turn based on several principles of operation, such as amperometry, fluorescence, surface plasmon resonance (SPR), the piezoelectric effect, surface acoustic wave (SAW), etc. Finally, biosensors are interfaced with the appropriate electronics for signal processing and proper display of the results.

In this third part of Chapter 2, some classifications of biosensor types are provided. Then, an overview of the state-of-the-art of ITO-based biosensors is provided. In Section 2.3.2, some strategies for surface modification and detection of species are described; first, several crosslinkers for electrode derivatization are mentioned, followed by the most popular electrochemical principles of transduction (current and impedance based), and finishing with a description of the immunoassays studied in this work.

2.3.1 Classification of biosensors and state-of-the-art

2.3.1.1 Bioreceptor and transducer-wise classifications of biosensors

Some of the most common bioreceptors as well as principles of operation are described in two separate item lists in this section. Moreover, a schematic representation of the different types of classification of biosensors is shown in Figure 2.23. Regarding the bioreceptor-wise classification, some of themost popular interaction biocomponents are itemized down below.

(i) Bioreceptors:

- **Antibody–antigen interactions**. Antibodies (or immunoglobulins) are Y-shaped proteins produced by the immune system to neutralize pathogen agents in a unique and specific way. Antigens are structural parts of the pathogen agents once these have overcome the primary barriers of the immune system (this process is detailed in Section 2.3.3.1), and they are recognized in a lock-key manner in the Fab's variable region at the tips of the Y-shaped antibodies (please see Figure 2.24a) [156]. A physicochemical change occurs as a result of the binding event, which triggers a signal in combination of an auxiliary molecule (e.g. enzyme or radioisotope).

- **Enzymatic interactions**. Enzymes are macromolecular biological substances that act as catalyzers of biochemical reactions (Figure 2.24b), increasing the reaction rates without being consumed and thus being capable of iteratively acting as long as the enzyme stability is maintained. Several mechanisms are available for enzymatic analyte recognition; for example, the properties of the enzyme could be modified (or it could even be inhibited or activated) as a result of the interaction with the analyte, or most typically the enzyme would convert the analyte into a sensor-detectable product. Generally, enzymes are very popular bioreceptors due to their ability to catalyze a large number of reactions and their adaptability to different transduction mechanisms.

- **Cells**. These structural, functional and biological basic units of living organisms are often used as bioreceptors due to their high sensitivity and responsiveness to stimuli of the surrounding environment, being common for the detection of stress conditions, toxicity and organic derivatives. Cells can be easily immobilized on

sensor surfaces and remain active and stable for a long period, thus making cell-based sensors reusable devices.

- **Tissues**. These are biological organizations of same-type cells and their extracellular matrix that have specific functionality. Tissues host a great deal of enzymes in their natural environment, which adds stability to the resulting biosensor and makes them cheaper since there is no need for extraction, centrifugation and purification of the catalyzers. However, a lack of sensor specificity arises from the interferences between different enzymes, as well as longer response time due to transport barrier effect of the extracellular matrix.

- **Organelles**. An organelle is defined as a specialized subunit inside an eukaryotic cell (some prokaryotic cells host protein-based bacterial microcompartments acting as primitive organelles). Organelles perform functions independently, and several of them contain enzymes. Popular organelle-based biosensors use mitochondria, chloroplasts and lysosomes, amongst others.

- **Nucleic acid interactions**. Nucleic acids are the small biomolecules constituting the material encoding and storing genetic information inside each living cell. If the basic repeating structure of the nucleic acid sequence is a ribose, then we talk about ribonucleic acid (RNA); on the contrary, we talk about deoxyribonucleic acid (DNA) if the repeating structure is a deoxyribose (please see Figure 2.24c). All in all, a nucleic acid is composed of the repeating structure (ribose or deoxyribose), a phosphate group and a nitrogenous base (which can be adenine, guanine, cytosine and thymine –in the case of DNA– or uracil –in the case of RNA–). The recognition process in genosensors is based on the principle of complementary base pairing (thymine/uracil – adenine, guanine – cytosine). Konwn the target nucleic acid sequence, then the complementary sequence can be synthesized, labeled and tethered to the sensor surface for then pursuing hybridization of both sequences and generation of a measurable signal.

- **Others**. Less common bioreceptors than those itemized above include artificial binding proteins and affinity binding receptors, amongst others. The former consist of low-cost, artificially engineered recombinant binding fragments or domains of antibodies with the ability of binding to several target proteins and still retaining the favorable properties of the parent antibody. On the other hand, affinity binding receptors consist of proteins with a high specificity for their target partner but with much lower binding constant than the corresponding antbodies (which result in almost irreversible associations).

Hereafter, some popular biotransducer principles of operation are described. These and the previously described bioreceptors are organized in a classification diagram in Figure 2.23.

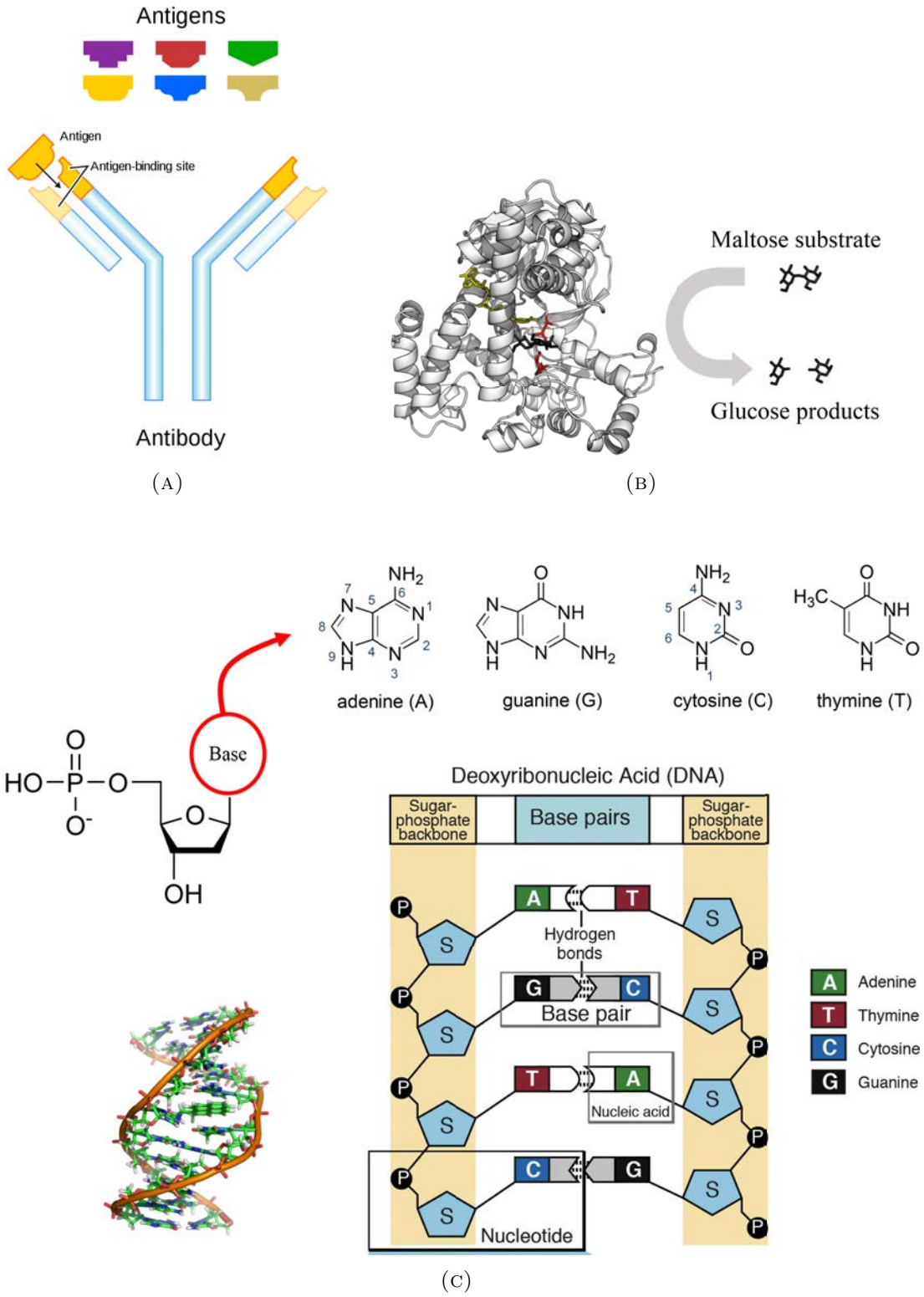

FIGURE 2.24: (A) Antibody-antigen interaction.[8](B) The effect of glucosidase enzyme on the dissociation of maltose.[9](C) Chemical structure of nucleotides and the nitrogenous bases of DNA, as well as pair-wise interaction between them.[10]

(ii) Transducers:

- **Electrochemical transducers**. These usually operate in liquid medium with the aid of three electrodes: the working electrode (WE), where the reactions take place; the reference electrode (RE), against which the WE is polarized; and the counter electrode (CE), which collects the current flowing through the WE as a result of the polarization. In few occasions, such as in potentiometric biosensors, only two electrodes (WE and RE) are enough. Potentiometric sensors measure the voltage potential at zero current, they are highly sensitive and robust, and they measure physical changes at the sensor surface (typically made of a plastic substrate coated with a conducting polymer) as a result of pH, hydration and redox reactions or ionic strength. Other electrochemistry-based principles of operation include amperometry and impedance spectroscopy (which measure the passing current at a fixed potential). All of them are usually based on the enzymatic catalysis of a reaction producing or consuming electrons in which the target analyte is involved. All in all, detailed information on the operation principles of electrochemical transducers, which is of major interest in the scope of this thesis, was provided in Section 2.2.4.

- **Optical transducers**. These exploit principles of operation involving light to account for a biorecogniton event. Such principles of operation include absorbance, transmittance, chemiluminescence, fluorescence, etc. In label-free biosensors, the target material interacts directly with the transducer and an optical signal is generated as a result of this interaction; on the other hand, labelled biosensors employ a label (which can be for instance a fluorescent molecule) to trigger the optical signal at the recognition event. On another note, surface plasmon resonance (SPR), evanescent wave and optical waveguide interferometry take advantage of the evanescent field close to the sensor surface in order to detect the biorecognition event.

- **Mass-based transducers**. Recognition reactions at sensor surfaces imply that some molecules may become attached to the subtrate, or that those already present experiment a variation in mass as a result of their participation in chemical reactions. This mass variation can be detected and quantified to account for biosensing. In this context, many operation principles can be employed for the detection of mass variation. For example, the piezoelectric effect employs crystals that undergo elastic deformation at the application of an electrical potential. Indeed, the application of an alternating potential produces a standing wave at a characteristic frequency on the crystal. This frequency depends on the elastic properties of the crystal, which become affected regarding the recognition events occurring at its surface.

[8] Created by Fvasconcellos, `https://en.wikipedia.org/wiki/Antibody$#$/media/File:Antibody.svg`.

[9] Created by Thomas Shafee, `https://en.wikipedia.org/wiki/Enzyme$#$/media/File:Glucosidase_enzyme.png`.

[10] `https://businessdocbox.com/Biotech_and_Biomedical/79182949-3-1-5-nucleic-acids\-structure-of-dna-and-rna.html`.

2.3.1.2 ITO-based biosensors: the state-of-the-art

Over the past fifteen years, a number of electrochemical biosensors based on indium tin oxide thin film substrates have been reported. Many of them employ gold nanoparticles as surface area and conductivity enhancers [157–160]. In the majority of cases, the gold nanoparticles were electrodeposited onto the ITO substrates by cyclic voltammetry, which permits a fine control over the size of the particles (of great importance in the performance of enzyme electrodes). Some works have reported that small size nanoparticles (between 20–24 nm) deliver a higher catalytic capability of certain enzyme-based biosensors than large size gold nanoparticles [157, 161]. Most of these gold nanoparticle-coated ITO-based senors have been devoted to the detection and quantification of hydrogen peroxide (H_2O_2). H_2O_2 is an essential mediator in industry, medicine, food, biology and environmental analysis [162]. In this sense, the biosensor must be prepared by chemically entrapping the horseradish peroxidase (HRP) enzyme on the sensor surface; typically this is done by means of an intermediate layer of crosslinkers, such as self-assembled monolayers by L-Cysteine [157] or membrane of chitosane [158].

Other works studied the aggregation of gold nanoparticles onto thin ITO films in a more fundamental way. Hu *et al.* investigated the morphologies of gold nanoparticles on ITO-coated glass by cyclic voltammetry and scanning electron microscopy, and their performance as streptavidin sensor by surface plasmon resonance [160]. An alternative electrode based on nickel ion implanted-modified ITO was presented by Tian *et al.* [163]. This was conceived for chronoamperometric detection of glucose, achieving good sensitivity and limit of detection levels as well as acceptable reproducibility and long-term stability. Other authors also used bare indium tin oxide electrodes for glucose sensing by amperometry [164]; such biosensor is based on direct electrochemical oxidation of H_2O_2 (which is the product of the oxidation reaction of glucose at the glucose oxidase-functionalized ITO electrode) at an auxiliary electrode. Generally, most glucose biosensors are based on two well defined chemical reactions: the oxidation of glucose catalyzed by the glucose oxidase (GOx) enzyme,

$$d-\text{glucose} + O_2 \longrightarrow \text{GOx}H_2O_2 + d-\text{gluconolactone}, \tag{2.28}$$

followed by a non-enzymatic hydrolysis:

$$d-\text{gluconolactone} + H_2O \longrightarrow d-\text{gluconic acid}. \tag{2.29}$$

A great variety of bioreceptors have been immobilized on ITO surfaces for electrochemical and optical sensing, which include not only the aforementioned enzymes but also antibodies and nucleic acids for DNA detection [165, 166]. Indeed, the use of a transparent conducting oxide such as ITO is suitable for bridging the gap between electrochemical and optical sensing by offering the capability of dual detection [165]. Yang *et al.* developed an ITO-based impedimetric sensor for *Escherichia coli* O157:H7 by immobilizing anti–*E. coli* antibodies. In this work, a self-assembled monolayer of epoxysilane was used as crosslinker to attached the organic antibodies to the ITO surface. Similarly, silane chemistry was also employed as crosslinker layer in [165] to functionalize ITO electrodes for DNA hybridization. The mentioned works prove that silane chemistry can be used to properly derivatize thin ITO films, and this leads to the investigation of the adequacy of nanostructured ITO electrodes for the formation of self-assembled silane monolayers, as will be developed in Chapter 3. Regarding the advantage of ITO in the complementation of electrical and optical applications, this material was used

as a coating for non-conductive optical fiber tips, electrochemically derivatized with biotin-labelled polymers and used for optical detection of several concentrations of an electroluminescent label attached to the target biomolecule.

Recently, a few investigations of the effect of ITO nanostructuration on both biomolecule and gas sensing have been reported [167–169]. However, the use of nanostructured ITO films is still very emerging and hence the present dissertation aims to contribute in reporting the behaviour of such electrodes as electrochemical sensors.

2.3.2 Strategies for surface modification and detection of species

Along the previous section, a general overview on biosensor classification was provided. Bearing in mind that, in the context of this work, electrochemical biosensors are the main object of study, here a series of biosensor preparation techniques will be revised. In the first place, some of the most popular methods of surface derivatization, this is, the preparation of an inorganic substrate for tethering organic biomolecules, are described. These include silane coupling agents, aryl diazonium salts and thiolation of gold surfaces. Then, the two basic principles of operation of electrochemical transducers (impedance and current-based methods) are explained in order to justify the choice of specific enzymes and other biomolecules for labelling the target species in the immunoassays performed in this work. The latter are also described in the final subsection of this part.

2.3.2.1 Crosslinkers for electrode derivatization

Crosslinkers are intermediate molecules useful to attach organic substances to inorganic substrates. The most common of them will be explained in this section. Two of these methods (silanization and CMA electroaddressing) were widely used in the scope of the thesis, and the other (gold thiolation) is also very commonly employed with the studied materials.

2.3.2.1.1 Silane coupling agents

Silane compounds (Figure 2.25) are bifunctional molecules that can attach one substance to another. They have been used for many years as "adhesive" agents to promote the bonding of an organic layer to an inorganic layer [170].

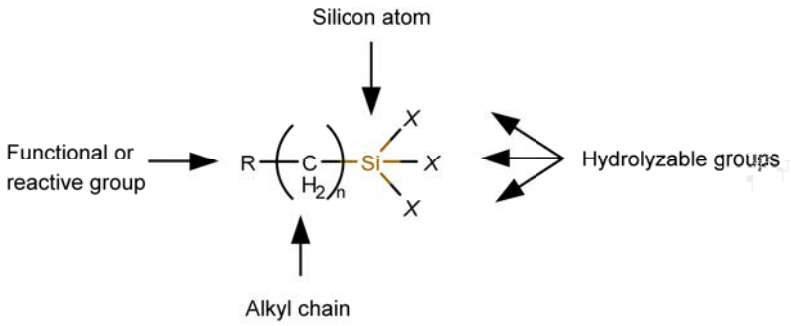

FIGURE 2.25: Silane coupling agents include a functional group R at the end of the alkyl chain $(CH_2)_n$. The latter is attached to the core silicon atom, which also has up to three hydrolysable groups X attached to it.

As observed in Figure 2.25, a silane compound is a monomeric silicon-based molecule that contains four constituents, as the other silicon and carbon-like compounds. Nevertheless, silicon is less electronegative than carbon, which makes it undergo more specific reactions than carbon and other typical organic compounds. *Organosilanes* have at least one bonded carbon atom, and the silicon atom core can also have hydrogen, oxygen or halogen atoms directly attached. Some of these derivatives are highly reactive, and can be used to form covalent linkages with other molecules or surfaces. In particular, those organosilanes containing a functional organic component on one side and a hydrolizable group on the other side allow conjugation of silanes to other organic compounds. Hydrolizable groups in organosilanes typically are unreactive to organic compounds, yet they can be covalently coupled to certain inorganic substrates. The whole silane molecule is named depending on which type of hydrolizable group is attached to the silicon atom, e.g. *silicon hydride* if the hydrolizable group is simply a hydrogen atom, *chlorosilane* if the hydrolizable group is a chlorine atom, *silanol* if the terminal group is –OH, and so on.

The general chemical structure of a functional silane coupling agent is shown in Figure 2.25. Figure 2.26 depicts the general reactions involved in the coupling of silane agents onto inorganic substrates. The illustration shows the particular reaction of *alkoxysilanes* (silanes where the reactive groups are alkoxy), as it is the case of the silane in Figure 2.25), which must first undergo hydrolysis to form silanols, the highly reactive forms that will couple to hydroxyls (–OH groups) in the neighbouring molecules. This occurs spontaneously as a result of the high instability of silanols. Then, the silane coupling agents condensate all together to form a polymer matrix linked by covalent Si–O–Si bonds. The growing silane network interacts with the inorganic substrate through the formation of a hydrogen bonding network with the superficial –OH groups. Then, another condensation reaction occurs to result in an organosilane polymer covalently linked (by siloxane linkages) to the substrate. Ideally, the silane coating should be a monolayer, although this actually does not occur. The thickness of the silane layer depends on the concentration of the silane coupling agent, as well as on the amount of water present in solution during the process. It is worth mentioning that the hydrolysis can only occur in aqueous media, but the attachment of organosilanes to inorganic substrates can also be conducted in organic media (e.g. toluene, pure ethanol). In the latter case, no hydrolysis can be produced, and hence no thick polymer layer is formed on the substrate but a thin organosilane layer where each agent is coupled directly to the substrate. It is worth highlighting that inorganic substrates suitable for silane coupling must present functional –OH groups on their surfaces, as do silica, glass, tin oxide, aluminium oxide and zinc oxide, amongst others. The bifunctional nature of silane coupling agents has popularized their use in many industries such as electronics, materials for construction, automotion, and of course bioconjugate chemistry, amongst others. Exhaustive reviews on the use of silane coupling agents can be found in the literature [171, 172].

The reaction techniques that can be employed with these compounds are varied, and the choice of strategy mainly depends on the substrate being modified and also on the inorganic reactive groups of the silane. Therefore, firstly the inorganic reactive groups must be chosen; and once the reactive groups are chosen, the silanization protocol must be established. Hermanson [170] provides an exhaustive review of available organosilanes for surface modification. In particular, in Chapter 3 of this thesis, the *glycidoxy* compound containing a reactive *epoxy* group was chosen, the so-called 3–Glycidoxypropyltrimethoxysilane (GOPTS). Surfaces covalently coated with

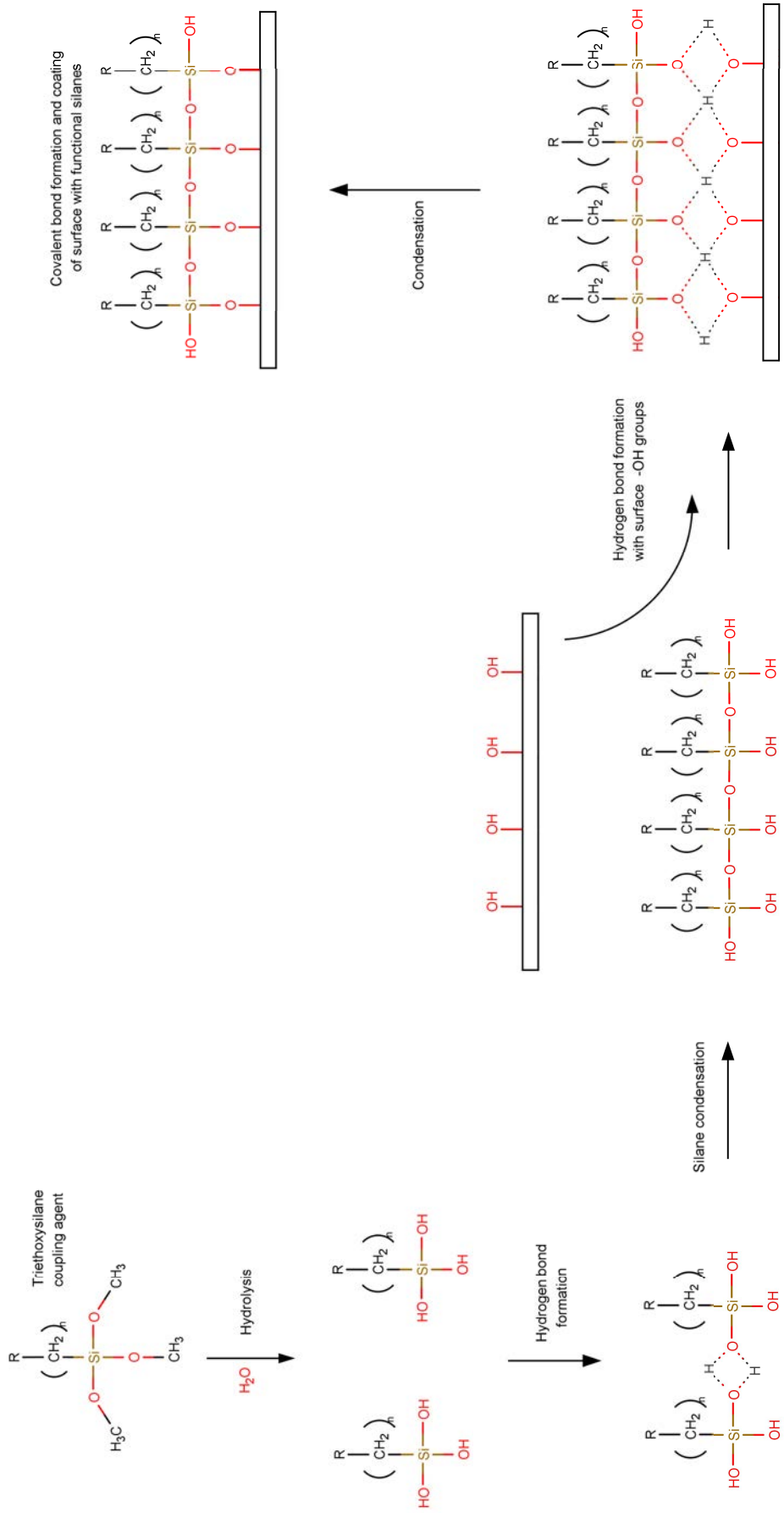

FIGURE 2.26: Reactions involved with the coupling of organosilane compounds to an inorganic surface containing -OH groups.

such molecules can be used to conjugate thiol–, amine– or hydroxyl-containing ligands, for then attaching biomolecules to them, in regard of the pH at which the reaction takes place. These three possible ligands have been represented as X in Figure 2.27, and the box symbol □ represents the biomolecule being attached to the surface. Thiol-containing ligands are of particular interest in the present project. GOPTS has been used most often in bioconjugation applications [173–176], and the particular reactions it undergoes are illustrated in Figure 2.27. Inorganic terminals in the silane molecule undergo hydrolisis to form reactive silanols, which interact with the inorganic surface as shown in Figure 2.26. The functional termination in GOPTS is called *epoxy* group, which consists of an oxygen O and two CH_2 in this triangle-like disposition. When GOPTS reacts with an organic biomolecule, the epoxy ring breaks to accomodate the biomolecule ligand X.

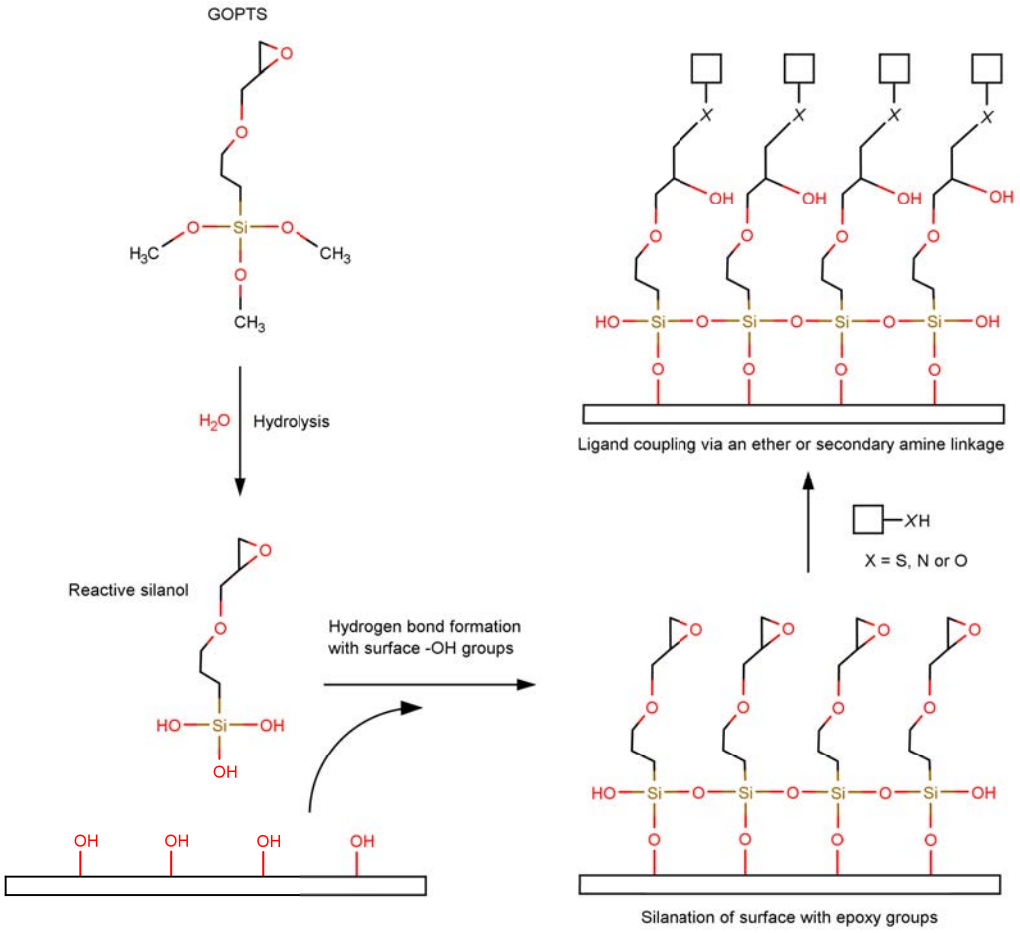

FIGURE 2.27: Epoxy-containing silanol coupling agents can be disposed into reactive surfaces, which in turn can be used to couple amine–, thiol– or hydroxyl-containing ligands: NH_3-, S− and OH−, respectively.

2.3.2.1.2 Diazonium salt electroaddressing (grafting reactions)

Diazonium salts are a set of organim molecules sharing a common functional group of the form R–$N_2^+X^-$. Generally, R is an aryl or alkyl organic group, and X usually is an halogen or any organic or inorganic anion. As a result of electrochemical reduction of diazonium salts, aryl radicals are formed and these become eventually grafted on the surface of the working electrode.

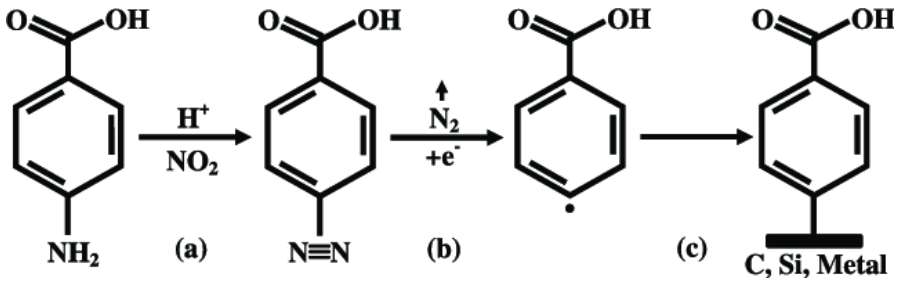

FIGURE 2.28: Electrochemical reduction of diazonium salts onto conducting surfaces, where (A) represents the spontaneous diazotation, in (B) is represented the electrochemical reduction and the grafting on the electrode surface in (C). Extracted from [177].

The grafting of diazonium salts on conductive surfaces by electroaddressing requires a controlled environment and must be performed very cautiously and rapidly. Figure 2.28 schematizes the steps by which aryl diazonium is processed and finally attached to a conductive surface. Of most importance is step (a) in Figure 2.28, where the spontaneous diazotation is only achieved in a relly controlled acid medium, generally achieved by an aqueous mixture of hydrochloric acid and sodium nitrite at 0 ^{o}C (see the detailed mechanism in Figure 2.29). The intermediates resulting from this primary diazotation are highly unstable. Hence, a proper derivatization of conductive surfaces with aryl diazonium salts must be done quickly and within controlled pH and temperature conditions. A really effective way of electroaddressing the coating is by cyclic voltammetry using the target conducting surface as working electrode. Indeed, once the diazonium salt is diazotated, the application of the proper voltage drives the reduction of the molecules on the conductive surface. Sweeping the potential at the working electrode within a reasonable voltage range (that will depend on the molecule to be reduced and the working electrode material) and cycling it three or four times leads to a highly covered (derivatized) working electrode surface, which results in decreased conductivity. This can be checked out by further cyclic voltammetry with a sensitive redox species such as ferrocyanide, whose redox peaks visible before electrode derivatization cannot be observed any more after diazonium salt electroaddressing (or appear strongly damped). Similarly, the Nyquist semicircle in electrochemical impedance spectroscopy can be widened more than three orders of magnitude.

This derivatization method can only be performed on specific conductive surfaces, so in this sense its applicability is much more reduced than organosilane conmpounds' is. On the other hand, the fact that it is done in an electroaddressed fashion is useful when having micropatterned electrodes in a multielectrode configuration, where it is impossible to avoid some of them from being soaked in the solution.

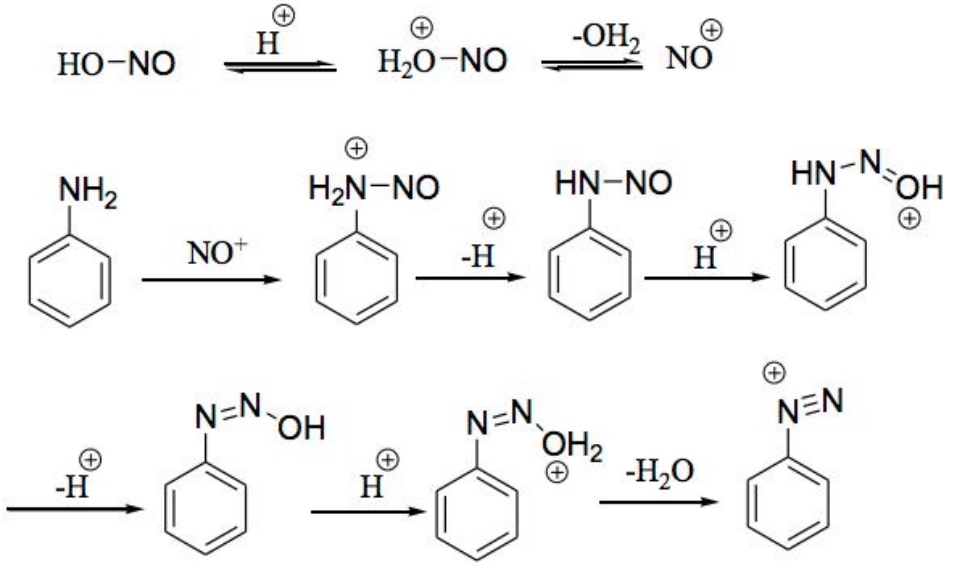

FIGURE 2.29: Mechanism of diazotation of aryl diazonium salts.

2.3.2.1.3 Thiolation of surfaces

The elements known as thiols consist of organic molecules with one carbon atom bonded to a sulfhydryl group (*R*–SH). The sulphur-gold interface has been far one of the most popular ones for creating self-assembled monolayers (SAMs). SAMs consist of highly-ordered chemisorbed species on a substrate which allow precise control on topology, chemistry and functionality at the molecular level, serving as structural or functional parts of (bio)sensors and other nanotechnology-based devices [178]. Thiol SAMs covering a surface can be prepared by exposure of the surface to thiols in both liquid and gas phases [179–181].

Figure 2.30a shows model thiol molecules and their interaction with gold surfaces and nanoparticles. Almost any functional or structural molecule can be thiolated by synthetic procedures [182–184]. Generally, one end of a bifunctional crosslinker consists of a sulfhydryl reactive group, whereas the other one tends to be an amine-reactive group already coupled to the target molecule. One of the most popular ways of thiolating molecules is by thiol-disulfide exchange reactions. A thiol molecule and a compound containing a disulfide group can participate in a reaction where the thiol attacks at the disulfide, breaking the –S–S– bond and resulting in the formation of a new disulfide as a mix of the reagents (general reaction shown in Figure 2.30b). These bonds are reversible under the action of disulfide reducing agents.

2.3.2.2 Transduction mechanisms

In the previous section, a brief overview of the options available for derivatizing electrode surfaces was presented. Now the electrode surface is ready for hosting an immunoassay on it. The immunoassays studied during the development of this thesis are described in the following section. Typically, after the surface derivatization, a first layer consisting of an antigen (or an antibody, regarding the kind of measurement we are interested in performing) is attached to the surface by chemical interaction with the

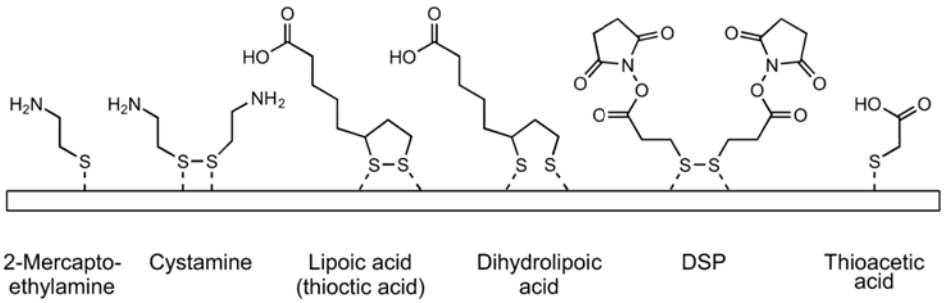

(A)

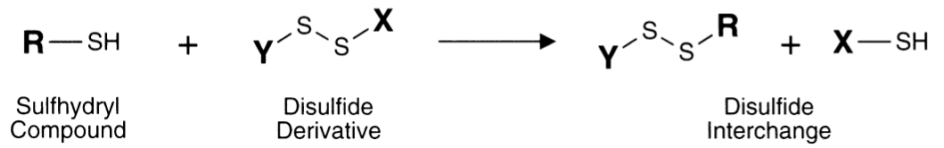

(B)

FIGURE 2.30: (A) Thiolated gold nanoparticles and surfaces. (B) Formation of a disulfide compound by breaking the –S–S– bond of an already existing molecule. Both images were extracted from [185].

crosslinker. Then, the detection of corresponding antibody (or antigen) can be done in several ways, regarding the transduction mechanism. The simplest method for detecting subsequent concentrations of species on top of the electrode is by performing electrochemical impedance spectroscopy. However, the physicochemical interpretation of the phenomena occurring during detection is not direct. Moreover, system stabilization issues are common when dealing with electrochemical impedance spectroscopy. Thus, detection by amperometry usually becomes an interesting alternative in spite of requiring some more steps and time during the immunoassay. Here are described both transduction principles and how they were implemented.

2.3.2.2.1 Impedance

Let us recall from Part II of this chapter that if electrochemical impedance spectroscopy is performed in a liquid medium containing one redox species, if the electrode is conductive enough then the typical equivalent circuit for the system consists of a series resistor in series with the parallel association of a pseudocapacitor and a resistor in series with a Warburg element. The series resistor is the one that offers the medium, which is supposed to be maintained constant as long as the medium does not vary. The parallel resistor corresponds to the difficulty of the charge to be transferred from solution to the working electrode and *viceversa*. This parameter is essential when performing biodetection by electrochemical impedance spectroscopy. Typically, the charge transfer resistor value increases when the biological layer between the electrode and the solution thickens. This is illustrated in Figure 2.31, reproduced here with permission from [186]. The geometry of the biosensor is shown in Figure 2.31a, as well as the immunoasay studied. Regarding the biosensor, a circular working electrode surrounded by the reference and counter electrodes are observed. This geometry is identical to the screen-printed electrodes based on carbon and commercialized by DropSens[11] (Asturias, Spain).

[11] `http://www.dropsens.com/en/screen_printed_electrodes_pag.html`.

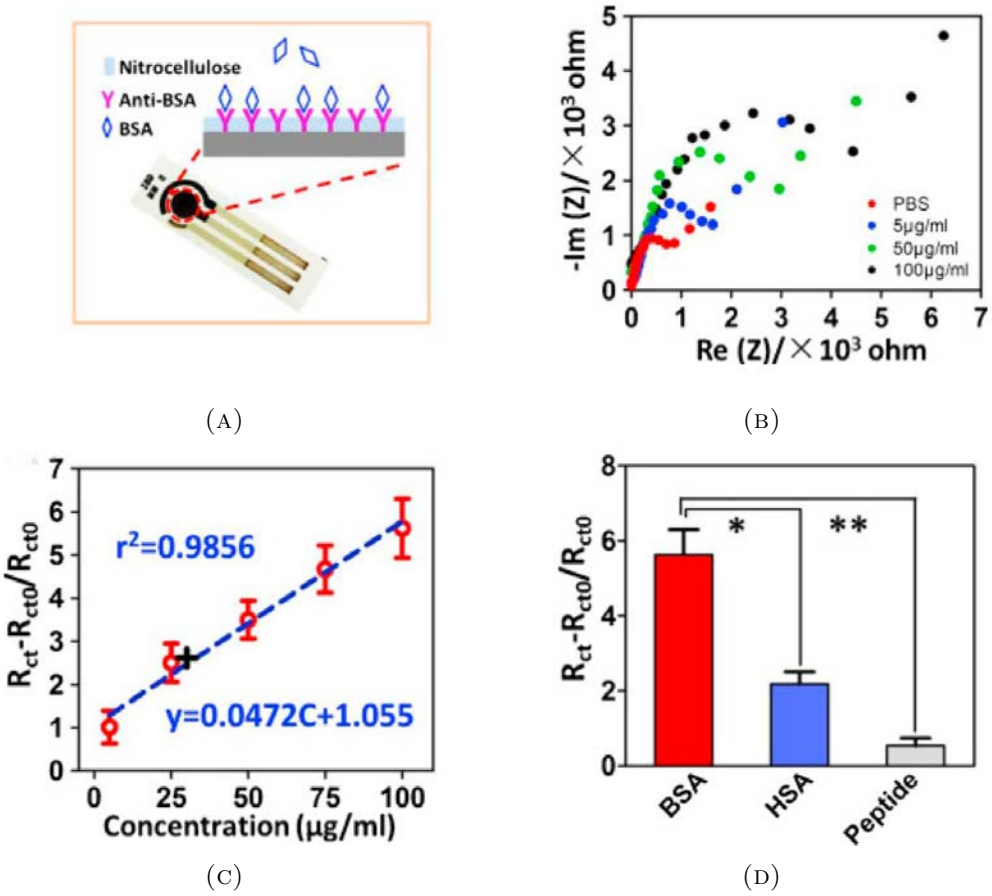

FIGURE 2.31: (A) Screen-printed working electrode modified by a nitrocellulose membrane with anti–BSA for BSA detection. (B) Detection of BSA at increasing concentrations by EIS measurement of Nyquist plots. (C) Linear calibration plot of normalized charge transfer resistance R_{CT} - R_{CT0}/R_{CT0} *versus* BSA concentration. (D) Selective responses of the system to BSA, HSA, and a peptide (mean ± standard deviation, $n = 5$). Extracted from [186].

The working electrode was derivatized with a nitrocellulose membrane, useful for hosting a coating of anti–BSA (bovine serum albumin) antibodies on the electrode surface. Detection of BSA antigen at subsequent increasing concentrations was performed by electrochemical impedance spectroscopy. In Figure 2.31b, the Nyquist plots of the system at subsequent increasing concentrations of BSA shows that the charge transfer resistance of the system increases accordingly. Figure 2.31c shows a linear calibration of the relative charge transfer resistance with the basal value with no BSA detection (just PBS). The authors show the specificity to BSA of their biosensor in Figure 2.31d, where the response of the device is benchmarked against the response to human serum albumin (HSA) and another peptide, showing a notable selectivity for BSA.

2.3.2.2.2 Current

As previously stated, electrochemical impedance spectroscopy measurements are not always easy to stabilize or to be conducted at the optimal levels for measurement parameters. Hence, in some cases it may be useful to include an additional step to the immunoassay procedure in order to label the target substance with an electroactive molecule or substance. Very frequently (especially in enzyme-linked immunosorbent assays, ELISA) this is an enzyme with redox activity, such as horseradish peroxidase (HRP) or alkaline phosphatase (AP). Figure 2.32 shows the most common types of enzyme-linked immunoassays; regarding the target molecule and the required sensitivity, ELISA can be performed as direct, indirect, sandwich or competitive assay.

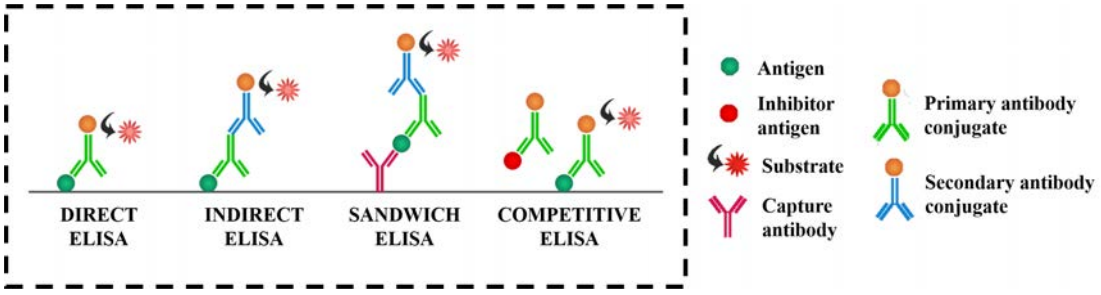

FIGURE 2.32: Types of enzyme-linked immunosorbent assays.[12]

In direct ELISA, the antigen is directly coated to the substrate and detected by a primary antibody conjugated to the enzyme. Although this is the least time-consuming and costly type of assay, the signal amplification may be concerned due to an eventual diminished immunoreactivity of the primary antibody caused by its labeling. This is overcome with indirect assays, since the primary antibody is not labelled there. Moreover, the sensitivity is further increased, for each primary antibody has several epitopes where labeled secondary antibodies can be bound. As a major drawback, cross-reactivity with the secondary antibody may occur. On the contrary, sandwich ELISA is highly specific, because both capture and detection antibodies are specific for different and non-overlapping epitopes. Regarding the competitive ELISA, a constant and known amount of enzyme-conjugated recombinant protein (competitive molecule) is added to the sample containing the target antigen. The known antigen surface coating competes with the target antigen in solution for the enzyme-labelled antibody, and thus, after incubation and washing steps, the lower the detection signal, the higher the target antigen concentration.

Now the question is, how to turn the presence of an enzyme-labelled antibody into a measurable signal? Let us take HRP as our study enzyme, since it is the one used in the scope of this thesis. HRP catalyzes the oxidation of hydrogen peroxide in the presence of a reduceable substrate. If current or colorimetric changes are to be measured, 3,3',5,5'–tetramethylbenzidine (TMB) is used as substrate. Figure 2.33a schematizes the chemical changes in this molecule when present in a redox reaction with hydrogen peroxide catalyzed by HRP. Interestingly, not only current and colorimetric changes can be measured with an inmunoassay involving HRP; using Luminol (Figure 2.33b) instead

[12] `https://www.bosterbio.com/protocol-and-troubleshooting/elisa-principle`.

of TMB produces photon emission when HRP catalyzes the oxidation of hydrogen peroxide, which could be quantified by spectrophotometry.

An interesting example of biomarker detection by amperometry is shown in Figure 2.34. The authors derivatized gold working electrodes with NH_2 terminated crosslinkers, and a coating of tumour necrosis factor α (TNF–α) was immobilized on them. Then, subsequent concentration levels of TNF–α antigen were added, with a final constant concentration of secondary TNF–α antibody labelled with HRP. Figure 2.34a shows the amperometric response of the sensor, where increasing current levels can be observed for increasing antigen (and thus HRP) concentrations. Figure 2.34b shows the linear

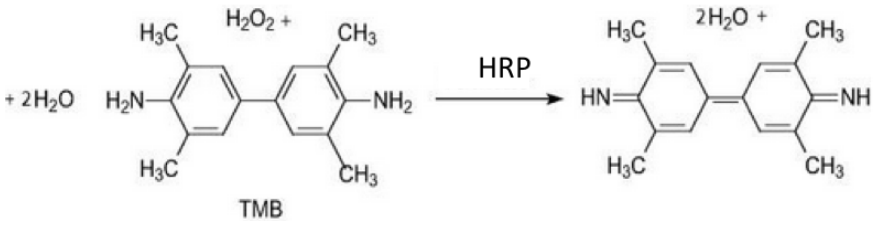

(A)

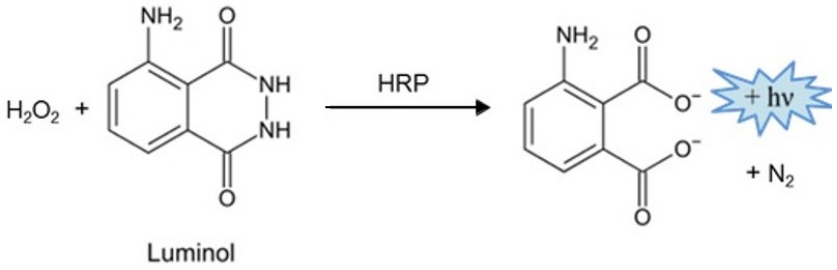

(B)

FIGURE 2.33: (A) Reduction of tetramethylbenzidine (TMB) and oxidation of hydrogen peroxide and (B) reduction of luminol and oxidation of hydrogen peroxide with the emission of a photon; both reactions catalyzed by horseradish peroxidase.

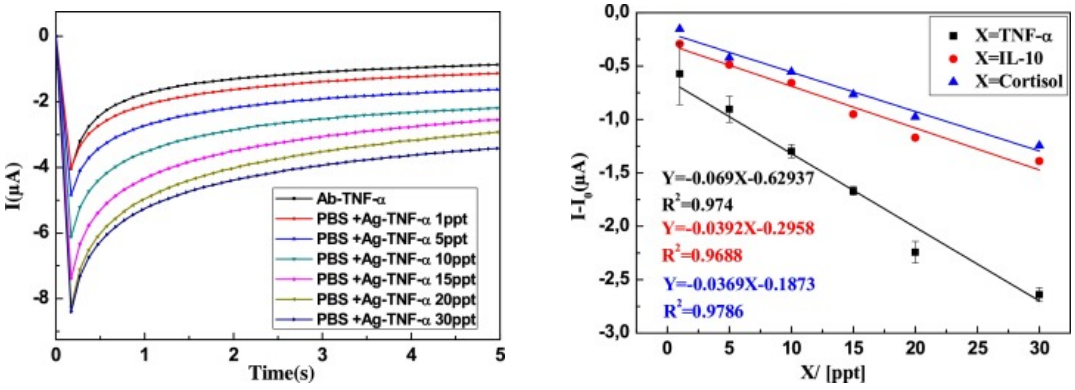

(A) (B)

FIGURE 2.34: (A) Amperometric response of a gold working electrode-based biosensor to increasing concentrations of tumour necrosis factor α. (B) Linear calibration of the sensor response to TNF–α and interfering molecules. Reproduced with permission from [187].

response of the sensor with TNF–α concentration, as well as its behaviour to interfering molecules such as cortisol and Interleukin–10.

2.3.3 Assays of interest used in this work

In this section, background on the nature of the immunoassays tested in this thesis will be provided: the type of target analytes and their possible implications in human health or environmental care, as well as the necessary steps for building the immunoassay and detection principles.

2.3.3.1 Bovine serum albumine

Bovine serum albumin (BSA) is a protein chemically similar to human serum albumin (HSA), and it is found in cows blood plasma. Albumins are a kind of globular (spherical) proteins, soluble in water and also in concentrated salt solutions, whose main function is to regulate blood volume by maintaining the colloid osmotic pressure (exerted by dissolved proteins) of blood. BSA is extensively used as standard protein in laboratory experiments. It is composed of 583 aminoacids and weights around 66.5 kDa. The three-dimensional structure of BSA is shown in Figure 2.35.

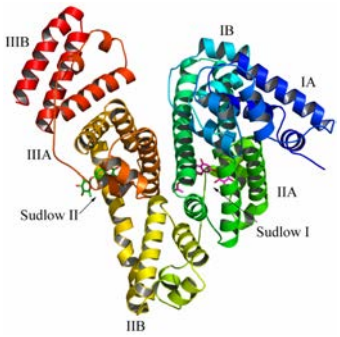

FIGURE 2.35: Three-dimensional model of bovine serum albumin. Extracted from [188].

Monoclonal anti–bovine serum albumin antibody is specific for BSA. Antibodies are substances generated by the immune system[13] to identify and neutralize foreing objects, and each antigen is specific for recognizing a specific antigen. Monoclonal antibodies are produced by a single type of immune cell and so they are identical. On the contrary, polyclonal antibodies are derived from different cell lines and so they differ in the aminoacids sequence. For the purposes of this thesis and concretely in the case of this immunoassay, derivatized surfaces are coated with BSA, and monoclonal anti–BSA is employed for biorecognition of BSA. Detection is performed by amperometry, and thus a reactive enzyme (HRP) is incorporated as a label to immunoglobulin G antibodies (anti–IgG). In this case, IgG acts as secondary antibody (please see Indirect ELISA in Figure 2.32) to assist in detection. Indeed, primary antibodies not only exhibit high specificity for the corresponding antigen, but also for secondary antibodies.

2.3.3.2 Biotin – streptavidin

Biotin is a water-soluble vitamin (also known as vitamin B_7, vitamin H or coenzyme R) that is involved in several metabolic processes regulating the utilization of fats, carbohydrates and amino-acids, also helping in the steady upkeep of blood sugar levels. A deficiency of biotin is believed to cause hair thinning and skin rush on human bodies, among other effects. Such deficiency may be caused by an inadequate dietary uptake or by the inheritance of inborn genetic disorders related to biotin metabolism.

[13] Some notes on the production of antibodies can be found in Appendix B.

Biotin presents a high affinity for a protein known as avidin or streptavidin, a biomolecule weighting 52.8 kDa that is obtained from the *Streptomyces avidinii* bacterium. Moreover, streptavidin presents up to four binding sites for biotin (Figure 2.36), which can be exploited for immunoassay signal amplification, as will be explained below. The biotin–streptavidin complex presents a dissociation constant of around $K_{\mathrm{d}} \approx 10^{-14} - 10^{-15}$ mol L^{-1} [189], resulting in one of the strongest non-covalent interactions known in nature [190]. This provides the complex a high resistance to organic solvents, denaturants, detergents, proteolytic enzymes, and extreme pH and temperatures. However, regarding the nature of the final application, such a strong binding may become a problem rather than an advantage, yet certain avidin variations (mutations) are available which allow a reversible interaction.

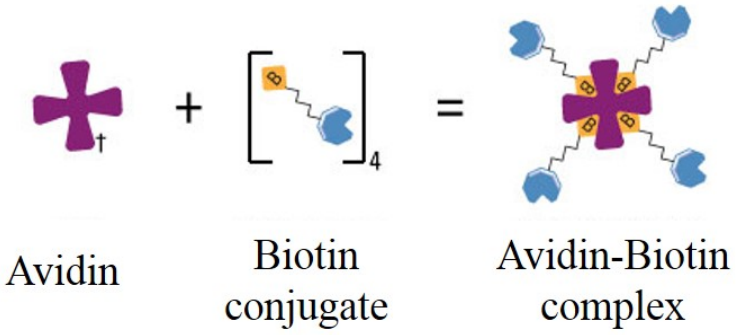

FIGURE 2.36: Up to four biotin molecules can be bound to a single streptavidin.[14]A typical immunoassay configuration involves a first biotin layer to which a second streptavidin layer is conjugated, and taking advantage of the multi-binding site provided by streptavidin, a top layer of biotin-labelled functional molecules is added to build the biosensor.

The reasons for such a high affinity between biotin and streptavidin are both physical and chemical, and can be enumerated as follows:

- The first physical reason why biotin and streptavidin present that strong affinity is the high shape complementarity between the vitamin and the protein's binding pocket.
- Such pocket is hydrophobic, and thus several van der Waals force-mediated contacts and hydrophobic interactions are exherted to the biotin when the latter is accomodated in the pocket.
- An extensive network of hydrogen bonds is formed between the vitamin and its binding site in the protein.
- Finally, the binding event is accompanied by the stabilization of a flexible loop on the structure of the protein, which closes over the bound biotin and further tightens the biotin–streptavidin liaison.

The biotin–streptavidin interaction has been used as a reference in biosensor research, to attach biomolecules to one another or onto a solid support, and in the detection and purification of biomolecules [191, 192], or as a building block for linking biomolecules to

[14] `https://www.thermofisher.com/content/dam/LifeTech/Images/integration/Avidin-Biotin-Interaction1.jpg`.

create nanoscale devices or structures [193, 194]. This complex has also immunotherapeutic uses, for streptavidin conjugated to a monoclonal antibody can be introduced in the body to face determined cancer cell-specific antigens. This is followed by an injection of radiolabelled biotin that will deliver the radiation only to the target cancerous cell to whose antigens the streptavidin-conjugated antibodies have been bound. The process of attaching a biotin molecule to other species is known as biotinylation.

2.3.3.2.1 Biotinylation and signal amplification

As mentioned before, biotinylation is a laboratory technique that consists in labelling molecules of interest with biotin in order to study a variety of processes such as protein localization and protein interactions and signal amplification (Figure 2.37), as well as DNA transcription and replication.[15]

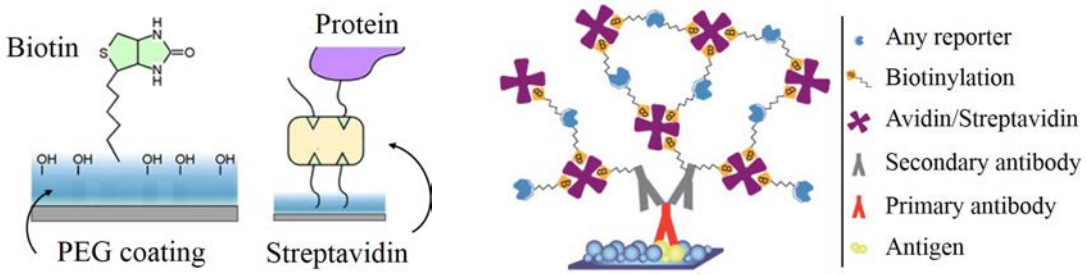

(A) (B)

FIGURE 2.37: (A) Molecular representation of biotin and preparation of a biosensing electrode based on biotin–streptavidin interaction.[16] (B) Example of signal amplification by multiple binding of biotin to streptavidin.[17]

The process of labelling proteins and other biomolecules with biotin can be performed either by enzymatic or chemical means, being the latter the most commonly used. Three reagents are needed in order to proceed with chemical biotinylation: the biotinyl group on one end and a reactive group on the other end, both separated by a spacer arm. The latter provides the whole complex with some relevant physicochemical features; for example, the length of the spacer arm affects the biotin disposition to bind the streptavidin: long spacer arms tend to be hydrophobic, thus they render less soluble labelled proteins, which are in turn ideal to be employed in hydrophobic organic solvents (e.g. when modifying hydrophobic peptides). Overall, the solubilty of biotinylation reagets influences the possibility of modifying proteins located in membrane-bound compartments or either altering the solubility of the labelled target proteins.

As mentioned before, spacer arms link a biotin to the reactive group responsible for interacting with certain functional groups composing the target protein. Regarding the reactive groups of the biotinylation agents, the most common of them are listed below, together with their respective targets in proteins:

[15] https://www.thermofisher.com/es/es/home/life-science/protein-biology/protein-biology-learning-center/protein-biology-resource-library/pierce-protein-methods/overview-protein-labeling.html#/legacy=www.piercenet.com.

[16] http://www.proteinslides.com/sites/default/files/Biotin_2.jpg.

[17] https://www.thermofisher.com/content/dam/LifeTech/Images/integration/avidin-biotin-complex-alone.jpg.

- N–hydroxysuccinimide (NHS) and Sulfo–NHS ⟶ primary amines;
- Maleimide, iodoacetyl groups or pyridyl disulfides ⟶ sulfhydryls;
- Primary amines in combination with EDC ⟶ carboxyls;
- Hydrazines and alkoxyamines ⟶ glycoproteins.

2.3.3.3 Tumour necrosis factor α

Tumour necrosis factor (TNF) is a cytokine with a role in systemic inflammation and acute phase reaction that causes several clinical disorders related to autoimmune diseases (e.g. psoriasis, rheumatoid arthritis, inflammatory bowel disease). TNF is produced in its primary stage as a 233 amino-acid long transmembrane protein, from which the final TNF–α is released. The proteic structure of TNF–α is shown in Figure 2.38a.

TNF is produced by several cell types, including macrophages, lymphoid cells, cardiac myocites, neurons, fibroblasts, mast cells, adipose tissue and endothelial cells [195], and is released in response to inflammatory stimuli. TNF–α binds mainly to the transmembrane receptor TNFR1, which is expressed in most tissues (TNFR2 is expressed in cells of the immune system), and triggers a signaling cascade, which is shown in Figure 2.38b. Out of all the effects that TNF–α has on various organ systems, generally together with Interleukin-1 and Interleukin–6, the most important of them are suppression of appetite and fever (effect on the hypothalamus); increase of insuline resistance (on the liver); stimulation of phagocytosis (on macrophages); etc. It has also been found to have a role in Alzheimer's disease, major depression and cancer, amongst others [196–199].

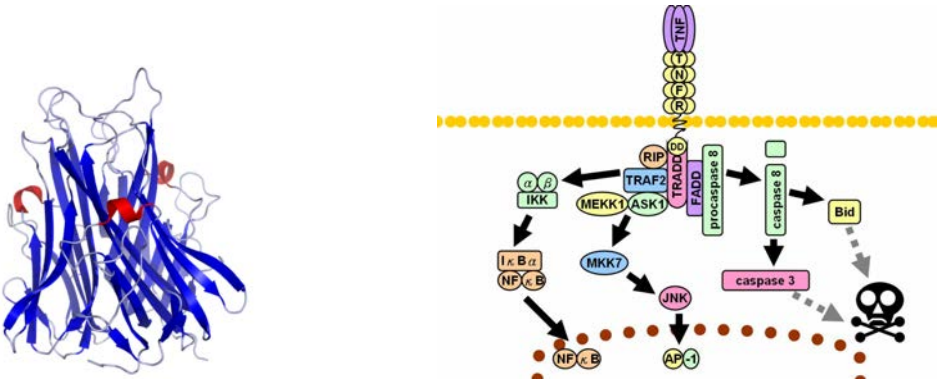

(A) (B)

FIGURE 2.38: (A) Crystal structure of TNF–α as published in the Protein Data Bank.[18] (B) Simple representation of TNFR signaling pathways, where dashed lines represent multiple steps.[19]

[18]Created by Ramin Herati from PDB1 TNF and rendered with Pymol, `https://upload.wikimedia.org/wikipedia/commons/thumb/3/3b/TNFa_Crystal_Structure.rsh.png/250px-TNFa_Crystal_Structure.rsh.png`.

[19]Original uploaded by Subclavian (Transfered by Vojtech.dostal) to Wikipedia, `https://en.wikipedia.org/wiki/Tumor_necrosis_factor_alpha#/media/File:TNF_signaling.jpg`.

Chapter 3

Study of the viability of nanostructured ITO as electrode for electrochemistry

Prior to the development of an immunoassay to test a material as working electrode for biosensing, the behaviour of this material must be thoroughly studied. In this thesis, indium tin oxide (ITO) is the subject of study for the reasons explicited in the previous chapter. All the ITO electrodes used in this thesis were either prepared by electron beam evaporation in the facilities of the Universitat de Barcelona, or purchased as commercial transparent slices for comparing both results.

First thing we became aware of was that, although used to produce good-quality thin ITO films at low temperatures, the electron beam evaporator beared higher temperatures, which resulted in highly-densed nanostructured ITO films. Thus, the first tests performed in the frame of this thesis were oriented to comparing the electrochemical performance between thin films and nanostructured electrodes. This was done by computing the equivalent electrochemical surface area from measurements of the faradaic current across the electrodes under redox reactions, and will be thoroughly described in Article 1, included in Section 3.1.

The natural continuation of this work was to investigate the role of substrate temperature during deposition in the nanostructuration of the resulting surface, and to determine the lowest temperature producing good-quality electrodes for electrochemistry applications. This is shown in the first part of Section 3.2 (Article II). Additionally, the influence of target composition in the quality of the resulting films was also investigated.

Having optimized the fabrication parameters to obtain the optimal material in terms of electrochemical performance, an interesting thing to investigate is whether it is suitable for micropatterning arbitrarily shaped electrodes. The micropatterning was achieved by photolithography and the results of these experiments are gathered in Section 3.3.

3.1 Thin film *versus* nanostructured indium tin oxide

The experiments comparing the electrochemical performance of thin films and nanostructured ITO electrodes are gathered in *Article I: Electrochemical characterization of organosilane-functionalized nanostructured ITO surfaces*. The main objectives of this article can be summarized as follows:

1. surface characterization of the resulting nanostructured ITO electrodes;
2. comparison of the electrochemical performance of thin ITO films and nanostructured electrodes;
3. determination of the influence of post-annealing treatment in the electrochemical performance of thin and nanostructured ITO films and
4. proof-of-concept in a real sensing environment: detection of the redox activity of ferrocene molecules immobilized on the electrodes' surface.

Thin and nanostructured ITO films were prepared by electron beam evaporation at 100 °C and 700 °C, respectively, and some were left as-deposited whereas the rest of them were submitted to a post-annealing process to promote the crystallization and consequent transparency of the ITO films. The resulting films were observed by scanning electron microscopy (SEM) and atomic force microscopy (AFM), showing a dense nanostructuration with wires of diameter around 30 nm.

The electrochemical surface area was computed by performing successive cyclic voltammetries at increasing scan rates in a classical redox medium and verifying the Randles-Sevcik equation in a constant-sized electrochemical cell. Annealed nanostructured ITO electrodes presented the highest electrochemically active surface area. In this work, the first attempt of functionalizing the ITO structure was made, just to confirm that an increase in the electrochemical surface area of nanostructured electrodes compared to thin films was also observable in a real sensing scenario. For this, a model organic molecule with redox activity was chemically attached to the surface, and its redox electrochemical behaviour was tested again by cyclic voltammetry. Nanostructured electrodes delivered a better signal, presumably because their increased surface area accomodated a higher number of functionalizing molecules. Moreover, this increased signal was more pronounced in the case of annealed surfaces due to the effect this process has in the conductivity of the electrodes.

Please note that in this and subsequent articles reproduced in this dissertation, section, equation, figure and table labels as well as figure, table and reference numbering are those of the published version.

The article has been reproduced from Applied Physics Letters; vol. 109; R. Pruna, F. Palacio, M. López, J. Pérez, M. Mir, O. Blázquez, S. Hernández and B. Garrido, "Electrochemical characterization of organosilane-functionalized nanostructured ITO surfaces", 063109, 2016; with permission from the American Institute of Physics (AIP) Publishing.

Electrochemical characterization of organosilane-functionalized nanostructured ITO surfaces

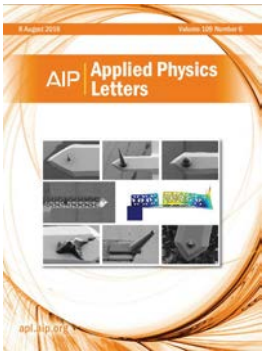

Raquel Pruna,[1] Francisco Palacio,[1] Manel López,[1] Judit Pérez,[2] Mònica Mir,[2,3] Oriol Blázquez,[4] Sergi Hernández,[4] and Blas Garrido[4]

[1)] *SIC, Departament d'Enginyeries: Electrònica, Universitat de Barcelona, Martí i Franquès 1, E-08028 Barcelona, Spain*

[2)] *Institute for Bioengineering of Catalonia, Parc Científic de Barcelona, Baldiri Reixac 4-12-15, E-08028 Barcelona, Spain*

[3)] *Centro de Investigación Biomédica en Red en Bioingeniería, Biomateriales y Nanomedicina (CIBER-BBN), Monforte de Lemos 3-5 Pabellón 11, E-28029 Madrid, Spain*

[4)] *MIND-IN^2 UB, Departament d'Enginyeries: Electrònica, Universitat de Barcelona, Martí i Franquès 1, E-08028 Barcelona, Spain*

Applied Physics Letters, 109(6) (2016), 063109
doi: 10.1063/1.4960734

ABSTRACT

The electroactivity of nanostructured indium tin oxide (ITO) has been investigated for its further use in applications such as sensing biological compounds by the analysis of redox active molecules. ITO films were fabricated by using electron beam evaporation at different substrate temperatures and subsequently annealed for promoting their crystallization. The morphology of the deposited material was monitored by scanning electron microscopy, confirming the deposition of either thin films or nanowires, depending on the substrate temperature. Electrochemical surface characterization revealed a 45 % increase in the electroactive surface area of nanostructured ITO with respect to thin films, one third lower than the geometrical surface area variation determined by atomic force microscopy. ITO surfaces were functionalized with a model organic molecule known as 6-(ferrocenyl)hexanethiol. The chemical attachment was done by means of a glycidoxy compound containing a reactive epoxy group, the so-called 3-glycidoxypropyltrimethoxy-silane. ITO functionalization was useful for determining the benefits of nanostructuration on the surface coverage of active molecules. Compared to ITO thin films, an increase in the total peak height of 140 % was observed for as-deposited nanostructured electrodes, whereas the same measurement for annealed electrodes resulted in an increase of more than 400 %. These preliminary results demonstrate the ability of nanostructured ITO to increase the surface-to-volume ratio, conductivity and surface area functionalization, features that highly benefit the performance of biosensors.

During the last decade there has been an increasing interest in ultrasensitive, low-cost and miniaturized biosensors. Nanostructured materials have been key research subjects due to their high surface-to-volume ratio, favorable electronic properties as well as electrocatalytic activity [1–3]. In particular, carbon nanowires and carbon nanotubes (CNTs) have received particular attention, as they have proven to be highly robust and

sensitive [4 and 5]. However, the use of carbon has been generally avoided on electronic devices because of its polluting action [6]. For instance, during thermal oxidation of a contaminated silicon surface, the pyrolysis of organic contaminants degrades the silicon oxide and exerts adverse influences on the device performance [7]. This and other facts hinder the integration of carbon-based nanotechnology with the silicon chip technology and make necessary to use other compounds compatible with it. Several authors are currently working on the integration of CNTs with contemporary technology, yet such integration is presently unfeasible due to a number of unsolved critical issues [8 and 9].

Recently, there has been a growing interest in fabricating biosensors by standard silicon technology using complementary metal-oxide-semiconductor (CMOS) compatible processes, which allow integration with microelectronics [10]. As stated by Libertino *et al.*, such silicon-based devices would provide many potential advantages, mainly small size, reduced weight and on-chip integration, which would lead to a low-cost mass production of portable and miniaturized microanalysis systems. Besides, silicon-based devices also permit fast response and low output impedance, providing highly reliable results, which is crucial for the development of biosensors. In this scenario, the need for new CMOS-integrable materials arises. Indium tin oxide (ITO) is a transparent material with excellent conductivity that has been extensively studied and used in the field of opto-electronics [11 and 12], enabling the design of light detectors or photovoltaic devices that can be integrated with the silicon technology. Besides, ITO thin films have been widely employed for sensing applications, for ITO is a material that can be easily functionalized like some other common oxides [13–15]. In addition, the integrability of this material with the silicon chip technology allows fast sensors prototyping, i.e., their mass-production at low costs. Choi *et al.* reported a system capable of obtaining optical images at the same time they performed microimpedance analysis of time-dependent cellular growth [16]. Thus, they were able to correlate the higher cell-covered area increase with the impedance increase on the electrode. This system evolved towards an opto-electronic biosensor able to perform simultaneous optical and electrical measurements to examine the dynamic cellular attachment, spreading and proliferation of endothelial cells [17]. A different approach was followed by Muhammad-Tahir [18] that, by combining highly specific antibody molecules and conductive polymer compounds with excellent electrochemical properties, developed a ITO-polyaniline biosensor capable of identifying multiple targets of detection, namely, potential bioterrorism agents. Recently, Wu *et al.* presented an electrochemiluminescence biosensor based on a gold-ITO hybrid bipolar electrode for detecting cancer cell surface proteins using a ferrocene-labeled aptamer as a signal recognition and amplification probe [19].

This letter reports on the viability of increasing biosensor sensitivity by means of nanostructured ITO surfaces. The interest in this material is justified by the ease of its fabrication, together with its good conducting and optical properties, which ultimately permit mass fabrication of electrochemical biosensors and their integration with the silicon chip technology, to take advantage of the many possibilities that this entails. After electrode fabrication by electron beam evaporation and observation by scanning electron microscopy (SEM), geometrical surface area was measured by atomic force microscopy (AFM). Cyclic voltammetry (CV) helped deducing the available conductive surface area, and results were compared with the previous ones. Next, the surfaces were chemically functionalized with a ferrocene-labeled organic molecule known as 6-(ferrocenyl)hexanethiol. Immobilization of the organic molecule and its surface coverage was also determined by CV.

ITO was grown by means of the electron beam evaporation technique onto crystalline N^+-doped Si substrates. The system used was a Pfeiffer Vacuum Classic 500 with a Ferrotec Genius electron beam controller and a Ferrotec Carrera high-voltage supply. Commercial ITO targets were employed as raw materials during

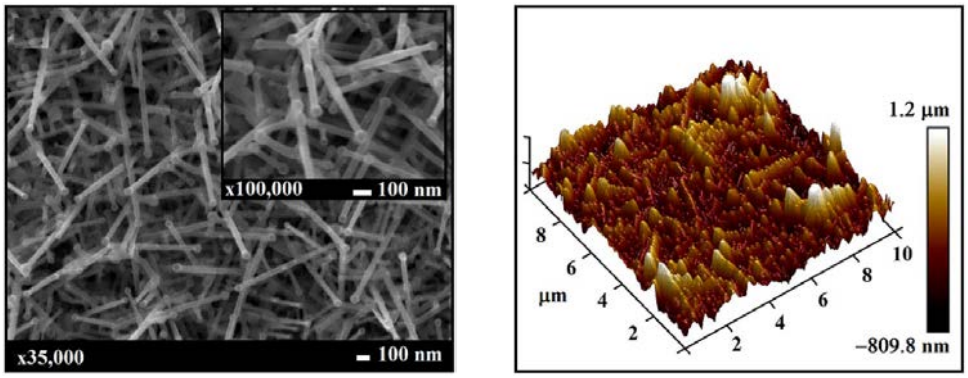

(a) (b)

FIG. 1: Microscopy images of as-deposited nanostructured ITO films. (a) ×35,000 and ×100,000 magnified SEM images and (b) 10×10 μm^2 AFM topographical image.

evaporation. The substrate temperature was set at 200 °C and 700 °C for thin film and nanostructured growth, respectively. In both cases, the deposition rate was set at 1 Å s^{-1}, and the evaporation time was programmed to obtain an equivalent thin film thickness of 500 nm. At this point, half of the samples were left as-deposited, whereas the rest were submitted to an annealing process at 600 °C under nitrogen atmosphere for 1 h. The dependence of ITO electrical and optical characteristics on annealing parameters has been so far widely reported in the literature [20–22]; thus the aforementioned annealing specifications were chosen to promote the ITO crystallization and to achieve good electrical conductivity. The resulting electrodes were observed by SEM. The geometrical surface area of the different ITO morphologies was determined from the analysis of AFM data, taking the area under the z-displacement versus the scanning direction. AFM observations were carried out in a Multimode 8 with a Nanoscope V electronics from Bruker. The electroactive surface area was deduced by CV, which was carried out in a conventional three-electrode Teflon electrochemical cell containing 5 mM ferricyanide/ferrocyanide ($Fe(CN)_6^{3-}/Fe(CN)_6^{4-}$) in 0.1 M KCl solution at 25 °C and connected to a Biologic-EC-Lab SP300 potentiostat interface. A platinum wire was used as a counter electrode and a Ag/AgCl as reference electrode. The working electrode was the corresponding ITO surface under analysis. The electrode geometrical projected area exposed to the redox ferrocyanide solution was 0.7 cm^2.

ITO functionalization has been widely described. Ref. 23 provides an exhaustive review of available organosilane molecules for surface modification. In particular, a glycidoxy compound called 3-glycidoxypropyltrimethoxy silane (GOPTS), containing a reactive epoxy group, was chosen for the present study. Surfaces covalently coated with such molecules can be used to conjugate thiol-, amine- or hydroxyl-containing ligands, for then attaching biomolecules to them [24 and 25]. One way to attach specific functional molecules to the GOPTS-functionalized surface was demonstrated by covalently linking a ferrocene-labeled thiolated molecule, i.e., 6-(ferrocenyl)hexanethiol, via reaction of epoxy rings with sulfide terminations. ITO surfaces were first cleaned with acetone for 10 min and dichloromethane for another 10 min. All ITO electrodes were rinsed with ultrapure water three times, and then immersed in 5:1 H_2O + H_2O_2 (30 %) solution for 10 min. Finally, all ITO electrodes were rinsed and dried with a stream of nitrogen. For ITO film silanization, a solution of GOPTS at 4 % (v/v) in toluene was prepared. All slides were immersed in the prepared solution for 8 h under soft mixing. Immediately afterwards, the epoxy ring opening was performed by immersing the substrates in 500 μM solution of 6-(ferrocenyl)hexanethiol in *N*,*N*-dimethylformamide (DMF). Reaction between the epoxy group (on the

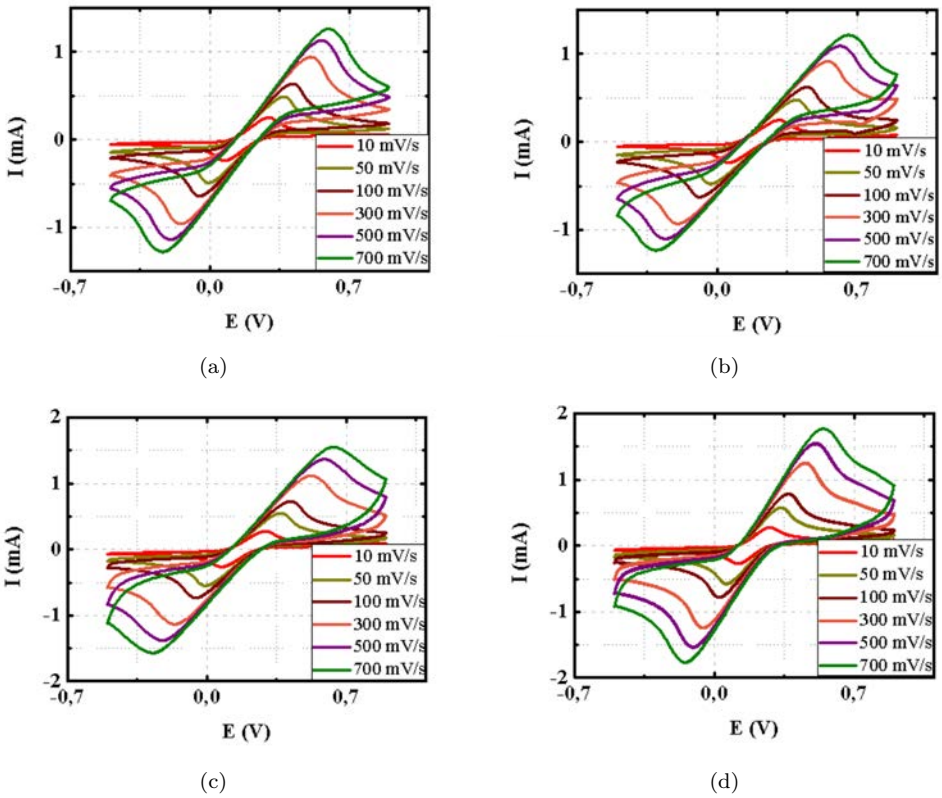

FIG. 2: Cyclic voltammetry at different scan rates (10 mV s^{-1}, 50 mV s^{-1}, 100 mV s^{-1}, 300 mV s^{-1}, 500 mV s^{-1} and 700 mV s^{-1}) of (a) as-deposited and (b) annealed thin film electrodes, and (c) as-deposited and (d) annealed nanostructured electrodes. An increase in redox current peaks occurs as a result of surface nanostructuration.

electrode's surface, coming from GOPTS) and the thiol termination was let to take place at room temperature and kept from light for 8 h, under physiological pH for the sake of efficient coupling. Finally, all ITO surfaces were rinsed with washing solution three times and with 10 mM NaCl one more time.

Fig. 1 shows the resulting images from (a) SEM and (b) AFM analysis for one of the bare nanostructured ITO films, allowing the calculation of its geometrical surface area. The geometrical surface area was calculated by triangulation algorithms on AFM data in Nanoscope Analysis v.1.5 software, Veeco Instruments (see Ref. 26 for more details regarding the surface area evaluation from AFM measurements), and we found that nanostructured film area was 2.54 times the projected area, for both as-deposited and annealed samples. On the other hand, electroactive surface area was deduced by CV analysis using a redox solution. The cathodic and anodic currents and the potentials at which this solution is reduced and oxidized are (I_{pc}, E_{pc}) and (I_{pa}, E_{pa}), respectively. The anodic peak current can be expressed by the Randles-Sevcik equation as in Eq. 1

$$I_{\mathrm{pa}} = \kappa n F A C \sqrt{\frac{nF\nu D}{RT}}, \tag{1}$$

where $\kappa = 0.4463$ is an adimensional proportionality constant; n is the number of electrons for the redox couple, 1 in the present case; F and R are Faraday's (96,485 C mol^{-1}) and universal gas (8.314 J mol^{-1} K^{-1}) constants, respectively; A is the electrode area in cm^2; ν is the rate at which the potential is swept, in V s^{-1};

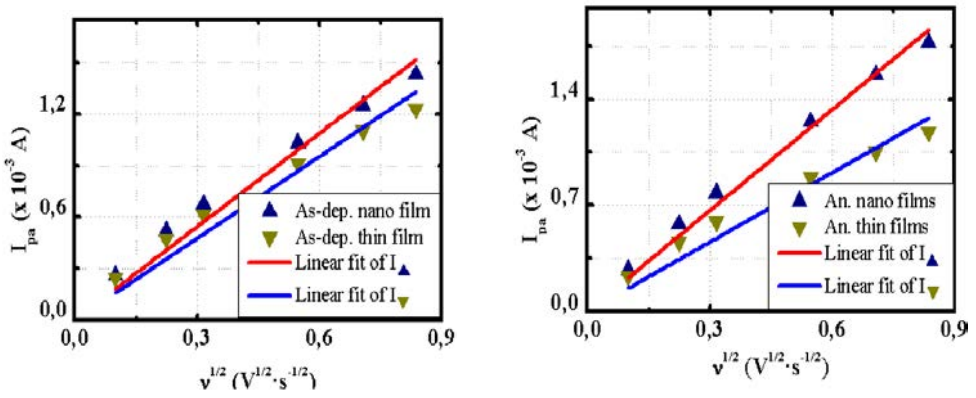

FIG. 3: Representation of anodic intensity peak in ampères vs. square root of scan rate in $V^{1/2}$ $s^{-1/2}$ for (a) as-deposited ITO electrodes and (b) annealed ITO electrodes. An equation $y = a * x$ was adjusted for each dataset. The increase in nanostructured sensor sensitivity with respect to thin film's, which is determined by the slope of the equation, is higher in the case of annealed electrodes.

D is the analyte's diffusion coefficient in cm^2 s^{-1}; C is the analyte's concentration in mol cm^{-3} and T is the solution temperature in K. The latter parameter was 25 °C, the analyte's concentration was 5×10^{-6} mol cm^{-3} and its diffusion coefficient was 2.7×10^{-6} cm^2 s^{-1}. Eq. 1 predicts a proportionality between the oxidation peak current and the electrode area when voltammograms are taken at different scan rates. Cyclic voltammograms of the different studied samples are presented in Fig. 2. The images show the $Fe(CN)_6^{3-/4-}$ reversible one-electron redox peaks in bare ITO electrodes, with an average peak-to-peak separation $\Delta E_P = E_{pa} - E_{pc} \sim 55$ mV at $\nu = 50$ mV s^{-1} for as-deposited electrodes. Annealed electrodes present a shorter average peak-to-peak separation of 40 mV at $\nu = 50$ mV s^{-1}. The peak separation is related to the speed of the electrons interchanging in the redox reaction. The faster electron transfer in the case of annealed nanostructured electrodes demonstrates a more conductive electrode surface. The peak separation is increased with scan rate increase. Similarly, the current intensity is higher at greater scan rate values, as predicted by Eq. 1. These results are in accordance with cyclic voltammograms of thin ITO films published in the literature [27].

The linear representation of Eq. 1 is shown in Figs. 3(a) and 3(b) for as-deposited and annealed ITO electrodes, respectively (the fitting parameters are summarized in Table I). The slope of the fitting equation is directly proportional to the electroactive surface area. In the case of as-deposited electrodes, an electroactive surface area of 0.44 cm^2 and 0.50 cm^2 was deduced for thin film and nanostructured electrodes, respectively, which resulted in a net increase of $\frac{A_{nano} - A_{tf}}{A_{tf}} \times 100 = 14$ % after nanostructuration of the ITO surface. In the case of annealed electrodes, an electroactive surface area of 0.42 cm^2 and 0.62 cm^2 corresponding to thin film and nanostructured electrodes was observed, respectively, resulting in a net increase of 45 %. Crystallization of the nanostructured ITO produced a reorganization of atoms in In_2O_3 and SnO_2, with a subsequent highly ordered microscopic structure, which enhances the conductivity of the material due to the decrease in sheet resistance, as reported in Refs. 20 and 28. Thus, these results point out that not only the nanostructured surface but also its crystalline degree plays an important role in terms of electrochemical performance.

Up to now, the proof of geometrical as well as electroactive surface area increase for nanostructured ITO electrodes with respect to thin film ITO electrodes was presented. The corroboration of these results implies

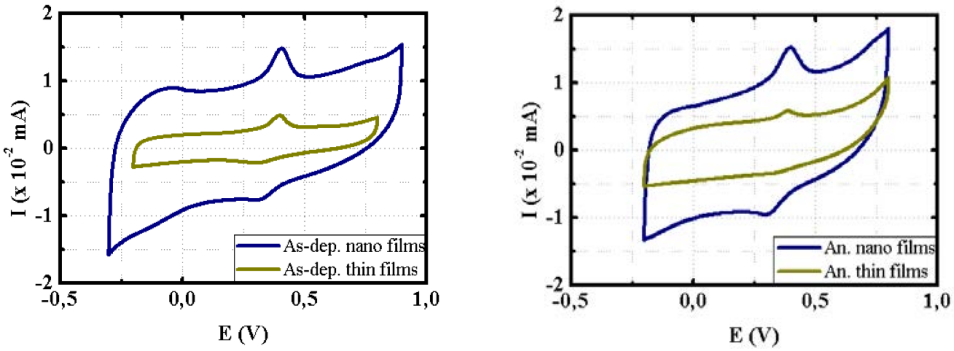

(a) (b)

FIG. 4: CV of 6-(ferrocenyl)hexanethiol functionalized (a) as-deposited and (b) annealed ITO electrodes. An increase in the total peak height indicates a higher nanostructured surface coverage than thin in the case of thin films.

that nanostructured ITO electrodes should increase biosensor sensitivity because of their more conductive and larger electroactive surface area, which would improve the signal-to-noise ratio. To prove this hypothesis, a model organic molecule was attached to the ITO surfaces. For this purpose, previous self-assembling of GOPTS was performed to construct an active epoxy monolayer, which was covalently attached with a thiolate-ferrocene molecule. The presence of the ferrocene-labeled organic molecule onto the ITO surface was detected by CV, as ferrocene provides the necessary redox couple for electron transfer to be measured. In this case, CV measurements were carried out within the electrochemical cell containing 10 mM NaCl electrolyte at 25 °C. CV measurements of these structures at $\nu = 50$ mV s^{-1} are shown in Figs. 4(a) and 4(b) for as-deposited and annealed ITO surfaces, respectively. Redox peaks, which are the proof that ferrocene molecules are present in the electrodes surfaces, can be clearly observed in all voltammograms at the expected position [29]. An increase in the total peak height of 140 % was observed for as-deposited electrodes, whereas the same calculation for annealed electrodes resulted in more than 400 %, and these values are of the same order of magnitude as the geometrical area increase. The redox intensity peak height is indirectly related to the surface coverage of molecules surface coverage by the following equation:

$$Q = nFA\Gamma, \tag{2}$$

where Q is the total charge consumed during the reduction or oxidation of the adsorbed ferrocene, and Γ is the ferrocene surface coverage on the ITO surfaces. Assuming that $\frac{Q_{\text{nano}}}{Q_{\text{tf}}}$ is equal to the total peak height increase,

TABLE I: R-squared R^2, slope a and standard deviation $S.D.$ as fitting parameters of linear regression equations in Fig. 4. $S.D.$ and a are expressed in A s$^{1/2}$ V$^{-1/2}$. *Area* is expressed in cm^2.

	R^2	a	$S.D.$
As-dep. nano. ITO	0.991	0.00181	6.9×10^{-5}
As-dep. thin. ITO	0.980	0.00159	7.4×10^{-5}
Ann. nano. ITO	0.996	0.00222	5.5×10^{-5}
Ann. thin. ITO	0.980	0.00153	7.2×10^{-5}

and taking the areas from Table I, the nanostructured surface coverage resulted in 1.3 times higher than thin film's for as-deposited electrodes. In the case of annealed electrodes, the nanostructured surface coverage was 2.7 times higher than thin film surface coverage. The nanostructuration of ITO surfaces generates a larger area available for the immobilization of redox active molecules, and the surface coverage is enhanced in the case of annealed electrodes. These results show that in the future, biomolecules such as modified nucleic acids with thiol functionality could be covalently attached to GOPTS-functionalized nanostructured ITO surfaces, for developing sensitivity-enhanced bioelectronics that could be fully integrable with the silicon technology. However, every single application may be specifically optimized, since the volume and chemical structure of each type of bioreceptor could behave differently on the nanostructured ITO, thus modifying the observed features.

In summary, the results presented here indicate the viability and the benefits of electrochemical sensors based on nanostructured ITO films. These nanostructured films present higher geometrical as well as electroactive surface area, which increases the intensity current when redox reactions take place. We also observed a substantial difference between amorphous and crystallized structures in terms of electrochemical performance. Besides, the functionalization of ITO surfaces with organosilanes containing ferrocene functionality was also carried out. For this purpose, a model organic molecule, 6-(ferrocenyl)hexanethiol, was immobilized on the GOPTS-coated ITO surfaces. All these analyses were more effective for annealed substrates, due to the enhanced conductivity properties as a result of a higher molecular-level organization.

ACKNOWLEDGMENTS

The authors wish to acknowledge the 7th Frame program European Project *SEA-on-a-CHIP* (ref. 614168). CIBER-BBN is an initiative funded by the VI National R&D&i Plan 2008-2011, Iniciativa Ingenio 2010, Consolider Program, CIBER Actions and financed by the Instituto de Salud Carlos III with assistance from the *European Regional Development Fund*.

REFERENCES

[1] Joseph Wang. Nanomaterial-based electrochemical biosensors. *Analyst*, 130(4):421–426, 2005.

[2] Nathaniel L Rosi and Chad A Mirkin. Nanostructures in biodiagnostics. *Chemical reviews*, 105(4):1547–1562, 2005.

[3] Kai Xu, Junran Huang, Zunzhong Ye, Yibin Ying, and Yanbin Li. Recent development of nano-materials used in dna biosensors. *Sensors*, 9(7):5534–5557, 2009.

[4] Zhiqiang Gao, Ajay Agarwal, Alastair D Trigg, Navab Singh, Cheng Fang, Chih-Hang Tung, Yi Fan, Kavitha D Buddharaju, and Jinming Kong. Silicon nanowire arrays for label-free detection of dna. *Analytical Chemistry*, 79(9):3291–3297, 2007.

[5] Gustavo A Rivas, Maria D Rubianes, Marcela C Rodriguez, Nancy F Ferreyra, Guillermina L Luque, Maria L Pedano, Silvia A Miscoria, and Concepcion Parrado. Carbon nanotubes for electrochemical biosensing. *Talanta*, 74(3):291–307, 2007.

[6] BO Kolbesen and A Mühlbauer. Carbon in silicon: properties and impact on devices. *Solid-State Electronics*, 25(8):759–775, 1982.

[7] Kwang-Salk Kim, Ja-Young Kim, Hee-Bog Kang, Bo-Young Lee, and Su-Moon Park. Effects of organic contaminants during metal oxide semiconductor processes. *Journal of The Electrochemical Society*, 155(6):H426–H431, 2008.

[8] AP Graham, GS Duesberg, W Hoenlein, F Kreupl, M Liebau, R Martin, B Rajasekharan, W Pamler, R Seidel, W Steinhoegl, et al. How do carbon nanotubes fit into the semiconductor roadmap? *Applied Physics A*, 80(6):1141–1151, 2005.

[9] Søren Stobbe, PE Lindelof, and J Nygård. Integration of carbon nanotubes with semiconductor technology: fabrication of hybrid devices by iii–v molecular beam epitaxy. *Semiconductor science and technology*, 21(11):S10, 2006.

[10] S Libertino, S Conoci, A Scandurra, and C Spinella. Biosensor integration on si-based devices: Feasibility studies and examples. *Sensors and Actuators B: Chemical*, 179:240–251, 2013.

[11] AH Khalid and AA Rezazadeh. Fabrication and characterisation of transparent-gate field effect transistors using indium tin oxide. *IEE Proceedings-Optoelectronics*, 143(1):7–11, 1996.

[12] Shabbir A Bashar. Study of indium tin oxide (ito) for novel optoelectronic devices. *UMIST, Manchester*, pages 106–109, 1998.

[13] A Kolmakov, DO Klenov, Y Lilach, S Stemmer, and M Moskovits. Enhanced gas sensing by individual sno2 nanowires and nanobelts functionalized with pd catalyst particles. *Nano Letters*, 5(4):667–673, 2005.

[14] Marie-Alexandra Neouze and Ulrich Schubert. Surface modification and functionalization of metal and metal oxide nanoparticles by organic ligands. *Monatshefte für Chemie-Chemical Monthly*, 139(3):183–195, 2008.

[15] Esther Amstad, Marcus Textor, and Erik Reimhult. Stabilization and functionalization of iron oxide nanoparticles for biomedical applications. *Nanoscale*, 3(7):2819–2843, 2011.

[16] Chang Kyoung Choi, Kenneth D Kihm, and Anthony E English. Optoelectric biosensor using indium-tin-oxide electrodes. *Optics letters*, 32(11):1405–1407, 2007.

[17] Chang K Choi, Chuck H Margraves, Seung I Jun, Anthony E English, Philip D Rack, and Kenneth D Kihm. Opto-electric cellular biosensor using optically transparent indium tin oxide (ito) electrodes. *Sensors*, 8(5):3257–3270, 2008.

[18] Zarini Muhammad-Tahir. *Indium Tin Oxide-polyaniline Biosensor: Fabrication and Performance Analysis*. ProQuest, 2007.

[19] Mei-Sheng Wu, Da-Jing Yuan, Jing-Juan Xu, and Hong-Yuan Chen. Sensitive electrochemiluminescence biosensor based on au-ito hybrid bipolar electrode amplification system for cell surface protein detection. *Analytical chemistry*, 85(24):11960–11965, 2013.

[20] Hamid Reza Fallah, Mohsen Ghasemi, and Ali Hassanzadeh. Influence of heat treatment on structural, electrical, impedance and optical properties of nanocrystalline ito films grown on glass at room temperature prepared by electron beam evaporation. *Physica E: Low-dimensional Systems and Nanostructures*, 39(1):69–74, 2007.

[21] Hamid Reza Fallah, Mohsen Ghasemi, Ali Hassanzadeh, and Hadi Steki. The effect of annealing on structural, electrical and optical properties of nanostructured ito films prepared by e-beam evaporation. *Materials Research Bulletin*, 42(3):487–496, 2007.

[22] V Senthilkumar, P Vickraman, M Jayachandran, and C Sanjeeviraja. Structural and optical properties of indium tin oxide (ito) thin films with different compositions prepared by electron beam evaporation. *Vacuum*, 84(6):864–869, 2010.

[23] Greg T Hermanson. *Bioconjugate techniques*. Academic press, 2013.

[24] Sandeep Kumar Vashist, Edmond Lam, Sabahudin Hrapovic, Keith B Male, and John HT Luong. Immobilization of antibodies and enzymes on 3-aminopropyltriethoxysilane-functionalized bioanalytical platforms for biosensors and diagnostics. *Chemical reviews*, 114(21):11083–11130, 2014.

[25] Xuexin Duan, Luye Mu, Sonya D Sawtelle, Nitin K Rajan, Ziyu Han, Yanyan Wang, Hemi Qu, and Mark A Reed. Functionalized polyelectrolytes assembling on nano-biofets for biosensing applications. *Advanced Functional Materials*, 25(15):2279–2286, 2015.

[26] PJ Ramon-Torregrosa, MA Rodríguez-Valverde, A Amirfazli, and MA Cabrerizo-Vílchez. Factors affecting the measurement of roughness factor of surfaces and its implications for wetting studies. *Colloids and Surfaces A: Physicochemical and Engineering Aspects*, 323(1):83–93, 2008.

[27] Anees A Ansari, A Kaushik, PR Solanki, and BD Malhotra. Sol–gel derived nanoporous cerium oxide film for application to cholesterol biosensor. *Electrochemistry communications*, 10(9):1246–1249, 2008.

[28] Hamid Reza Fallah, Mohammad Javad Vahid, et al. Substrate temperature effect on transparent heat reflecting nanocrystalline ito films prepared by electron beam evaporation. *Renewable Energy*, 35(7):1527–1530, 2010.

[29] A Muthurasu and V Ganesh. Electrochemical characterization of self-assembled monolayers (sams) of silanes on indium tin oxide (ito) electrodes–tuning electron transfer behaviour across electrode–electrolyte interface. *Journal of colloid and interface science*, 374(1):241–249, 2012.

3.2 Nanostructuration of ITO by electron beam evaporation

Once nanostructured ITO electrodes were proved to increase the sensitivity of electrochemical systems with respect to thin ITO films, the next logical step was to study the influence of the configuration parameters during electron beam evaporation in the quality of film nanostructuration. From the literature, it can be deduced that both substrate temperature during deposition and the composition of raw ITO targets are the most influent paramenters in the quality of the final films, and so this was studied in the present section.

3.2.1 Influence of substrate temperature and study of the electrical double layer

In *Article II: Tuning the deposition parameters for optimizing the faradaic and non-faradaic electrochemical performance of nanowire array-shaped ITO electrodes prepared by electron beam evaporation*, the influence of substrate temperature during deposition on the quality of nanostructuration was studied. Successive deposits were performed at increasing temperatures from 100 °C to 500 °C maintaining the rest of parameters, e.g. deposition rate or chamber pressure, at constant values. The resulting electrodes were exhaustively characterized morphologically by electron microscopy. Moreover, a basic experiment with adhesive tape was performed to test the adherence of the nanostructured film to the transparent substrate, concluding that in all cases the material is well-adhered and no or very few nanowhiskers are released during electrode manipulation. Moreover, the electrode transparency to optical and near infrared wavelengths was also monitored before and after thermal annealing of the samples, confirming that in all cases the transmittance increases after the thermal process. Similarly, the resistivity of the films was also evaluated by monitoring the sheet resistance with a four points probe station. A decrease in sheet resistance was observed in all cases after thermal annealing.

After the structural description of the films, the influence of nanostructuration in the interaction between the electrode surface and a covering liquid was studied. First, the dependence of electrochemical surface area with deposition temperature was monitored to determine the evolution of the degree of aparent nanostructuration. This again was found by the Randles-Sevcick faradaic analysis, which was used in Article I.

Moreover, non-faradaic cyclic voltammetry was performed to obtain the relation of electrochemical specific capacitance with substrate temperature during deposition. This experiment shared results with the faradaic one: electrodes prepared at 300 °C presented the highest aparent surface area and consequently also the highest specific capacitance. In the same line, and due to the semiconducting nature of ITO, the Mott-Schottky electrochemical experiment was conducted to retrieve some characteristic physical parameters of this material. This technique was used to quantify, as a proof-of-concept, the change in flatband voltage regarding the type of surface chemistry previously conducted on the electrodes.

To sum up, the objectives of this paper can be summarized as follows:

1. systematic structural characterization of nanostrucutred ITO electrodes prepared by electron beam evaporation at different substrate temperatures;

2. quantification and comparison of the degree of aparent nanostructuration by faradaic cyclic voltammetry and Randles-Sevcik analysis;

3. determination and comparison of electrochemical specific capacitance by non-faradaic cyclic voltammetry and study and application of the electrical double layer theory;

4. application of the Mott-Schottky theory to the analysis of the semiconductor electrode from the solid state physics point of view;

5. first attempt at derivatizing a nanostructured ITO-based electrode by electroaddressed reduction of organic linker molecules on the surface and

6. determiantion of quantitative changes in electrode flatband voltage after surface derivatization and dependence on substrate temperature during electrode preparation.

The article has been reproduced from Nanoscale; vol. 11(1); R. Pruna, F. Teixidor and M. López, "Tuning the deposition parameters for optimizing the faradaic and non-faradaic electrochemical performance of nanostructured ITO electrodes prepared by electron beam evaporation", 276–284, 2019; with permission from the Royal Society of Chemistry.

Tuning the deposition parameters for optimizing the faradaic and non-faradaic electrochemical performance of nanowire array-shaped ITO electrodes prepared by electron beam evaporation

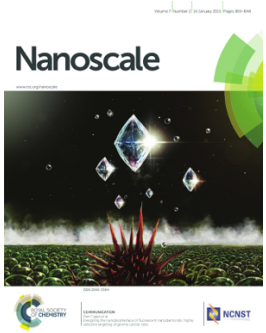

Raquel Pruna,[1] Manel López,[1] and Francesc Teixidor[2]

[1)] *Departament d'Enginyeries: Electrònica i Biomèdica, Universitat de Barcelona, Martí i Franquès 1, E-08028 Barcelona, Spain*

[2)] *Institut de Ciència de Materials de Barcelona, ICMAB-CSIC, Campus UAB, E-08193 Bellaterra, Spain*

Nanoscale, 100 (2018), 533-540
doi: 10.1016/j.bios.2017.09.049

ABSTRACT

Nanostructured indium tin oxide (ITO) surfaces present an interesting yet unusual combination of properties (high electrical conductivity and optical transparency) at a high surface-to-volume ratio. Thus, previous studies presented nanostructured ITO electrodes as potentially suitable platforms for electrochemical biosensors, but still there is lack of research on the optimization of preparation methods for such electrodes. We present a systematic study on the properties of nanostructured ITO electrodes prepared by physical deposition, where the substrate temperature was tuned for achieving the best combination of structural properties (namely electrical conductivity and optical transparency) and electrochemical performance. Analysis of faradaic cyclic voltammetry (CV) was performed to determine the electroactive surface area of the samples, and these results were benchmarked against those obtained by non-faradaic CV and Mott-Schottky (MS) analysis. The latter was useful to determine the dependence of some intrinsic features of the semiconductor on the substrate temperature during deposition. The results show that, out of a wide temperature range covering from 200 °C to 500 °C, there is a two-phase temperature-dependent growth, explained by the Stranski-Krastanov and self-catalytic vapor-liquid-solid (VLS) methods; and, on the other hand, that there is an optimal growth temperature at 300 °C that maximizes the electroactive surface area and sensitivity. This means that cost-effective electrodes can be prepared at low temperatures outperforming in terms of electroactive surface area, surface capacitance and sensitivity. As a proof-of-concept, nanostructured ITO electrodes were electrochemically derivatized with aryl diazonium salts (as a first step towards biochemical functionalization), and the performance of the optimized electrodes was tested in a real scenario.

I. INTRODUCTION

Indium tin oxide (ITO) is a degenerate n-type semiconductor, traditionally classified as a transparent conductive oxide (TCO). Simultaneous good transparency and conducting properties result from a band gap energy of 3.2 eV [1] and have been exhaustively exploited for years in optoelectronics. However, this falls short of what is required by innovative and high-tech applications, and the assessment of quantum effects at the nanoscale becomes crucial at this point. Recently, a nanostructured variation of ITO electrodes has gathered attention due to the additional value of increased surface-to-volume ratio: they have been reported more than 40 % increase in electrochemical surface area in small projected regions with respect to their thin film counterparts [2–4], showing noticeable advantages in terms of electrochemical detection.

The use of nanostructured ITO films has already shown improvement with respect to thin layers in several applications. For instance, in chromophore-type electrochromic devices, the area available for electrochromophoric molecules to undergo redox reactions is directly related to the contrast ratio between on-off states [5]. In the field of optoelectronics, an improved performance of organic light emitting devices (OLEDs) by increasing the surface area contact between the electrode and the organic film has been reported, and this was achieved by nanostructuration of the ITO deposit [6–8]. In energy applications, such as organic photovoltaics, high surface area electrodes in dye-sensitized solar cells can overcome limited efficiency by increasing the sites for light absorption and charge extraction [9].

On the whole, nanomaterials have gained much interest recently in biosensors, for they can supply increased sensitivities required in early-stage detection point of care systems. Carbon nanowires and nanotubes [10], porous silicon [11] and silicon carbide nanostructures [12], amongst others, have been used as substrates for highly sensitive biosensing devices. To our knowledge, just one attempt to use nanostructured ITO electrodes in this field has been reported in the literature [13], where they are employed as electrochemical biosensors and detection of a heart failure biomarker is shown as case study. Despite promising results, still fabrication processes need to be tuned for optimal performance. However, among the aforementioned nanostructured materials, ITO shows powerful advantages, such as its compatibility with the standard complementary metal oxide semiconductor (CMOS) silicon technology, and the unique possibility to perform simultaneous electrochemical and optical measurements due to its high transparency and good conductivity [14 and 15].

This work provides semi-quantitative and qualitative electrochemical and structural characterization of transparent nanostructured ITO electrodes prepared by electron beam evaporation at several substrate temperatures. The physical structure of the electrodes was controlled by tuning the deposition rate during evaporation and the substrate material, and the results of a pull-off test suggested the Stranski-Krastanov as epitaxial growth mechanism for the nanowires, complementary to the widely reported self-catalytic vapor-liquid solid method. A thorough analysis of the electrode behavior under faradaic and non-faradaic electrochemical regimes proves useful to determine the electrochemical surface area of the samples, as well as their surface capacitance, showing that low temperatures (around 300 °C) are enough to prepare high-performance electrodes. Moreover, since we are dealing with semiconductor electrodes, Mott-Schottky (MS) analysis leads to a complete theoretical description of the electrodes in terms of solid-state physics and electronics. With all, surface modification with aryl diazonium salts was quantified in a final experiment, and the obtained results light up high future prospects in the use of nanostructured ITO electrodes for electrochemical biosensing.

II. MATERIALS AND METHODS

A. Sample preparation

Several studies reported the fabrication of nanostructured ITO surfaces in the past, either by physical [8, 16–20] or chemical [21–24] methods. Of them, electron beam evaporation is the most effective for allowing nanostructuration without the need for any metal catalyst or additional oxygen gas and control on the crystallographic growth direction [25 and 26]. Kumar *et al.* [27] investigated the dependence of the physical properties of nanostructured ITO films with deposition parameters by systematically varying one parameter (substrate temperature, deposition rate, growth time or partial oxygen pressure) at a time, from where it can be deduced that the substrate temperature during deposition has major influence in the morphology of the nanowires and the porosity of the deposit. For this reason, we focused our study on the variation of this parameter, slightly widening the range previously studied by the cited authors (from 150 °C–400 °C to 100 °C–500 °C), and pinning the rest of parameters at levels that allow for thermodynamic control on the growth process. Kumar and co-workers prepared their samples at evaporation rates ranging from 2.5 Å s^{-1} to 5 Å s^{-1} during 10–30 min, thus working in a kinetic regime. Moreover, they used silicon and glass as substrates, but none of them present a crystalline atomic distribution similar to Sn-doped In_2O_3. In this work, the ITO nanowires were grown on fused silica at a rate of 1.0±0.5 Å s^{-1} (an accelerating voltage of 6 kV was used for the electron beam) during 33 min (for an equivalent thickness of 200 nm) in a basal vacuum of 10^{-6} mbar in order to study the influence of the substrate and the kinetics on the epitaxial growth. Commercial ITO pellets with a composition of In_2O_3/SnO_2 90/10 % wt. were used as raw target material.

B. Structural characterization

1. Field-effect scanning electron microscopy (FE-SEM)

A JSM-7100F (JEOL, US) Field-Emission Scanning Electron Microscope (FE-SEM) equipped with an energy dispersive X-ray (EDX) spectroscopy module was used to analyze the morphology and composition of the nanowires. A LED source of 15 kV was employed for electron acceleration.

2. Transmittance measurements

A Bentham PVE300 Spectral Response analyzer coupled to an integrating sphere was used for measuring transmittance spectra. A monochromator with grid resolution between 0.3 nm and 0.6 nm and dispersion between 2.7 nm and 5.4 nm selected wavelengths from two light sources: a 75 W xenon light source for wavelengths between 300 to 700 nm and a 100 W quartz halogen light source for wavelengths between 700 nm to 1700 nm.

3. Sheet resistance measurements

The sheet resistance of the samples was measured with a four points probe system based on a Keysight Technologies B2912A dual precision source–measurement unit (SMU), with a minimum source and measurement resolution of 10 fA/100 nV. The four probes were distributed horizontally with a separation of 1 mm between needles. The current was injected through the inner surface needles, and the potential difference between the

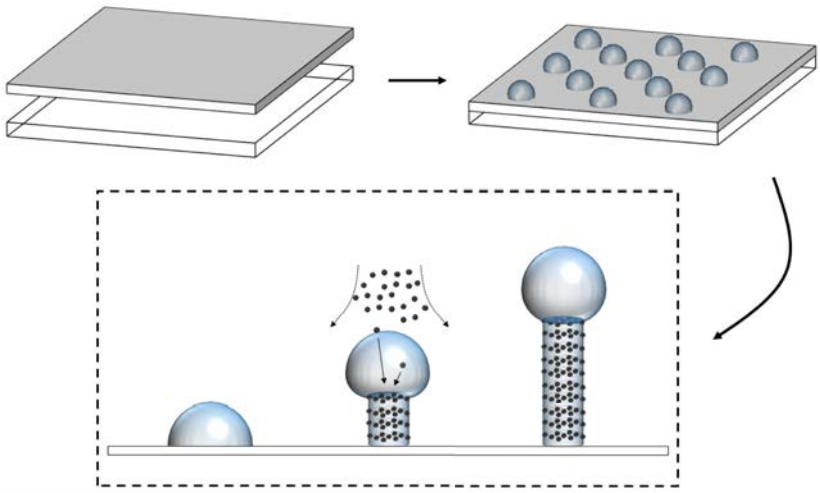

FIG. 1: Schematic model of the growth of ITO nanowires by self-catalytic VLS. Several steps are shown: deposition of a uniform thin ITO film of several atomic layers, temperature-driven formation of seeds on the surface as a result of the melting of In-Sn atoms/molecules and growth of nanowires by crystallization of atoms/molecules at the seed-semiconductor interface.

outer needles was measured, and the probes were positioned at the center of aleatory-shaped electrodes of appropriate size to avoid edge effects (mainly a distortion of the electric field lines). Three independent samples prepared at each temperature were measured, and no appreciable Schottky barrier was observed at the interfaces of the needles (conductor) and the electrodes (semiconductor).

4. Electrochemical measurements

All electrochemical measurements were performed with a SP150 (Biologic, France) potentiostat and EC-Lab V11.12 software. The measurements were conducted on a three-electrode polycarbonate cell, with a geometrical projected area for the working electrode (WE) exposition to ionic solution delimited by an O-ring of 6 mm diameter (area ~ 0.28 cm^2). ITO films were used as WEs, a platinum wire was used as counter electrode (CE), and KCl saturated Ag/AgCl was used as reference electrode (RE); stabilized voltammograms were obtained after 5 cycles between the anodic and cathodic limits. All experiments were performed in aqueous solution (ultrapure water, milliQ–Millipore). Phosphate buffer saline (PBS, Sigma Aldrich, Spain) was used as supporting electrolyte in all cases. Potassium hexacyanoferrate II and III ($Fe(CN)_6^{-3/-4}$, Sigma Aldrich, Spain) was used as redox couple in faradaic experiments.

III. RESULTS AND DISCUSSION

A. Morphology analysis

Resulting nanostructured ITO electrodes were observed by scanning electron microscopy. An ×80 000 amplified image of the nanostructures for each substrate temperature is shown in Figure S1 in the Electronic Supplementary Information†. Nanowires can be observed from 200 °C to 500 °C. However, at 100 °C the

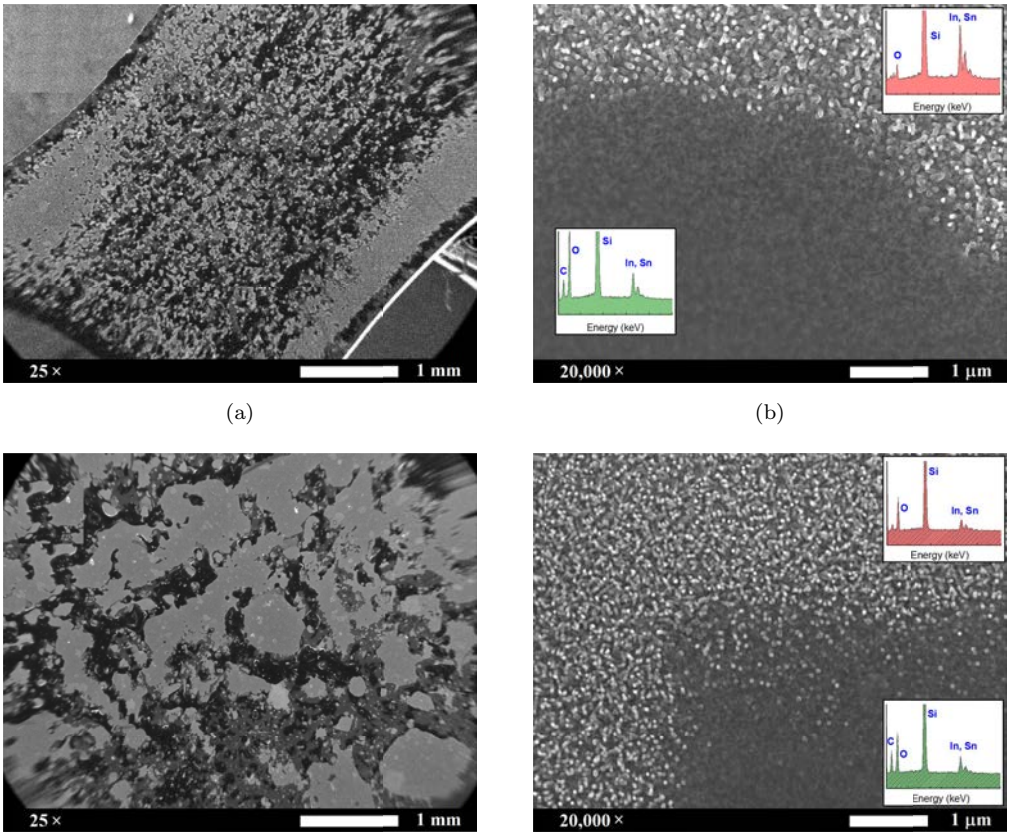

FIG. 2: SEM images of nanostructured ITO electrodes pressed for 10 s with (a) and (b) transparent Scotch sellotape, and (c) and (d) black electrical tape. Insets in (b) and (d) contain EDX spectra of the two distinguishable regions in the SEM images. The red spectra point the bare ITO nanowires, whereas the green spectra show the carbon peak corresponding to the organic tapes.

deposit is a true thin film (Figure S2 in the Electronic Supplementary Information†), which implies that nanostructuration starts at an intermediate temperature, presumably closer to 200 °C, as suggested by the phase diagram of the In-Sn system[28 and 29]. In fact, the electrodes prepared at 200 °C consist of a thin layer of material with emerging nanowires sparsely distributed. The results presented by Kumar and co-workers [27] show electrodes densely populated with nanowires grown at 150 °C. They prepared the deposits at 2.5 Å s^{-1} on a crystalline silicon substrate, whereas those presented here were prepared in twice the time at 1 Å s^{-1} on crystalline SiO_2. Comparing the results, the importance of the substrate and the kinetics of the deposition process must be highlighted. Indeed, the similarity in crystalline atomic structures between SiO_2 and Sn-doped In_2O_3 together with a slow deposition rate facilitate that the first atomic layers of deposited material follow those of the substrate. This explains why at 200 °C we can observe how nanowires begin to grow from a thin epitaxial layer. This can be interpreted as the Stranski-Krastanov method of epitaxial growth [30], which postulates that the deposition follows a two-step process as shown in Figure 1. First, a few layers of adsorbates grow up to several monolaters thick until a physicochemical feature triggers a change in the growth fashion, which keeps on through nucleation and coalescence of adsorbates. The latter has been stated to be the fusion of SnO_2 and In_2O_3 molecules into 'seeds' due to the elevated temperatures, which thermodynamically favor the system to achieve its eutectic point [19, 27, 31, and 32]. Some authors proposed the self-catalytic vapor-liquid-solid (VLS)

as growth mechanism for ITO nanowires prepared by electron beam evaporation [16 and 19]. This is briefly discussed in Section 1 of the Electronic Supplementary Information†.

A rather rudimentary yet efficient adherence test was conducted to support the proposed epitaxial growth mechanism. This was initially envisaged as a competing procedure to learn if the nanostructured pristine ITO was able to be drawn from a coating material initially deposited on a separate backing material. The coating material must be strongly adhered to the backing material. As we shall see, the nanostructured ITO draws all the adhesive material, which indicates its high surface area and compatibility with the adhesive. The experiment also provided information on the way the nanowires are adhered to the ITO surface. When a piece of adhesive tape was pressured for 10 s on the nanostructured ITO surface and further released, two possibilities existed: that the nanowires remained on the ITO or that they were transferred to the adhesive backed material. To discern it, both the ITO surface and the detached adhesive tape were observed by SEM to learn on the fate of the nanowires. They remained on the ITO surface, which indicates that the nanowires are rooted in the ITO surface and grow from raw material rather than being deposited already in that shape on the ITO film. confirming the self-catalytic VLS hypothesis by which initial 'seeds' lead to full-grown wires (please see Figure 1). Here, two pressure-sensitive adhesives (PSAs) were used: conventional transparent office sellotape (3M Scotch, US) and black electrical tape (Thorlabs, US). SEM images in Figure 2 show how in both cases (Figures 2(a)–2(b) for Scotch tape and Figures 2(c)–2(d) for electrical tape) not only the nanowires were prevented from being detached from the electrode surface, but the adhesive glues were transferred to the nanowires. These conclusions are confirmed by the EDX spectra shown as insets in Figures 2(b) and 2(d): the red spectra correspond to the bare ITO nanowires, and the peaks of indium, tin and oxygen can be appreciated, together with the intense peak of the substrate silicon; the green spectra correspond to the glue-covered nanowires, and new intense carbon peaks can be observed. On the other hand, no ITO traces were found on the remaining glue in the PSAs (images not shown). The transfer of the adhesive material from the tape to the nanostructured ITO surface can only be interpreted by either a higher affinity of the adhesive material for the nanostructured ITO due to their hydrophilicity or by a high surface area of the nanowires, or by a combination of both.

B. Electro-optical properties

The optical and infrared transmittance spectra for all samples are shown in Figure 3(a). The low optical transparency of the 200 °C sample compared to the rest of samples can be observed by naked eye (please see Figure S3 in the Electronic Supplementary Information†). Some authors [17] ascribe this to an eventual oxygen deficiency in the deposit, suggesting that oxidation of the material is promoted at higher substrate temperatures. The rest of the samples present similar optical transmittance spectra (higher than 80 % as deposited). After rapid thermal annealing, the transmittance spectra of all samples converge and skim values around 100 % in visible wavelengths. Some works also report an improvement of transmission properties after plasma treatment of the samples [17 and 33].

The reliance of sheet resistance with substrate temperature during deposition is shown in Figure 3(b). A progressive decrease in sheet resistance with increasing growth temperatures can be observed, with a minimum at 300 °C, which could be explained by a change in the final solid phase of the system. Kumar *et al.* [27] presented a slightly shifted yet very similar pattern, which correlated with the atomic percentage of tin in the samples. The sheet resistance values reported in this work stay an order of magnitude below those presented in the cited article (which move around 1 kΩ sq^{-1}). This could be explained by local differences in the geometry of the nanowires and the thickness of the deposit.

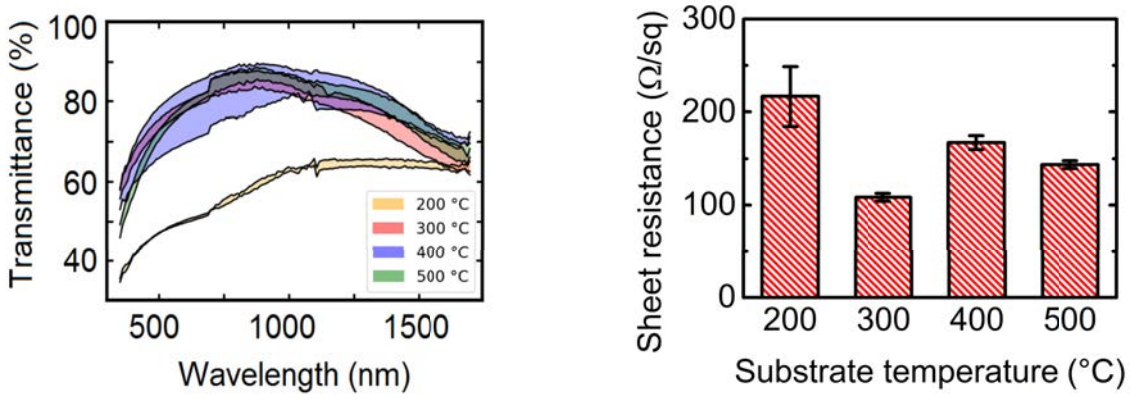

(a) (b)

FIG. 3: (a) Transmittance spectra (in %) for as-deposited samples prepared at 200 °C, 300 °C, 400 °C and 500 °C. (b) Sheet resistance (in Ω sq^{-1}) for samples prepared in the aforementioned conditions.

C. Faradaic analysis of voltammograms

Cyclic voltammetry in liquid medium containing a redox probe ($Fe(CN)_6^{-3/-4}$) was used to conduct faradaic electrochemical analysis. The as-recorded cyclic voltammograms of all samples are collected in Figure S4 in the Electronic Supplementary Information†. The two-peaks motif, typical of single redox-pair systems, can be observed as expected [2 and 34]. The behavior of the faradaic current peaks is described by the Randles-Sevcik equation [35–37]:

$$I_f = \kappa n F A C \sqrt{\frac{nF\nu D}{RT}}. \quad (1)$$

Here, $\kappa = 0.4463$ is a non-dimensional proportionality constant; n is the number of electrons for the redox couple (1 in the case of $Fe(CN)_6^{-3/-4}$); F and R are Faraday's (96 485 C mol^{-1}) and universal gas (8.314 J mol^{-1} K^{-1}) constants, respectively; A is the electrode area in cm^2; ν is the rate at which the potential is swept, in V s^{-1}; D is the analyte's diffusion coefficient in cm^2 s^{-1}; C is the analyte's concentration in mol cm^{-3} and T is the solution temperature in K. This process was thoroughly described elsewhere [2], but briefly, all parameters were known except for the area of the nanostructured electrode. In order to retrieve this area, successive CVs at different scan rates must be performed and the oxidation current against the square rooted scan rate should be plotted. The slope of this plot is directly proportional to the electroactive surface area of the electrode. This, as can be deduced from Eq. 1, is only dependent on the electrolyte solution and redox probe composition, providing the electrode is conductive enough. The electrode features are not affecting the intensity of the peak but its position. Indeed, the more resistive the electrode, the wider the separation between reduction and oxidation peaks. This is because redox reactions occur reversibly at the ideal electrode surface, but this reversibility is hindered by non-ideal conducting properties of the electrode.

The linear dependence of both anodic and cathodic current peaks height (after capacitive current subtraction by EC-Lab software) on the square root of the voltage scan rate (as described in Eq. 1) is shown in Figure 4(a). The highest linearity can be appreciated at low scan rate values, where processes occurring at the electrode-solution interface are quasi-static and quasi-reversible. The results of all linear regressions are summarized in

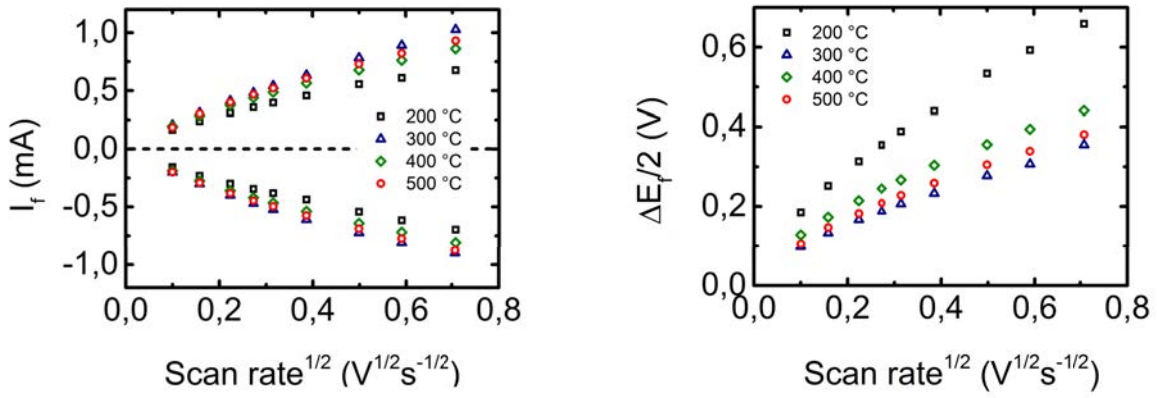

(a) (b)

FIG. 4: (a) Representation of anodic (upper datasets) and cathodic (lower datasets) faradaic current peaks as a function of the square root of voltage scan rate and (b) dependence of anodic-cathodic voltage peaks separation on square root of voltage scan rate for as-deposited electrodes prepared at several substrate temperatures.

Table I. As previously stated, the geometrical projected area of the WE in the electrochemical cell is ~ 0.3 cm^2. Consequently, all samples present evident surface nanostructuration, as observed by SEM, except for the electrode prepared at 200 °C, where nanostructuration is not statistically evident from numerical data. The sample prepared at 300 °C presents the highest available electroactive surface area. Since the computed surface area seems to correlate with the inverse sheet resistance measured before, the logical question to be asked would be if the effect of surface nanostructuration is being masked by the conductivity of the electrode. Despite that the theory leading to Eq. 1 is built upon the assumption of conductive (metal) electrodes, it is not less true that ITO is considered a transparent conductive electrode yet its applicability in electrochemistry is extensively supported in the literature [38–40]. However, let us assume that, given the semi-conductive nature of ITO, the dependence of measured electrochemically active area on sheet resistance and eventually on the atomic percentage of tin in sample is a second order effect. But, from Figure 3(b), differences in sheet resistance are within a range of few ohms, which are hardly observable as a second order effect. On the other hand, differences in conductivity between samples indeed influence the dependence of anodic-cathodic peak separation on the preparation substrate temperature of the electrodes, as shown in Figure 4(b). Here, the electrode conductivity indeed plays the role of first order effect through the entire voltage scan rate range.

D. Non-faradaic analysis of voltammograms

When no redox probe is present in the aqueous medium, interactions at the electrode-solution interface are assumed to be non-faradaic. As there is no redox species, no charge transfer occurs at the electrode surface. Moreover, during cyclic voltammetry, all the current becomes capacitive; no faradaic peaks appear (please see Figure S5 in the Electronic Supplementary Information†). In this case the current height (ideally constant) is proportional to the scan rate, and the differential capacitance becomes the proportionality constant, as shown

in the following expression:

$$I_{\mathrm{nf}} = C_{\mathrm{d}}\nu. \tag{2}$$

The differential capacitance is directly proportional to the area of the electrode. This is a faster and more precise method than the classical one for retrieving the electrode's capacitance, which consists in integrating the voltammogram curve and dividing this by the potential scan rate to find the capacitance [41].

The cyclic voltammograms of nanostructured ITO films in PBS solution (shown as dotted line in Figure 5(a)), performed at 50 mV s^{-1}, show no remarkable features. The cathodic peak occurs below −0.3 V due to irreversible reduction of the tin oxide [42], eventually producing electrode damage. On the other hand, a current rise would appear around 1 V due to oxygen-related phenomena [43]. To avoid these undesirable effects, differential voltammograms (DV) at the same scan rates were performed in three narrower potential ranges of width 0.2 V (see solid lines in Figure 5(a)). According to some authors [44 and 45], differences between DV and complete voltammograms occur because of hysteretic phenomena, e.g. slow capacitive processes and charge accumulation. The capacitance for all samples was measured as previously described from the cathodic and anodic current measurements in the three potential ranges. There is now a linear dependence between the anodic and cathodic non-faradaic currents and the voltage scan rate, and the proportionality constant is directly related to the double layer capacitance (see Eq. 2). This is shown in Figure 5(b), from which a clearly differentiated capacitance value can be observed for samples prepared at 300 °C. This is consistent with the fact that this is the sample presenting the highest surface area (retrieved by the faradaic method); assuming that the expression of the parallel-plate capacitor [46] can be applied locally in this case, an increase in capacitance is directly explained by an increase in surface area. Specific (per unit area) and mass capacitances for all samples in the three voltage regions (in the region around 0.2 V in the case of mass capacitance) are summarized in Table II. As predicted by the Mott-Schottky equation [47–49] (Eq. 3) for n-type semiconductors, the capacitance decreases with increasing potentials. Further details on this will be analyzed in the following section.

E. Proof-of-concept: surface derivatization for biosensing applications

Careful analysis of the results presented in Sections III C and III D reveals that figures of merit obtained from non-faradaic studies are more sensitive to changes in the electrode-solution interface. This may be due to the fact that faradaic processes in semiconductor electrodes become masked by simultaneous non-faradaic ones when capacitive effects are strong. Thereupon, the power of non-faradaic analysis will be used to illustrate the potential use of nanostructured ITO electrodes in biosensing applications, where the quantification of the

TABLE I: Summary of linear fitting parameters for the expression $y = a * x$ to the data shown in Figure 4(a) at low voltage scan rates. Parameters a and $S.D.$ are expressed in mA $s^{1/2}$ $V^{-1/2}$. The absolute area (in cm^2) is obtained from Eq. 1 and parameter a.

Sample	R^2	a	$S.D.$	$Area$
200 °C	0.993	1.38	0.06	0.31
300 °C	0.997	1.84	0.05	0.42
400 °C	0.995	1.68	0.06	0.38
500 °C	0.998	1.77	0.04	0.40

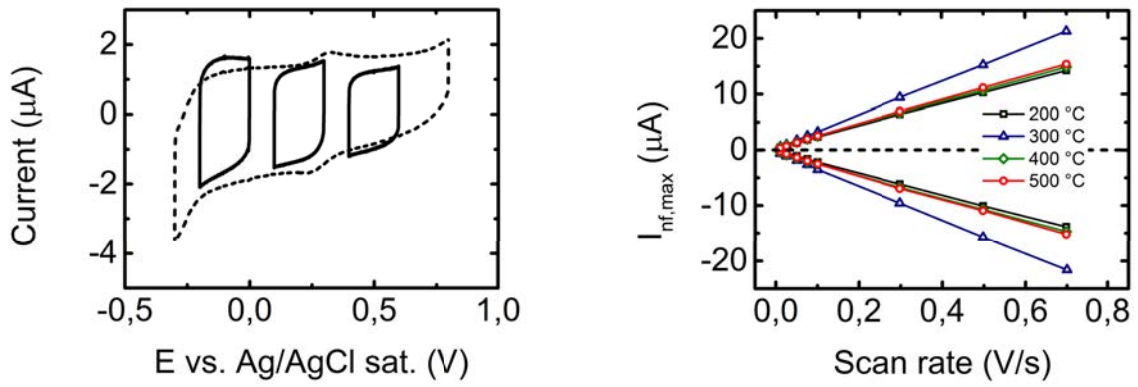

(a) (b)

FIG. 5: (a) The dashed line corresponds to the non-faradaic CV at 50 mV s^{-1} of an ITO electrode prepared at 500 °C. The solid lines correspond to the differential voltammograms used to retrieve the double layer capacitance of the samples. (b) Representation of anodic (upper datasets) and cathodic (lower datasets) non-faradaic current values as a function of the potential scan rate for as-deposited electrodes prepared at several substrate temperatures.

TABLE II: Summary of specific (μF cm^{-2}) and mass capacitance (MF g^{-1}) values obtained from data represented in Figure 5(b) and Eq. 2.

Sample	Specific capacitance			Mass capacitance
	-100 mV	200 mV	500 mV	
200 °C	71.63	59.95	51.17	0.42
300 °C	111.7	91.25	77.18	0.64
400 °C	76.31	62.16	53.08	0.44
500 °C	80.96	65.09	56.32	0.46

change in a physicochemical magnitude due to a binding/recognition event at the electrode surface becomes essential. In this section, we will only present the first step of the whole process, which consists in the derivatization of the electrode surface with a layer of molecules (crosslinkers) capable of attaching organic biomolecules (eventually an antibody) to an inorganic substrate (ITO electrode). This insulating crosslinker layer acts as part of the semiconductor electrode in the whole electrochemical system, and thus the physical properties of the electrode become modified. The same would apply to further modification layers, such as capture antibodies and subsequent antigen detection.

In the present work, Mott-Schottky analysis was conducted by measuring subsequent electrochemical impedance spectra (EIS) in a limited frequency range and at varying DC voltage polarization values. The AC frequency in the present study ranged from 100 Hz to 10 kHz. This range was chosen after some tests and based on other studies previously reported in the literature [49 and 50].

At a determined polarization voltage, the evolution of the charge transfer resistance with subsequent functionalization steps provides qualitative and pseudo-quantitative information on the nature of the insulating layer

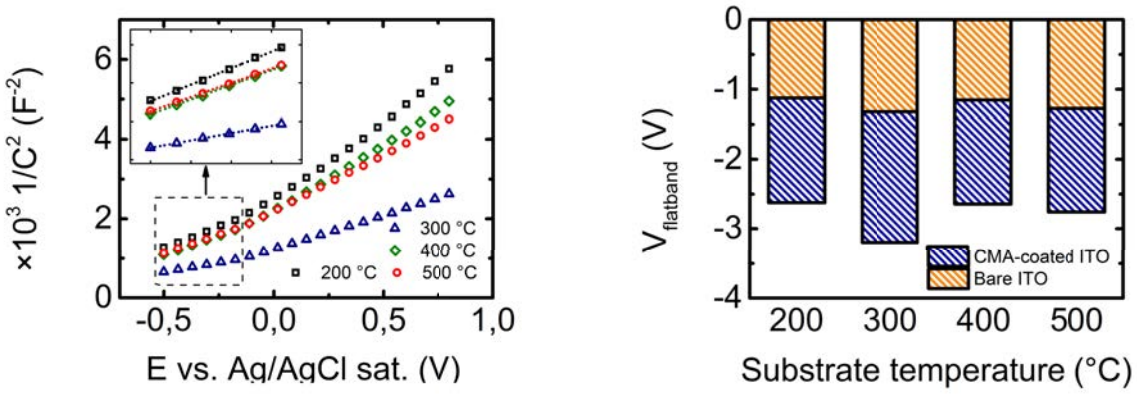

(a) (b)

FIG. 6: (a) Representation of measured $1/C^2$ *vs.* DC polarization at 100 Hz, known as Mott-Schottky analysis. Magnification of the linear region at most negative potentials is shown as inset, and the subsequent linear regressions correspond to these data points. (b) Bar diagram showing the change in flat band potential measured by Mott-Schottky analysis at 1 kHz for all samples before (orange) and after (blue) CMA-derivatization of the surfaces.

between the electrode and the solution. On the other hand, the evolution of the electrode capacitance with the polarization voltage accounts for physical properties of the semiconductor electrode (e.g. the flat band potential of the semiconductor and the density of charge dopants). The latter is gathered in the Mott-Schottky equation, which in turn is derived from the Poisson's equation, i.e. the assumption of charge neutrality inside the semiconductor, and Boltzmann's statistics. The Mott-Schottky equation for n-type semiconductor electrodes can be written as [47]

$$\frac{1}{C_{\mathrm{sc}}^2} = \frac{2}{\epsilon\epsilon_0 A^2 e N_{\mathrm{D}}}\left(V - V_{\mathrm{FB}} - \frac{k_{\mathrm{B}}T}{e}\right), \tag{3}$$

where C_{sc} is the capacitance of the semiconductor electrode; ϵ and ϵ_0 are the relative and absolute dielectric constants of the semiconductor and vacuum, respectively; A is the area of the electrode in contact with the electrolyte solution; e is the unitary charge; N_{D} is the density of donors (doping atoms) in the n-type semiconductor; V and V_{FB} are the polarization potential and the semiconductor's flat band potential, respectively; T is the temperature of the electrochemical system and k_{B} is the Boltzmann's constant.

Capacitance values can be retrieved by data adjustment of subsequent EIS measurements at several DC polarization voltages in the frequency range of interest. Representation of the measured $1/C^2$ against DC polarization voltage at a determined frequency value may present several regions with different behavior [49]. Linear fitting of the data points in the region attributable to C_{sc} in Eq. 3 eventually leads to the determination of the flat band voltage and carrier density. In this case, the resulting data was fitted to an equivalent circuit consisting in the series association of a resistor (corresponding to the electrolyte solution) and the constant phase element (accounting for the total electrode capacitance), since we are dealing with a non-faradaic system. The total electrode capacitance (C_{tot}), in turn, consists of the series addition of the double layer capacitance (C_{dl}, electrode-electrolyte interface) and the semiconductor electrode's internal capacitance (C_{sc}). The latter occurs because of an internal charge distribution due to the external polarization. Since these two capacitances

are added serially, C_{tot} is computed as the inverse of the sum of their reciprocals. Thus, if $C_{sc} < C_{dl}$, then $C_{tot} \approx C_{sc}$, and reversely if $C_{dl} < C_{sc}$, $C_{tot} \approx C_{dl}$. These two regimes can be clearly identified in Figure 6(a), where the dependence of the square inverse of the total electrode capacitance against the DC polarization at 100 Hz is plotted for the unmodified ITO electrodes, prepared at the usual substrate temperatures. The lowest region (inside the dotted square) was taken for linear fitting. Figure 6(b) shows the evolution of the flat band potentials at 1 kHz for the different electrodes before and after 4-carboxymethyl aryl diazonium (CMA, Sigma Aldrich, Spain) derivatization. Details on the derivatization process are thoroughly described elsewhere [13]. In all cases, there is an evolution towards more negative voltage values, which occurs due to a decrease in capacitance: the additional insulating layer (CMA) widens the spatial charge region in the semiconductor electrode (again the parallel-plate capacitor), which means that a larger potential is needed to flatten the electronic bands in the semiconductor. Again, the change in the flat band potential becomes larger in the case of electrodes prepared at a substrate temperature of 300 °C, confirming them as the most sensitive for electrochemical sensing applications.

IV. CONCLUSIONS

An exhaustive structural and electrochemical analysis of nanostructured ITO electrodes prepared by electron beam evaporation at several substrate temperatures is presented in this work. Some specific conclusions can be drawn:

- Self-catalytic VLS growth of ITO nanostructures is promoted by the raise of substrate temperature during deposition, achieving the eutectic point of the SnO_2–In_2O_3 system. Small nanowires are present at substrate temperature of 200 °C, and the surface area is increased at high temperatures. A controlled Stranski-Krastanov epitaxial growth was achieved by working in a thermodynamic regime and on a crystalline SiO_2 substrate. This was proved with a pull-off test, resulting in the adhesive material being transferred to the nanostructured surface, which may be due to the combination of similar hydrophilicity for both materials, a large surface area and the physical attachment of the nanowires to the substrate.

- Faradaic current analysis revealed the highest electrochemical surface area for electrodes prepared at 300 °C. This may be because at 300 °C the separation between nanowires is optimal for redox reactions to reach the electrode surface, whereas (1) at lower temperatures, nanostructuration is not important enough to provide increased surface area and (2) at higher temperatures the increased density of whiskers hinders an eventual electron exchange between the solution and the electrode. This implied an increased double layer capacitance for these electrodes, which was confirmed by non-faradaic CV analysis.

- The use of nanostructured ITO electrodes in electrochemical sensing applications was shown by Mott-Schottky analysis of bare and CMA-derivatized electrodes, and those prepared at 300 °C proved to be the most sensitive, as expected. This was useful to characterize the solid-state electronic behavior of the *n*-type semiconductor electrodes, showing that subsequent addition of isolating layers on top of the electrode shifts the flat band potential towards more negative values. The whole analysis is sound with the description of electronic band diagram of the semiconductor electrode-electrolyte system.

ACKNOWLEDGMENTS

This work has been funded by the Spanish Ministerio de Economía y Competitividad (CTQ2016-75150-R) and the Generalitat de Catalunya (2014/SGR/149). Centro Nacional de Microelectrónica CNM-CSIC is acknowledged for the technical support. R.P. acknowledges an FPU grant (FPU15/00771) from the Spanish Ministerio de Educación, Cultura y Deporte.

REFERENCES

[1] Arthur Edward Dixon and James D Leslie. *Solar Energy Conversion: An Introductory Course*. Elsevier, 2013.

[2] Raquel Pruna, Francisco Palacio, Manuel López, Judit Pérez, Mònica Mir, Oriol Blázquez, Sergi Hernández, and Blas Garrido. Electrochemical characterization of organosilane-functionalized nanostructured ITO surfaces. *Applied Physics Letters*, 109(6):063109, 2016.

[3] R Pruna, F Palacio, M Martínez, O Blázquez, S Hernández, B Garrido, and M López. Organosilane-functionalization of nanostructured indium tin oxide films. *Interface Focus*, 6(6):20160056, 2016.

[4] Raquel Pruna, Francisco Palacio, and Manel López. Towards Nanostructured ITO-Based Electrochemical Sensors: Fabrication, Characterization and Functionalization. In *Multidisciplinary Digital Publishing Institute Proceedings*, volume 1, page 288, 2017.

[5] Jen Hsien Huang, Min Hsiang Hsu, Yu Sheng Hsiao, Peilin Chen, Peichen Yu, and Chih Wei Chu. Performance of chromophore-type electrochromic devices employing indium tin oxide nanorod optical amplification. *Solar Energy Materials and Solar Cells*, 98:191–197, 2012.

[6] Yeh Yee Kee, Sek Sean Tan, Thian Khok Yong, Chen Hon Nee, Seong Shan Yap, Teck Yong Tou, György Sfrn, Zsolt Endre Horvth, Jason P. Moscatello, and Yoke Khin Yap. Low-temperature synthesis of indium tin oxide nanowires as the transparent electrodes for organic light emitting devices. *Nanotechnology*, 23(2):025706, 2012.

[7] Arunandan Kumar, Ritu Srivastava, M N Kamalasanan, and Dalip Singh Mehta. Enhancement of light extraction efficiency of organic light emitting diodes using nanostructured indium tin oxide. *Optics letters*, 37(4):575–7, 2012.

[8] C H Chiu, Peichen Yu, C H Chang, C S Yang, M H Hsu, H C Kuo, and M a Tsai. Oblique electron-beam evaporation of distinctive indium-tin-oxide nanorods for enhanced light extraction from InGaN/GaN light emitting diodes. *Optics express*, 17(23):21250–21256, 2009.

[9] Hong-Wen Wang, Chi-Feng Ting, Miao-Ken Hung, Chwei-Huann Chiou, Ying-Ling Liu, Zongwen Liu, Kyle R Ratinac, and Simon P Ringer. Three-dimensional electrodes for dye-sensitized solar cells: synthesis of indium–tin-oxide nanowire arrays and ito/tio2 core–shell nanowire arrays by electrophoretic deposition. *Nanotechnology*, 20(5):055601, 2009.

[10] Gustavo A Rivas, Maria D Rubianes, Marcela C Rodriguez, Nancy F Ferreyra, Guillermina L Luque, Maria L Pedano, Silvia A Miscoria, and Concepcion Parrado. Carbon nanotubes for electrochemical biosensing. *Talanta*, 74(3):291–307, 2007.

[11] Keiki Pua S. Dancil, Douglas P. Greiner, and Michael J. Sailor. A porous silicon optical biosensor: Detection of reversible binding of IgG to a protein A-modified surface. *Journal of the American Chemical Society*, 121(34):7925–7930, 1999.

[12] Nianjun Yang, Hao Zhuang, René Hoffmann, Waldemar Smirnov, Jakob Hees, Xin Jiang, and Christoph E. Nebel. Nanocrystalline 3C-SiC electrode for biosensing applications. *Analytical Chemistry*, 83(15):5827–5830, 2011.

[13] Raquel Pruna, Abdoullatif Baraket, Anne Bonhommé, Nadia Zine, Abdelhamid Errachid, and Manuel López. Novel nanostructured indium tin oxide electrode for electrochemical immunosensors: suitability for the detection of TNF-α. *Electrochimica Acta*, 283:1632–1639, 2018.

[14] Chang Kyoung Choi, Kenneth D Kihm, and Anthony E English. Optoelectric biosensor using indium-tin-oxide electrodes. *Optics letters*, 32(11):1405–1407, 2007.

[15] Chang K Choi, Chuck H Margraves, Seung I Jun, Anthony E English, Philip D Rack, and Kenneth D Kihm. Opto-electric cellular biosensor using optically transparent indium tin oxide (ITO) electrodes. *Sensors*, 8(5):3257–3270, 2008.

[16] M.K. Fung, Y.C. Sun, A.M.C. Ng, A.B. Djurišić, and W.K. Chan. Indium tin oxide nanorods by dc sputtering. *Current Applied Physics*, 11(3):594–597, 2011.

[17] Jae Hyoung Park, Hoo Keun Park, Jinhoo Jeong, Woong Kim, Byoung Koun Min, and Young Rag Do. Wafer-Scale Growth of ITO Nanorods by Radio Frequency Magnetron Sputtering Deposition. *Journal of The Electrochemical Society*, 158(5):K131, 2011.

[18] Neng Wan, Jun Xu, Guran Chen, Xinhui Gan, Sihua Guo, Ling Xu, and Kunji Chen. Broadband anti-reflection and enhanced

field emission from catalyst-free grown small-sized ITO nanowires at a low temperature. *Acta Materialia*, 58(8):3068–3072, 2010.

[19] A L Beaudry, R T Tucker, J M Laforge, Michael T Taschuk, and Michael J Brett. Indium tin oxide nanowhisker morphology control by vapour-liquid-solid glancing angle deposition. *Nanotechnology*, 23:105608, 2012.

[20] T.-K. Yong, S.-S. Tan, C.-H. Nee, S.-S. Yap, Y.-Y. Kee, G. Sáfrán, Z.E. Horváth, J. Moscatello, Y.-K. Yap, and T.-Y. Tou. Pulsed laser deposition of indium tin oxide nanowires in argon and helium. *Materials Letters*, 66(1):280–281, 2012.

[21] Jaron G. Van Dijken and Michael J. Brett. Nanopillar ITO electrodes via argon plasma etching. *Journal of Vacuum Science & Technology A: Vacuum, Surfaces, and Films*, 30(4):040606, 2012.

[22] C. O'Dwyer, M. Szachowicz, G. Visimberga, V. Lavayen, S. B. Newcomb, and C. M.Sotomayor Torres. Bottom-up growth of fully transparent contact layers of indium tin oxide nanowires for light-emitting devices. *Nature Nanotechnology*, 4(4):239–244, 2009.

[23] Hoon-Sik Jang, Do-Hyung Kim, Hyeong Rag Lee, and Sung-Youp Lee. Field emission from cone-like single crystalline indium tin oxide nanorods. *Materials Letters*, 59(12):1526–1529, 2005.

[24] KP Kalyanikutty, Gautam Gundiah, Christopher Edem, A Govindaraj, and CNR Rao. Doped and undoped ito nanowires. *Chemical physics letters*, 408(4-6):389–394, 2005.

[25] A. Irrera, E. F. Pecora, and F. Priolo. Control of growth mechanisms and orientation in epitaxial Si nanowires grown by electron beam evaporation. *Nanotechnology*, 20(13):135601, 2009.

[26] Pietro Artoni, Emanuele Francesco Pecora, Alessia Irrera, and Francesco Priolo. Kinetics of si and ge nanowires growth through electron beam evaporation. *Nanoscale Research Letters*, 6(1):162, 2011.

[27] R Rakesh Kumar, K Narasimha Rao, K Rajanna, and AR Phani. Low temperature and self catalytic growth of ultrafine ito nanowires by electron beam evaporation method and their optical and electrical properties. *Materials Research Bulletin*, 52:167–176, 2014.

[28] Charles ET White. *Phase diagrams of indium alloys and their engineering applications*, volume 8. Asm Intl, 1992.

[29] N David, Khadija El Aissaoui, JM Fiorani, J Hertz, and M Vilasi. Thermodynamic optimization of the in–pb–sn system based on new evaluations of the binary borders in–pb and in–sn. *Thermochimica acta*, 413(1-2):127–137, 2004.

[30] Arvind Baskaran and Peter Smereka. Mechanisms of Stranski-Krastanov growth. *Journal of Applied Physics*, 111(4), 2012.

[31] Qiang Li, Feng Yun, Yufeng Li, Wen Ding, and Ye Zhang. Fabrication and application of indium-tin-oxide nanowire networks by polystyrene-assisted growth. *Scientific Reports*, 7(1):1600, 2017.

[32] N. Yamamoto, K. Morisawa, J. Murakami, and Y. Nakatani. Formation of ITO Nanowires Using Conventional Magnetron Sputtering. *ECS Solid State Letters*, 3:84–86, 2014.

[33] C Lee. Effects of plasma treatment on the electrical and optical properties of indium tin oxide films fabricated by r.f. reactive sputtering, 2001.

[34] Anees A Ansari, A Kaushik, P R Solanki, and B D Malhotra. Sol–gel derived nanoporous cerium oxide film for application to cholesterol biosensor. *Electrochemistry communications*, 10(9):1246–1249, 2008.

[35] Allen J Bard and Larry R Faulkner. *Electrochemical methods: fundamentals and applications*, volume 2. Wiley New York, 1980.

[36] Vincent Gau, Shu-Ching Ma, Hua Wang, Joni Tsukuda, John Kibler, and David A. Haake. Electrochemical molecular analysis without nucleic acid amplification. *Methods*, 37(1):73–83, 2005.

[37] Janice C. Myland and Keith B. Oldham. An analytical expression for the current-voltage relationship during reversible cyclic voltammetry. *Journal of Electroanalytical Chemistry*, 153(1-2):43–54, 1983.

[38] Maciej Mierzwa, Emmanuel Lamouroux, Ivan Vakulko, Pierrick Durand, and Mathieu Etienne. Electrochemistry and Spectroelectrochemistry with Electrospun Indium Tin Oxide Nanofibers. *Electrochimica Acta*, 202:55–65, 2016.

[39] Akash Deep, Sanjeev Kumar Bhardwaj, A. K. Paul, Ki Hyun Kim, and Pawan Kumar. Surface assembly of nano-metal organic framework on amine functionalized indium tin oxide substrate for impedimetric sensing of parathion. *Biosensors and Bioelectronics*, 65:226–231, 2015.

[40] Yuanyuan Lin, Yang Peng, and Junwei Di. Electrochemical detection of Hg(II) ions based on nanoporous gold nanoparticles modified indium tin oxide electrode. *Sensors and Actuators, B: Chemical*, 220:1086–1090, 2015.

[41] Anis Allagui, Todd J. Freeborn, Ahmed S. Elwakil, and Brent J. Maundy. Reevaluation of Performance of Electric Double-layer Capacitors from Constant-current Charge/Discharge and Cyclic Voltammetry. *Scientific Reports*, 6:38568, 2016.

[42] Sarra Bouden, Antoine Dahi, Fanny Hauquier, Hyacinthe Randriamahazaka, and Jalal Ghilane. Multifunctional Indium Tin Oxide Electrode Generated by Unusual Surface Modification. *Scientific Reports*, 6:36708, 2016.

[43] Ying Liu and William E. Mustain. High stability, high activity Pt/ITO oxygen reduction electrocatalysts. *Journal of the American Chemical Society*, 135(2):530–533, 2013.

[44] Y. Oren and A. Soffer. The electrical double layer of carbon and graphite electrodes. Part II. Fast and slow charging processes. *Journal of Electroanalytical Chemistry*, 186(1-2):63–77, 1985.

[45] F. Montilla, E. Morallón, A. De Battisti, and J. L. Vázquez. Preparation and Characterization of Antimony-Doped Tin Dioxide Electrodes. Part 1. Electrochemical Characterization. *The Journal of Physical Chemistry B*, 108(16):5036–5043, 2004.

[46] Celine Largeot, Cristelle Portet, John Chmiola, Pierre Louis Taberna, Yury Gogotsi, and Patrice Simon. Relation between the ion size and pore size for an electric double-layer capacitor. *Journal of the American Chemical Society*, 130(9):2730–2731, 2008.

[47] K. Gelderman, L. Lee, and S. W. Donne. Flat-Band Potential of a Semiconductor: Using the MottSchottky Equation. *Journal of Chemical Education*, 84(4):685, 2007.

[48] Krishnan Rajeshwar. Fundamentals of Semiconductors Electrochemistry and Photoelectrochemistry. In *Encyclopedia of Electrochemistry*, pages 1–53. Wiley-VCH Weinheim, Germany, 2007.

[49] Nandhinee Radha Shanmugam, Sriram Muthukumar, Anjan Panneer Selvam, and Shalini Prasad. Electrochemical nanostructured ZnO biosensor for ultrasensitive detection of cardiac troponin-T. *Nanomedicine*, 11(11):1345–1358, 2016.

[50] Osbel Almora, Clara Aranda, Elena Mas-Marzá, and Germà Garcia-Belmonte. On Mott-Schottky analysis interpretation of capacitance measurements in organometal perovskite solar cells. *Applied Physics Letters*, 109(17):173903, 2016.

Electronic Supplementary Information

Tuning the deposition parameters for optimizing the faradaic and non-faradaic electrochemical performance of nanowire array-shaped ITO electrodes prepared by electron beam evaporation

Raquel Pruna[a], Manel López[a], Francesc Teixidor[b]

[a] Departament d'Enginyeria Electrònica i Biomèdica, Universitat de Barcelona, C/Martí i Franquès 1, E-08028 Barcelona, Spain

[b] Institut de Ciència de Materials de Barcelona, ICMAB-CSIC, Campus UAB, E-08193 Bellaterra, Spain

1. SEM images of the nanostructured electrodes prepared at several substrate temperatures

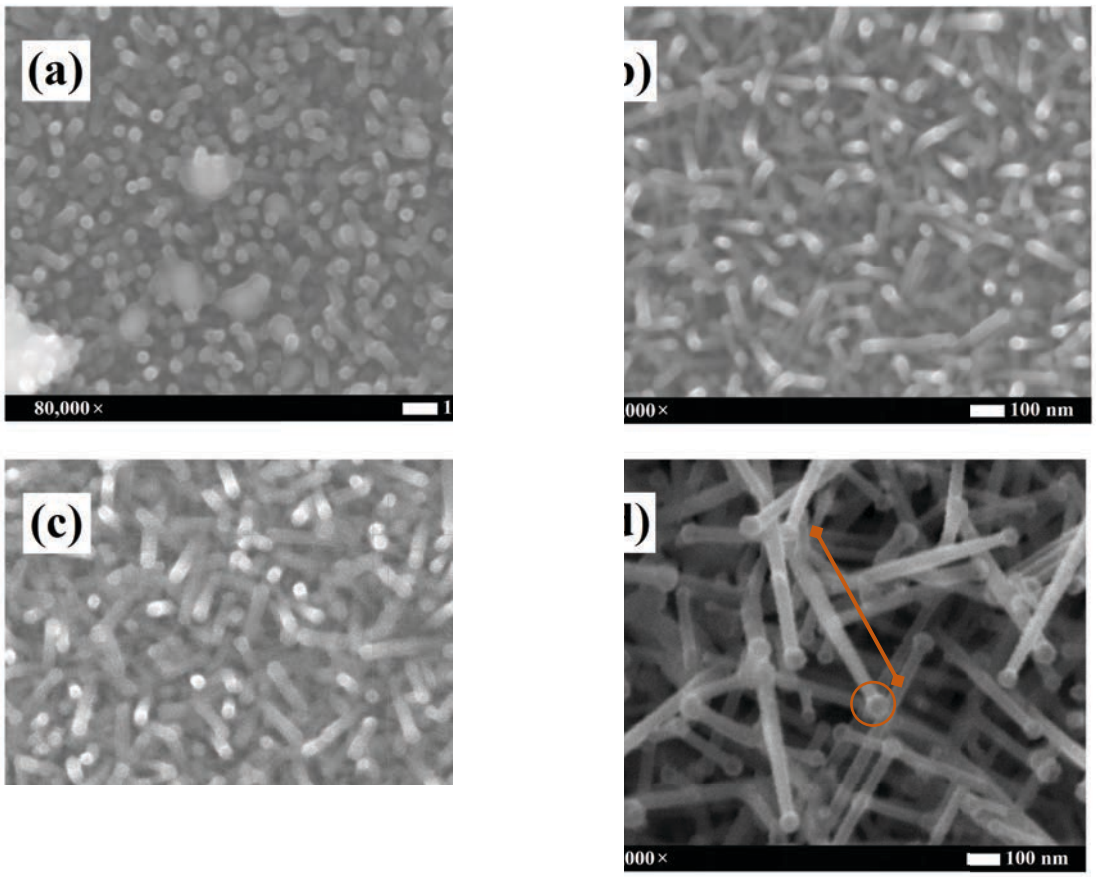

Figure S1. SEM images of nanostructured ITO electrodes prepared by electron beam evaporation, with substrate temperatures of (a) 200 °C, (b) 300 °C, (c) 400 °C and (d) 500 °C. In the latter image, a representative 'seed' and 'stick' appear circled and outlined, respectively.

The self-catalytic VLS growth occurs from “seeds” that constitute regions offering high probabilities for the material to accumulate, inducing the nanostructuration appreciated in the SEM micrographs. Let us consider the substrate as a region activated by catalyst drops (the In-Sn alloy). Atomic or molecular particles of the semiconductor raw target material impact the catalyst drops either from an external flux at an arbitrary angle from the surface or by diffusion from the surface. Nanowire growth occurs by supersaturation of the catalyst drops with the flux material: the semiconductor is dissolved in the drop and the crystallization occurs at the drop-material interface[1]. A proof of the self-catalytic VLS growth method can be assessed again from the images shown in Figure S1. Indeed, if we take a careful look at the shape of the nanowires, we observe that although there are different lengths and widths, in all cases the aforementioned “seeds” are present at the tip of the whisker. This is indicative of the growth process for the nanostructures. Very precise compositional studies were conducted elsewhere[2], showing by transmission electron microscopy (TEM) that the composition and crystallinity at the tips is essentially the same of the sticks’. Moreover, the stoichiometry of the target material is also conserved, altogether accounting for the accuracy and degree of precision this method provides for nanowire fabrication.

1 A. G. Nastovjak, I. G. Neizvestny and N. L. Shwartz, *Pure Appl. Chem.*, 2010, **82**, 2017–2025.

2 R. R. Kumar, K. N. Rao, K. Rajanna and A. R. Phani, *Mater. Res. Bull.*, 2014, **52**, 167–176.

2. SEM image of a thin ITO film prepared at 100 ºC

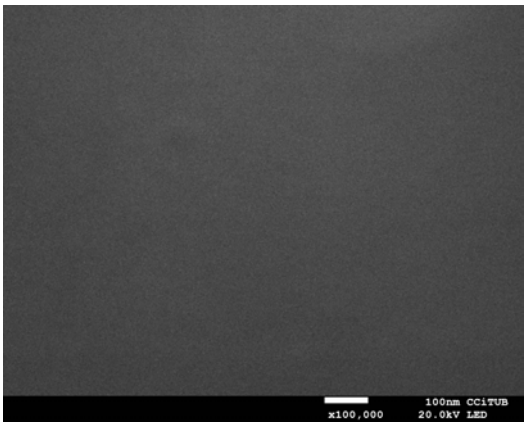

Figure S2. SEM image of a thin ITO film prepared by electron beam evaporation at a substrate temperature of 100 ºC. No nanowhiskers or other structures can be appreciated.

3. Transparency of ITO electrodes prepared at several temperatures

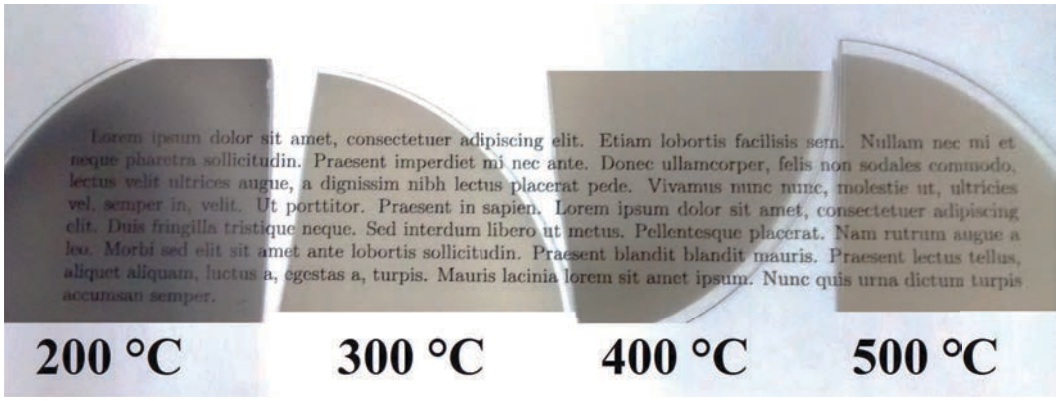

Figure S3. Transparency of the as-deposited nanostructured ITO electrodes at naked eye.

4. Faradaic cyclic voltammetry

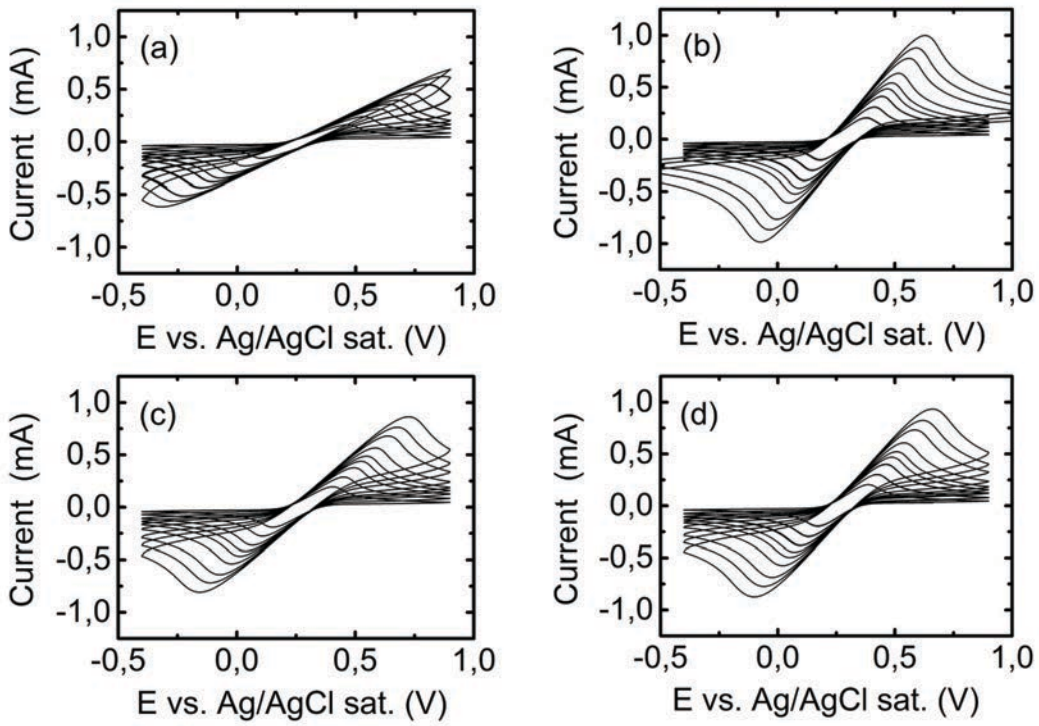

Figure S4. Faradaic cyclic voltammetry of ITO electrodes prepared at (a) 200 ºC, (b) 300 ºC, (c) 400 ºC and (d) 500 ºC. The cycles were taken at scan rates of 10, 25, 50, 75, 150, 250, 350, 500 mV s^{-1} (increasing order in the figures).

5. Non-faradaic cyclic voltammetry

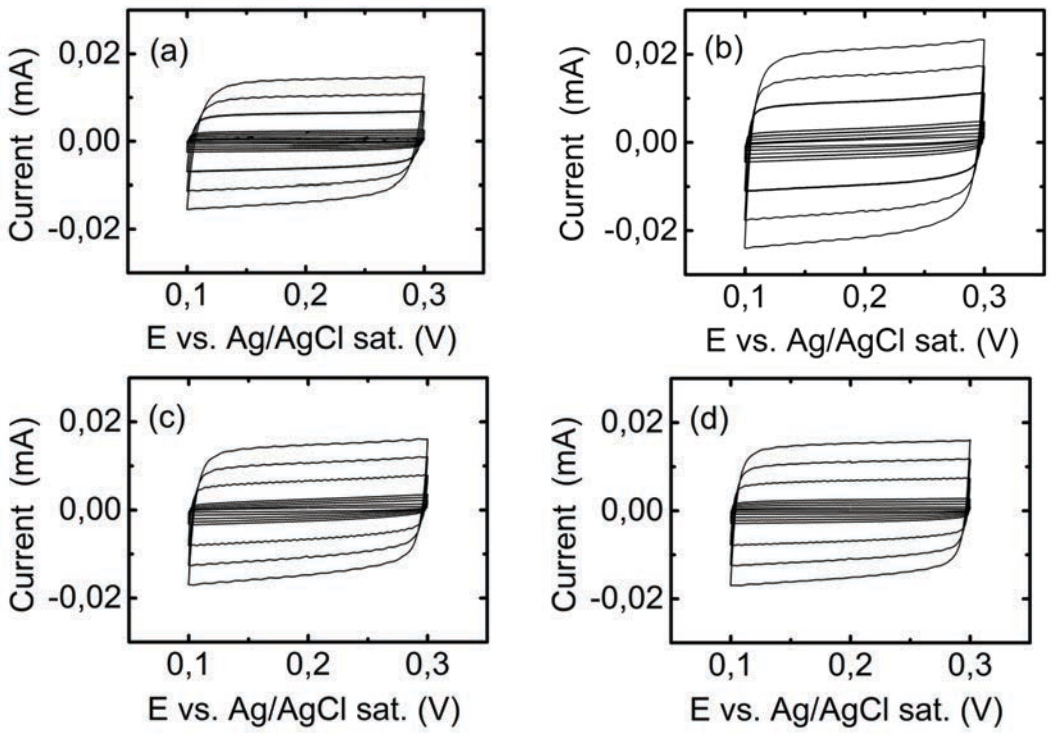

Figure S5. Non-faradaic cyclic voltammetry of ITO electrodes prepared at (a) 200 ºC, (b) 300 ºC, (c) 400 ºC and (d) 500 ºC. The cycles were taken at scan rates of 10, 25, 50, 75, 100, 300, 500 mV s^{-1} (increasing order in the figures).

3.2.2 Influence of target composition

It has long been known that the optimal composition maximizing ITO's optical transmittance and electrical conductivity is 90/10 (atomic weight) In/Sn [200]. This was assumed in this work, and all the experiments published and gathered in this dissertation were conducted with ITO electrodes prepared with indium and tin oxides in the mentioned proportion. However, we studied the effect of increasing the percentage of tin oxide in the raw target material. Namely, a proportion of 70/30 (atomic weight) In/Sn was prepared by mixing the separate components (In_2O_3 and SnO_2); electron beam evaporation at 1 Å s^{-1} with a substrate temperature of 500 °C was conducted to prepare working electrodes of the new composition.

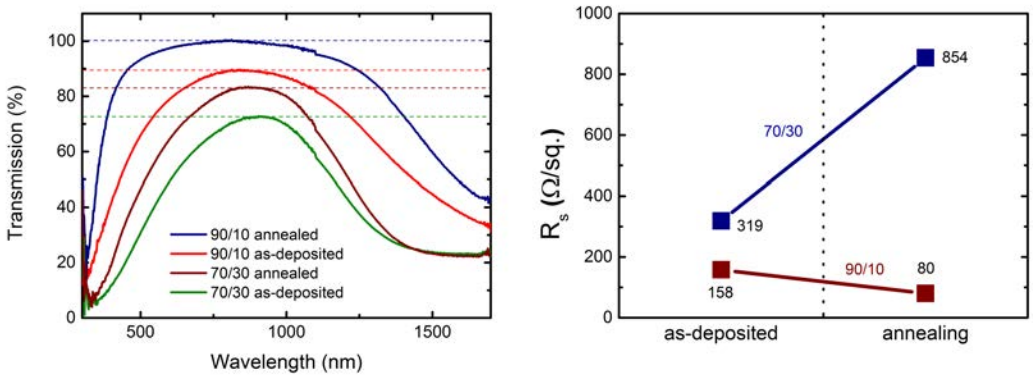

(A) (B)

FIGURE 3.1: (A) Optical transmittance and (B) sheet resistance of ITO electrodes prepared at 70/30 and 90/10 In/Sn proportions, as-deposited and after an annealing process.

The optical transmittance and sheet resistance were measured for 90/10 (atomic weight) and 70/30 (atomic weight) In/Sn ITO electrodes, both for as-deposited samples and after an annealing process of 1 h at 600 °C conducted under nitrogen atmosphere. In both cases (for 90/10 and 70/30 proportions), the optical transmittance was increased after the annealing process, as shown in Figure 3.1a. On the other hand, the sheet resistance increased substantially after annealing in the case of 70/30 proportion, whereas this parameter was reduced, i.e. the conductivity increased, in the 90/10 case after annealing, as shown in Figure 3.1b.

3.3 Micropatterning of transparent ITO electrodes

3.3.1 Objective

The deposition of ITO by electron beam evaporation cannot be easily targeted at a micrometric level. Indeed, unless a mask made of an adequate material (which could bear the temepratures reached during evaporation) was used to delimit the regions where the material was to be deposited, the micropatterning needs to be done after macroelectrode preparation.

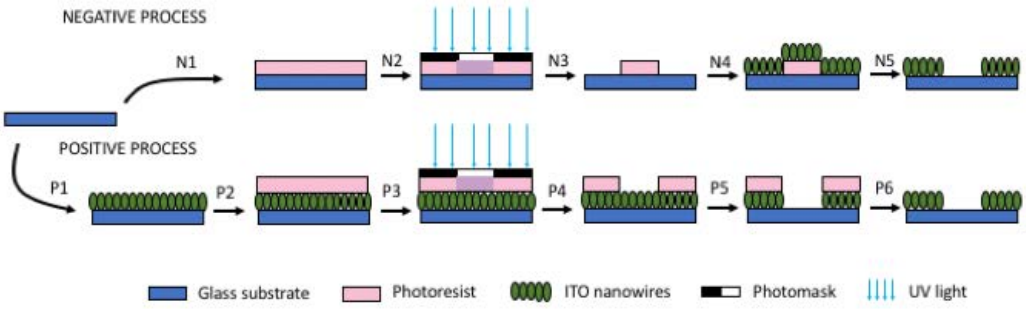

FIGURE 3.2: Schematic of the several steps for transfering a micropattern to an electrode by photolithography using a positive photoresist.[1]

The interesting thing about electrode micropatterning is the possibility to create electrodes of aleatory shapes for being integrated in miniaturized systems or even lab-on-a-chip architectures. It is important to highlight that the experiment detailed in the following sections was conducted in the last period of the thesis, once the viability of using the material as electrochemical biosensor was proved. Thus, the results need to be improved in the future to optimize the quality of the resulting microelectrodes.

3.3.2 Materials and methods

3.3.2.1 Method I: photolithography

In photolithography, UV light is used to transfer a pattern from a photomask to a light sensitive chemical photoresist previously coated on the substrate surface (before or after ITO deposition depending on whether we are pursuing a positive or negative pholithographic process). It must be done in a clean room environment, and the substrates must be gently cleaned from organic and inorganic contaminants before photoresist coating.

In a photolithographic process involving a positive photoresist, those parts exposed to UV light will be removed after resist development. This process is illustrated in Figure 3.2. On the contrary, a negative photoresist-based photolithographic process will keep those parts of the resist exposed to UV light and those unexposed will be removed after development. Both processes were tested to pattern nanostructured ITO electrodes, yet only the one involving negative photoresist produced highly qualified electrodes, as will be explained in the following lines.

Positive photoresist With a positive photoresist (Figure 3.2), the black motifs in the photomask will be transferred to the resist (which correspond to the parts unexposed to light). Thus, the photoresist must be spin-coated on the already prepared ITO electrode (P1 and P2 in the image). In the present case, a first ramp was applied to accelerate the wafer from 0 rpm to 500 rpm in 9 s; then a second ramp of total duration 30 s reaching 4000 rpm in 9 s was applied, achieving a resist thickness of 1.4 μm.[2] Immediately after resist coating, the whole electrode was pre-baked for 1 min in a hotplate at 90 °C to drive off any excess of photoresist solvent. Now, the electrode is ready for the photomask

[1] Inspired from `https://en.wikipedia.org/wiki/Photolithography#/media/File:Photolithography_etching_process.svg`.

[2] AZ5214E photoresist datasheet – `http://dvh.physics.illinois.edu/pdf/AZ5214E.pdf`.

pattern to be transferred to it. The resist-coated ITO electrode must be placed on the UV exposer holder, and the photomask must be properly aligned. A glass may be placed on top of the photomask to increase contact between the latter and the photoresist. At this point, UV exposure is maintained for 6 s (P3 in the image). Then, the whole electrode is immersed in a solution of developer (diluted in a proportion 1:4 in water) for 1 min to remove the exposed photoresist thanks to a chemical change induced by UV light that makes it soluble. Afterwards, the electrode must be rinsed with abundant water to remove the excess of developer (P4). Now, the etching of the regions uncovered by the photoresist may be performed (P5). In the case of ITO, the indications provided by [201] were followed. These will be detailed in Section 3.3.2.2. Once the etching is done the photoresist may be stripped by rinsing in acetone (P6).

Negative photoresist In this case (Figure 3.2), it will be the photoresist unexposed to UV light that will be removed by the developer. Thus, if the same photomask is to be used, then the microelectrode pattern must be created on the glass substrate prior to ITO evaporation[3] (please see steps N1 and N2 in the image). Then, the undesired ITO will be removed together with the photoresist after evaporation. Taking this into account, the whole process is conducted identically, except for the illumination step, where two UV exposures are perfomed, of 3.5 s and 30 s each. A post-baking step after the first UV exposure must be conducted, leaving the coated glasses in a hotplate at 120 °C for 110 s. After the second UV exposure, the photoresist is developed, yet it is now the exposed regions of the pattern which remain (N3). In this case, the development must be conducted very carefully and the exact amount of time, otherwise the exposed photoresist will undergo the reverse chemical process and be removed as well. After photoresist development, the samples must be rinsed in abundant water and dried carefully with a stream of nitrogen to stop the chemical process. Now the photoresist pattern coated glasses may be used as substrates for ITO evaporation by an electron beam machine (N4). Finally, the remaining photoresist must be dissolved together with the unwanted ITO (N5) by an adequate chemical (e.g. acetone).

3.3.2.2 Method II: ITO etching

During the tests of the positive photolithographic process, an etching of the unwanted ITO was required in step P5 in Figure 3.2. The process followed here was based on one reported by Huang *et al.* in [201]. After some tests, immersing the electrode in a solution of HCl 9 M and controlling the etching by eye proved to be the most effective method, although not enough to reach the desired precision. Indeed, the solution of HCl 3 M acted too slowly and, due to the high electrode porosity, a very strong underetching occurred before the unwanted ITO disappeared.

3.3.2.3 Materials and reagents

AZ5214E (MicroChemicals, Germany) was used as photoresist and AZ400K (MicroChemicals, Germany) was used as photoresist developer. Acetone was used as photoresist remover after ITO etching. The photomask was designed with a computer assisted design (CAD) software. The design is of no importance to this thesis, but it reproduces small enough patterns that could be required in any project.

[3] In this case, it is important to work with a photoresist that bears the high temperatures reached during electron beam evaporation.

3.3.3 Results and discussion

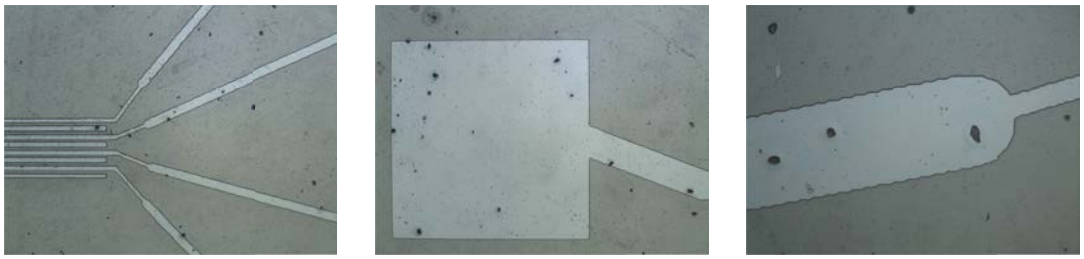

FIGURE 3.3: Optical images before ITO etching. The dark regions correspond to the excess ITO to be etched, and the light regions correspond to the photoresist-coated ITO electrodes to be patterned.

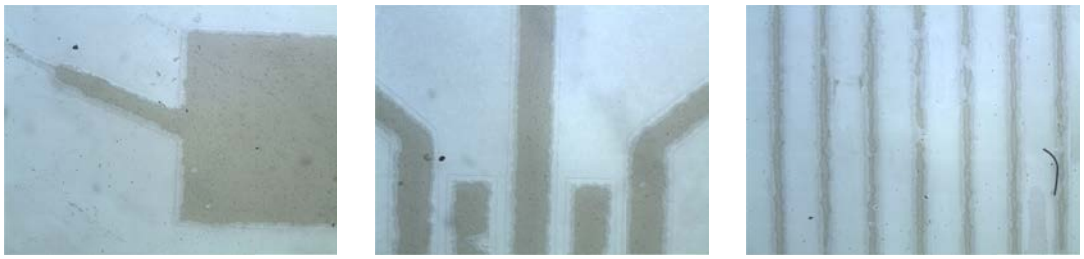

FIGURE 3.4: Optical images after ITO etching and after photomask removal. The patterned ITO electrodes are observed in dark colour with irregular borders as a result of strong underetching.

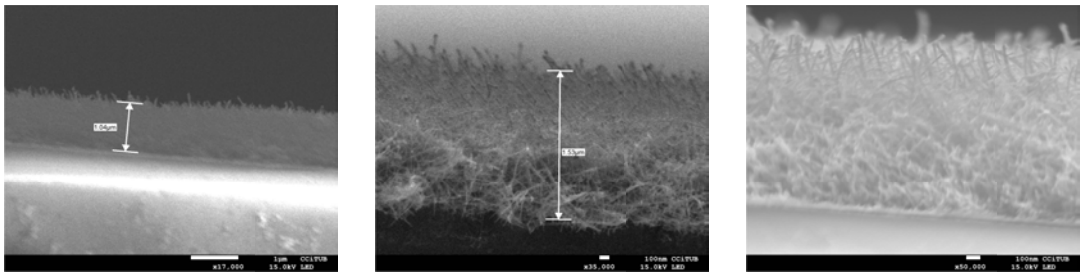

FIGURE 3.5: Lateral SEM images after ITO etching during the process involving the positive photoresist.

Photolithography was first performed with a positive photoresist as previously described. Figure 3.3 shows some optical microscopy images of the ITO electrodes as after step P4 in Figure 3.2. The light areas correspond to the photoresist-coated ITO regions to be conserved (patterned), whereas the dark areas correspond to the ITO to be etched. Some unresolved issues with the positive photoresist method arise:

- There is a high underetching at the borders of the patterns due to the porosity of the nanostructured surface, as explained before. This happens even when using a solution of HCl 9 M to decrease the time of excess ITO etching, as can be observed

in Figure 3.4, which shows the optical image of the micropatterned electrode after ITO etching.

- There is also a strong degradation of the lateral profile of the ITO deposit at the borders of the electrodes. This can be fully appreciated in Figure 3.5, where a SEM micrograph of the material after ITO etching and photoresist removal is shown. The morphology of the nanowires becomes irreversibly damaged at the edges of the pattern, although the material still keeps its physicochemical properties.

This was partly solved by the negative photoresist method at the cost of spending more time during the whole process. Nonetheless, the geometry of the ITO film was degraded during photoresist removal. The strong point in this case was that the borders of the pattern were perfectly delimited, and obviously no ITO excess appeared at blank regions. This still needs to be optimized, especially the removal of the photoresist during the negative process, since we observed this irreversively damages the moprhology of the nanowires.

Chapter 4

Surface modification and sensing: nanostructured ITO as electrochemical biosensor

The experiments presented in Chapter 3 demonstrated an enhanced electrochemical performance of nanostructured ITO electrodes compared to thin ITO films. The present chapter gathers the results of the experiments conducted to test the suitability of nanostructured ITO electrodes as electrochemical biosensors.

Some preliminary results on the ITO surface modification by organosilane linker molecules were shown in Article I, where the oxidation of an additional molecule (containing a ferrocene termination) attached to the organosilane was detected by cyclic voltammetry and quantified on nanostructured electrodes in relation to thin films. In Section 4.1 of the present chapter we study the chemical modification of the surfaces with organosilanes in terms of composition, and its effect in electrochemical impedance spectroscopy.

During the performance of these experiments we became aware that the surface modification of ITO by organosilanes presented some difficulties. Temperature, humidity and pH must be very well controlled for the whole procedure to succeed, and even so the impedance change (which can be considered proportional to the derivatized surface area) is not very pronounced. This is the reason why an alternative way of derivatizing ITO substrates was explored; a technique widely implemented on gold-based electrodes and based on the electroadressed reduction of crosslinker molecules onto the electrode substrate was chosen, obtaining interesting results. These are gathered in Article IV included in Section 4.2. There, this new surface derivatization is physicochemically characterized and further surface modification is performed towards detection of an actual disease biomarker. Section 4.3 includes some preliminary results, which have not been published yet, on the performance of bovin serum albumin and biotin-streptavidin based immunoassays on thin film and nanostructured ITO used as working electrodes in electrochemical biosensors.

4.1 Surface modification of nanostructured ITO and first experiments

In *Article III: Organosilane-functionalization of nanostructured indium tin oxide films*, an in-depht characterization of organosilane-derivatized nansotructured ITO electrodes

(which was already proved in Article I) is presented. The main objectives of this article can be summarized as follows:

1. morphological characterization of nanostructured ITO substrates by atominc force microscopy (AFM) and scanning electron microscopy (SEM);

2. derivatization of nanostructured ITO substrates with (3-glycidoxy propyl) trimethoxy silane molecules;

3. compositional and chemical characterization of the derivatized substrates by X-ray photoelectron spectroscopy (XPS) and comparison with bare ITO substrates and

4. conduction of electrochemical studies by cyclic voltammetry (CV) and electrochemical impedance spectroscopy (EIS) comparing bare and derivatized ITO substrates, and analyzing the influence of the derivatization strategy in electrochemical parameters such as double layer capacitance and substrate impedance.

Organosilane-functionalization of nanostructured ITO films

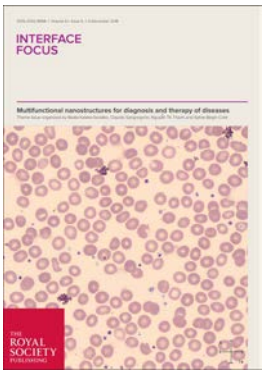

Raquel Pruna,[1] Francisco Palacio,[1] Mònica Martínez,[2] Oriol Blázquez,[1] Sergi Hernández,[1] Blas Garrido,[1] and Manel López[1]

[1)] *Departament d'Enginyeries, Universitat de Barcelona, Martí i Franquès 1, E-08028 Barcelona, Spain*

[2)] *Departament de Ciència de Materials i Química Física, Universitat de Barcelona, Marí i Franquès 1, E-08028 Barcelona, Spain*

Interface Focus, 6(6) (2016), 20160056
doi: 10.1098/rsfs.2016.0056

ABSTRACT

Fabrication and organosilane-functionalization and characterization of nanostructured ITO electrodes are reported. Nanostructured ITO electrodes were obtained by electron beam evaporation, and a subsequent annealing treatment was selectively performed to modify their crystalline state. An increase in geometrical surface area in comparison with thin-film electrodes area was observed by atomic force microscopy, implying higher electroactive surface area for nanostructured ITO electrodes and thus higher detection levels. To investigate the increase in detectability, chemical organosilane-functionalization of nanostructured ITO electrodes was performed. The formation of 3-glycidoxypropyltrimethoxysilane (GOPTS) layers was detected by X-ray photoelectron spectroscopy. As an indirect method to confirm the presence of organosilane molecules on the ITO substrates, cyclic voltammetry and electrochemical impedance spectroscopy (EIS) were also carried out. Cyclic voltammograms of functionalized ITO electrodes presented lower reduction-oxidation peak currents compared with non-functionalized ITO electrodes. These results demonstrate the presence of the epoxysilane coating on the ITO surface. EIS showed that organosilane-functionalized electrodes present higher polarization resistance, acting as an electronic barrier for the electron transfer between the conductive solution and the ITO electrode. The results of these electrochemical measurements, together with the significant difference in the X-ray spectra between bare ITO and organosilane-functionalized ITO substrates, may point to a new exploitable oxide-based nanostructured material for biosensing applications. As a first step towards sensing, rapid functionalization of such substrates and their application to electrochemical analysis is tested in this work. Interestingly, oxide-based materials are highly integrable with the silicon chip technology, which would permit the easy adaptation of such sensors into lab-on-a-chip configurations, providing benefits such as reduced size and weight to facilitate on-chip integration, and leading to low-cost mass production of microanalysis systems.

I. INTRODUCTION

Indium tin oxide (ITO) is a degenerate n-type semiconductor with wide band gap energy around 3.2 eV [1] that has been highly exploited in the field of optoelectronics due to its simultaneously good conducting and transparency properties [2 and 3]. ITO thin films have been widely used to develop organic light emitting diodes (OLEDs), solar cells, flat panel displays and transparent conducting electrodes, among others [4–7]. Moreover, some nanostructured materials have been extensively used for developing ultrasensitive, low-cost and miniaturized sensors, as they present large surface-to-volume ratio, favorable electrocatalytic activity and excellent electronic properties [8 and 9]. Actually, some applications of sensors based on thin film structured ITO can be found in the literature [10–13], yet no electrochemical sensor application based exclusively on nanostructured ITO has been developed to our knowledge.

Covalent attachment of specific biomolecules to nanostructured conductive surfaces is of great importance for the development of sensitive biosensors based on molecular recognition. The attachment of organic biomolecules to inorganic substrates requires an intermediate layer of molecules. A group of molecules that have been widely used are the so-called organosilanes, which participate in the first steps of immobilization procedures for the fabrication of on-chip biodevices [14]. Although being quite unstable in aqueous solutions at the time of forming the dense and homogeneous layer on the electrode's surface, organosilanes have proved to be very useful for biosensing [15 and 16]. Many authors have reported the fabrication of oxide-based biosensors functionalized with organosilanes for the detection of biomolecules in aqueous environaments. For instance, Wang & Wang described hydrogen peroxide detection with a horseradish-functionalized gold-modified ITO electrode in phosphate-buffered solution (PB, pH 7.0) wtih a limit of detection of 8 μM estimated at a signal-to-noise ratio of 3 [17]. Yang & Li measured *Escherichia coli* O157:H7 by electrochemisty in aqueous solution of $[Fe(CN)_6]^{3-/4-}$ in PBS [18]. Other systematic investigations on functionalization of ITO-based devices have been reported [19–21]. Hanson *et al.* [19] described a method for surface modification of ITO with α-quarterthiophene-2-phosphonate to enhance charge transport across anodic and cathodic interfaces in OLEDs. High current densities in simple single-layer devices and double-layer light-emitting devices were obtained compared with those with untreated ITO anodes. Similarly, Hatton *et al.* [20] reported functionalization of ITO-coated glass thin films with small molecule chlorosilanes, dramatically improving the performance of ITO anodes in OLEDs. Cossement *et al.* [21] reported n-hexyltrichlorosilane and 6-(1'-pyrrolyl)-n-hexyltrichlorosilane modification of ITO substrates, for further polypyrrole polymerization of the substrates, which is halfway optoelectronics and sensing applications. Such conducting organic polymers have been found to have extensive sensing applications [22–24]. The intermediate molecule used to functionalize ITO substrates in the present work is (3-glycidoxypropyl)trimethoxysilane (GOPTS), and its use has been widely reported in the literature [18, 25, and 26]. This molecule helps controlling ITO physical and chemical properties for biosensing purposes. Hillebrandt & Tanaka [26] reported ITO thin films functionalization with self-assembled monolayers of octyltrimethoxysilane and octadecyltrimethoxysilane, demonstrating the behaviour of the alkylsiloxane monolayer as a barrier for ions in the electrolyte, as well as the passivation effect of the monolayers against electrochemistry. This feature may be used as the basic principle for the development of a biosensor. For instance, Ruan *et al.* reported the use of GOPTS for immobilizing anti-*Escherichia coli* antibodies onto ITO thin films in order to fabricate an immunosensor for the detection of *E. coli* O157:H7, achieving a detection limit of 6×10^3 cells ml^{-1} [27]. The same authors presented a study on the AFM and impedance spectroscopy characterization of the specific recognition of *E. coli* O157:H7 cells by the immobilized anti-*E. coli* antibodies. They observed a systematic increase in the impedance spectra on GOPTS-functionalized substrates, anti-*E. coli* antibodies immobilization

and biorecognized *E. coli* O157:H7 with respect to bare ITO substrates. The same principle is investigated in the present work.

Our long-term aim is to test the feasibility of developing robust electrochemical sensors taking advantage of the structural and technological characteristics of nanostructured ITO, i.e., enhanced surface-to-volume ratio, together with other useful properties such as good conductivity and high stability under physiological conditions because of its polarizability [28 and 29]. In this paper, we report on the interaction of GOPTS with -OH terminated nanostructured ITO surfaces, to test the viability of functionalizing such nanostructured ITO surfaces. The experiments were carried out under two conditions: with as-deposited nanostructured ITO electrodes and also with annealed electrodes, thus observing the effect of the annealing treatment on organosilane adsorption. As-deposited nanostructured ITO substrates were observed by scanning electron microscopy (SEM) and characterized by atomic force microscopy (AFM) for the determination of geometrical surface area. The electroactive surface area was measured by cyclic voltammetry (CV) and results are shown elsewhere [30]. Surface functionalization was monitored by X-ray photoelectron spectroscopy (XPS) as a microscopic charcterization. XPS results may point to a better organosilane-functionalization of as-deposited ITO slides, so CV and electrochemical impedance spectroscopy (EIS) were performed on as-deposited substrates for better characterizing them at the macroscopic level. Electrochemical measurements also confirmed the presence of organosilanes on the ITO electrode.

II. METHODS

A. Substrates fabrication: electron beam evaporation

ITO was deposited on one face of double-sided polished n^+-type Si substrates by electron beam evaporation using a Pfeiffer vacuum classic 500 growth chamber. Substrate temperature was set at 500 °C, and deposition rate was set at 1 Å s^{-1} for depositing an equivalent thin film thickness of 200 nm of ITO. Then, half the samples were left as-deposited, and the rest were submitted to an annealing process, at 600 °C under nitrogen atmosphere for 1 h. There is an enhancement of the surface conductivity when films are annealed [31 and 32], due to the decrease in sheet resistance produced by the crystalline organization of In_2O_3 and SnO_2 molecules in the evaporated ITO. That is the reason why we extended our study to explore the possibilities that annealed substrates may open in the field of surface functionalization.

B. Substrate characterization: atomic force microscopy, X-ray photoelectron spectroscopy and electrochemical measurements

AFM observations of as-deposited nanostructured ITO films were carried out in a Multimode 8 with a Nanoscope V electronics from Bruker. Height images were obtained under peak force tapping mode using a 25 μm scanner and SNL tips with force constant of 0.35 N m^{-1} purchased from Bruker.

XPS meaurements of as-deposited and annealed nanostructured ITO substrates were performed in a PHI 5500 Multitechnique System (Physical Electronics) with a monochromatic X-ray source (Al Kα line of 1486.6 eV energy and 350 W), placed perpendicular to the analyser axis and calibrated using the $3d_{5/2}$ line of Ag with a full width at half maximum (FWHM) of 0.8 eV. The analised area was a circle of 0.8 mm in diameter, and the selected resolution for the spectra was 23.5 eV of pass energy and 0.1 eV $step^{-1}$. All measurements were made

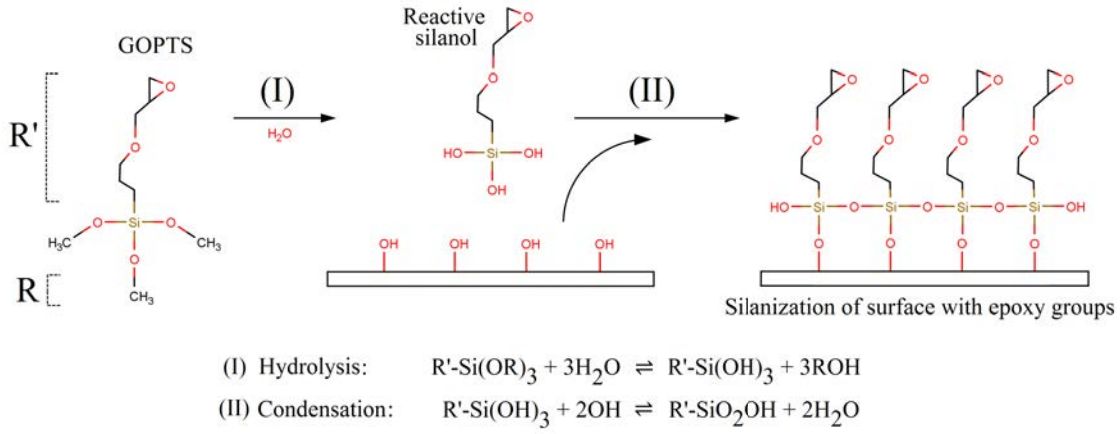

FIG. 1: Schematic representation of the formation of (3-glycidoxypropyl)trimethoxysilane layer on the ITO substrates. Adapted from [14].

in ultra-high vacuum chamber pressure between 5×10^{-9} Torr and 2×10^{-8} Torr.

All electrochemical measurements (CV, EIS) were carried out in a conventional three-electrode Teflon electrochemical cell, with a solution of 5 mM ferricyanide/ferrocyanide ($Fe(CN)_6^{3-}/Fe(CN)_6^{4-}$) in 0.1 M KCl at 25 °C. The ITO geometrical projected working electrode area, defined by the inner diameter of an O-ring, was 0.7 cm^2. A platinum wire was used as a counter electrode, and an Ag/AgCl reference electrode was placed inside the cell. The electrochemical cell was connected to a Biologic-EC-Lab SP150 potentiostat.

C. Sample cleaning and functionalization

The samples were cleaned and prepared for the chemical deposition of epoxysilane compounds. ITO slides were treated with acetone and dichloromethane for 10 min each, then rinsed with ultrapure water and finally immersed in 5:1 H_2O+H_2O_2 30 % for another 10 min. Then, all slides were rinsed with ultrapure water and dried with a gentle stream of nitrogen. For nanostructured ITO films silanization, a solution of GOPTS at 4 % (v/v) in toluene was prepared and slides were immersed in it for overnight reaction at room temperature and physiological pH. Figure 1 shows the schematic of the assembly of the epoxysilane layer onto the ITO electrodes, which consists in a hydrolysis (1), described as follows:

$$R' - Si(OR)_3 + 3H_2O \leftrightarrow R' - Si(OH)_3 + 3ROH, \quad (1)$$

followed by a condensation

$$R' - Si(OH)_3 + 2OH \leftrightarrow R' - SiO_2OH + 2H_2O. \quad (2)$$

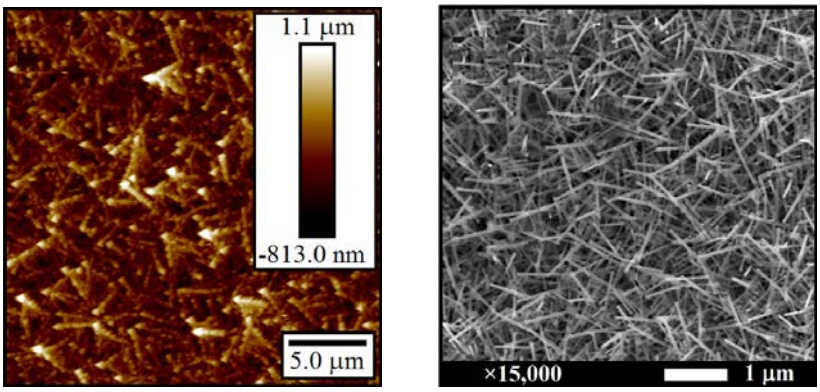

(a) (b)

FIG. 2: (a) AFM 25×25 μm^2 topographical scan and (b) SEM micrograph of as-deposited nanostructured ITO electrode.

III. RESULTS AND DISCUSSION

A. Atomic force microscopy and scanning electron microscopy

Surface morphology of the clean as-deposited nanostructured ITO electrodes is represented as an AFM topographical scan in Figure 2(a): nanostructuration is clearly appreciated in the image. The effective geometrical surface area can be calculated by triangularization algorithms from the AFM data. We found that nanostructured geometrical surface area increases 2.5 times with respect to projected area. There is direct correlation between the latter and the increase in electroactive surface area with respect to thin ITO films, which yields enhanced sensitivity in terms of electrochemical performance [30]. This AFM image shows that we are able to fabricate nanostructured ITO films by controlling the electron beam evaporation conditions, according to recent publications [33 and 34]. Figure 2(b) shows the nanostructured surface morphology observed by SEM as a complement to AFM measurements. Nanowire formation can be clearly appreciated.

B. X-ray photoelectron spectroscopy

Our XPS analysis is focused on the intensity and position of XPS binding energy peaks for O 1s and Si 2p bounds. Figures 3(a)–3(d) show general binding energy spectra for as-deposited ITO electrodes, GOPTS-coated as-deposited ITO electrodes, annealed ITO electrodes and GOPTS-coated annealed ITO electrodes. GOPTS-coated ITO electrodes spectra show an overall intensity baseline reduction with respect to non-functionalized ITO electrodes. The same effect can be observed between as-deposited ITO electrodes and annealed ITO electrodes. Besides, Si 2p bounds (red circles in Figures 3(b) and 3(d)) can be appreciated in GOPTS-functionalized ITO electrodes spectra. Insets in each graphic correspond to spectral regions where In 3d and Sn 3d peaks can be found. In all cases, Sn 3d bounds are splitted in two peaks centered at 495 eV and 485 eV for Sn $3d_5$ and Sn $3d_3$, respectively, while In 3d bounds are splitted into peaks at 451 eV for In $3d_3$ and 444 eV for In $3d_5$. The separation between two peaks of the same element stands for spin orbital splitting. Spin orbital splittings of a core level of a particular element in different compounds are nearly the same, and so it happens with peak area ratios. This is characteristic of ITO, as some references in the literature show [34 and 35].

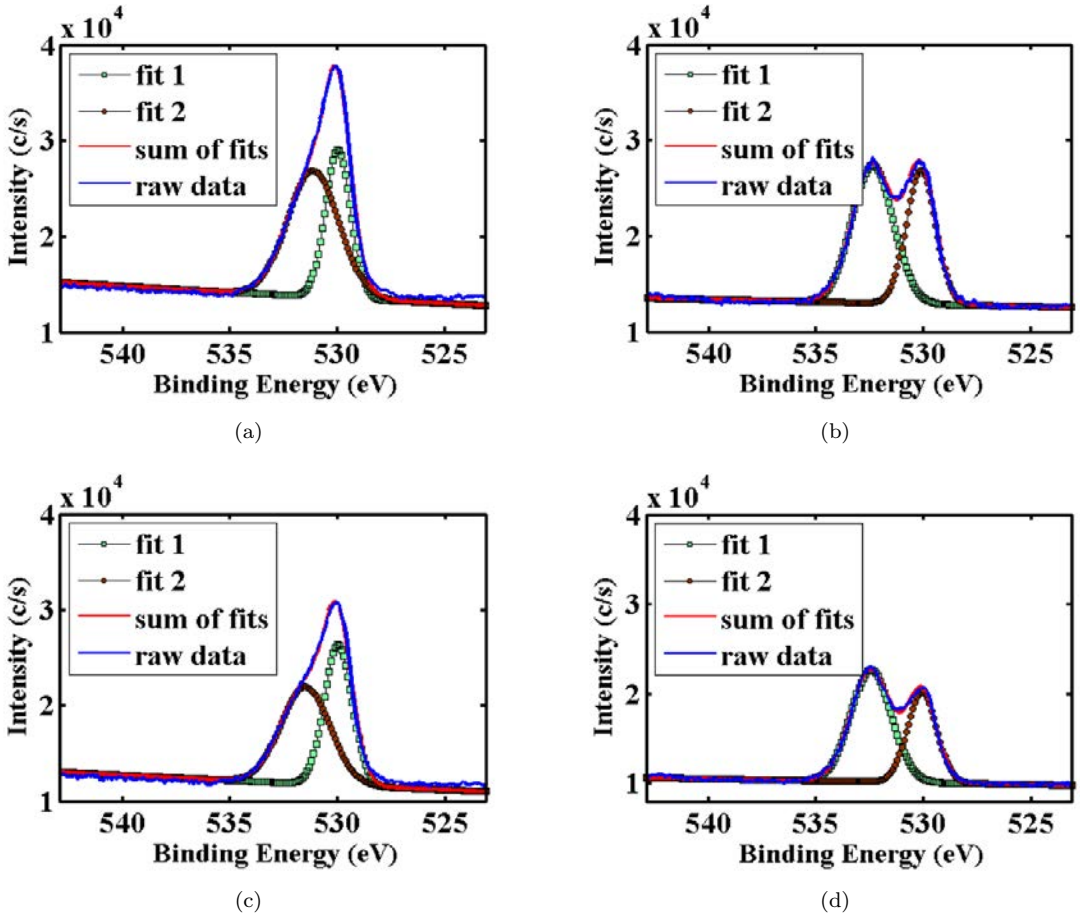

FIG. 3: XPS spectra of (a) as-deposited ITO, (b) GOPTS-functionalized as-deposited ITO, (c) annealed ITO and (d) GOPTS-functionalized annealed ITO. Each image contains zoom plots corresponding to energy regions of Sn 3d and In 3d peaks, respectively. Si peaks are found and circled in graphics (b) and (d).

The first sign of ITO functionalization appears when observing the O 1s bonds. Indeed, this is shown in Figure 4, where a peak splitting due to Si-O bond formation can be appreciated in Figures 4(b) and 4(d), which correspond to GOPTS-coated as-deposited and annealed ITO slides, respectively. GOPTS is attached to the ITO surface by covalent binding with -OH terminals in the ITO surface. Indeed, the Si core atom binds to surface oxygen and this produces a shift in the corresponding binding energy peak. Figures 4(a) and 4(c) correspond to non-functionalized ITO slides, thus showing no oxygen peak separation. Non-functionalized as-deposited and annealed ITO O 1s peak can be fitted by two Gaussians, centred at 530.0 eV and 531.1 eV (as-deposited films) and 530.0 eV and 531.5 eV (annealed films), and resulting in a single oxygen peak in the generalized spectra. This is not the case for GOPTS-coated ITO surfaces, which do show an O 1s peak separation. The corresponding fitting Gaussians are centred at 530.1 eV and 532.4 eV for both as-deposited and annealed films, respectively. This can be correlated with som studies that show the variations in XPS spectra for functionalized ITO. Brewer *et al.* [25] investigated the formation of thiolate and phosphonate adlayers on ITO. Similar to our results, they found that the fitting Gaussians for the O 1s peak were centred at 530.0 and 531.7 eV for bare ITO, and 530.8 and 532.2 eV for adlayer-coated ITO.

Figure 5 shows the amplified spectral region for Si 2p binding energies. Figures 5(a) and 5(c) correspond to

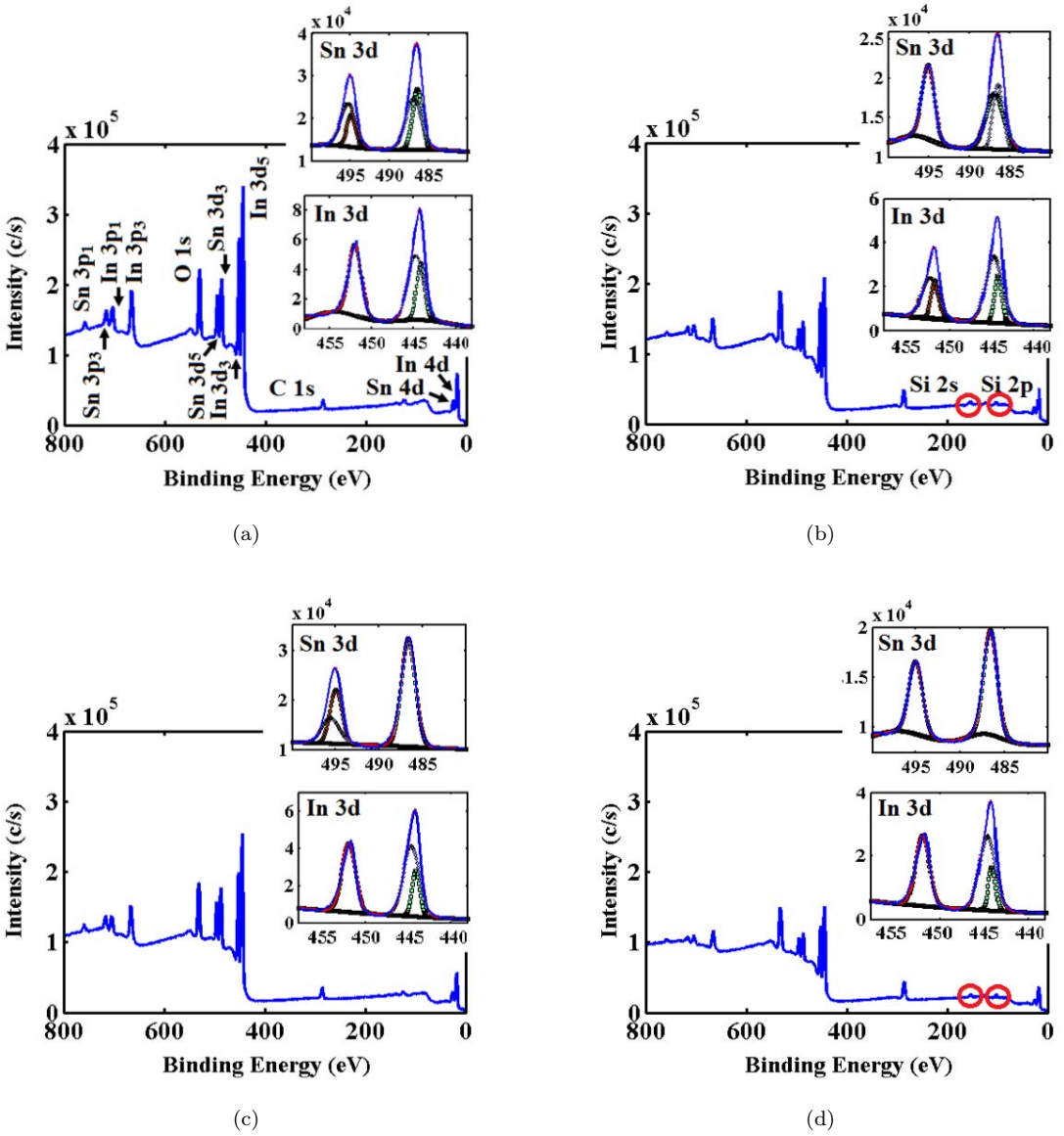

FIG. 4: Gaussian fit of XPS O 1s peak for (a) as-deposited ITO, (b) GOPTS-functionalized as-deposited ITO, (c) annealed ITO and (d) GOPTS-functionalized annealed ITO. GOPTS-functionalized substrates spectra clearly show a peak splitting due to Si-O bond formation.

bare as-deposited and annealed ITO, respectively, and they show weak features in the low energy range, which is probably a result of impurities due to ITO evaporation onto Si substrates. Figures 5(b) and 5(d) correspond to GOPTS-functionalized as-deposited and annealed ITO slides, respectively, and a five-time magnified peak at $\approx$ 102 eV with higher signal-to-noise ratio can be observed. This may be indicative of the presence of Si on the substrate surface, as a result of GOPTS functionalization. The Si 2p peak position is in accordance with the information provided by Materne *et al.* in their review on organosilane technology in coating applications [36]. Table I contains a numerical description of Gaussian curves used for peak fitting and depicted in Figures 4 and 5, where μ is the mean binding energy in which gaussian curves are centered, σ is the standard deviation of the mean, and α is a scaling factor, attending to the following equation: $y_{\text{fit}} = \alpha e^{-(x-\mu)^2/\sigma^2}$. In

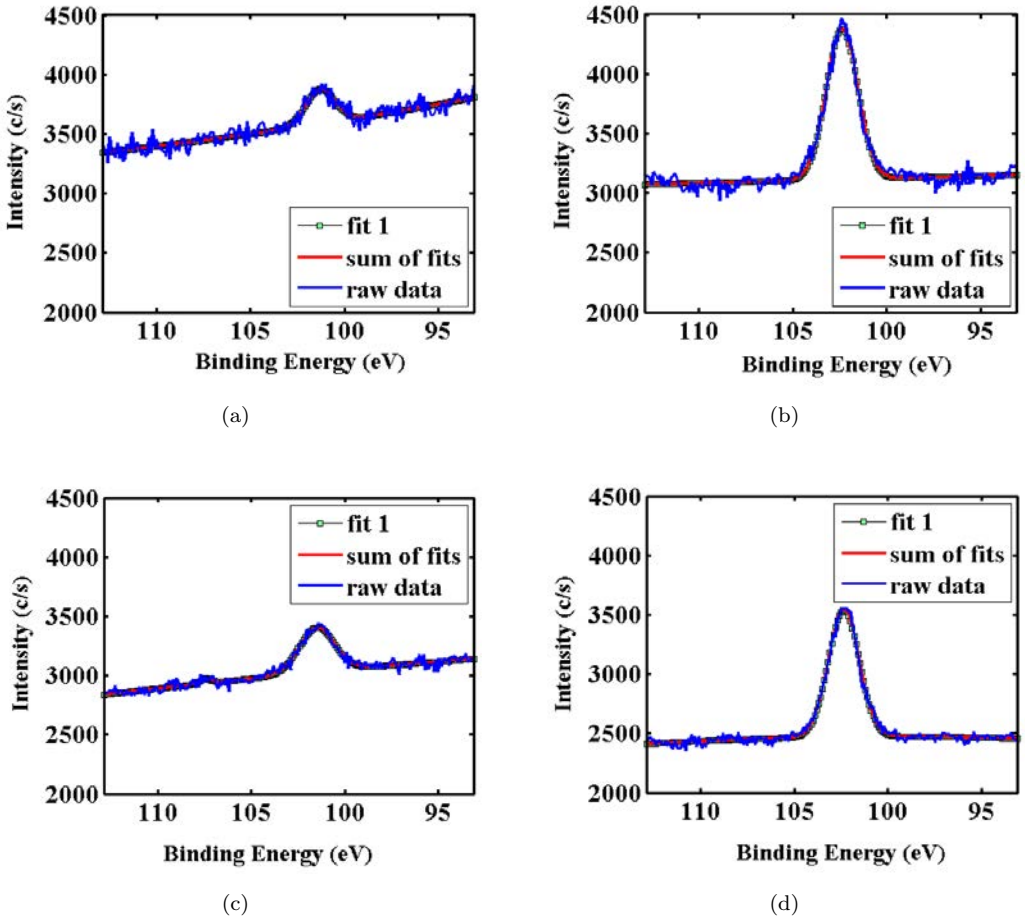

FIG. 5: XPS Si 2p peak for (a) as-deposited ITO, (b) GOPTS-functionalized as-deposited ITO, (c) annealed ITO and (d) GOPTS-functionalized annealed ITO.

the particular case of oxygen, the lowest peak corresponds to O 1s and the highest binding energy corresponds to SiO_2, as reported in the literature [37]. The Si-related peaks shown in Figures 5(b) and 5(d) correspond to SiO binding energy [37]. A small shift ($\approx$ 1 eV) can be observed for the Si peak. More notorious is the case of the O 1s peak splitting, which is increased by more than 1 eV in the case of GOPTS-functionalized slides.

TABLE I: Summary of gaussian fit characteristics for peaks shown in Figures 4 and 5. All data is expressed in eV.

	μ_{Si}	σ_{Si}	$\mu_O^{fit\ 1}$	$\sigma_O^{fit\ 1}$	$\mu_O^{fit\ 2}$	$\sigma_O^{fit\ 2}$
As-dep. ITO	101.3	1.09	530.0	0.84	531.1	1.70
Func. As-dep. ITO	102.4	1.19	530.1	0.97	532.4	1.35
Ann. ITO	101.5	1.33	530.0	0.92	531.5	1.61
Func. Ann. ITO	102.4	1.16	530.1	0.96	532.4	1.33

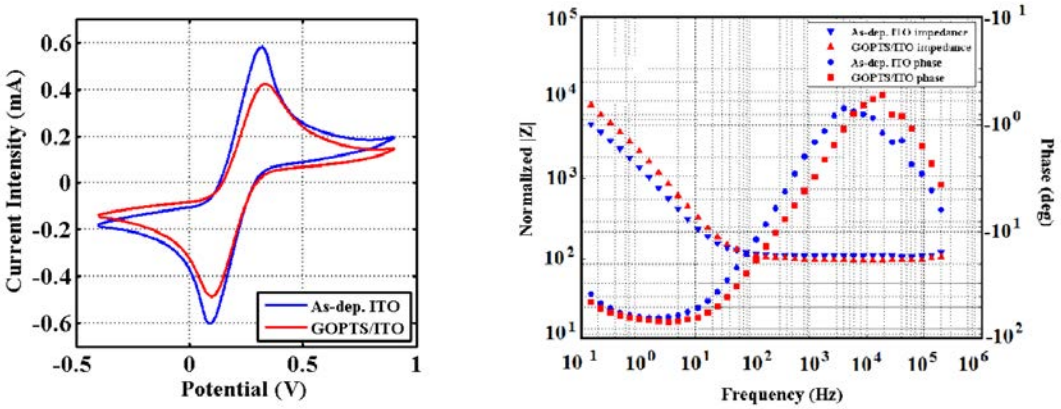

(a) (b)

FIG. 6: Electrochemical measurements to prove the presence of GOPTS on the ITO surface. (a) Cyclic voltammetry before (blue line) and after (red line) GOPTS immobilization on the ITO surface. Three repetitive potential cycles were applied from −0.4 V to 0.9 V at a scan rate of 50 mV s^{-1}. (b) Bode impedance plot from 200 kHz to 100 mHz for as-deposited ITO (blue line) and after GOPTS immobilization (red line), demonstrating the presence of functionalizing molecule on the working electrode surface.

Table II summarizes the atomic concentrations in percentage of different elements on the differently treated surfaces. This analysis was done taking into account the background noise level and atomic characteristics of the elements under analysis. Quantitative analysis of XPS spectra leads to the determination of the atomic concentration of the ith element by knowing the intensity of its peak, $I_i = N_i\sigma_i\lambda_i K$, where N_i is the average atomic concentration of element i on the surface under analysis, σ_i is the photoelectron cross-section for element i as expressed by peak p, λ_i stands for the inelastic mean free path of a photoelectron from element i as expressed by peak p and K combines all other factors related to quantitative detection of a signal. Clearly, there is a correlation between the Si atomic concentrations and the intensity of the corresponding binding energy peaks, which is coherent with whether the substrates were GOPTS-coated or not.

C. Cyclic voltammetry and electrochemical impedance spectroscopy

Electrochemical measurements were performed on bare and functionalized as-deposited nanostructured ITO films in order to test the presence of epoxysilane compounds on the sensor surface at a macroscopic level. Figure 6(a) shows CV measurements on bare (blue line) and GOPTS-functionalized (red line) ITO electrodes.

TABLE II: Atomic concentrations expressed in %.

	O 1s	**In 3d**	**Sn 3d**	**Si 2p**
As-dep. nano. ITO	50.0	38.7	11.3	0.0
As-dep. thin. ITO	57.9	27.4	7.6	7.1
Ann. nano. ITO	51.5	35.0	12.5	1.0
Ann. thin. ITO	60.9	25.7	7.6	5.8

The experiment was carried out in a 5 mM $Fe(CN)_6^{3-}/Fe(CN)_6^{4-}$ solution in 0.1 M KCl buffer. Potentials were scanned at 50 mV s^{-1} from −0.4 V to 0.9 V. Oxidation peaks appear around 0.3 V, which is in accordance with published information [38 and 39]. GOPTS-functionalized ITO presents lower intensity current than non-functionalized ITO electrodes, which indicates that the organic layer of epoxysilane compounds acts as an insulator between the $Fe(CN)_6^{3-}/Fe(CN)_6^{4-}$ medium and the conducting ITO working electrode. Figure 6(b) shows the impedance response of the $Fe(CN)_6^{3-}/Fe(CN)_6^{4-}$ redox couple probe on the bare (blue lines) and the GOPTS-functionalized (red lines) ITO electrodes in a Bode impedance plot representation. Frequency was varied from 200 kHz to 100 mHz, and the excitation signal consisted of a 10 mV amplitude sine waveform centred at 200 mV DC. The Bode impedance plot shows the normalized absolute impedance and phase response as a function of frequency in a linear-logarithmic scale representation. No significant difference can be observed in the absolute impedance values for frequencies above 10^2 Hz. This could indicate that the resistance of the solution was not significantly affected by the immobilization of the epoxysilane layer on the ITO electrodes. On the contrary, there is a difference in the absolute impedance values for bare and functionalized electrodes at frequencies below 10^2 Hz, indicating a change in the double-layer capacitance and also in the polarization resistance values as a result of the chemical surface modification, supporting the hypothesis that the epoxysilane layer behaves as a diffusion barrier for ions in the electrolyte [18 and 26]. An increase in electron transfer resistance can be observed in the low-frequency range for organosilane-functionalized substrates with respect to bare substrates.

Future work will involve the optimization of annealing conditions (time of annealing and temperature) for a better adhesion of organosilanes on the electrode surface. Besides, an in-depth study of ITO substrates as electrochemical transductors will be done, analysing their behaviour under different electrochemical conditions.

IV. CONCLUSIONS

In summary, the current study presents an analysis on the viability of developing nanostructured ITO electrodes for biosensing applications. The AFM image shows very densely distributed ITO nanostructures grown on Si substrates during electron beam evaporation at high temperatures. Nanostructures have higher surface-to-volume ratio and thus higher geometrical and electroactive surface area than thin films, permitting the flow of elevated currents and increasing the sensitivity of such working electrodes as electrochemical sensors. As-deposited and annealed nanostructured ITO electrodes were analysed by XPS at the microscopic level, before and after organosilane-functionalization. XPS allowed qualitative and semi-quantitative information from the films, indicating that the level of attachment of silanes may be slightly higher on as-deposited ITO electrodes than on annealed ITO electrodes. This could be ascribed to a better adhesion of GOPTS molecules on disorganized atomic distributions (as-deposited ITO films) rather than on crystalline organized annealed ITO substrates. Finally, the macroscopic electrochemical behaviour of both bare and functionalized as-deposited nanostructured ITO electrodes was analysed by CV and EIS. These techniques also permitted semi-quantitative analysis of the effect of the organic epoxysilane layer on the electron transfer between redox species in solution and conducting nanostructured ITO substrates. A slight increase in polarization resistance can be observed in organosilane-functionalized ITO electrodes, which accounts for the behaviour of the organic layer as an electronic barrier.

The obtained results may indicate that a basic and systematic functionalization of nanostructured ITO is possible, which would open the door to a wide scope of possible applications in fields such as biomedicine and environmental sciences.

ACKNOWLEDGMENTS

This project was supported by the 7th Frame Program European project "Real-time monitoring of SEA contaminants by an autonomous lab-on-a-CHIP biosensor (*SEA-on-a-CHIP*)", grant no. 614168. We thank the Universitat de Barcelona for support, especially the people/teams in charge of the clean room and nanotechnology platform facilities.

REFERENCES

[1] Arthur Edward Dixon and James D Leslie. *Solar Energy Conversion: An Introductory Course*. Elsevier, 2013.

[2] Shabbir A Bashar. Study of indium tin oxide (ito) for novel optoelectronic devices. *UMIST, Manchester*, pages 106–109, 1998.

[3] AH Khalid and AA Rezazadeh. Fabrication and characterisation of transparent-gate field effect transistors using indium tin oxide. *IEE Proceedings-Optoelectronics*, 143(1):7–11, 1996.

[4] V Sivaji Reddy, K Das, A Dhar, and SK Ray. The effect of substrate temperature on the properties of ito thin films for oled applications. *Semiconductor science and technology*, 21(12):1747, 2006.

[5] Shui-Yang Lien. Characterization and optimization of ito thin films for application in heterojunction silicon solar cells. *Thin Solid Films*, 518(21):S10–S13, 2010.

[6] Sung Kyu Park, Jeong In Han, Won Keun Kim, and Min Gi Kwak. Deposition of indium–tin-oxide films on polymer substrates for application in plastic-based flat panel displays. *Thin Solid Films*, 397(1):49–55, 2001.

[7] Yu Yang, Qinglan Huang, Andrew W Metz, Jun Ni, Shu Jin, Tobin J Marks, Mark E Madsen, Antonio DiVenere, and S-T Ho. High-performance organic light-emitting diodes using ito anodes grown on plastic by room-temperature ion-assisted deposition. *Advanced Materials*, 16(4):321–324, 2004.

[8] Joseph Wang. Nanomaterial-based electrochemical biosensors. *Analyst*, 130(4):421–426, 2005.

[9] Nathaniel L Rosi and Chad A Mirkin. Nanostructures in biodiagnostics. *Chemical reviews*, 105(4):1547–1562, 2005.

[10] Chang Kyoung Choi, Kenneth D Kihm, and Anthony E English. Optoelectric biosensor using indium-tin-oxide electrodes. *Optics letters*, 32(11):1405–1407, 2007.

[11] Chang K Choi, Chuck H Margraves, Seung I Jun, Anthony E English, Philip D Rack, and Kenneth D Kihm. Opto-electric cellular biosensor using optically transparent indium tin oxide (ito) electrodes. *Sensors*, 8(5):3257–3270, 2008.

[12] Zarini Muhammad-Tahir. *Indium Tin Oxide-polyaniline Biosensor: Fabrication and Performance Analysis*. ProQuest, 2007.

[13] Mei-Sheng Wu, Da-Jing Yuan, Jing-Juan Xu, and Hong-Yuan Chen. Sensitive electrochemiluminescence biosensor based on au-ito hybrid bipolar electrode amplification system for cell surface protein detection. *Analytical chemistry*, 85(24):11960–11965, 2013.

[14] Greg T Hermanson. *Bioconjugate techniques*. Academic press, 2013.

[15] Gerald L Witucki. A silane primer: chemistry and applications of alkoxy silanes. *Journal of coatings technology*, 65:57–57, 1993.

[16] Nesrine Aissaoui, Latifa Bergaoui, Jessem Landoulsi, Jean-François Lambert, and Souhir Boujday. Silane layers on silicon surfaces: mechanism of interaction, stability, and influence on protein adsorption. *Langmuir*, 28(1):656–665, 2011.

[17] Li Wang and Erkang Wang. A novel hydrogen peroxide sensor based on horseradish peroxidase immobilized on colloidal au modified ito electrode. *Electrochemistry Communications*, 6(2):225–229, 2004.

[18] Liju Yang and Yanbin Li. Afm and impedance spectroscopy characterization of the immobilization of antibodies on indium–tin oxide electrode through self-assembled monolayer of epoxysilane and their capture of escherichia coli o157: H7. *Biosensors and Bioelectronics*, 20(7):1407–1416, 2005.

[19] Eric L Hanson, Jing Guo, Norbert Koch, Jeffrey Schwartz, and Steven L Bernasek. Advanced surface modification of indium tin oxide for improved charge injection in organic devices. *Journal of the American Chemical Society*, 127(28):10058–10062, 2005.

[20] Ross A Hatton, Stephen R Day, Michael A Chesters, and Martin R Willis. Organic electroluminescent devices: enhanced carrier injection using an organosilane self assembled monolayer (sam) derivatized ito electrode. *Thin Solid Films*, 394(1):291–296, 2001.

[21] D Cossement, F Plumier, J Delhalle, L Hevesi, and Z Mekhalif. Electrochemical deposition of polypyrrole films on organosilane-modified ito substrates. *Synthetic Metals*, 138(3):529–536, 2003.

[22] Manju Gerard, Asha Chaubey, and BD Malhotra. Application of conducting polymers to biosensors. *Biosensors and Bioelectronics*, 17(5):345–359, 2002.

[23] Jiri Janata and Mira Josowicz. Conducting polymers in electronic chemical sensors. *Nature materials*, 2(1):19–24, 2003.

[24] Basudam Adhikari and Sarmishtha Majumdar. Polymers in sensor applications. *Progress in polymer science*, 29(7):699–766, 2004.

[25] Scott H Brewer, Derek A Brown, and Stefan Franzen. Formation of thiolate and phosphonate adlayers on indium-tin oxide: Optical and electronic characterization. *Langmuir*, 18(18):6857–6865, 2002.

[26] Heiko Hillebrandt and Motomu Tanaka. Electrochemical characterization of self-assembled alkylsiloxane monolayers on indium-tin oxide (ito) semiconductor electrodes. *The Journal of Physical Chemistry B*, 105(19):4270–4276, 2001.

[27] Chuanmin Ruan, Liju Yang, and Yanbin Li. Immunobiosensor chips for detection of escherichia c oli o157: H7 using electrochemical impedance spectroscopy. *Analytical Chemistry*, 74(18):4814–4820, 2002.

[28] Oliver M-R Chyan and Krishnan Rajeshwar. Heterojunction photoelectrodes ii. electrochemistry at tin-doped indium oxide/aqueous electrolyte interfaces. *Journal of the Electrochemical Society*, 132(9):2109–2115, 1985.

[29] Stefan Gritsch, Peter Nollert, Fritz Jähnig, and Erich Sackmann. Impedance spectroscopy of porin and gramicidin pores reconstituted into supported lipid bilayers on indium-tin-oxide electrodes. *Langmuir*, 14(11):3118–3125, 1998.

[30] R Pruna, F Palacio, M López, J Pérez, M Mir, O Blázquez, S Hernández, and B Garrido. Electrochemical characterization of organosilane-functionalized nanostructured ito surfaces. *Applied Physics Letters*, 109(6):063109, 2016.

[31] Hamid Reza Fallah, Mohsen Ghasemi, and Ali Hassanzadeh. Influence of heat treatment on structural, electrical, impedance and optical properties of nanocrystalline ito films grown on glass at room temperature prepared by electron beam evaporation. *Physica E: Low-dimensional Systems and Nanostructures*, 39(1):69–74, 2007.

[32] Hamid Reza Fallah, Mohammad Javad Vahid, et al. Substrate temperature effect on transparent heat reflecting nanocrystalline ito films prepared by electron beam evaporation. *Renewable Energy*, 35(7):1527–1530, 2010.

[33] Neng Wan, Tao Wang, Hongcheng Sun, Guran Chen, Lei Geng, Xinhui Gan, Sihua Guo, Jun Xu, Ling Xu, and Kunji Chen. Indium tin oxide thin films for silicon-based electro-luminescence devices prepared by electron beam evaporation method. *Journal of Non-Crystalline Solids*, 356(18):911–916, 2010.

[34] R Rakesh Kumar, K Narasimha Rao, K Rajanna, and AR Phani. Low temperature and self catalytic growth of ultrafine ito nanowires by electron beam evaporation method and their optical and electrical properties. *Materials Research Bulletin*, 52:167–176, 2014.

[35] Mika Yamaguchi, Ari Ide-Ektessabi, Hiroshi Nomura, and Nobuto Yasui. Characteristics of indium tin oxide thin films prepared using electron beam evaporation. *Thin solid films*, 447:115–118, 2004.

[36] Thierry Materne, François de Buyl, and Gerald L Witucki. Organosilane technology in coating applications: Review and perspectives. *Dow Corning Corporation., AGP11933, Form No*, 2012.

[37] BV Crist. Be lookup table for signals from elements and common chemical species. *Handbook of Monochromatic XPS Spectra, The Elements of Native Oxides*, 1999.

[38] Anees A Ansari, Ajeet Kaushik, Pratima R Solanki, and B emsp14D Malhotra. Electrochemical cholesterol sensor based on tin oxide-chitosan nanobiocomposite film. *Electroanalysis*, 21(8):965–972, 2009.

[39] Chinnasamy Thiruppathiraja, Veerappan Saroja, Senthilkumar Kamatchiammal, Periyakaruppan Adaikkappan, and Muthukaruppan Alagar. Development of electrochemical based sandwich enzyme linked immunosensor for cryptosporidium parvum detection in drinking water. *Journal of Environmental Monitoring*, 13(10):2782–2787, 2011.

4.2 Detection of biomolecular species: design of the first biosensor

As previously introduced in this chapter, the derivatization approach was modified in *Article IV: Novel nanostructured indium tin oxide electrode for electrochemical immunosensors: Suitability for the detection of TNF-α*, as an attempt to enhance the effectiveness of this surface modification step and to facilitate further steps in an eventual immunoassay performed on the substrates. Thus, an electroaddressed reduction of diazonium salts as crosslinker molecules on the nanostructured ITO electrodes was conducted by cyclic voltammetry. Then, subsequent modification steps were performed towards the construction of an immunosensor for the detection of tumour necrosis factor α (TNF–α), a biomarker with an accused influence in several cardiovascular diseases and also in many cancer types. The main objectives of this article can be summarized as follows:

1. derivatization of nanostructured ITO substrates by electroaddressed (voltammetric) reduction of diazonium salts in a temperature and pH-controlled medium;
2. electrochemical characterization of diazonium-modified ITO substrates and comparison with bare ITO electrodes;
3. chemical and compositional characterization of diazonium-modified ITO substrates by common spectral techniques such as XPS and infrared (IR) spectroscopy;
4. construction of a whole sandwich-type immunoassay Ab–TNF–α/TNF–α/Ab–TNF–α–Rhodamine for the determination of the biosensor specificity to the target cytokine by detecting the fluorescence of Rhodamine labels by flourescence microscopy;
5. construction of a label-free immunosensor for the detection of TNF–α by electrochemical impedance spectroscopy (EIS) and
6. detection by EIS of several TNF–α concentrations in physiological medium and pseudo-quantification of equivalent circuit parameters.

The article has been reproduced from Electrochimica Acta; vol. 283; R. Pruna, A. Baraket, A. Bonhommé, N. Zine, A. Errachid and M. López,"Novel nanostructured indium tin oxide electrode for electrochemical immunosensors: Suitability for the detection of TNF-α", 1632-1639, 2018; with permission from Elsevier.

Novel nanostructured indium tin oxide electrode for electrochemical immunosensors: Suitability for the detection of TNF-α

Raquel Pruna,[1] Abdoullatif Baraket,[2] Anne Bonhommé,[2] Nadia Zine,[2] Abdelhamid Errachid,[2] and Manel López[1]

[1)] *Departament d'Enginyeries: Electrònica i Biomèdica, Universitat de Barcelona, Martí i Franquès 1, E-08028 Barcelona, Spain*

[2)] *Université de Lyon 1, Institut des Sciences Analytiques, UMR 5280, CNRS, 5 rue de la Doua, F-69100, Villeurbanne, France*

Electrochimica Acta, 283 (2018), 1632-1639
doi: 10.1016/j.electacta.2018.07.066

ABSTRACT

The need for new and innovative point of care (POC) systems providing a feasible alternative to costly and time consuming standard laboratory techniques is becoming more evident every day, particularly in the case of cardiovascular diseases. Coupling optical and electrochemical principles for highly specific and sensitive detection of biomarkers could boost the successful implementation of POC systems in biomedical environments. We suggest indium tin oxide (ITO) as a promising material for working electrodes in optoelectrochemical sensors, owing to the rare combination of high electrical conductivity and optical transparency it presents. Moreover, the nanostructured nature of the electrodes' surface is crucial for an eventual miniaturization of the POC system. In this work, we describe the construction and characterization of a nanostructured ITO electrode modified with aryl diazonium salt as transparent substrate for electrochemical immunosensors. The developed electrode was tested for the detection of tumour necrosis factor α (TNF–α), a cardiac biomarker playing an important role in the prevention of heart failure. Macro and microscopic evidences (gathered from electrochemical and spectral techniques) of covalent bonding and high surface coverage are provided. Specific interaction between antigen (TNF–α) and monoclonal antibody (Ab–TNF–α) was verified by fluorescence patterning, confirming the proper bio-recognition of the cytokine. As a proof-of-concept, results of electrochemical impedance spectroscopy (EIS) show stabilized semi-quantitative label-free detection of TNF–α at several concentrations (from 10 pg mL^{-1} to 100 pg mL^{-1}). These preliminary results demonstrate the feasibility of using transparent substrates for the detection of cytokines at low concentrations, and the consequent application in POC systems for the monitoring of cardiovascular diseases.

I. INTRODUCTION

Heart failure is a very fast growing cardiovascular disease, with around 1 million new patients being diagnosed (only in the US) per year with this illness [1 and 2]. Symptoms such as shortness of breath, leg swelling and

exercise intolerance manifest as a consequence of an insufficient pump action of the heart, which is thus unable to maintain an adequate blood flow [3–5]. Several device-based therapeutic implants, e.g. left ventricle assisted devices (LVADs), have been proposed as potential solutions to the lack of donor organs. Nevertheless, multiple organ failure syndrome (MOFS) is commonly triggered by LVAD implants and is one of the main causes of patient mortality after cardiac surgery [6]. Specific biomarkers are secreted as a consequence of this fatal acute rejection, causing inflammation in both cellular and biochemical stages.

Biomarkers related to cardiovascular diseases have been traditionally detected with well-established laboratory techniques such as immunoaffinity column assay, fluorimetric immunoassay and enzyme-linked immunosorbent assay (ELISA), amongst others [6–10]. These methods, although sophisticated and highly sensitive and selective, are still handicapped by some inexorable requirements: the two former techniques require trained personnel and are costly and time consuming, whilst ELISA needs large amounts of disposable material. Thus, the proper assistance of patients and hence their quality of life is compromised, for they may not be diagnosed in time. At this point, it becomes urgent the need for highly reliable alternatives based on easy-to-use devices that provide real-time information for point-of-care (POC) theranostics, i.e. rapid identification of the severity of the inflammatory state to facilitate early intervention [11 and 12]. However, POC systems for in situ follow-up of cardiovascular diseases are still not well-established, and new and innovative biosensor architectures will play a key role in this respect.

In this context, electrochemical biosensors provide a sensitive, label-free, rapid and portable solution based on the biochemical recognition of a biomarker of interest by biochemical interactions [13 and 14]. Besides, the low production costs make biosensors a real and affordable alternative to the aforementioned laboratory techniques. In the past years, biosensors have been used for the detection of Interleukin-6 (IL-6), IL-8, IL-10 and tumour necrosis factor α (TNF–α) at very low concentrations [15–20]. The latter is a particularly interesting biomarker due to its potential implication in a number of autoimmune diseases. TNF–α is found at very low concentrations in body fluids such as serum and saliva. Healthy humans present TNF–α concentrations below 10 pg mL^{-1} and 3 pg mL^{-1} in serum and saliva, respectively. On the contrary, TNF–α concentrations in patients with severe autoimmune diseases range between 10 and 300 pg mL^{-1} in serum and 30 pg mL^{-1} in saliva [21–24].

Traditionally, gold has been the standard material for the development of electrochemical biosensors due to the ease of its manipulation and functionalization [19, 20, 25–28]; Baraket *et al.* presented a multichannel biosensors platform based on gold working electrodes (WEs) for the detection of several heart failure biomarkers at low concentrations [29]. Others have focused their attention on nanomaterials-based TNF–α immunosensors; examples of this are gold nanoparticles, magnetic microbeads and carbon nanotubes, amongst others [30–32]. Nevertheless, due to the increased interest in new materials compatible with complementary metal-oxide-semiconductor (CMOS) processes and the silicon technology [33], researchers have also focused their attention on the semiconducting properties of silicon-based compounds (SiO_2, Si_3N_4), which were used in the past as transistor gates within field effect transistors (FETs) [34–36]. The necessary compromise between high capacitance of CMOS dielectrics and minimal gate oxide leakage led to investigations of new materials with increased dielectric constants, such as Al_2O_3, Ta_2O_5, TiO_2, ZrO_2 and HfO_2 [18, 37–42]. In particular, Lee *et al.* [18] reported a device based on HfO_2, achieving detection of IL-10 by electrochemical impedance spectroscopy (EIS) with a wide linear range and high sensitivity. Aydin and co-workers [43] covered indium tin oxide (ITO) thin films with a semi-conductive conjugated polymer in order to increase the electrode's surface-to-volume ratio and serve as a matrix for immobilization of TNF–α antibodies. They developed an impedimetric TNF–α

immunosensor with good analytical performance and high sensitivity, selectivity and reproducibility.

In the light of this trend, ITO has recently been used as substrate for optical and electrochemical biosensors. Indeed, ITO is one of the most used transparent conductive oxides (TCOs) in optoelectronics owing to its simultaneous good electrical conductivity and excellent optical transparency. Back in the field of biosensors, Choi *et al.* developed an optoelectronic ITO-based biosensor for simultaneous optical imaging and microimpedance analysis of time-dependent cellular attachment, spreading and proliferation [44 and 45]. Similarly to authors in [43], Muhammad-Tahir [46] used a conductive polymer to develop a ITO-polyaniline biosensor for identification of multiple targets. However, to avoid the introduction of polymers or other layers over the ITO electrodes, nanostructured ITO arose as a self-contained alternative for achieving high surface-to-volume ratio without the need for extra materials that could increase the cost, fabrication time and risk of contamination. It has already been shown that nanostructured ITO presents higher electrochemical surface area compared to thin ITO films, and also that it can be properly derivatized with organosilanes for further functionalization, resulting in a promising material for electrochemical bio and immunosensing applications [47–49].

In this work, we describe the fabrication process, characterization and functionalization of a novel biosensor based on a transparent nanostructured ITO electrode. The performance of the developed ITO-based biosensor was tested for TNF–α cytokine as a proof-of-concept. The nanostructured electrodes were fabricated by physical deposition and derivatized with diazonium salt by cyclic voltammetry (CV) electroaddressing. The surface was exhaustively characterized before and after functionalization by electrochemical techniques and also by X-ray and infrared spectroscopy, thus obtaining information on the nature of the covalent bonds and the extent of functionalization. We believe this may be of interest, since electroaddressed diazonium salt reduction on nanostructured ITO electrodes has been hardly reported in the literature [50]. Finally, antibody-antigen biorecognition was demonstrated by fluorescence imaging, and EIS was used for preliminary semi-quantitative evaluation of this novel nanostructured ITO-based biosensor, proving suitable for POC systems devoted to the monitoring of cardiovascular diseases.

II. EXPERIMENTAL DETAILS

A. Materials

1. Reagents

4-carboxymethyl aryl diazonium (CMA), sodium nitrite ($NaNO_2$), hydrochloric acid (HCl) 37 %, N-hydroxysuccinimide (NHS), N-(3-dimethylaminopropyl)-N'-ethyl-carbodiimide hydrochloride (EDC), potassium ferrocyanide (II) and potassium ferricyanide (III) ($K_3[Fe(CN)_6]/K_4[Fe(CN)_6]$), and phosphate buffered saline (PBS) were purchased from Sigma-Aldrich, France. All immunoreagents, i.e. TNF–α cytokines, Ab–TNF–α and Rhodamine-labelled Ab–TNF–α antibodies were purchased from R & D Systems, France.

2. Antibodies and cytokines preparation

Antibodies and cytokines were diluted in PBS buffer, aliquoted, and stored at -20 °C following the protocol of the supplier. TNF–α cytokines were aliquoted at five different concentrations: 1 pg mL^{-1}, 5 pg mL^{-1},

10 pg mL^{-1}, 15 pg mL^{-1} and 100 pg mL^{-1}, and stored at 4 °C. The Ab–TNF–α antibody solution was aliquoted at 2.5 μg mL^{-1} in PBS.

B. Instrumentation

1. X-ray photoelectron spectroscopy (XPS)

XPS measurements of bare and functionalized nanostructured ITO substrates were performed in a PHI 5500 Multitechnique System (Physical Electronics) with a monochromatic X-ray source (Al Kα line of 1486.6 eV energy and 350 W), placed perpendicular to the analyser axis and calibrated using the $3d_{5/2}$ line of Ag with a full width at half maximum (FWHM) of 0.8 eV. The analysed area was a circle of 0.8 mm in diameter, and the selected resolution for the spectra was 23.5 eV of pass energy and 0.1 eV $step^{-1}$. All measurements were made in ultra-high vacuum (UHV) chamber pressure between 5×10^{-9} Torr and 2×10^{-8} Torr. Multipak v8.2B software (Ulvac-phi, Inc., USA) was used for peaks identification and analysis.

2. Fourier transform infrared spectroscopy (FTIR)

Attenuated total reflectance infrared (ATR-IR) spectra were acquired on a Nexus 470 Thermo-nicolet Fourier transform infrared (FTIR) spectrometer (Thermoscientific) using Harrick's GATR^{TM}. The GATR^{TM} is a grazing angle ATR accessory with a fixed 60 ° incident angle and a hemispherical germanium crystal. All spectra were recorded with 256 scans at 4 cm^{-1} resolution with a mercury-cadmium-telluride (MCT) detector cooled by liquid nitrogen.

3. Cyclic voltammetry (CV) and electrochemical impedance spectroscopy (EIS)

Electrochemical measurements, i.e. CV and EIS, were performed with a multichannel potentiostat analyser (Biologic-EC-Lab VMP3). The ITO samples were placed in a three-electrode Teflon electrochemical cell (schematized in Figure 2(a)), and all the experiments were carried out at room temperature. An aqueous solution of 5 mM ferrocyanyde/ferricyanyde ($Fe(CN)_6^{3-}/Fe(CN)_6^{4-}$) in PBS was used for electrodes characterization (CV) and cytokine detection at several concentrations (EIS).

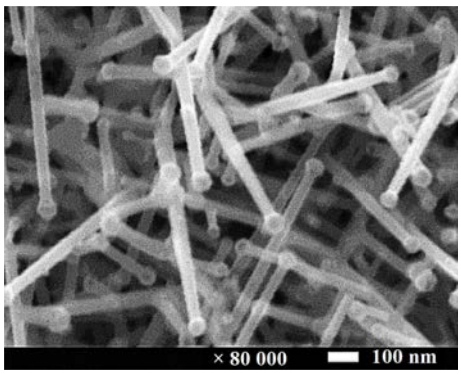

FIG. 1: Surface characterization of the nanostructured electrode by scanning electron microscopy.

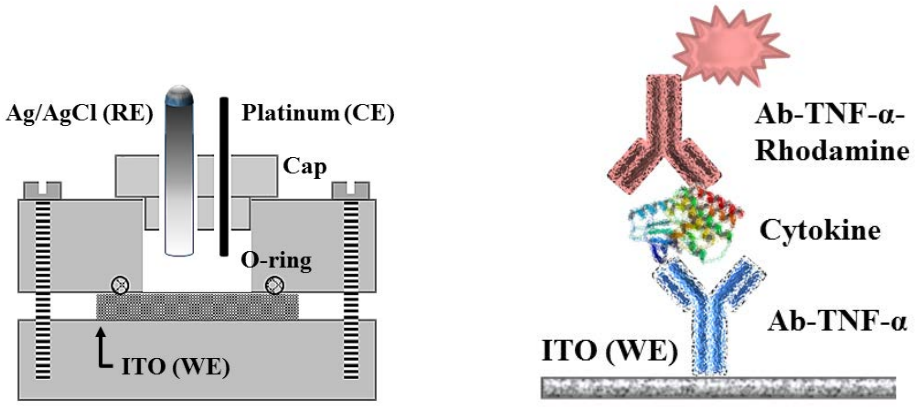

(a) (b)

FIG. 2: (a) Electrochemical Teflon cell with KCl saturated Ag/AgCl reference electrode (RE), platinum counter electrode (CE) and ITO working electrode (WE). The latter was sandwiched between the two parts of the Teflon cell with an O-ring to avoid leakage of electrolyte. (b) Schematic illustration of sandwich-type detection <Ab–TNF–α–cytokine–Ab–TNF–α–Rhodamine>.

4. Fluorescence microscopy

Fluorescence images were taken using a fluorescence microscope (Zeiss Axioplan 2 Imaging apparatus, equipped with 10× and 40× lenses and a monochrome camera). Fluorescence microscopy was used to observe ITO substrates, which were first excited with a 550 (±25) nm band-pass filter (green light), whilst fluorescence from the sample (red light) was observed with a 605 (±70) nm band-pass filter.

C. Procedures

1. ITO substrates

Electron beam evaporation was used to grow nanostructured ITO layers onto fused silica substrates. A Pfeiffer Vacuum Classic 500 with a Ferrotec Genius electron beam controller and a Ferrotec Carrera high-voltage supply was employed. Commercial ITO targets with a composition of 90/10 (w/w) In_2O_3/SnO_2 were used as raw material during evaporation. Substrate temperature was set at 500 °C to promote vapour liquid solid (VLS) self nanostructuration of ITO, and the deposition rate was set at 0.1 nm s^{-1} during a total growth time of 33 min. After fabrication, the electrodes were submitted to rapid thermal annealing (RTA) in an oven at 600 °C under nitrogen atmosphere during 1 h. Figure 1 shows a topographical scanning electron microscopy (SEM) image of the morphology of the nanowires. Branched nanowires presenting lengths around 700 nm and with a catalyst particle of diameter around 50 nm at their ends (tip), the latter accounting for self-VLS growth, are densely present at the electrodes. Self-VLS growth mechanism has been exhaustively detailed elsewhere [51–53].

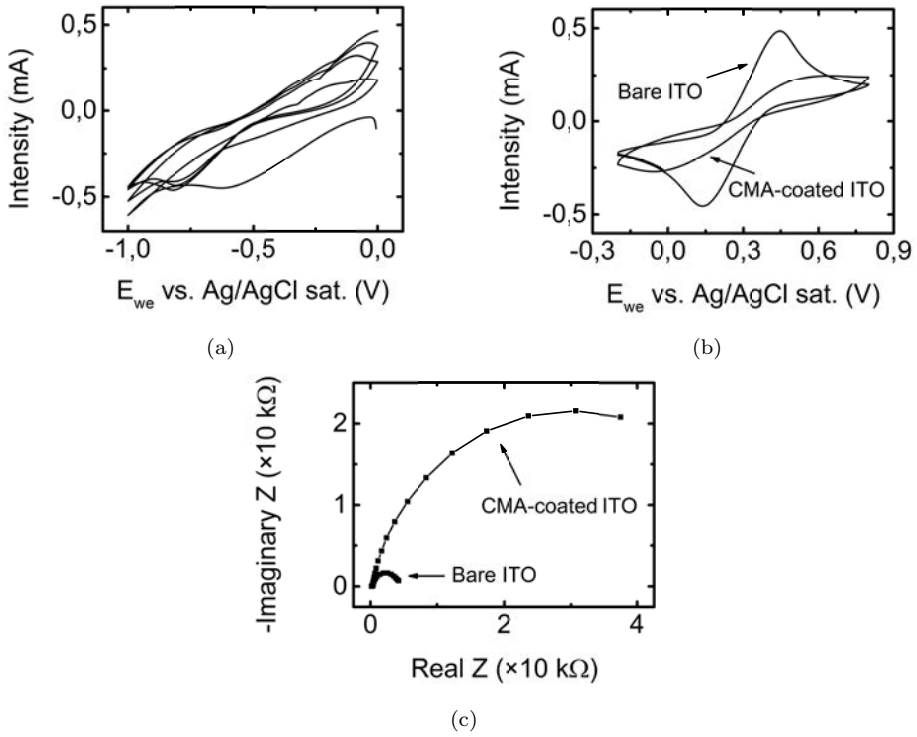

FIG. 3: (a) Cyclic voltammetry showing CMA deposition onto ITO substrates. Four repetitive scans were performed at 100 mV s^{-1} from 0 V to −1 V vs. saturated Ag/AgCl RE. (b) Difference in voltammogram shapes between bare ITO and CMA-coated ITO. These were performed at a scan rate of 50 mV s^{-1} from −0.2 V to 0.8 V vs. saturated Ag/AgCl RE. (b) Electrochemical impedance spectroscopy showing increase in polarization resistance for CMA-coated surfaces compared to bare ITO.

2. Cleaning and derivatization of ITO surfaces

Prior to CMA electroaddressing, the ITO surfaces were cleaned with ethanol and acetone for 10 min and dried under a gentle stream of nitrogen, followed by UV/ozone exposure for 20 min in order to remove all organic contaminants. CMA (5 mM) was diazotated in an aqueous solution of HCl (20 mM) and $NaNO_2$ (20 mM) for 10 min at 4 °C. Then, four repetitive CV cycles between 0 V and −1 V were applied to the ITO electrodes, with a scan rate of 100 mV s^{-1}.

3. Immobilization of antibodies and fluorescence microscopy assssment

Ab–TNF–α monoclonal antibodies were covalently attached to the CMA-coated surfaces by EDC/NHS (0.1 M) crosslinking both at 0.1 M following a protocol widely reported for conductive electrodes [54].

Fluorescence microscopy was used to qualitatively assess immobilization of antibodies on ITO substrates and to determine non-specific adsorption of cytokine on the nanostructured electrode surface. Therefore, antibodies (Ab–TNF–α) were immobilized through EDC/NHS as previously stated. Then, the Ab–TNF–α modified immunosensor was incubated at 4 °C for 30 min in a solution of TNF–α cytokines at a concentration of 2.5 μg mL^{-1} in PBS. The antibodies were immobilized only inside the area limited within the O-ring using

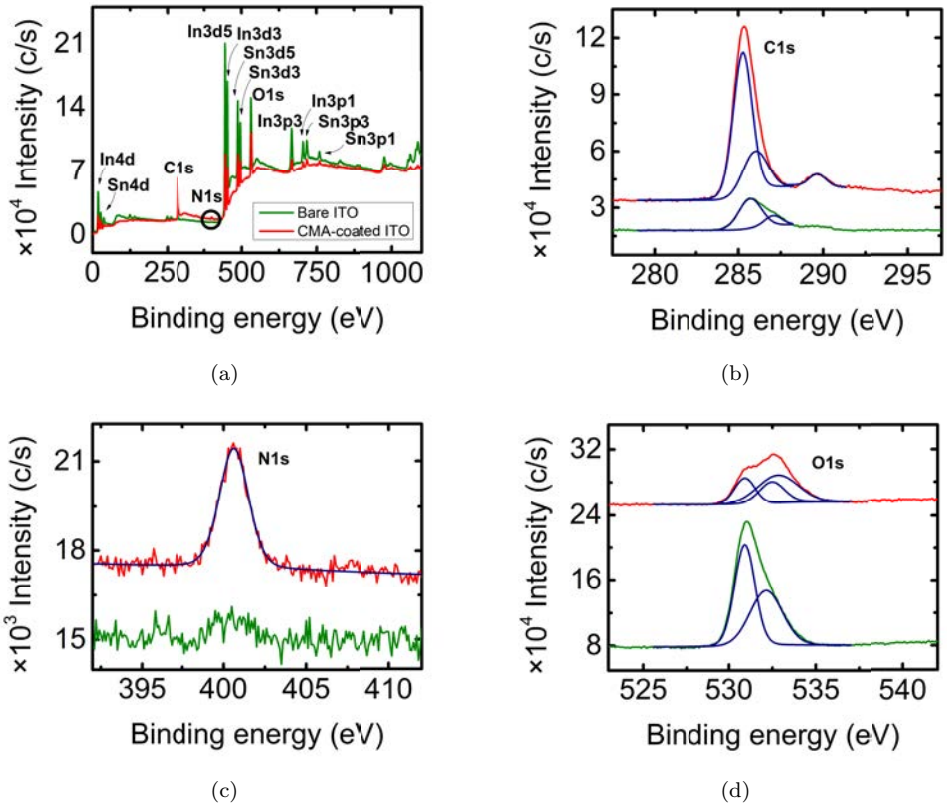

FIG. 4: XPS analysis of ITO electrodes before (green) and after (red) CMA-coating. (a) General spectra from 0 to 1 keV, and details on (b) C 1s, (c) N 1s and (d) O 1s peaks.

the aforementioned electrochemical Teflon cell (Figure 2(a)). Then the biosensor was rinsed with PBS and incubated again in Rhodamine-labelled Ab–TNF–α for 30 min to form a sandwich <Ab–TNF–α–cytokines–Ab–TNF–α–Rhodamine> (please see schematic in Figure 2(b)). Afterwards, the ITO substrate was dried and observed by fluorescence light as described in Section II B 4.

III. RESULTS AND DISCUSSION

A. Derivatization of ITO

TABLE I: Summary of Gauss-Lorentz fits characteristics for peaks shown in Figures. 4(b)–4(d). All values are expressed in eV.

	$\mu_C^{fit\ 1}$	$\sigma_C^{fit\ 1}$	$\mu_C^{fit\ 2}$	$\sigma_C^{fit\ 2}$	$\mu_C^{fit\ 3}$	$\sigma_C^{fit\ 3}$	μ_N	σ_N	$\mu_O^{fit\ 1}$	$\sigma_O^{fit\ 1}$	$\mu_O^{fit\ 2}$	$\sigma_O^{fit\ 2}$	$\mu_O^{fit\ 3}$	$\sigma_O^{fit\ 3}$
Before CMA coating	285.7	1.6	287.1	1.2	-	-	-	-	530.9	1.4	532.1	1.2	-	-
After CMA coating	285.2	1.3	286.0	1.7	289.7	1.1	400.6	2.1	530.9	1.4	532.5	1.7	532.8	2.7

Derivatization of nanostructured ITO was done by electrochemical reduction of diazonium salts (CMA) on its surface, taking advantage of the good electrical conductivity of this transparent conductive oxide. This is a

TABLE II: Quantitative XPS results for the analyzed samples. Atomic concentration expressed in %.

	O 1s	In $3d_5$	Sn $3d_5$	C 1s	N 1s
Before CMA coating	45.1	28.8	11.2	14.4	0.5
After CMA coating	27.8	8.6	4.9	57.1	1.6

very common technique for coating electroaddressing on gold microelectrodes that was in the past reported on commercial thin ITO films [50] but not yet on nanostructured ITO to our knowledge. The electroaddressing of the coating was done by CV in four repetitive cycles from 0 V to −1 V at a scan rate of 100 mV s^{-1}. The corresponding CV is shown in Figure 3(a), where a first broad and irreversible cathodic peak around −0.6 V accounts for diazotised CMA covalent linkage to the ITO surface by diazonium salt reduction. Successive cycles show reduced cathodic peak as a consequence of an already large passivated area of the electrode. This appears macroscopically confirmed in Figures 3(b) and 3(c) by CV and EIS, respectively. The voltammogram in Figure 3(b) shows how $Fe(CN)_6^{-3}/^{-4}$ redox peaks on bare ITO electrodes were weakened considerably after CMA surface coating. To endorse these results, EIS analysis shown in Figure 3(c) reveals a wider semicircle in the case of the ITO electrode after CMA coating. This can be interpreted as an increase in polarization resistance due to the insulating coating between the conductive electrode and the electrolyte, which hinders the electron exchange between these two media. In general terms, the shape of the voltammogram for CMA-coated ITO electrodes is similar to those reported for gold microelectrodes [19, 20, and 55].

As this is the first time that, to our knowledge, nanostructured ITO is derivatized with CMA by electroaddressed diazonium salt reduction, it is worth showing some microscopic evidences on how this coating modifies the surface of the electrode. Results of XPS analysis are shown in Figure 4. General binding energy spectra from 0 to 1 keV can be observed in Figure 4(a), whereas Figures 4(b)–4(d) show amplified spectral regions for C 1s, N 1s and O 1s, respectively. Direct evidence of organic coating onto the ITO electrode comes from the substantial increase in C 1s (Figure 4(b)) peak and the occurrence of the N 1s peak (Figure 4(c)). In the former case, the C 1s core level spectrum can be fitted to three peaks with binding energies 285.2, 286.0 and 289.7 eV, which are attributed to hybrid orbitals Csp^2/Csp^3, -C-O and -COOH, respectively [56–58]. This last peak is particularly important, as it does not appear in the XPS spectrum of bare ITO, and it corresponds to the functional group by means of which the antibodies are linked to the electrode surface. Figure 4(c) shows a small peak corresponding to N 1s (notice that the scale is an order of magnitude smaller than the rest in Figure 4), which could be attributed to few molecules adsorbed on the nanostructured surface after CMA electroaddressing. Finally, the O 1s core level spectrum can be fitted to two peaks that are separated in the CMA-coated electrode. This is a common behaviour, as has been reported previously [47 and 59]. Table I contains numerical data of Gaussian curves used for peak fitting and which are also depicted in Figures 4(b)–4(d). In the table, μ is the mean binding energy where the peaks are centred, and σ is the standard deviation of the mean.

Table II summarizes the atomic concentrations in % of the different elements found on both bare and CMA-coated ITO surfaces. Clearly, there is a correlation between the evolution of the concentration of the species under study and the superficial state of the electrode. Bare ITO electrodes present similar atomic proportion of O, In and Sn to previously reported results [47]. When the CMA coating is electroaddressed to the electrode surface, the species of the new molecules screen superficial indium and tin oxides, whose atomic concentrations become considerably reduced. Instead, an increase of more than 40 % in the superficial atomic concentration of

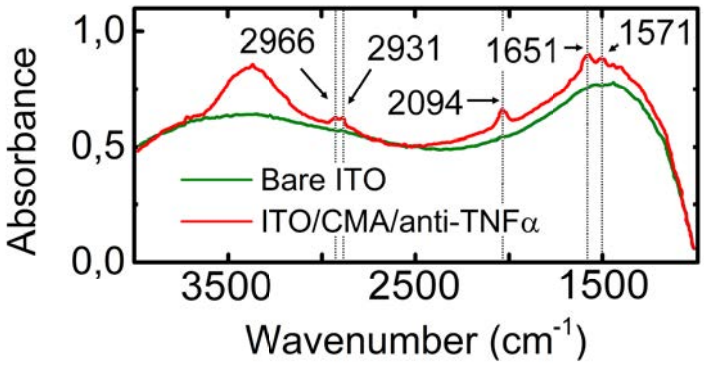

FIG. 5: Normalized FTIR spectra of ITO electrodes before (green) and after (red) functionalization.

carbon can be observed, due to the organic nature of CMA molecules, and also the occurrence of the nitrogen peak. This can also be deduced by careful observation of the spectra in Figure 4(a).

Further microscopic evidences on ITO functionalization were searched after antibody binding to CMA-modified electrodes. In this case, FTIR was used to characterize the samples. Figure 5 shows the normalized FTIR spectra for bare ITO and for electrodes derivatized with CMA and functionalized with Ab–TNF–α. While the FTIR spectrum for bare electrodes is quite uniform, several absorption peaks appear in the case of modified electrodes. Indeed, some alkane-compatible bands appear at 2966 cm^{-1} (νCH_3), 2931 cm^{-1} (νCH_2) and 1651 and 1571 cm^{-1} (both corresponding to secondary amides). A very representative band is the one at 2094 cm^{-1}, which can be attributed to alkyls and amides present in diazonium salts. Indeed, the IR band related to diazonium salts usually appears between 2130 and 2300 cm^{-1}, yet it can be reduced in 40 cm^{-1} in the presence of aromatic compounds (this corresponds to the peak in 2094 cm^{-1}), which is the case of CMA. Similarly, the band observed at 1512 cm^{-1} is also compatible with aromatic compounds.

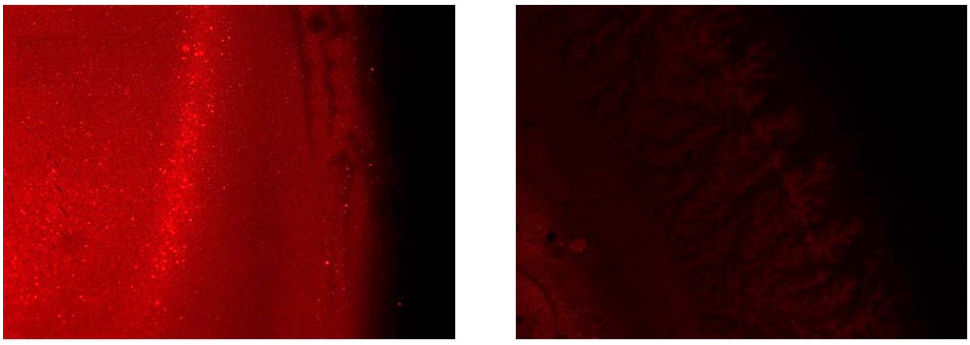

(a) (b)

FIG. 6: (a) Rhodamine fluorescence observed after forming the sandwich <Ab–TNF–α–cytokine–Ab–TNF–α–Rhodamine>. (b) No fluorescence was observed in the negative test <Ab–TNF–α–PBS–Ab–TNF–α–Rhodamine>.

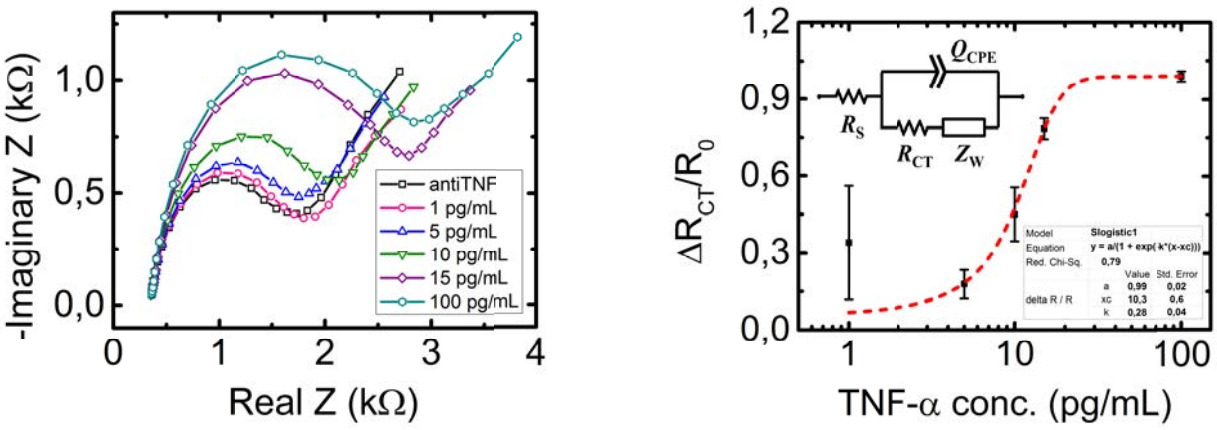

(a) (b)

FIG. 7: Detection of TNF–α by EIS. (a) Nyquist plots for different TNF–α concentrations in PBS in a frequency range of 100 kHz to 100 mHz. A polarization potential of 0.3 V plus a small sine potential of amplitude 80 mV were used. (b) Normalized curve showing the relative variation of charge transfer resistance with increasing cytokine concentrations, taking bare Ab–TNF–α functionalized electrode as a reference. Inset figure shows the equivalent electrical circuit employed for results fitting, and inset table contains the adjusted parameters for the logistic curve.

B. Fluorescence microscopy

The sandwich <Ab–TNF–α–cytokine–Ab–TNF–α–Rhodamine> was formed onto the ITO substrate as previously described in Section II C 3. Here, the fluorescence of Rhodamine [60 and 61] will confirm the good interaction between TNF–α cytokines and immobilized Ab–TNF–α (please see Figure 6). Indeed, the red surface in Figure 6(a) corresponds to the area inside the rubber ring, and it contains the fluorescent antibodies. The latter were not only adsorbed onto ITO surface, but they were also placed well oriented outwards from the surface, forming the sandwich <Ab–TNF–α–cytokine–Ab–TNF–α–Rhodamine>. This was confirmed by a negative test after the same fluorescence experimental process, but without TNF–α cytokines. Thus, Ab–TNF–α antibodies were immobilized onto ITO substrate through EDC/NHS as previously described. Then, the Ab–TNF–α modified immunosensor was rinsed with PBS and directly incubated in Rhodamine-labelled Ab–TNF–α for 30 min. Afterwards, the biosensor was abundantly rinsed with PBS and dried. Results in Figure 6(b) show no florescence, confirming that, indeed, nanostructured ITO is an adequate substrate for cytokine detection by specific interaction with antibodies, and non-specific adsorption hardly takes place.

C. Electrochemical impedance spectroscopy

Electrochemical impedance spectroscopy is an effective technique for studying interfacial properties of the modified surfaces of working electrodes. Previously in this work, EIS proved useful to have an idea on the degree of surface passivation of CMA-modified electrodes when compared to bare ITO. Now, EIS was used to monitor the detection of TNF–α cytokines at several concentrations by Nyquist plot analysis. As detailed in Section II B 3, a solution of the $Fe(CN)_6^{3-}/Fe(CN)_6^{4-}$ redox couple in PBS (pH 7.4) was employed for characterization. A modulation potential difference of 80 mV over a fixed WE potential of 0.3 V vs. Ag/AgCl sat.

was set, and the frequency was varied from 100 kHz to 100 mHz.

Figure 7(a) shows the Nyquist impedance plot for TNF–α detection. The inner semicircle corresponds to bare Ab–TNF–α immobilized onto CMA-modified ITO electrodes, this is without TNF–α detection. Subsequent semicircles correspond to increasing concentrations of TNF–α, after 30 min incubation at 4 °C in a solution of TNF–α at the corresponding concentration (1, 5, 10, 15 and 100 pg mL^{-1}). This gradual increase of semicircles is directly related to an increase in charge transfer resistance, R_{CT}, which is part of the electrical circuit employed for modelling the behaviour of the biosensor impedance, and which is shown as inset in Figure 7(b). This consists in R_{S} as the solution resistance, and the parallel combination of a constant phase element, Q_{CPE}, as the non-ideal capacitance of the functionalized nanostructured surface-electrolyte interface, with the series of the aforementioned R_{CT} and the Warburg (Z_{W}) impedance, accounting for the electron flow between the solution and the electrode and the diffusion phenomenon, respectively. All fitting parameters can be calculated from impedance spectra at different concentrations of TNF–α, and are summarized in Table III. The change in charge transfer resistance (data in Figure 7(b)) demonstrates the bio-recognition of the cytokine to the fixed mAb on the ITO electrode. The high error associated to the concentration of 1 pg mL^{-1} could be ascribable to a hindered optimization and stabilization of the ITO nanowires at low concentration ranges. The data was adjusted to a Logistic behaviour, considering a low responsiveness at very low concentrations, a highly sensitive linear behaviour at middle cytokine concentrations and a saturation plateau at high concentrations. A table summarizing the fitting Logistic equation and values and standard error for the fitting parameters is also included as inset in Figure 7(b). These preliminary results show that semi-quantitative detection of TNF–α is possible with this novel nanostructured substrate. Moreover, the lowest concentration triggering a stable response in this work (5 pg mL^{-1}) seems enough to discriminate unusual traces of TNF–α either in blood or in saliva in healthy patients, as pointed out in Section I.

TABLE III: Fitting parameters for the equivalent electrical circuit of ITO-based TNF–α biosensor. R_{S} and R_{CT} are the solution and the charge transfer resistances, Q_{CPE} is the capacitance of the constant phase element, a measures the ideality of the CPE, and w is the Warburg coefficient.

Ag conc.	R_{S} (Ω)	R_{CT} (Ω)	Q_{CPE} (μ**F** $\mathbf{s}^{a-1}$)	a	w (Ω $\mathbf{s}^{-1/2}$)
0 pg mL^{-1}	360.1 ± 0.2	1202 ± 3	15.9 ± 0.1	0.9 ± 0.5	793 ± 1
1 pg mL^{-1}	331.4 ± 0.5	1349 ± 2	17.8 ± 0.2	0.9 ± 0.5	689 ± 1
5 pg mL^{-1}	398.1 ± 0.5	1355 ± 3	17.2 ± 0.1	0.9 ± 0.5	726 ± 1
10 pg mL^{-1}	388.3 ± 0.4	1583 ± 3	16.4 ± 0.2	0.9 ± 0.5	762 ± 1
15 pg mL^{-1}	402.8 ± 0.5	2221 ± 2	16.2 ± 0.1	0.9 ± 0.5	700 ± 2
100 pg mL^{-1}	492.3 ± 0.5	2348 ± 2	16.1 ± 0.1	0.9 ± 0.5	902 ± 2

IV. CONCLUSIONS

A novel nanostructured transparent substrate with biosensing capabilities was presented in this work. Nanostructured ITO electrodes were fabricated by electron beam evaporation and were derivatized by electroaddressed diazonium salt reduction. Derivatized surfaces were carefully characterized at a macroscopic (CV and EIS) and microscopic (XPS and FTIR) level, as this is the first time such surface treatment is reported. The effectiveness of the covalent bonding of antibodies to CMA-modified ITO electrodes and corresponding cytokine detection

was tested by fluorescence microscopy. Finally, semi-quantitative detection of TNF–α cytokines at varying concentrations from 1 pg mL^{-1} to 100 pg mL^{-1} was conducted by electrochemical impedance spectroscopy. To our knowledge, this is the first nanostructured ITO-based biosensor for the monitoring of cardiac biomarkers.

Although ELISA is still the gold standard for the quantification of cytokines, all the necessary steps it entails, i.e. immobilization, bioconjugation, washing and quantification, are material and time consuming. Besides, the time a sample takes to be analysed is contingent upon the resources of the clinical laboratory, sometimes being necessary to collect and freeze samples until the amount of them makes analysis economically viable. By all means, this compromises the safety of patients, hindering useful knowledge of protein concentration during the first few hours after LVAD implantation, and thus preventing adequate therapeutic intervention in crucial cases. For this reason, it is important to keep focused on the development and improvement of alternative diagnostic techniques based on electrochemical biosensors, and to take advantage of the reduced costs and preparation and analysis time they offer. Eventually, electrochemical sensing could be backed up with optical transduction thanks to the use of a transparent conductive electrode material like ITO, further improving the reliability of POC tests outcome. Moreover, an enhanced sensitivity favoured by the nanostructured nature of such electrode would be of utmost importance in the development of POC systems.

Future research will focus on further electrochemical characterization of this novel nanostructured ITO-based biosensor in terms of linearity, response time, sensitivity and selectivity. Moreover, new lines of research will be opened to explore the feasibility of developing biosensors based on FETs with ITO as gate material, and also the integration of nanostructured ITO as highly sensitive transparent support for biomolecules with optical instrumentation for immunodetection. This is a response to the need for developing and consolidating POC technology.

ACKNOWLEDGMENTS

The research leading to these results has received funding from the European Union's 7FP (*SEA-on-a-CHIP*, Grant Agreement no. 614168) and the European Union's Horizon 2020 (*HEARTEN*, Grant Agreement no. 643694). R.P. acknowledges an FPU grant from the Spanish Ministerio de Educación, Cultura y Deporte.

REFERENCES

[1] S. Brozena Jessup, M. Medical progress. heart failure. *New England Journal of Medicine*, 348:2007–2018, 2003.

[2] Gianluigi Savarese and Lars H Lund. Global public health burden of heart failure. *Cardiac failure review*, 3(1):7, 2017.

[3] Lars Gullestad, Thor Ueland, Leif Erik Vinge, Alexandra Finsen, Arne Yndestad, and Pål Aukrust. Inflammatory cytokines in heart failure: mediators and markers. *Cardiology*, 122(1):23–35, 2012.

[4] Ståle H Nymo, Johannes Hulthe, Thor Ueland, John McMurray, John Wikstrand, Erik T Askevold, Arne Yndestad, Lars Gullestad, and Pål Aukrust. Inflammatory cytokines in chronic heart failure: interleukin-8 is associated with adverse outcome. results from corona. *European journal of heart failure*, 16(1):68–75, 2014.

[5] Mark S Slaughter, Francis D Pagani, Joseph G Rogers, Leslie W Miller, Benjamin Sun, Stuart D Russell, Randall C Starling, Leway Chen, Andrew J Boyle, Suzanne Chillcott, et al. Clinical management of continuous-flow left ventricular assist devices in advanced heart failure. *The Journal of Heart and Lung Transplantation*, 29(4):S1–S39, 2010.

[6] Raffaele Caruso, Salvatore Trunfio, Filippo Milazzo, Jonica Campolo, Renata De Maria, Tiziano Colombo, Marina Parolini, Aldo Cannata, Claudio Russo, Roberto Paino, et al. Early expression of pro-and anti-inflammatory cytokines in left ventricular assist device recipients with multiple organ failure syndrome. *ASAIO Journal*, 56(4):313–318, 2010.

[7] Kenneth G-J Ooi, Grazyna Galatowicz, Hamish MA Towler, Susan L Lightman, and Virginia L Calder. Multiplex cytokine detection versus elisa for aqueous humor: Il-5, il-10, and ifnγ profiles in uveitis. *Investigative ophthalmology & visual science*, 47(1):272–277, 2006.

[8] Raffaele Caruso, Alessandro Verde, Manuela Cabiati, Filippo Milazzo, Chiara Boroni, Silvia Del Ry, Marina Parolini, Claudia Vittori, Roberto Paino, Luigi Martinelli, et al. Association of pre-operative interleukin-6 levels with interagency registry for mechanically assisted circulatory support profiles and intensive care unit stay in left ventricular assist device patients. *The Journal of Heart and Lung Transplantation*, 31(6):625–633, 2012.

[9] Chris J Watson, Mark T Ledwidge, Dermot Phelan, Patrick Collier, Jennifer C Byrne, Michael J Dunn, Kenneth M McDonald, and John A Baugh. Proteomic analysis of coronary sinus serum reveals leucine-rich α2-glycoprotein as a novel biomarker of ventricular dysfunction and heart failureclinical perspective. *Circulation: Heart Failure*, 4(2):188–197, 2011.

[10] Michaela Maurer, Sonja Burri, Stefano de Marchi, Roger Hullin, Michele Martinelli, Paul Mohacsi, and Otto M Hess. Plasma homocysteine and cardiovascular risk in heart failure with and without cardiorenal syndrome. *International journal of cardiology*, 141(1):32–38, 2010.

[11] Mouna Hnaien, Florence Lagarde, Joan Bausells, Abdelhamid Errachid, and Nicole Jaffrezic-Renault. A new bacterial biosensor for trichloroethylene detection based on a three-dimensional carbon nanotubes bioarchitecture. *Analytical and bioanalytical chemistry*, 400(4):1083–1092, 2011.

[12] S Bourigua, M Hnaien, F Bessueille, F Lagarde, S Dzyadevych, A Maaref, J Bausells, A Errachid, and N Jaffrezic Renault. Impedimetric immunosensor based on swcnt-cooh modified gold microelectrodes for label-free detection of deep venous thrombosis biomarker. *Biosensors and Bioelectronics*, 26(4):1278–1282, 2010.

[13] Jasmina Vidic, Mateu Pla-Roca, Jeanne Grosclaude, Marie-Annick Persuy, Régine Monnerie, David Caballero, Abdelhamid Errachid, Yanxia Hou, Nicole Jaffrezic-Renault, Roland Salesse, et al. Gold surface functionalization and patterning for specific immobilization of olfactory receptors carried by nanosomes. *Analytical Chemistry*, 79(9):3280–3290, 2007.

[14] Syrine Chebil, I Hafaiedh, Hélène Sauriat-Dorizon, Nicole Jaffrezic-Renault, Abdelhamid Errachid, Zulfiqur Ali, and Hafsa Korri-Youssoufi. Electrochemical detection of d-dimer as deep vein thrombosis marker using single-chain d-dimer antibody immobilized on functionalized polypyrrole. *Biosensors and Bioelectronics*, 26(2):736–742, 2010.

[15] Ting Li and Minghui Yang. Electrochemical sensor utilizing ferrocene loaded porous polyelectrolyte nanoparticles as label for the detection of protein biomarker il-6. *Sensors and Actuators B: Chemical*, 158(1):361–365, 2011.

[16] Bernard S Munge, Amy L Coffey, Jaimee M Doucette, Brian K Somba, Ruchika Malhotra, Vyomesh Patel, J Silvio Gutkind, and James F Rusling. Nanostructured immunosensor for attomolar detection of cancer biomarker interleukin-8 using massively labeled superparamagnetic particles. *Angewandte Chemie International Edition*, 50(34):7915–7918, 2011.

[17] Bernard S Munge, Colleen E Krause, Ruchika Malhotra, Vyomesh Patel, J Silvio Gutkind, and James F Rusling. Electrochemical immunosensors for interleukin-6. comparison of carbon nanotube forest and gold nanoparticle platforms. *Electrochemistry communications*, 11(5):1009–1012, 2009.

[18] Michael Lee, Nadia Zine, Abdellatif Baraket, Miguel Zabala, Francesca Campabadal, Raffaele Caruso, Maria Giovanna Trivella, Nicole Jaffrezic-Renault, and Abdelhamid Errachid. A novel biosensor based on hafnium oxide: Application for early stage detection of human interleukin-10. *Sensors and Actuators B: Chemical*, 175:201–207, 2012.

[19] Abdoullatif Baraket, Michael Lee, Nadia Zine, Monique Sigaud, Nourdin Yaakoubi, Maria Giovanna Trivella, Miguel Zabala, Joan Bausells, Nicole Jaffrezic-Renault, and Abdelhamid Errachid. Diazonium modified gold microelectrodes onto polyimide substrates for impedimetric cytokine detection with an integrated ag/agcl reference electrode. *Sensors and Actuators B: Chemical*, 189:165–172, 2013.

[20] Abdoullatif Baraket, Michael Lee, Nadia Zine, Nourdin Yaakoubi, Joan Bausells, and Abdelhamid Errachid. A flexible electrochemical micro lab-on-chip: application to the detection of interleukin-10. *Microchimica Acta*, 183(7):2155–2162, 2016.

[21] Paul Scully, Declan P McKernan, John Keohane, David Groeger, Fergus Shanahan, Timothy G Dinan, and Eamonn MM Quigley. Plasma cytokine profiles in females with irritable bowel syndrome and extra-intestinal co-morbidity. *The American journal of gastroenterology*, 105(10):2235, 2010.

[22] Jingyi Liu and Yixiang Duan. Saliva: A potential media for disease diagnostics and monitoring. *Oral oncology*, 48(7):569–577, 2012.

[23] Shuai Wang, Xiaohong Han, Xingsheng Hu, Xiaoyuan Wang, Lingdi Zhao, Le Tang, Yun Feng, Di Wu, Yan Sun, and Yuankai Shi. Clinical significance of pretreatment plasma biomarkers in advanced non-small cell lung cancer patients. *Clinica Chimica Acta*, 430:63–70, 2014.

[24] J Martinez-Borra, C Lopez-Larrea, S Gonzalez, D Fuentes, A Dieguez, EM Deschamps, JM Perez-Pariente, A Lopez-Vazquez, R de Francisco, and L Rodrigo. High serum tumor necrosis factor-α levels are associated with lack of response to infliximab in fistulizing crohn's disease. *The American Journal of Gastroenterology*, 97(9):2350–2356, 2002.

[25] Xing-You Lang, Hong-Ying Fu, Chao Hou, Gao-Feng Han, Ping Yang, Yong-Bing Liu, and Qing Jiang. Nanoporous gold supported cobalt oxide microelectrodes as high-performance electrochemical biosensors. *Nature communications*, 4:2169, 2013.

[26] Sunil K Arya, Karen Yanping Wang, Chee Chung Wong, and Abdur Rub Abdur Rahman. Anti-epcam modified lc-spdp monolayer on gold microelectrode based electrochemical biosensor for mcf-7 cells detection. *Biosensors and Bioelectronics*, 41:446–451, 2013.

[27] Huei-Yu Bai, F Javier Del Campo, and Yu-Chen Tsai. Sensitive electrochemical thrombin aptasensor based on gold disk microelectrode arrays. *Biosensors and Bioelectronics*, 42:17–22, 2013.

[28] Patthara Kongsuphol, Hui Hwee Ng, Joanna P Pursey, Sunil K Arya, Chee Chung Wong, Eugen Stulz, and Mi Kyoung Park. Eis-based biosensor for ultra-sensitive detection of tnf-α from non-diluted human serum. *Biosensors and Bioelectronics*, 61:274–279, 2014.

[29] Abdoullatif Baraket, Michael Lee, Nadia Zine, Monique Sigaud, Joan Bausells, and Abdelhamid Errachid. A fully integrated electrochemical biosensor platform fabrication process for cytokines detection. *Biosensors and Bioelectronics*, 93:170–175, 2017.

[30] Abdoullatif Baraket, Michael Lee, Nadia Zine, Nourdine Yaakoubi, Maria Giovanna Trivella, Abdelhamid Elaissari, Monique Sigaud, Nicole Jaffrezic-Renault, and Abdelhamid Errachid. A flexible label-free biosensor sensitive and selective to tnf-[alpha]: Application for chronic heart failure. *Sensors & Transducers*, 27(5):15, 2014.

[31] U Eletxigerra, J Martinez-Perdiguero, S Merino, R Villalonga, JM Pingarrón, and S Campuzano. Amperometric magnetoimmunoassay for the direct detection of tumor necrosis factor alpha biomarker in human serum. *Analytica chimica acta*, 838:37–44, 2014.

[32] Ting Li, Zhongzhou Si, Liqiang Hu, Haizhi Qi, and Minghui Yang. Prussian blue-functionalized ceria nanoparticles as label for ultrasensitive detection of tumor necrosis factor-α. *Sensors and Actuators B: Chemical*, 171:1060–1065, 2012.

[33] S Libertino, S Conoci, A Scandurra, and C Spinella. Biosensor integration on si-based devices: Feasibility studies and examples. *Sensors and Actuators B: Chemical*, 179:240–251, 2013.

[34] Joseph Wang. Electrochemical biosensors: towards point-of-care cancer diagnostics. *Biosensors and Bioelectronics*, 21(10):1887–1892, 2006.

[35] Johan Gustavsson, George Altankov, Abdelhamid Errachid, Josep Samitier, Josep A Planell, and Elisabeth Engel. Surface modifications of silicon nitride for cellular biosensor applications. *Journal of Materials Science: Materials in Medicine*, 19(4):1839–1850, 2008.

[36] M Castellarnau, N Zine, J Bausells, C Madrid, A Juarez, J Samitier, and A Errachid. Integrated cell positioning and cell-based isfet biosensors. *Sensors and Actuators B: Chemical*, 120(2):615–620, 2007.

[37] Joan Marc Rafí, Miguel Zabala, Oihane Beldarrain, and Francesca Campabadal. Effect of processing conditions on the electrical characteristics of atomic layer deposited al2o3 and hfo2 films. *ECS Transactions*, 28(2):213–221, 2010.

[38] F Campabadal, JM Rafí, M Zabala, O Beldarrain, A Faigón, H Castán, A Gómez, H García, and S Dueñas. Electrical characteristics of metal-insulator-semiconductor structures with atomic layer deposited al 2 o 3, hfo 2, and nanolaminates on different silicon substrates. *Journal of Vacuum Science & Technology B, Nanotechnology and Microelectronics: Materials, Processing, Measurement, and Phenomena*, 29(1):01AA07, 2011.

[39] Glen D Wilk, Robert M Wallace, and JM Anthony. High-κ gate dielectrics: Current status and materials properties considerations. *Journal of applied physics*, 89(10):5243–5275, 2001.

[40] Tae Joo Park, Jeong Hwan Kim, Jae Hyuck Jang, Choong-Ki Lee, Kwang Duk Na, Sang Young Lee, Hyung-Suk Jung, Miyoung Kim, Seungwu Han, and Cheol Seong Hwang. Reduction of electrical defects in atomic layer deposited hfo2 films by al doping. *Chemistry of Materials*, 22(14):4175–4184, 2010.

[41] JF Kang, HY Yu, C Ren, M-F Li, DSH Chan, H Hu, HF Lim, WD Wang, D Gui, and D-L Kwong. Thermal stability of nitrogen incorporated in hfn x o y gate dielectrics prepared by reactive sputtering. *Applied physics letters*, 84(9):1588–1590, 2004.

[42] Yi Wei Chen, Maozi Liu, Tetsuya Kaneko, and Paul C McIntyre. Atomic layer deposited hafnium oxide gate dielectrics for charge-based biosensors. *Electrochemical and Solid-State Letters*, 13(3):G29–G32, 2010.

[43] Elif Burcu Aydın, Muhammet Aydın, and Mustafa Kemal Sezgintürk. A highly sensitive immunosensor based on ito thin films covered by a new semi-conductive conjugated polymer for the determination of tnfα in human saliva and serum samples. *Biosensors and Bioelectronics*, 2017.

[44] Chang K Choi, Chuck H Margraves, Seung I Jun, Anthony E English, Philip D Rack, and Kenneth D Kihm. Opto-electric cellular biosensor using optically transparent indium tin oxide (ito) electrodes. *Sensors*, 8(5):3257–3270, 2008.

[45] Chang Kyoung Choi, Kenneth D Kihm, and Anthony E English. Optoelectric biosensor using indium-tin-oxide electrodes. *Optics letters*, 32(11):1405–1407, 2007.

[46] Zarini Muhammad Tahir, Evangelyn C Alocilja, and Daniel L Grooms. Indium tin oxide-polyaniline biosensor: Fabrication

and characterization. *Sensors*, 7(7):1123–1140, 2007.

[47] R Pruna, F Palacio, M Martínez, O Blázquez, S Hernández, B Garrido, and M López. Organosilane-functionalization of nanostructured indium tin oxide films. *Interface focus*, 6(6):20160056, 2016.

[48] R Pruna, F Palacio, M López, J Pérez, M Mir, O Blázquez, S Hernández, and B Garrido. Electrochemical characterization of organosilane-functionalized nanostructured ito surfaces. *Applied Physics Letters*, 109(6):063109, 2016.

[49] Raquel Pruna, Francisco Palacio, and Manel López. Towards nanostructured ito-based electrochemical sensors: Fabrication, characterization and functionalization. In *Multidisciplinary Digital Publishing Institute Proceedings*, volume 1, page 288, 2017.

[50] Mohamed Mehdi Chehimi. *Aryl diazonium salts: new coupling agents and surface science*. John Wiley & Sons, 2012.

[51] R Rakesh Kumar, K Narasimha Rao, K Rajanna, and AR Phani. Low temperature and self catalytic growth of ultrafine ito nanowires by electron beam evaporation method and their optical and electrical properties. *Materials Research Bulletin*, 52:167–176, 2014.

[52] AL Beaudry, RT Tucker, JM LaForge, MT Taschuk, and MJ Brett. Indium tin oxide nanowhisker morphology control by vapour–liquid–solid glancing angle deposition. *Nanotechnology*, 23(10):105608, 2012.

[53] H Yumoto, T Sako, Y Gotoh, K Nishiyama, and T Kaneko. Growth mechanism of vapor–liquid–solid (vls) grown indium tin oxide (ito) whiskers along the substrate. *Journal of Crystal Growth*, 203(1-2):136–140, 1999.

[54] Francesca G Bellagambi, Abdoullatif Baraket, Alessia Longo, Monica Vatteroni, Nadia Zine, Joan Bausells, Roger Fuoco, Fabio Di Francesco, Pietro Salvo, Georgia S Karanasiou, et al. Electrochemical biosensor platform for tnf-α cytokines detection in both artificial and human saliva: Heart failure. *Sensors and Actuators B: Chemical*, 251:1026–1033, 2017.

[55] Ronen Polsky, Jason C Harper, David R Wheeler, Shawn M Dirk, Dulce C Arango, and Susan M Brozik. Electrically addressable diazonium-functionalized antibodies for multianalyte electrochemical sensor applications. *Biosensors and Bioelectronics*, 23(6):757–764, 2008.

[56] Yuwei Wang, Linghui Meng, Liquan Fan, Guangshun Wu, Lichun Ma, Min Zhao, and Yudong Huang. Carboxyl functionalization of carbon fibers via aryl diazonium reaction in molten urea to enhance interfacial shear strength. *Applied Surface Science*, 362:341–347, 2016.

[57] Feng Zhao, Yudong Huang, Li Liu, Yongping Bai, and Liwei Xu. Formation of a carbon fiber/polyhedral oligomeric silsesquioxane/carbon nanotube hybrid reinforcement and its effect on the interfacial properties of carbon fiber/epoxy composites. *Carbon*, 49(8):2624–2632, 2011.

[58] Linghui Meng, Dapeng Fan, Chunhua Zhang, Zaixing Jiang, and Yudong Huang. The effect of oxidation treatment by kclo 3/h 2 so 4 system on intersurface performance of carbon fibers. *Applied Surface Science*, 268:225–230, 2013.

[59] Scott H Brewer, Derek A Brown, and Stefan Franzen. Formation of thiolate and phosphonate adlayers on indium- tin oxide: Optical and electronic characterization. *Langmuir*, 18(18):6857–6865, 2002.

[60] Min Hee Lee, Jia-Sheng Wu, Jeong Won Lee, Jong Hwa Jung, and Jong Seung Kim. Highly sensitive and selective chemosensor for hg2+ based on the rhodamine fluorophore. *Organic Letters*, 9(13):2501–2504, 2007.

[61] Michelle R Longmire, Mikako Ogawa, Yukihiro Hama, Nobuyuki Kosaka, Celeste AS Regino, Peter L Choyke, and Hisataka Kobayashi. Determination of optimal rhodamine fluorophore for in vivo optical imaging. *Bioconjugate chemistry*, 19(8):1735–1742, 2008.

4.3 On the performance of nanostructured ITO electrodes as electrochemical biosensors

In this section, the preliminary results of the bovine serum albumin and biotin–streptavidin based immunoassays employing nanostructured ITO electrodes as electrochemical sensors are presented. These results have not been published yet, and are presented here just as a proof of concept to validate the suitability of both thin and nanostructured ITO films as electrochemical biosensors, and to show the increased sensitivity presented by the nanostructured electrodes as compared to the flat ones.[1]

4.3.1 Bovine serum albumin

As detailed in the third part of Chapter 2 (Section 2.3.3.1), bovine serum albumin (BSA) is a protein typically found in the blood plasma of cows, and its function consists in regulating the blood volume in the body by maintaining the colloid osmotic pressure of blood. The BSA immunoassay is very commonly performed in the laboratory as part of the research towards validating new substrates for optical and electrochemical biodetection. Figure 4.1 shows a general schematic of the biofunctionalization process and detection principle for the BSA assay performed on thin film and nanostructured ITO as working electrode substrates. First, the ITO-based electrodes were derivatized for 1 h at 37 °C by immersion in a solution of (3-Glycidoxypropyl) trimethoxysilane (GOPTS, purchased from Sigma-Aldrich, Spain) at a concentration of 2.5 % in pure ethanol. Then the electrodes were rinsed in ethanol and dried with a stream of nitrogen. To perform step 2 in Figure 4.1, 5 mg of BSA were dissolved in PBS to prepare a stock solution of 500 μg, from which a 100 μg ml^{-1} dilution of BSA in PBS was prepared. A 20 μl drop was added to the silane-derivatized electrodes and left react for 30 min at room temperature. Afterwards, the samples were rinsed with PBS. During step 3, successive aliquotes of anti–BSA in PBST were prepared at volumetric dilutions of 1/1000, 1/2000 and 1/3000 (this is, 1 part of antibody for 999, 1999 and 2999 parts of PBST, respectively), and were left react with the BSA-functionalized electrodes for 30 min at room temperature, followed by rinsing with PBST and drying with a stream of nitrogen. Finally, step 5 consisted in preparing a constant concentration of immunoglobulin G antibody (anti–IgG) labelled with the enzyme horseradish peroxidase (HRP). The

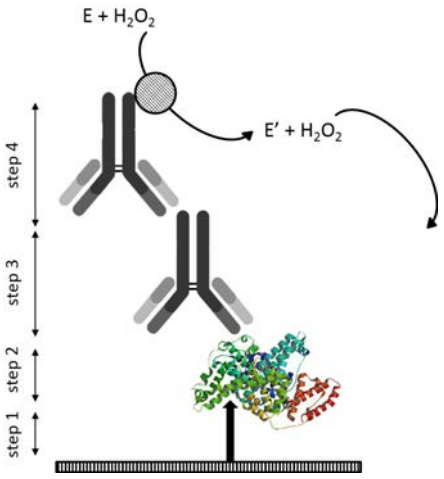

FIGURE 4.1: Schematic summarizing the steps towards performing the BSA immunoassay and detection on an inorganic substrate (ITO). Step 1: surface derivatization with organosilane self assembled monolayer; step 2: BSA immobilization; step 3: anti–BSA bioconjugation; step 4: conjugation of anti–IgG labelled with HRP.

[1] All the electrodes employed in the experiments described in this section were submitted to a cleaning protocol prior to further manipulation. The electrodes were immersed for 10 min in acetone and for 10 min in ethanol, and then rinsed three times with ultrapure water. Next, they were immersed in a solution of pure dichloromethane (CH_2Cl_2) for 10 min in soft agitation. Finally, they were thoroughly rinsed with ultrapure water and dried with a stream of nitrogen.

electrodes were left react with a 20 μl drop of 1/1000 anti–IgG–HRP in PBST for 30 min at room temperature and isolated from light.

The functionalization process was monitored by Fourier transform infrared (FTIR) spectroscopy, in order to benchmark the spectra of BSA-functionalized ITO electrodes against the spectra obtained from bare ITO electrodes. The results are shown in Figure 4.2a, where three absorption bands can be observed for functionalized ITO electrodes compared to bare ITO films; these absorption peaks occur around 3700 cm^{-1}, 3000 cm^{-1} and 1000 cm^{-1}. These absorption peaks correspond to bonds present in organic molecules deposited on the electrode as a result of the functionalization process. Mainly, the footprints of secondary amides and carbon-based compounds (such as $–CH_2$ and $–CH_3$) can be observed in the spectra.

The suitability of ITO electrodes as electrochemical sensors was tested by monitoring the amperometric current flowing between the working electrode and a platinum auxiliary electrode as a result of the reduction of hydrogen peroxide catalyzed by HRP in presence of the reducing 5'-tetramethylbenzidine (TMB) substrate (represented as E in Figure 4.1, which becomes oxidized $–E'–$). Figure 4.2b shows the amperometric current measured for a geometrical projected area of the ITO working electrode of 0.7 cm^2, as defined by the inner diameter of an O-ring in a Teflon-based electrochemical cell. A DC voltage of -100 mV was applied between the working and reference electrodes, and the current was recorded for 60 s. An increase in amperometric current can be observed with increasing anti–BSA concentrations (directly related to the concentration of HRP on the electrode surface). Moreover, nanostructured ITO electrodes offer a substantial increase in amperometric current due to a higher electroactive surface area, being the nanostructures capable of hosting a greater quantity of HRP enzyme than the flat surface of thin ITO films.

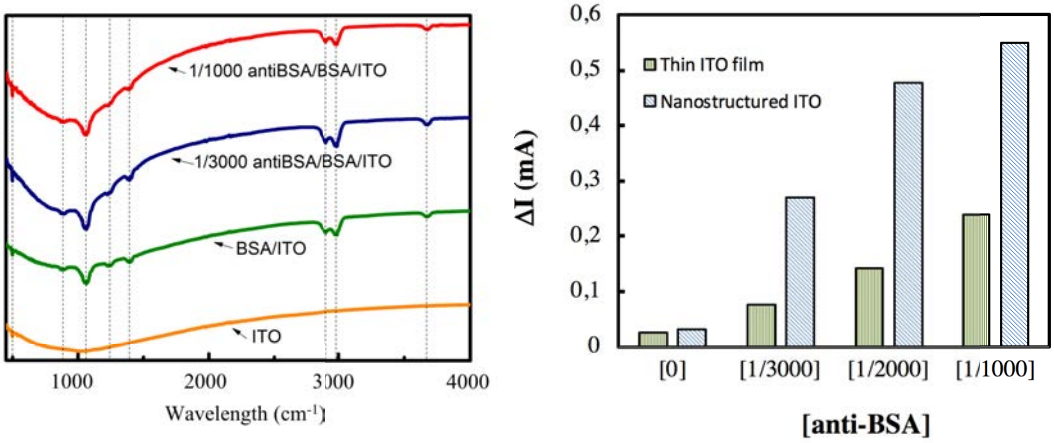

(A) (B)

FIGURE 4.2: (A) FTIR spectroscopy results of bare ITO and electrodes after BSA functionalization and anti–BSA detection at several concentrations, showing the presence of several species after functionalization; (B) bar diagram showing the increase in amperometric current at the addition of hydrogen peroxide for several concentrations of anti–BSA (which limit the amount of HRP present on the electrode surface).

4.3.2 Biotin–streptavidin

The performance of ITO films as electrochemical sensors was also tested basing on another principle of operation requiring no labelling molecules: electrochemical impedance spectroscopy (EIS). For this, a new immunoassay based on the interaction between biotin and streptavidin was studied. Streptavidin was detected at several concentrations by EIS, and the effect of interfering antigens was useful to determine the sensor selectivity.

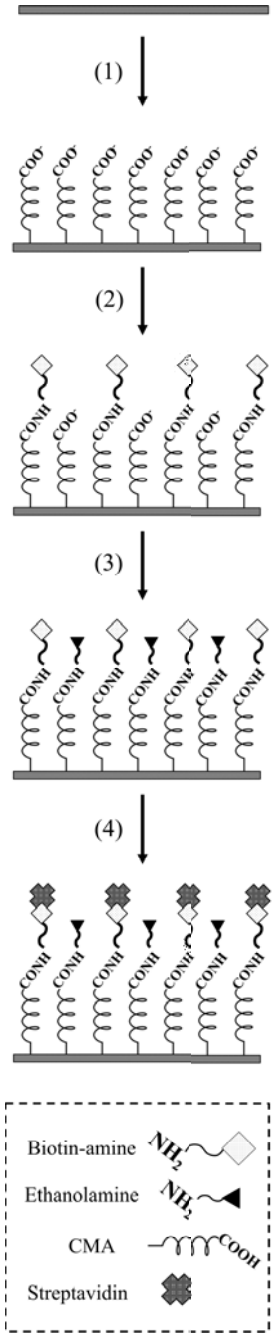

FIGURE 4.3: Schematic of the four-step process for the immobilization of the biotin-streptavidin complex on nanostructured ITO electrodes.

First, the derivatization of the electrode surface with a layer of crosslinkers is required as usual in order to couple organic biomolecules to inorganic substrates. In the present case, the nanostructured ITO surface was derivatized by the electroaddressed reduction of 4-carboxymethyl aryl diazonium (CMA) salts (see step 1 in Figure 4.3). This was done by cycling a DC voltage at the ITO electrode from 0 V to −1 V at 100 mV s^{-1} with respect to a KCl saturated Ag/AgCl reference electrode in a solution containing the diazotated CMA (by storing 5 mM of the latter for 10 min at 4 °C in a 20 mM HCl and 20 mM $NaNO_2$ aqueous solution). The resulting voltammogram is shown in Figure 4.4a. A first peak at −0.5 V can be observed, which corresponds to the CMA reduction on the electrode surface. The intensity of subsequent cycles is damped as a result of a large passivated area of the electrode surface, which hinders the electron transfer between the medium and the electrode. The quality of the CMA-deposited film was tested by cyclic voltammetry (Figure 4.4b). These results show a considerable weakening of the ferrocyanide readox peaks after CMA deposition. Figure 4.4b also shows the effect of successive EIS analysis (Mott-Schottky technique) on the performance of the working electrode. A slight damage on the CMA layer can be appreciated after successive EIS measurements; the CMA layer is not removed since no redox peaks appear, but the capacitive current increases due to a slight deterioration of the whole surface.

Next step consists in activating the carboxylic acids present at the electrode surface after CMA derivatization. For this, the electrodes surfaces need to be activated by the EDC/NHS[2] chemistry, and

[2]EDC is the acronym for 1-ethyl-3-(-3-dimethylaminopropyl) carbodiimide hydrochloride, and NHS stands for *N*-hydroxysuccinimide.

this was done by incubating for 30 min at room temperature the electrodes in a EDC (80 mM) and NHS (20 mM) aqueous solution. After that, the electrodes were rinsed with PBS, and then incubated for 2 h at room temperature in a 0.1 mM solution of biotin–NH_2 in PBS (step 2 in Figure 4.3). Afterwards, the electrodes were rinsed with PBS and incubated for 30 min at room temperature in a 1 mM solution of ethanolamine in pure ethanol in order to block the unspecific sites where no biotin–NH_2 molecules were coupled (step 3 in Figure 4.3).

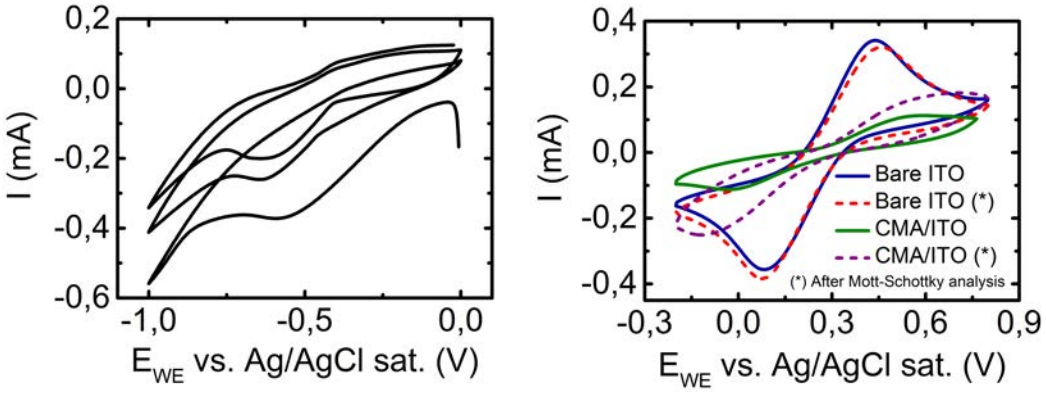

(A) (B)

FIGURE 4.4: (A) Electrodeposition of CMA on the ITO electrodes by cyclic voltammetry, performed at 100 mV s^{-1} from 0 V to −1 V vs. a KCl saturated Ag/AgCl reference electrode. (B) Voltammograms of ITO electrodes before and after CMA electrodeposition performed at 50 mV s^{-1} in a 5 mM ferrocyanide medium.

Finally, detection of streptavidin was achieved by incubation of successive aliquotes of the protein in PBS, for 1 h at room temperature. Figures 4.5a and 4.5b show primary EIS results, acquired by incubating three nanostructured ITO-based electrodes successively in 1 μM, 100 nM and 10 nM streptavidin solution in PBS. An increase in polarization resistance can be observed for increasing concentrations (with a logarithmic dependence). The polarization resistance was obtained, as usual, by fitting the result to an equivalent electrical circuit: a series resistance corresponding to the liquid medium, and the parallel association of a double layer pseudocapacitance on one side, and the polarization resistance together with the Warburg element, on the other side.

The experiment was extended to averaging the results obtained with five independent electrodes in order to minimize the variance of the measurements, increasing the concentration range studied down to 100 pM streptavidin and studying the selectivity of the sensor by measuring the change in polarization resistance introduced by the unspecific detection of interfering antigens (bovine serum albumin –BSA– and immunoglobulin G –IgG–). The results are shown in Figure 4.5c, from which one can still appreciate the logarithmic dependence of the polarization resistance change on the streptavidin concentration, and no relevant level of unspecific detection of BSA or IgG, which suggests the developed sensor is adequately selective.

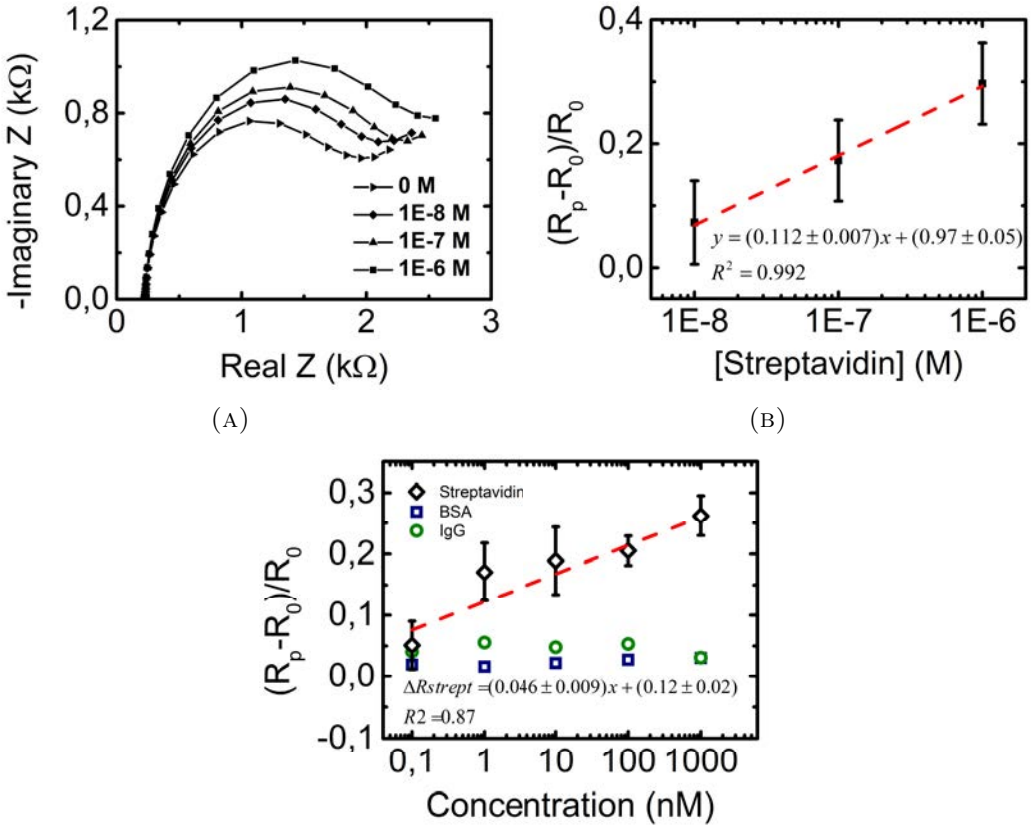

FIGURE 4.5: Detection of streptavidin by EIS. (A) Nyquist plot for four streptavidin concentrations in PBS in a frequency range of 200 kHz to 100 mHz, polarization voltage of 0.2 V plus a small sine potential of amplitude 50 mV. (B) Normalized curve showing the relative variation of charge transfer resistance with increasing streptavidin concentrations, taking the biotin-functionalized electrode as a reference. (C) Calibration curve showing the variation in polarization resistance for an extended concentration range of streptavidin and response of the sensor to interfering agents (BSA and IgG).

Chapter 5

Miniaturized readout electronics: from the laboratory to a chip

Along Chapter 3, the preparation process and characterization of a novel material (nanostructured ITO) was detailed, focusing on its electrochemical properties. This electrochemical behaviour was exploited along Chapter 4 for developing electrochemical biosensors. The chemistry of crosslinker derivatization was investigated on thin ITO films and on nanostructured ITO electrodes, and three different immunoassays were built on the electrodes for the quantification of several species of clinical interest by different principles of detection: amperometry and electrochemical impedance spectroscopy.

This chapter gathers some studies carried out along the thesis on the electronic designs required for exciting electrochemical sensors and measuring their response. Such devices are called *potentiostats*. Commercial potentiostats generally available at research laboratories are very large and heavy, expensive and need to be manipulated by trained personnel. Nevertheless, they have the advantage of offering several electrochemical techniques and a large number of possible configurations. But this feature may not be imperative in point of care (POC) applications. Indeed, rapidity, cheapness and ease of use are most demanded attributes for POC devices, for these are targeted to bedside patients and specialized medical staff.

Section 5.1 includes Article V, which presents a simplified electronic design and the implementation process of a low-cost and miniaturized device for electrochemical impedance spectroscopy measurements. Complementary designs for performing amperometric and potentiometric measurements are included in Section 5.2.

5.1 Integration of electrochemical impedance spectroscopy

In *Article V: A low-cost and miniaturized potentiostat for sensing of biomolecular species such as TNF–α by electrochemical impedance spectroscopy*, the design and implementation of a low-cost and portable electronic device for the monitorization of biosensors by electrochemical impedance spectroscopy is presented. The purposes of this work are:

1. to design an appropriate and simplified electronic configuration that permits the application of a voltage wave between two leads (working and reference electrodes) and the measurement of the current flowing through the working and auxiliary electrodes as a result of the voltage excitation;

2. to implement the designed potentiostat on a printed circuit board (PCB), placing the electronic components (hardware) and designing the appropriate firmware for the microcontrollers involved in the device;

3. to design a MATLAB®-based software implementing a graphical user interface (GUI) to set the device's configuration parameters and to process and represent the measured signals;

4. to validate the software and the device by testing several configurations of electronic components (resistors and capacitors) emulating the typical behaviour of electrochemical systems;

5. to derivatize and functionalize an array of gold microelectrodes with the appropriate immunoassay for the detection of a heart failure cardiac biomarker, tumour necrosis factor α (TNF–α);

6. to quantify several concentrations of TNF–α by electrochemical impedance spectroscopy with the developed potentiostat and to study the performance of the device, as well as its linearity and detectiveness and

7. to benchmark the results against those obtained with a commercial potentiostat.

The article has been reproduced from Biosensors and Bioelectronics; vol. 100; R. Pruna, F. Palacio, A. Baraket, N. Zine, A. Streklas, J. Bausells, A. Errachid and M. López,"A low-cost and miniaturized potentiostat for sensing of biomolecular species such as TNF–α by electrochemical impedance spectroscopy", 533–540, 2018; with permission from Elsevier.

A low-cost and miniaturized potentiostat for sensing of biomolecular species such as TNF-α by electrochemical impedance spectroscopy

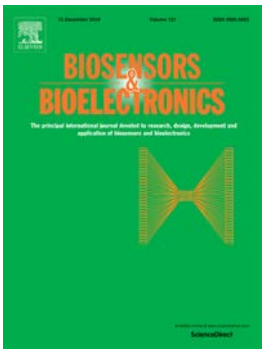

Raquel Pruna,[1] Francisco Palacio,[1] Abdoullatif Baraket,[2] Nadia Zine,[2] Angelos Streklas,[3] Joan Bausells,[3] Abdelhamid Errachid,[2] and Manel López[1]

[1)] *Departament d'Enginyeries: Electrònica i Biomèdica, Universitat de Barcelona, Martí i Franquès 1, E-08028 Barcelona, Spain*

[2)] *Université de Lyon 1, Institut des Sciences Analytiques, UMR 5280, CNRS, 5 rue de la Doua, F-69100, Villeurbanne, France*

[3)] *Instituto de Microelectrónica de Barcelona, IMB-CNM (CSIC), Campus UAB, E-08193 Bellaterra, Spain*

Biosensors and Bioelectronics, 100 (2018), 533-540
doi: 10.1016/j.bios.2017.09.049

ABSTRACT

Miniaturizing potentiostats, keeping their cost low and yet preserving full measurement characteristics (e.g. bandwidth, determination of capacitive/inductive contribution to sensor's impedance and parallel screening) is still an unresolved challenge in bioelectronics. In this work, the combination of simple analogue circuitry together with powerful microcontrollers and a digital filter implementation is presented as an alternative to complex and incomplete architectures reported in the literature. A low-cost acquisition electronic system fully integrated with a biosensors platform containing eight gold working microelectrodes and integrated reference and counter electrodes was developed and validated. The manufacturing cost of the prototype was kept below 300 USD. The performance of the proposed device was benchmarked against a commercial impedance analyzer through the electrochemical analysis of a highly sensitive biosensor for the detection of tumor necrosis factor α (TNF–α) within the randomly chosen range of 266 pg mL^{-1} to 666 ng mL^{-1} in physiological medium (PBS). A strong correlation between the outputs of both devices was found in a critical range of frequencies (1–10 Hz), and several TNF–α cytokine concentrations were properly discriminated. These results are very promising for the development of low-cost, portable and miniaturized electrochemical systems for point-of-care and environmental diagnosis.

I. INTRODUCTION

Heart failure (HF) is one of the fastest growing cardiovascular disorders (CVDs), since approximately 1 million new patients are diagnosed with this illness every year [1 and 2]. HF occurs when the heart cannot provide enough pump action to maintain an adequate blood flow, and it manifests in a number of symptoms such as shortness of breath, leg swelling and exercise intolerance [3–5]. To overcome the lack of donor organs, patients have been implanted with some bioelectronic devices such as pressure sensors and left ventricle assisted devices

(LVADs). However, these clinical interventions result in increased risk of triggering upregulated inflammatory cytokine levels (e.g. Interleukin 1 (IL-1), IL-6, IL-8, IL-10, tumor necrosis factor α (TNF–α)) in blood and in saliva [6 and 7].

Immunoaffinity column assay, fluorimetric and enzyme-linked immunosorbent assay (ELISA) are amongst the traditional gold-standard techniques for the detection of CVD biomarkers [6, 8–13]. The two former techniques, although accurate and sensitive, require highly specialized personnel and huge sample volumes for analysis, since they are based on sophisticated instrumentation. On the other hand, ELISA is relatively affordable in terms of cost and expertise, but is still handicapped by the large amount of disposable material needed and for being time-consuming. Thus, there is an urgent need for easy-to-use, real-time and yet highly sensitive and selective diagnostic tools for early-stage detection of inflammatory biomarkers to enable rapid intervention and improve the patients' quality of life. In this light, biosensors present a low-cost, portable, reproducible, rapid, sensitive and label-free alternative [14–22], being electrochemical biosensors the most used among them [23]. Several electrochemical biosensors have been developed for the monitoring of inflammatory cytokines. Electrochemical impedance spectroscopy (EIS) was used to detect IL-10 with a complementary metal oxide semiconductor (CMOS) based biosensor, achieving a limit of detection of 0.1 pg mL^{-1} [2]. Similarly, a biocompatible and flexible biosensor based on gold microelectrodes was developed to detect TNF–α by EIS [24]. Also in the frame of TNF–α detection, Pui *et al.* developed an electrochemical impedance based biosensor achieving detection limits of 1–100 pg mL^{-1} in cell culture medium [20]. A limit of detection of 10 pg mL^{-1} was achieved by Yin *et al.* by electrochemical monitoring of micropatterned aptamer-modified electrodes [25]. Liu and coworkers reported electrochemical detection of TNF–α in whole human blood with an aptasensor, achieving a limit of detection of 10 ng mL^{-1} [26 and 27]. On the other hand, it has been reported from the clinical point of view that plasma levels of TNF–α for HF patients in functional classes I to III is 1.95 ± 0.54, 2.63 ± 0.48 and 6.4 ± 1.9 pg mL^{-1} [28 and 29], respectively. These are high cytokine levels compared to age-matched control subjects (0.75 ± 0.05 pg mL^{-1}). Careful interpretation of these results indicates that it is still difficult to meet detection limit requirements for TNF–α with current biosensors and measurement systems, and even more to discriminate between patient functional classes.

With all, most effort in the literature has been devoted to biosensor miniaturization, whereas commercial potentiostats are still large in most cases, and also expensive and time-consuming [37]. Some trademarks have indeed commercialized portable versions of potentiostats [33–36]. Table I summarizes some technical specifications (focusing on impedance spectroscopy) of some of these portable and also of classic potentiostats, which can be directly benchmarked against the prototype presented in this work. Other characteristics such as geometry, weight and price are provided, as well as the number of channels available (at the indicated price) for real-time measurements. Overall, we are still far from meeting technical specifications such as frequency and voltage range presented by all commercial potentiostats, although our prototype can perform well in a variety of situations, as demonstrated hereinafter. Moreover, our prototype outperforms in terms of weight, number of channels (compared to portable, commercially-available potentiostats) and, most importantly, in terms of cost.

This illustrates the urgent need for low-cost miniaturized potentiostats that can be integrated into point-of-care (POC) diagnostic tools [38–41]. In spite of the importance for this to be pursued, there are few proposals on low-cost miniaturized potentiostats in the literature, and they are still not easily embeddable into POC environments. In this context, Cruz and coworkers [42] proposed a low-cost miniaturized potentiostat based on a LMP91000EVM commercial chip and a BeagleBone development board (Texas Instruments). The system was

customized to perform cyclic voltammetry (CV) measurements for electrochemical immunosensing of cortisol, achieving a limit of detection of 1 pM. Here, the developed potentiostat was fully described, yet no impedance measurements were reported, which is indeed the issue at hand. In terms of portable impedance meters, Li *et al.* developed such an instrument in combination with a 3D-printed USB-compatible sensor chip for the detection of aflatoxins in rice. Here, the authors evaluated the performance of the developed device in relation to a Zahner commercial station (ZAHNER-elektrik GmbH & Co KG, Germany) [43]. A calibration curve showing the sensor impedance as a function of frequency was presented, indicating that their system cannot achieve frequencies below 100 Hz. This seriously compromises the versatility of the technique, hindering the use of the portable electrochemical station to measure other biosensors, as important features may be visible only at low frequencies. A more detailed system was presented by Yu *et al.* [44]. They came up with an electronic architecture including open-loop rectifiers in order to determine absolute impedance values as well as two high speed complementary metal oxide semiconductor (CMOS) comparators and a two-input XOR gate followed by a low pass filter to measure impedance phases. However, only the absolute impedance versus frequency was shown, achieving good accuracy in their results. One could deduce that determining the impedance phase by hardware may not be the optimal approach. Another drawback of this system is that, again, frequencies below 100 Hz cannot be achieved, thus limiting its use in real-life biomedical environments. A very interesting approach was presented by Zhang *et al.* [45]. Here, the authors embedded a miniaturized commercial impedance analyzer (AD5933 from Analog Devices) into an integrated platform controlled by an Arduino UNO board. They also developed a smartphone application program and used a Bluetooth module to control the portable potentiostat. They tested the device with biological samples, and succeeded in detecting bovine serum albumin (BSA) at different concentrations. The main drawback was the limitation of the frequency range, which was 10 Hz–10 kHz. This range was indeed wider than the range in previously cited works [43 and 44], yet this may not be enough in some cases. As a matter of fact, many diffusion processes at the electrode-solution interface become important at low frequencies, i.e. below 10 Hz [46–49]. Moreover, their system was customized to perform one measurement at a time, and at some point this should be overcome for the sake of immediacy and multiplexed monitoring of analytes.

TABLE I: Comparison of several commercial potentiostats with the presented prototype in terms of orientative cost, geometry and specifications. Information missing in empty fields was not possible to obtain.

	Price (USD)	Freq. range (Hz)	V range (V)	Size $W \times D \times H$ (cm^3)	Weight (g)	Channels	References
ZENNIUM Electrochemical Workstation	-	$10^{-5} - 4 \times 10^6$	-	$36.4 \times 16 \times 37.6$	11400	5	[30]
Parstat MC	13000	$10^{-5} - 10^6$	± 10	$51.4 \times 40.6 \times 38.7$	-	3	[31]
VMP3	100000	$10^{-5} - 10^6$	$\pm 10/0 - 20$	$49.5 \times 46.5 \times 26$	20000	16	[32]
ACIP100	8500	$10^{-2} - 10^3$	± 2	$19.3 \times 11.2 \times 4.3$	650	1	[33]
MicroAnalyzer 160C	3200	$10^{-2} - 10^5$	± 2.4	$10 \times 6.4 \times 2.4$	150	1	[34]
CHI660E	13000	$10^{-5} - 10^6$	± 10	$36 \times 24 \times 12$	5400	1	[35]
Gamry 1010E	8000	$10^{-5} - 10^6$	± 12	$27 \times 24 \times 6$	3000	1	[36]
Our prototype	300	$10^{-1} - 10^4$	± 2.5	$12 \times 7 \times 2$	70	8	This work

In summary, the literature revised hitherto suggests that there are three main issues regarding the performance of low-cost portable potentiostats that have not been properly solved yet: (1) the expansion of the frequency range to low values, i.e. below 10 Hz (the reader should note from Table I that this is not an issue in the case of most commercially available miniaturized potentiostats, but they do not represent low-cost alternatives); (2) the determination of the capacitive/inductive contribution to the sensor complex impedance (magnitude and phase) and (3) the extension of the miniaturized electronic module to perform parallel measurements. In the present work we intend to individually tackle these issues. We developed a small and wearable potentiostat capable of measuring three-lead electrochemical biosensors, based on a well-described electronic circuit topology [50 and 51]. We designed some additional conditioning electronics to enable the measurement of eight parallel biosensors for redundant and/or multiplexed analyte detection, which is of crucial importance in some clinical and environmental scenarios [49, 52–54]. Moreover, the developed potentiostat allows the user to choose between a pure DC voltage signal for the sensor excitation (thus eventually permitting the performance of cyclic voltammetry as well as amperometric measurements, amongst others) or a DC voltage bias plus a small AC signal at a desired frequency (to perform electrochemical impedance analysis). A graphical user interface (GUI) was also developed in MATLAB R2012a (The Mathworks, Inc.) to enable total control over the device, thus permitting the user to choose which of the eight biosensors to measure, or to measure all of them. The portable potentiostat was tested and validated for the detection of TNF–α cytokines at several concentrations in physiological medium, specifically within the range of 266 pg mL^{-1} to 666 ng mL^{-1}. The authors would like to remark that, as documented previously in this section, the latter is no clinically significant range, and it was chosen arbitrarily to illustrate the performance of the reported potentiostat. Future work will involve the detection of cytokines in real conditions, i.e. in blood and/or saliva in the case of TNF–α, and the characterization of biosensors in terms of linearity, limit of detection, sensitivity and specificity.

II. EXPERIMENTAL: MATERIALS, METHODS AND ELECTRONIC DESIGN

A. Reagents

4-carboxymethyl aryl diazonium (CMA), sodium nitrite ($NaNO_2$), hydrochloric acid (HCl) 37 %, N-hydroxysuccinimide (NHS), N-(3-dimethylaminopropyl)-N'-ethyl-carbodiimide hydrochloride (EDC), potassium ferrocyanide (II), potassium ferricyanide (III) ($K_3[Fe(CN)_6]/K_4[Fe(CN)_6]$) and phosphate buffered saline (PBS) were purchased from Sigma-Aldrich, France. All immunoreagents, i.e. TNF–α cytokines and anti-TNF–α antibodies were purchased from R & D Systems, France.

B. Antibodies and cytokines preparation

Antibodies and cytokines were diluted in PBS buffer, aliquoted, and stored at −20 C following the protocol of the supplier. The TNF–α cytokines were aliquoted before EIS measurements at three arbitrary concentrations: 266 pg mL^{-1}, 13 ng mL^{-1} and 666 ng mL^{-1}, and stored at 4 C. The anti–TNF–α antibody solution was aliquoted at 2.5 μg mL^{-1} in PBS.

C. Miniaturizing the biosensor. Gold WEs chemical modification

The fabrication and characterization of the miniaturized biosensor platform has been previously described [16]. Prior to CMA electroaddressing, the gold working microelectrodes (WEs) surfaces were cleaned with ethanol in an ultrasonic bath for 10 min and dried under a gentle stream of nitrogen. The device was then placed under UV/ozone for 20 min in order to remove all organic contaminants. In parallel, CMA (5 mM) was diazotated in an aqueous solution of HCl (20 mM) and $NaNO_2$ (20 mM) for 10 min at 4 C. Then, four repetitive CV cycles between 0 V and −1 V were applied to the gold WEs, with a scan rate of 100 mV s^{-1}. Afterwards, the anti–TNF–α monoclonal antibodies were covalently attached to the CMA-coated WEs by EDC/NHS (0.1 M) crosslinking both at 0.1 M following a protocol available in the literature [17]. All eight gold WEs were functionalized and measured after the same protocol.

D. Miniaturizing the potentiostat. Design and development of the electronic system

The electronic board that was designed and customized as a miniaturized potentiostat is hereby described in two well-distinguishable parts: the digital and the analogue stages (Figure 1(a)). The power supply stage is described in an additional section for the sake of legibility. The digital stage includes two microcontrollers (μCs) for waveform generation, response acquisition, optional further *in situ* signal post-processing and serial communication with a computer and optionally with other modules. On the other hand, the analogue part includes an electronic circuit topology based on operational amplifiers (OpAmps) and feedback loops for measuring three-lead electrochemical biosensors. A GUI was developed in MATLAB to help the user set measurement parameters such as frequency and voltage amplitude, and for post-processing purposes. The GUI main window is shown in Figure 1(b) and further described in Subsection II D 2.

1. Power supply

A power supply stage is necessary to guarantee the correct operation of each active component in the board (green region in Figure 1(a)). Four low-power integrated chips were required in the present approach. Regarding the digital stage, the MCP1603B (Microchip) is a 2.0 MHz synchronous buck regulator that supplies both μCs with 3.3 V. Although the analogue-to-digital and digital to analogue converters (ADC/DAC) are embedded in the μCs, they require additional power supply in order to guarantee a stable voltage reference. This was provided by the low-noise and low-power ADR4525 from Analog Devices. As for the analogue part of the potentiostatic system, the LM1117 (Texas Instruments) linear regulator and the TC962 (Microchip) high voltage DC-to-DC converter were used to have a bipolar (5 V and −5 V) supply to the OpAmps.

2. Digital stage

In this section we will focus on the description of the digital part of the potentiostatic system, which comprises the intercommunication of two μCs and the computer interface. The PIC32MX795F512L (Microchip), PIC32 hereafter, is a 32–bit, 80 MHz, 1.56 DMIPS/MHz, M4K core with a five stage pipeline and Harvard architecture microcontroller that was given the role of central control unit in the potentiostat. It was programmed to interface a computer via its UART/USB peripheral. Simultaneously, the PIC32 was also programmed to establish serial communication with an additional PIC24FJ128GC010 (Microchip), PIC24, microcontroller based on a

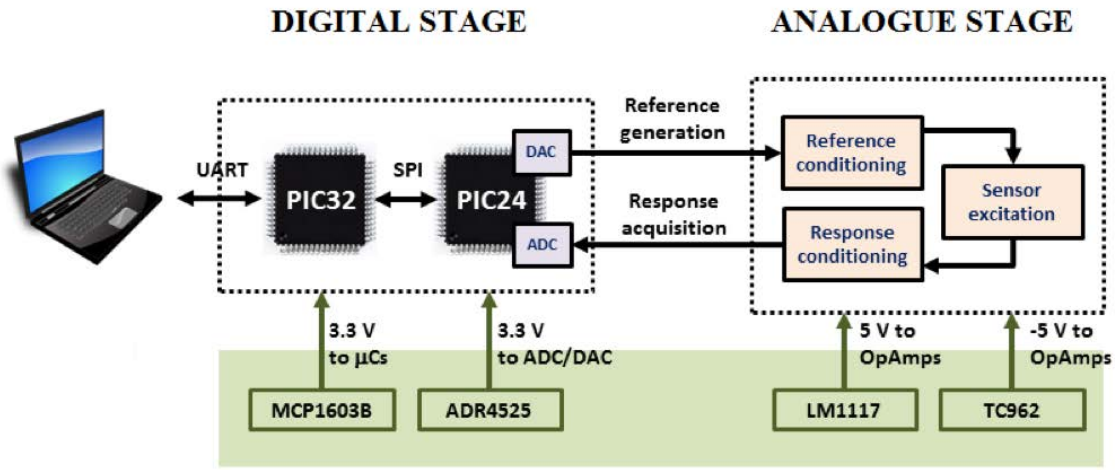

(a)

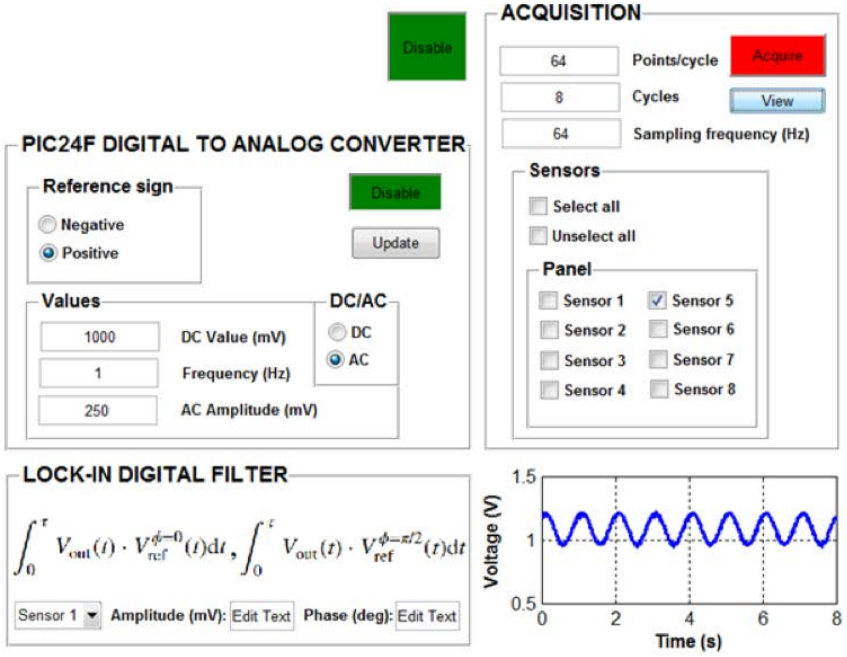

(b)

FIG. 1: (a) High level representation of the portable potentiostatic device, showing the interaction between the digital and analogue stages. The green region comprises the electronic elements responsible for power supply. (b) The graphical user interface and post-processing algorithms were developed in MATLAB. Here, measurement parameters such as frequency, DC polarization and small AC amplitude can be introduced in the GUI main window. This interface also allows for determination of positive/negative reference sign, and the user may choose between sensors 1–8 to measure the corresponding electrochemical impedance.

serial peripheral interface (SPI) protocol. A quick look at Figure 1(a) reveals the role of each μC in the system. In this respect, the PIC24 μC is responsible for waveform generation (sensor excitation) and acquisition of sensor's response for subsequent transmission to the PIC32. To do so, it includes a 10–bit DAC and a 16–bit ADC, respectively. This PIC24's 16–bit ADC is optimal for acquisition in the present application compared to the PIC32, whose 10–bit ADC could impede meeting the required standards of resolution and thus precision. In addition, the PIC32 has no DAC, and thus an external waveform generator would have been required. On the other hand, the PIC32 allows for better processing performance and data storage due to its 32–bit core. *In situ* signal post-processing will be implemented in the future, and if only the PIC24 had been included in the digital architecture, the need for further storage capacity would have arisen. Furthermore, the use of two separate microcontrollers for signal processing and data logging will eventually enable simultaneous measurement and data analysis with one device, which will speed up the monitoring process. Appendix A in the supplementary information includes a flowchart to illustrate the firmware implementation in both microcontrollers.

In parallel, a GUI was developed in MATLAB (1) to set voltage reference parameters and (2) for post-processing of the acquired sensor response. The software implementation of the GUI and processing algorithms is also described in Appendix A. Briefly, the first panel in the GUI (Figure 1(b)) allows for selection between positive or negative voltage reference signals. Regarding the desired electrochemical analysis, a pure DC voltage or a DC plus small AC signal is required. DC offset, AC amplitude and frequency need to be input by the user. In the acquisition panel, WEs 1–8 may be selected for response acquisition and plotting. Signal post-processing was done in the lock-in digital filter panel, where the deduced amplitude and phase were shown for the chosen WEs. As an alternative approach, the PIC32 could be programmed to autonomously generate the excitation signal and also to perform the necessary post-processing steps in case no computer was available. This may be useful in portable and autonomous lab-on-a-chip configurations, where the signal processing would be done *in situ* and displayed on the lab-on-a-chip device. However, this approach has a strong disadvantage: the reference voltage signal and frequency limits should be fixed *a priori*, and changing them would imply the need for reprogramming the board.

3. Analogue stage

First task in the analogue stage is to implement proper "Reference signal conditioning" (Figure 2) electronics. As the DAC in the PIC24 μC works between 0 and 3.3 V, the reference excitation signal is always generated in the positive voltage domain. Nevertheless, regarding the intrinsic nature of the biosensor under study, the user may need a negative voltage. To solve this, specific analogue circuitry was implemented in the electronic board. A switch allows the selection between either an inverter circuitry of gain 1 to create a negative reference from the positive one or a follower circuitry to maintain the positive reference. As already explained in the previous section, the user just needs to select the "negative" option in the DAC reference sign panel in the GUI (Figure 1(b)). In the analogue circuitry of the "Reference signal conditioning" stage, 1 nF decoupling capacitances were added to avoid interferences. Moreover, an additional switch was added in order to choose between a DC offset plus a small AC signal or a pure DC excitation signal. This once again is up to the user and the electrochemical measurement required to be performed on the biosensor, and needs to be indicated in the GUI. For instance, amperometry or cyclic voltammetry (CV) require DC signals, whereas for electrochemical impedance spectroscopy (EIS) analysis, small AC signals need to be applied to the sensor. As in typical three-lead electrochemical cell configurations, the reference voltage is applied to the biosensor between the reference (RE) and the working electrode (WE). In order to maintain this voltage constant, an electrical current flows

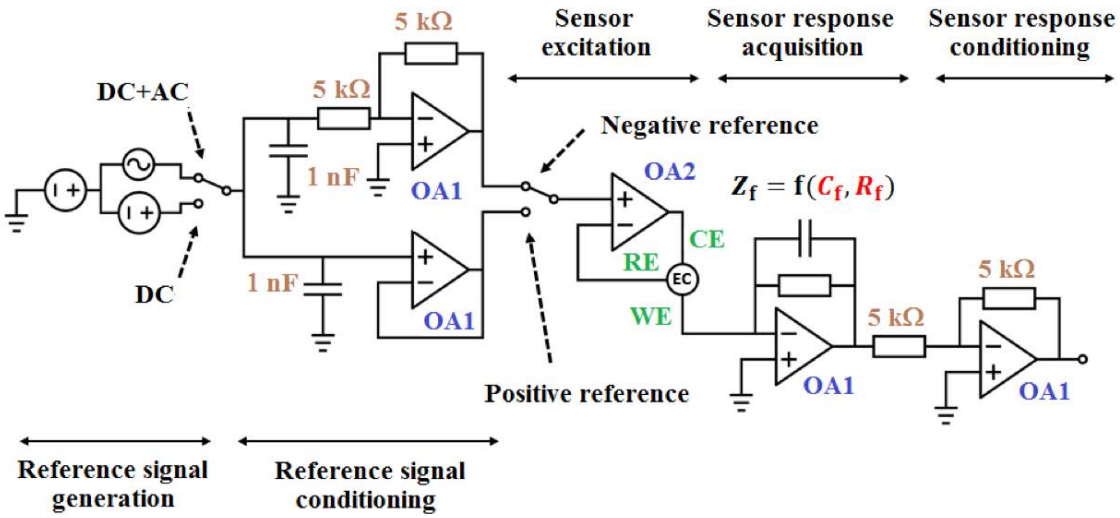

FIG. 2: Schematic of the electronics behind the portable potentiostat, including five main different stages: (1) the "reference signal generation", to choose between pure DC signal or DC bias plus small AC voltage; (2) the "reference signal conditioning" to select the sign of the voltage signal excitation; (3) the "sensor excitation" stage including a three-lead connection to an electrochemical cell (EC); (4) the inverter "sensor response acquisition" stage to transform the sensor response current to a measurable voltage, and finally, (5) the "sensor response conditioning" as a signal adaptation stage before ADC acquisition. OpAmps labelled as OA1 correspond to AD8672, whereas OA2 corresponds to LPC662. The feedback impedance Z_f can be calculated as a function of adjustable C_f and R_f.

between the counter electrode (CE) and the WE. This is described in the "Sensor excitation" stage in Figure 2. Furthermore, a "Sensor response acquisition" stage is needed in order to translate the aforementioned current flowing through the biosensor into a measurable voltage. For this purpose, a transimpedance amplifier (TIA) configuration with a feedback resistor R_f was used. Finally, and since the latter is an inverter configuration, the final "Sensor response conditioning" stage consists of a unity gain inverter configuration to obtain a positive voltage signal that can be digitalized by the ADC in the PIC24 microcontroller. Figure 3 shows the printed circuit board (PCB) of the miniaturized potentiostat connected to the biosensor platform. It is worth mentioning that stages 3 to 5 were implemented eight times in the board, since the biosensor array included eight integrated WEs. This was useful for performing eight measurements in parallel either for detecting different analytes or to study the repeatability of one single measurement.

Throughout the analogue stage, several OpAmps were employed. These can be sorted into two groups, regarding the technical specifications required for each of them. The OpAmp used in the "Sensor excitation" stage (labelled as OA2 in Figure 2) was the LPC662 (Texas Instruments). The only requirement at this stage was that the OpAmp had high enough input impedance (> 1 TΩ in the present case, which is achieved by an ultra-low input bias current of 2 fA), so that it could measure sensors with arbitrarily high impedance; otherwise, it would modify the measured sensor impedance. It should be noticed that the rest of OpAmps in the other stages act as voltage followers or as TIAs, and thus they require maximum precision in order to guarantee the output at the OpAmps. These were labelled as OA1 in Figure 2, and the AD8672 from Analog Devices was chosen in this case. Here, the OpAmp's maximum precision is achieved due to a low input

impedance that prevents any external undesired frequency to be coupled to the signal.

It is worth mentioning that the response signal may not be clean enough to properly deduce the sensor's impedance features. Possible noise sources may arise from (1) the biosensor's intrinsic nature, (2) undesired instabilities of certain electronic components in the potentiostat at some frequencies, (3) the coupling of the network's electrical noise (50/60 Hz and corresponding harmonics), (4) instabilities in the acquisition stage, etc. Indeed, oscillations due to instabilities of the TIAs in the circuitry at certain frequencies were detected due to the capacitive nature of the systems to be measured. Open-loop gain of operational amplifier-based circuitry with feedback such as the one we are dealing with is frequency-dependent, and from Barkhausen stability criterion, oscillations appear if the TIA circuit does not have sufficient phase margin [55]. The latter may be achieved by adding a bypass capacitor C_{f} (Figure 2) in parallel with the feedback resistance, R_{f}. The values of R_{f} and C_{f} need to be regulated regarding the effective impedance of the sensor. Here, values of 150 kΩ and 1 μF were enough to cover the whole range of measured impedances.

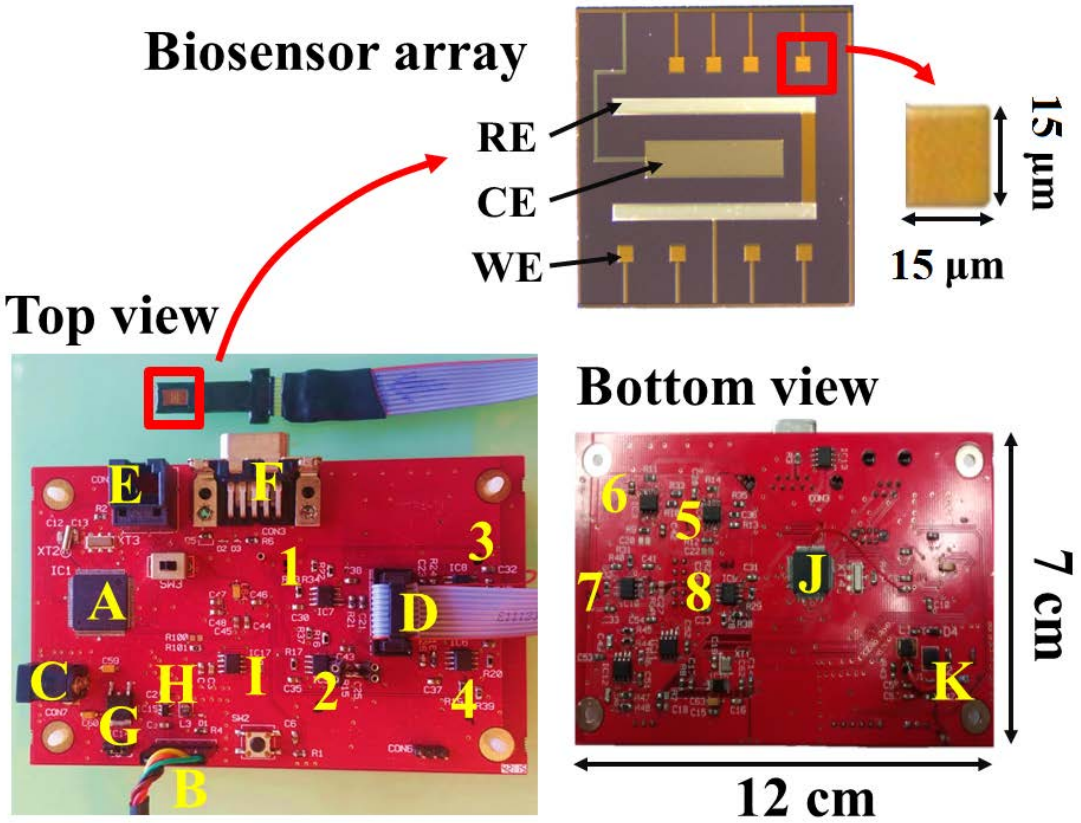

FIG. 3: Manufacturing details of the PCB and the biosensor array. Several electronic components are indicated in the top and bottom views of the PCB. The potentiostatic circuits for the different channels are labelled as 1–4 (top view) and 5–8 (bottom view). Regarding the rest of the elements, A) is the PIC32 microcontroller; B) is the UART connector for PC communication; C) is the external power supply; D) is the 10–pin connector for the biosensor array; E) is the RJ-11 connector to program the microcontrollers; F) is the data bus; G) is the LM1117 voltage regulator; H) is the MCP1603B voltage regulator; I) is the ADR4525 stable voltage reference; J) is the PIC24 microcontroller and K) is the TC962 voltage regulator.

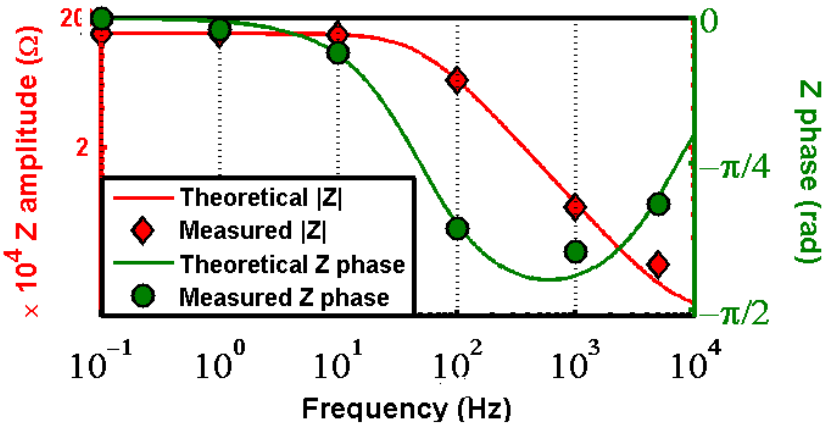

FIG. 4: Bode plot of the equivalent circuit shown in the inset as a proof of concept, showing both theoretical and measured impedance (magnitude in Ω and phase in radians), from 100 mHz to 10 kHz.

4. Signal processing and extraction of parameters

The digital implementation of a lock-in amplifier was used to extract the sensor response signal within a known carrier wave, the frequency of which was fixed by the excitation signal. Once the sensor response is known, i.e. the amplitude and phase shift of the acquired periodic signal, the determination of the sensor impedance just involves an $R_f \mid C_f$ feedback gain, as explained in Section II D 3. From careful circuit analysis of Figure 2, the following expression for the sensor impedance as a function of known parameters can be deduced:

$$Z_s = \frac{V_{ref}\left(\omega_r t + \phi_r\right)}{V_{out}\left(\omega_r t + \phi_s\right)} Z_f, \tag{1}$$

where Z_f is the complex feedback impedance, $V_{ref}\left(\omega_r t + \phi_r\right)$ is the voltage reference signal and $V_{out}\left(\omega_r t + \phi_s\right)$ is the response of the sensor to the reference excitation. Note that the frequency of the sensor response should be the same as the reference signal's, with an additional phase and gain accounting for the intrinsic nature of the sensor. However, due to interferences and additional noise, extra frequencies mask the desired and pure response. Equation 1 is true under the assumption that the equivalent solution resistance is negligible compared to the equivalent polarization resistance of the biosensor. The lock-in amplifier method consists in extracting the characteristic parameters (sensor response amplitude, V_s, and phase shift with respect to reference signal, $\Delta\phi = \phi_s - \phi_r$) of the response to a single-frequency well-defined excitation signal (reference) in an extremely noisy environment [56 and 57]. The lock-in filter is mathematically described in the Appendix B supplementary file.

E. System validation and performance

Having implemented the basic potentiostat as well as the necessary compensation circuitry, we proceeded to the calibration of the device. The validation process was performed with known SMD electrical components simulating Randles equivalent circuits [58 and 59]. A system composed of 1.5 kΩ in series with the parallel of 1 nF and 150 kΩ was used as a proof of concept (equivalent circuit shown as inset in Figure 4). Nine frequencies were taken between 100 mHz and 10 kHz, and the impedance magnitudes as well as phases were

deduced and compared with the theoretical values from impedance analysis, as shown in Figure 4. A sinusoidal AC signal of 500 mV peak-to-peak amplitude with a DC offset of 1 V was used for the calibration of the device. The results shown in Figure 4 demonstrate the applicability of the developed potentiostat in terms of frequency range and also the power of the lock-in digital filter to discriminate the impedance magnitude and phase.

The integrated biosensor array was first electrochemically characterized with a commercial VMP3 multichannel potentiostat (Biologic-EC-Lab, France). All the experiments were carried out at room temperature in an aqueous solution of 5 mM $K_3[Fe(CN)_6]/K_4[Fe(CN)_6]$ in PBS buffer at pH 7.4. CV was used to characterize the bare gold WEs, to electroaddress the CMA coatings and finally to characterize the CMA-modified WEs. EIS with commercial potentiostat was performed onto bare gold WEs and after each step of functionalization: after CMA deposition, after antibody modification and at three cytokine concentrations. After each EIS spectrum performed with the commercial potentiostat, the data were fitted by EC-Lab software. Extraction of EIS parameters gave enough information to optimize the feedback elements in the portable miniaturized potentiostat.

III. RESULTS AND DISCUSSION

A. Diazonium-antibody immobilization onto gold WEs

Figure 5(a) shows the voltammogram corresponding to the electroaddressing process of CMA deposition onto gold WEs. It consists of an initial broad and irreversible cycle with a peak potential at −0.8 V, which corresponds to the reduction of diazotated CMA onto the bare gold WEs surface. The immobilization of this salt was also confirmed by a difference in the shape of CV before and after gold modification, as can be observed in Figure 5(b). A huge decrease in peak-to-peak intensity corresponding to reduction/oxidation of $K_3[Fe(CN)_6]/K_4[Fe(CN)_6]$ on the electrode surface is observed as a result of a large passivation area in the microelectrodes.

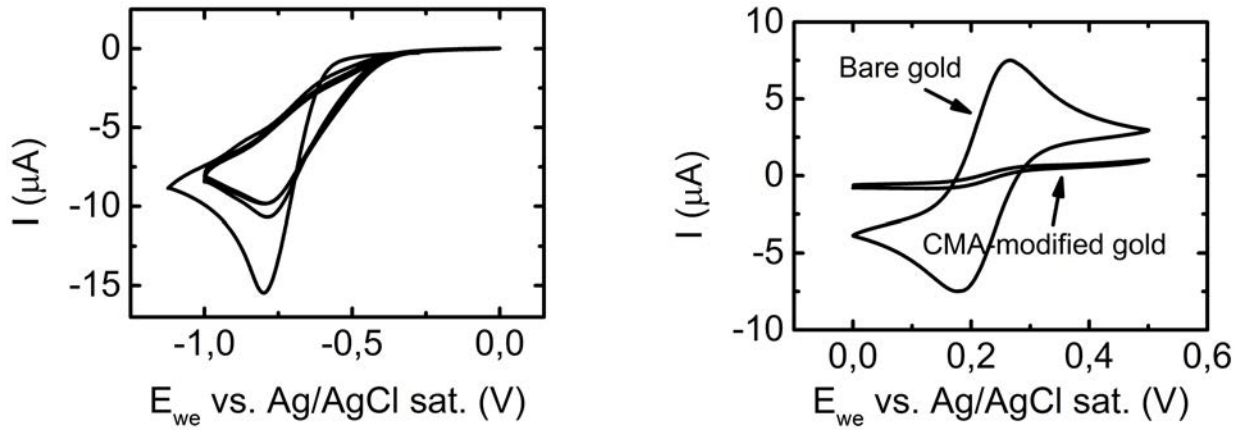

(a) (b)

FIG. 5: Cyclic voltammetry showing (a) CMA deposition onto gold WEs. Four repetitive scans were performed at 100 mV s^{-1} from 0 V to −1 V vs. integrated Ag/AgCl. (b) Difference in voltammogram shapes between bare gold and CMA-coated gold WEs. These were performed at a scan rate of 50 mV s^{-1} from 0 V to 0.5 V vs. integrated Ag/AgCl reference electrode.

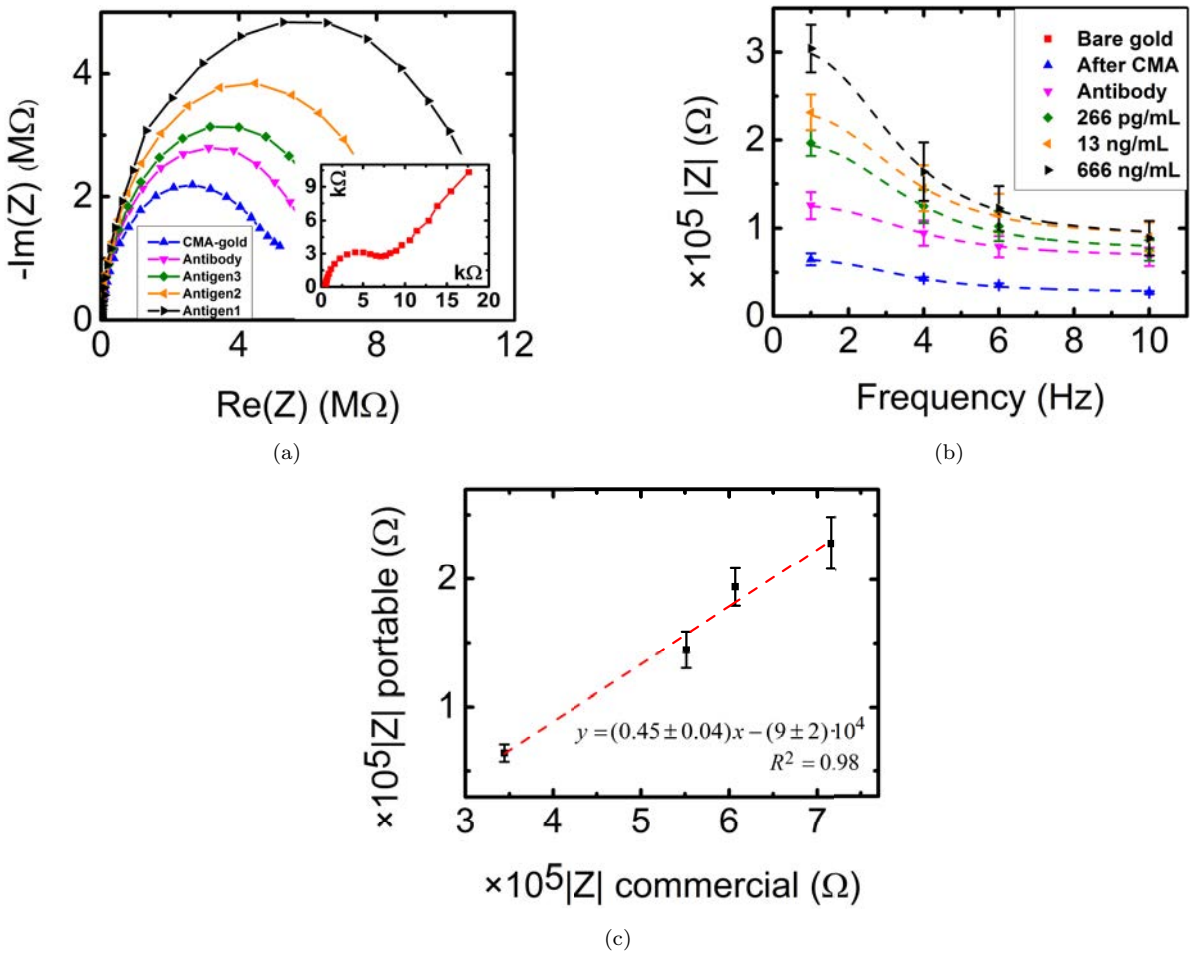

FIG. 6: (a) Nyquist (a) and Bode amplitude (b) plots showing the detection of varying TNF–α concentration measured with the commercial station and the developed potentiostat, respectively. In both cases, an increase in polarization resistance with increasing steps in the functionalization procedure, i.e. from bare gold, CMA-coated gold and anti–TNF–α antibody to cytokines interaction, can be clearly appreciated. (c) Linear calibration curve showing the relation between the absolute impedance at 1 Hz measured by the portable and the commercial potentiostats.

B. Cytokine detection by EIS with commercial potentiostat

EIS was performed with the commercial potentiostat to characterize each functionalization step. The measurements were taken in PBS buffer solution of 5 mM $K_3[Fe(CN)_6]$/ $K_4[Fe(CN)_6]$ at pH 7.4 for all WEs. Figure 6(a) shows Nyquist plots of all steps performed on a representative WE. First semicircle corresponds to CMA-coated gold WE, which is considerably bigger than the bare gold WE Nyquist plot, shown as inset. The second semicircle corresponds to the immobilized anti–TNF–α antibodies. Prior to cytokines incubation, the electrodes were rinsed abundantly with PBS to remove possible remaining electrolyte solution from the sensitive layer. The biosensor was then immediately immersed in a 266 pg mL^{-1} solution of TNF–α cytokines for 30 min incubation at 4 C. It is of crucial importance to perform this step as carefully and fast as possible, in order to prevent denaturation of the immobilized antibodies. Afterwards, the unbounded cytokines were removed by abundant rinsing with PBS, and EIS was performed. The corresponding Nyquist plot proves

for antigen-antibody recognition. These steps were repeated for subsequent increasing cytokines concentration (13 ng mL^{-1} and 666 ng mL^{-1}), providing the corresponding increase in electrochemical impedance, as shown in Figure 6(a).

C. Cytokine detection by EIS with miniaturized potentiostat

From the Nyquist plots shown in Figure 6(a) it can be deduced that the maximum impedance variation between subsequent steps was measured in the frequency range of 1–10 Hz. Thus, the portable electronic board was programmed to perform impedance measurements in such frequency range. The measurements were taken immediately after those with the commercial device. Results are shown as a Bode plot in Figure 6(b). The relation between the absolute impedance at 1 Hz measured by the portable and the commercial potentiostats is shown as a linear calibration plot in Figure 6(c).

We demonstrated that our device can perform electrochemical impedance spectroscopy at frequencies as low as 100 mHz, and also that the lock-in digital filter is useful for discrimination of impedance amplitude and phase, as shown in Figure 4. In the present case, frequencies above 10 kHz are tricky, especially when the sensor impedance achieves very low values. In such cases, the device response is saturated, for the system total gain is $\frac{Z_f}{Z_s}$. A solution to this could be lowering $\mid Z_f \mid$, at the risk of a possible noise coupling at low frequencies. Thus, the most efficient solution would be the implementation of a digital feedback resistor selector, e.g. a multiplexer. This will be considered in future work. Moreover, the implementation of fitting functionality in the MATLAB based GUI will be also addressed in the future, in pursuit of self-contained software to account for important electrochemical parameters measured by this compact and total autonomous miniaturized impedance analyzer.

IV. CONCLUSIONS

A low-cost and miniaturized potentiostat was designed, developed and interfaced with a miniaturized and integrated biosensor array to perform electrochemical impedance analysis at a critical frequency range. The potentiostat prototype was sized $12 \times 7 \times 2$ cm^3, weighed 70 g and had an approximate manufacturing cost of 300 USD. The electronic board design is flexible enough to leave a door open to completely autonomous operation and to the application of several electrochemical techniques, such as amperometry, cyclic voltammetry and electrochemical impedance spectroscopy, and future steps will consider remote data transmission through Internet connection. Impedance spectroscopy is one of the most precise techniques, and it provides detailed characterization of label-free biosensors. Our electronic device was tested on anti–TNF–α-immobilized over CMA-modified gold microelectrodes for the detection of TNF–α cytokines at several concentrations. Surface modification and antibody functionalization of gold electrodes were measured with the portable device, which also successfully discriminated between three concentrations of TNF–α cytokines. We measured impedance absolute values in the range of few hundreds kΩ, features that are comparable to those obtained with the VMP3 commercial impedance analyzer. Our approach succeeds in fixing some of which we consider important issues reported in the literature, such as the performance of measurements at low frequencies (below 10 Hz), the determination of the sensor's contribution to its complex impedance and the performance of eight parallel measurements for multiplexed analyte detection or for single measurement redundancy. The results suggest that the developed device could be useful and easily embeddable in POC environments.

ACKNOWLEDGMENTS

The research leading to these results has received funding from the European Union's 7FP (*SEA-on-a-CHIP*, Grant Agreement no. 614168) and the European Union's Horizon 2020 (*HEARTEN*, Grant Agreement no. 643694). R.P. acknowledges an FPU grant from the Spanish Ministerio de Educación, Cultura y Deporte.

REFERENCES

[1] Mariell Jessup and Susan Brozena. Medical progress. heart failure. *New England Journal of Medicine*, 348(20):2007–2018, 2003.

[2] Michael Lee, Nadia Zine, Abdellatif Baraket, Miguel Zabala, Francesca Campabadal, Raffaele Caruso, Maria Giovanna Trivella, Nicole Jaffrezic-Renault, and Abdelhamid Errachid. A novel biosensor based on hafnium oxide: Application for early stage detection of human interleukin-10. *Sensors and Actuators B: Chemical*, 175:201–207, 2012.

[3] Lars Gullestad, Thor Ueland, Leif Erik Vinge, Alexandra Finsen, Arne Yndestad, and Pål Aukrust. Inflammatory cytokines in heart failure: mediators and markers. *Cardiology*, 122(1):23–35, 2012.

[4] Ståle H Nymo, Johannes Hulthe, Thor Ueland, John McMurray, John Wikstrand, Erik T Askevold, Arne Yndestad, Lars Gullestad, and Pål Aukrust. Inflammatory cytokines in chronic heart failure: interleukin-8 is associated with adverse outcome. results from corona. *European journal of heart failure*, 16(1):68–75, 2014.

[5] Mark S Slaughter, Francis D Pagani, Joseph G Rogers, Leslie W Miller, Benjamin Sun, Stuart D Russell, Randall C Starling, Leway Chen, Andrew J Boyle, Suzanne Chillcott, et al. Clinical management of continuous-flow left ventricular assist devices in advanced heart failure. *The Journal of Heart and Lung Transplantation*, 29(4):S1–S39, 2010.

[6] Raffaele Caruso, Salvatore Trunfio, Filippo Milazzo, Jonica Campolo, Renata De Maria, Tiziano Colombo, Marina Parolini, Aldo Cannata, Claudio Russo, Roberto Paino, et al. Early expression of pro-and anti-inflammatory cytokines in left ventricular assist device recipients with multiple organ failure syndrome. *ASAIO Journal*, 56(4):313–318, 2010.

[7] Stephen Kaptoge, Sreenivasa Rao Kondapally Seshasai, Pei Gao, Daniel F Freitag, Adam S Butterworth, Anders Borglykke, Emanuele Di Angelantonio, Vilmundur Gudnason, Ann Rumley, Gordon Lowe, et al. Inflammatory cytokines and risk of coronary heart disease: new prospective study and updated meta-analysis. *European heart journal*, 35(9):578–589, 2014.

[8] Raffaele Caruso, Alessandro Verde, Manuela Cabiati, Filippo Milazzo, Chiara Boroni, Silvia Del Ry, Marina Parolini, Claudia Vittori, Roberto Paino, Luigi Martinelli, et al. Association of pre-operative interleukin-6 levels with interagency registry for mechanically assisted circulatory support profiles and intensive care unit stay in left ventricular assist device patients. *The Journal of Heart and Lung Transplantation*, 31(6):625–633, 2012.

[9] Michaela Maurer, Sonja Burri, Stefano de Marchi, Roger Hullin, Michele Martinelli, Paul Mohacsi, and Otto M Hess. Plasma homocysteine and cardiovascular risk in heart failure with and without cardiorenal syndrome. *International journal of cardiology*, 141(1):32–38, 2010.

[10] Romina Navarri, Stefano Lunghetti, Matteo Cameli, Sergio Mondillo, Roberto Favilli, Francesca Scarpini, and Luca Puccetti. Neurohumoral improvement and torsional dynamics in patients with heart failure after treatment with levosimendan. *IJC Heart & Vasculature*, 7:153–157, 2015.

[11] Kenneth G-J Ooi, Grazyna Galatowicz, Hamish MA Towler, Susan L Lightman, and Virginia L Calder. Multiplex cytokine detection versus elisa for aqueous humor: Il-5, il-10, and ifnγ profiles in uveitis. *Investigative ophthalmology & visual science*, 47(1):272–277, 2006.

[12] Gopalan Soman, Xiaoyi Yang, Hengguang Jiang, Steve Giardina, and Gautam Mitra. Comparison of gd2 binding capture elisa assays for anti-gd2-antibodies using gd2-coated plates and a gd2-expressing cell-based elisa. *Journal of immunological methods*, 373(1):181–191, 2011.

[13] Chris J Watson, Mark T Ledwidge, Dermot Phelan, Patrick Collier, Jennifer C Byrne, Michael J Dunn, Kenneth M McDonald, and John A Baugh. Proteomic analysis of coronary sinus serum reveals leucine-rich α2-glycoprotein as a novel biomarker of ventricular dysfunction and heart failureclinical perspective. *Circulation: Heart Failure*, 4(2):188–197, 2011.

[14] Albert Alcacer, Angelos Streklas, Abdoullatif Baraket, Nadia Zine, Abdelhamid Errachid, and Joan Bausells. Development of biosensors for non-invasive measurements of heart failure biomarkers in saliva. In *SPIE Microtechnologies*, pages 102460H–102460H. International Society for Optics and Photonics, 2017.

[15] Abdoullatif Baraket, Michael Lee, Nadia Zine, Nourdin Yaakoubi, Joan Bausells, and Abdelhamid Errachid. A flexible electrochemical micro lab-on-chip: application to the detection of interleukin-10. *Microchimica Acta*, 183(7):2155–2162, 2016.

[16] Abdoullatif Baraket, Michael Lee, Nadia Zine, Monique Sigaud, Joan Bausells, and Abdelhamid Errachid. A fully integrated electrochemical biosensor platform fabrication process for cytokines detection. *Biosensors and Bioelectronics*, 2016.

[17] Francesca G Bellagambi, Abdoullatif Baraket, Alessia Longo, Monica Vatteroni, Nadia Zine, Joan Bausells, Roger Fuoco, Fabio Di Francesco, Pietro Salvo, Georgia S Karanasiou, et al. Electrochemical biosensor platform for tnf-α cytokines detection in both artificial and human saliva: Heart failure. *Sensors and Actuators B: Chemical*, 2017.

[18] Mouhssine Benlarbi, Loïc J Blum, and Christophe A Marquette. Su-8-carbon composite as conductive photoresist for biochip applications. *Biosensors and Bioelectronics*, 38(1):220–225, 2012.

[19] Alessia Longo, Abdoullatif Baraket, Monica Vatteroni, Nadia Zine, Joan Baussells, Fabio Di Francesco, Georgia S Karanasiou, Dimitrios I Fotiadis, Arianna Menciassi, Abdelhamid Errachid, et al. Highly sensitive electrochemical biomems for tnf-α detection in humansaliva: Heart failure. *Procedia Engineering*, 168:97–100, 2016.

[20] Tze Sian Pui, Patthara Kongsuphol, Sunil K Arya, and Tushar Bansal. Detection of tumor necrosis factor (tnf-α) in cell culture medium with label free electrochemical impedance spectroscopy. *Sensors and Actuators B: Chemical*, 181:494–500, 2013.

[21] Anjum Qureshi, Yasar Gurbuz, and Javed H Niazi. Biosensors for cardiac biomarkers detection: A review. *Sensors and Actuators B: Chemical*, 171:62–76, 2012.

[22] E Sánchez-Tirado, C Salvo, A González-Cortés, P Yáñez-Sedeño, F Langa, and JM Pingarrón. Electrochemical immunosensor for simultaneous determination of interleukin-1 beta and tumor necrosis factor alpha in serum and saliva using dual screen printed electrodes modified with functionalized double–walled carbon nanotubes. *Analytica Chimica Acta*, 959:66–73, 2017.

[23] Patthara Kongsuphol, Hui Hwee Ng, Joanna P Pursey, Sunil K Arya, Chee Chung Wong, Eugen Stulz, and Mi Kyoung Park. Eis-based biosensor for ultra-sensitive detection of tnf-α from non-diluted human serum. *Biosensors and Bioelectronics*, 61:274–279, 2014.

[24] A Baraket, M Lee, N Zine, F Besseuille, N Yaakoubi, MG Trivella, J Bausells, M Zabala, N Jaffrezic-Renault, and A Errachid. P49 (ei0414) a highly sensitive biosensor for detecting tnf-α cytokine to predict the biocompatibility of transplanted organs. *Int J Artif Organs*, 34(8):661, 2011.

[25] Zhengzhi Yin, Yan Liu, Li-Ping Jiang, and Jun-Jie Zhu. Electrochemical immunosensor of tumor necrosis factor α based on alkaline phosphatase functionalized nanospheres. *Biosensors and Bioelectronics*, 26(5):1890–1894, 2011.

[26] Ying Liu, Qing Zhou, and Alexander Revzin. An aptasensor for electrochemical detection of tumor necrosis factor in human blood. *Analyst*, 138(15):4321–4326, 2013.

[27] Ying Liu, Timothy Kwa, and Alexander Revzin. Simultaneous detection of cell-secreted tnf-α and ifn-γ using micropatterned aptamer-modified electrodes. *Biomaterials*, 33(30):7347–7355, 2012.

[28] Arthur M Feldman, Alain Combes, Daniel Wagner, Toshiaki Kadakomi, Toru Kubota, Yun You Li, and Charles McTiernan. The role of tumor necrosis factor in the pathophysiology of heart failure. *Journal of the American College of Cardiology*, 35(3):537–544, 2000.

[29] Guillermo Torre-Amione, Samir Kapadia, Claude Benedict, Hakan Oral, James B Young, and Douglas L Mann. Proinflammatory cytokine levels in patients with depressed left ventricular ejection fraction: a report from the studies of left ventricular dysfunction (solvd). *Journal of the American College of Cardiology*, 27(5):1201–1206, 1996.

[30] Germany) ZAHNER-elektrik GmbH & Co KG (Kronach. Zennium electrochemical workstation.

[31] USA) Ametek Process & Analytical (Newark, DE. Parstat mc-1000.

[32] France) Bio-Logic Science Instruments (Seyssinet-Pariset. Vmp3.

[33] Taiwan) Zensor Research & Development (Taichung. Acip100.

[34] USA) Hormiangz LLC (Longmont, CO. Microanalyzer 160c.

[35] TX USA) CH Instruments, Inc. (Austin. Chi660e.

[36] USA) Gamry Instruments (Warminster, PA. Gamry 1000e.

[37] Ajeet Kaushik, Abhay Vasudev, Sunil K Arya, Syed Khalid Pasha, and Shekhar Bhansali. Recent advances in cortisol sensing technologies for point-of-care application. *Biosensors and Bioelectronics*, 53:499–512, 2014.

[38] Matthew Boyd and Tom Woolley. Point of care testing. *Surgery (Oxford)*, 34(2):91–93, 2016.

[39] Curtis D. Chin, Vincent Linder, and Samuel K. Sia. Commercialization of microfluidic point-of-care diagnostic devices. *Lab Chip*, 12:2118–2134, 2012.

[40] Dina Gomaa, John O Shinn, Joseph R Dowd, and Richard D Branson. Point of care testing: A comparison of two devices in the intensive care unit. *Respiratory Care*, 61(10), 2016.

[41] Joseph Wang. Electrochemical biosensors: towards point-of-care cancer diagnostics. *Biosensors and Bioelectronics*, 21(10):1887–1892, 2006.

[42] Andres Felipe Diaz Cruz, Nicolas Norena, Ajeet Kaushik, and Shekhar Bhansali. A low-cost miniaturized potentiostat for point-of-care diagnosis. *Biosensors and Bioelectronics*, 62:249–254, 2014.

[43] Zhanming Li, Zunzhong Ye, Yingchun Fu, Yonghua Xiong, and Yanbin Li. A portable electrochemical immunosensor for rapid detection of trace aflatoxin b 1 in rice. *Analytical Methods*, 8(3):548–553, 2016.

[44] Xiaojian Yu, Mihai Esanu, Scott MacKay, Jie Chen, Mohamad Sawan, David Wishart, and Wayne Hiebert. An impedance detection circuit for applications in a portable biosensor system. In *Circuits and Systems (ISCAS), 2016 IEEE International Symposium on*, pages 1518–1521. IEEE, 2016.

[45] Diming Zhang, Yanli Lu, Qian Zhang, Lei Liu, Shuang Li, Yao Yao, Jing Jiang, Gang Logan Liu, and Qingjun Liu. Protein detecting with smartphone-controlled electrochemical impedance spectroscopy for point-of-care applications. *Sensors and Actuators B: Chemical*, 222:994–1002, 2016.

[46] Motonari Adachi, Masaru Sakamoto, Jinting Jiu, Yukio Ogata, and Seiji Isoda. Determination of parameters of electron transport in dye-sensitized solar cells using electrochemical impedance spectroscopy. *The Journal of Physical Chemistry B*, 110(28):13872–13880, 2006. PMID: 16836336.

[47] Juan Bisquert, Luca Bertoluzzi, Ivan Mora-Sero, and Germa Garcia-Belmonte. Theory of impedance and capacitance spectroscopy of solar cells with dielectric relaxation, drift-diffusion transport, and recombination. *The Journal of Physical Chemistry C*, 118(33):18983–18991, 2014.

[48] Annemiek ter Heijne, Olivier Schaetzle, Sixto Gimenez, Lucia Navarro, Bert Hamelers, and Francisco Fabregat-Santiago. Analysis of bio-anode performance through electrochemical impedance spectroscopy. *Bioelectrochemistry*, 106:64–72, 2015.

[49] Qing Wang, Jacques-E. Moser, and Michael Grtzel. Electrochemical impedance spectroscopic analysis of dye-sensitized solar cells. *The Journal of Physical Chemistry B*, 109(31):14945–14953, 2005. PMID: 16852893.

[50] MM Ahmadi, G Jullien, and K Iniewski. Circuits for amperometric electrochemical sensors. *VLSI Circuits for Biomedical Applications*, pages 309–326, 2008.

[51] Mohammad Mahdi Ahmadi and Graham A Jullien. Current-mirror-based potentiostats for three-electrode amperometric electrochemical sensors. *IEEE Transactions on Circuits and Systems I: Regular Papers*, 56(7):1339–1348, 2009.

[52] Claudia Barzen, Andreas Brecht, and Guenter Gauglitz. Optical multiple-analyte immunosensor for water pollution control. *Biosensors and Bioelectronics*, 17(4):289–295, 2002.

[53] Jia Li and Joanne Macdonald. Multiplexed lateral flow biosensors: technological advances for radically improving point-of-care diagnoses. *Biosensors and Bioelectronics*, 83:177–192, 2016.

[54] Eleonora Petryayeva and W Russ Algar. Multiplexed homogeneous assays of proteolytic activity using a smartphone and quantum dots. *Analytical chemistry*, 86(6):3195–3202, 2014.

[55] Akshay Bhat. Stabilize your transimpedance amplifier. 2012.

[56] Richard Burdett. Amplitude modulated signals: The lock-in amplifier. *Handbook of Measuring System Design*, 2005.

[57] John H Scofield. Frequency-domain description of a lock-in amplifier. *American Journal of Physics*, 62(2):129–133, 1994.

[58] Andrzej Lasia. Electrochemical impedance spectroscopy and its applications. In *Modern aspects of electrochemistry*, pages 143–248. Springer, 2002.

[59] John Edward Brough Randles. Kinetics of rapid electrode reactions. *Discussions of the faraday society*, 1:11–19, 1947.

Appendix A

Firmware and software implementation: description and flowcharts

The digital stage of the potentiostatic system is based on the intercommunication of two microcontrollers and a computer interface. Scheme A.1 below describes in a flowchart the firmware running in both microcontrollers, and the role played by the MATLAB-based graphical user interface (GUI). The states and actions of each microcontroller and the PC-side software are organized column-wise. Briefly, the communication is established between MATLAB-PIC32 (*via* UART). The PIC32 (master) initiates communication with PIC24 (slave) *via* SPI, and eventually with other modules (dotted panel), yet the latter is out of the scope of this work. The user sets the measurement parameters in the GUI, and these are transmitted to the PIC24 by the PIC32. When the measurement starts, the GUI rests waiting for the resulting data. The PIC24, basing on the parameters introduced by the user, generates the reference signal to excite the sensor and acquires its response. Both reference and response signals are transmitted to the PIC32, which in turn transmits them to the computer, where they are further processed. Eventually, the processing algorithms could be implemented on-board in the PIC32 (dotted panel).

Scheme A.2 shows a detailed flowchart description of the MATLAB-based software, including the GUI and the post-processing algorithm. Concretely, the user can decide between a positive and a negative reference signal, and if it consists of a DC or AC waveform. In the latter case, frequency and small AC amplitude are required, apart from the DC offset voltage. Finally, the user may select the working electrode(s) to be measured. When the software receives the data arrays (including reference signal and sensor(s) response), these are used by the lock-in filter algorithm module as described in Appendix B.

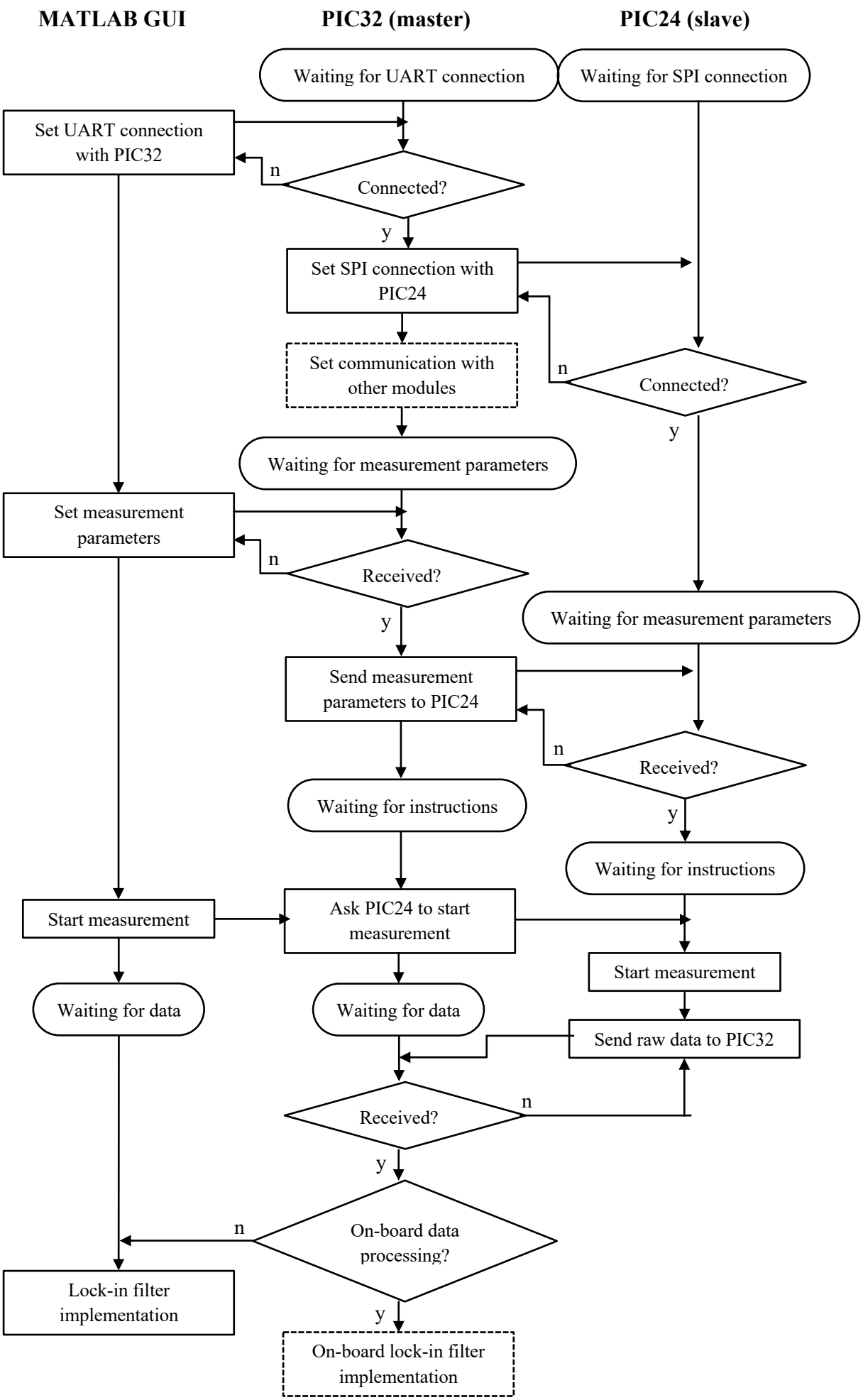

Scheme A.1. Flowchart description of firmware running in the microcontrollers and relation with the MATLAB software.

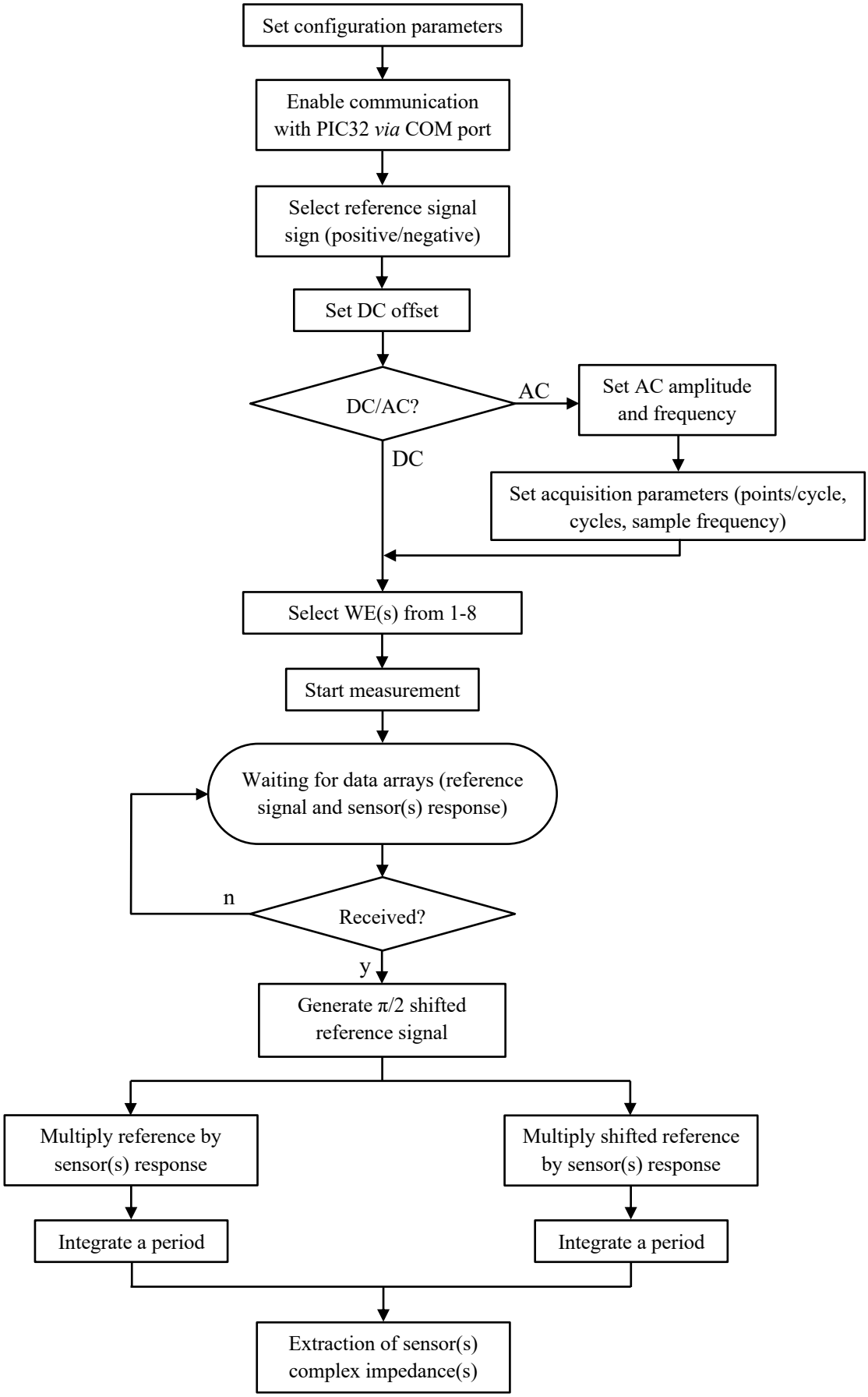

Scheme A.2. Flowchart description of MATLAB software.

Appendix B

On the working principle of the lock-in amplifier

The equations provided hereby describe in detail how V_s and $\Delta\varphi$ may be deduced by simple algebraic and geometrical manipulation.

$$V_{\mathrm{ref}}^{0}(t) = V_{\mathrm{r}} \sin(2\pi f_{\mathrm{r}} t + \varphi_{\mathrm{r}})$$

$$V_{\mathrm{ref}}^{\pi/2}(t) = V_{\mathrm{r}} \sin\left(2\pi f_{\mathrm{r}} t + \varphi_{\mathrm{r}} + \frac{\pi}{2}\right)$$

$$V_{\mathrm{out}}(t) = V_{\mathrm{s}} \sin(2\pi f_{\mathrm{s}} t + \varphi_{\mathrm{s}}) + \sum_{i \neq \mathrm{s}} V_i \sin\left(2\pi f_i t + \varphi_i\right) + N(t)$$

$$\alpha = \int_0^{T_{\mathrm{r}}=1/f_{\mathrm{r}}} V_{\mathrm{out}}(t) \cdot V_{\mathrm{ref}}^{0}(t)\, \mathrm{d}t \xrightarrow{f_{\mathrm{r}}=f_{\mathrm{s}}} \alpha = \frac{1}{2} V_{\mathrm{r}} V_{\mathrm{s}} T_{\mathrm{r}} \cos(\varphi_{\mathrm{s}} - \varphi_{\mathrm{r}})$$

$$\beta = \int_0^{T_{\mathrm{r}}=1/f_{\mathrm{r}}} V_{\mathrm{out}}(t) \cdot V_{\mathrm{ref}}^{\pi/2}(t)\, \mathrm{d}t \xrightarrow{f_{\mathrm{r}}=f_{\mathrm{s}}} \beta = \frac{1}{2} V_{\mathrm{r}} V_{\mathrm{s}} T_{\mathrm{r}} \sin(\varphi_{\mathrm{s}} - \varphi_{\mathrm{r}})$$

$$\boxed{\Delta\varphi = \operatorname{atan}\left(\frac{\beta}{\alpha}\right)}$$

$$\boxed{V_{\mathrm{s}} = \frac{2}{V_{\mathrm{r}} T_{\mathrm{r}}} \sqrt{\alpha^2 + \beta^2}}$$

5.2 Integration of amperometry and potentiometry

After successfully developing a low-cost and miniaturized device for measuring electrochemical impedance spectroscopy, we aimed at designing a complementary device capable of implementing both the amperometric and potentiometric techniques. The architecture of the device basically consists of a digital and an analogue stage. The former is composed of a PIC32MX795 (Microchip Technology) microcontroller interfacing a HUZZAH EPS8266 (Adafruit Industries) microcontroller that contains a full Wi-Fi front-end. The measurement settings are configured through the digital stage, which is also responsible for generating the voltage excitation signal through its digital-to-analogue converter (DAC). The sensor is interfaced in the analogue stage, and its response is acquired by the analogue-to-digital converter (ADC) back to the PIC32 microcontroller, which processes the data and sends it to the ESP8266 module through I2C communication. From there, the data is dump to the network via Wi-Fi.

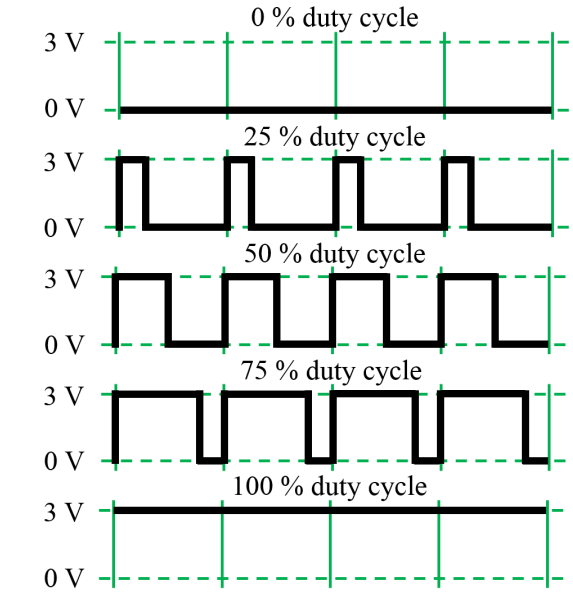

(A)

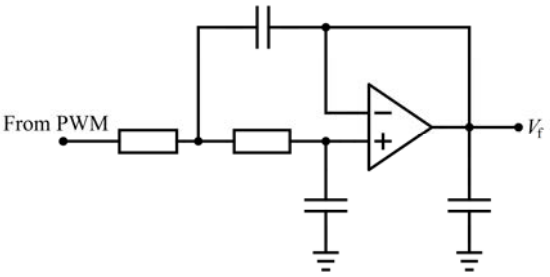

(B)

FIGURE 5.1: Generation of a DC voltage signal by PWM. (A) Schematic of the PWM method, with the equivalence between the width of the pulses and the expected DC value. (B) Second-order (∼ 40 dB attenuation per decade) Sallen-Key low-pass filter outputting an actual DC voltage.

The analogue part consists basically of six differentiated stages: the power stage, the generation of a voltage excitation for amperometry, the (current) detection circuitry for amperometry, the (open-source voltage) detection circuitry for potentiometry, the data processing circuitry and the transmission stage. It is worth mentioning that due to initial specifications and requirements, the whole system was designed for interfacing two-electrode sensors.

Along the following sections, technical details on the implementation of powering stage, amperometry and potentiometry measurements, software and preparation of ITO-based pH electrodes for proof-of-concept are provided.

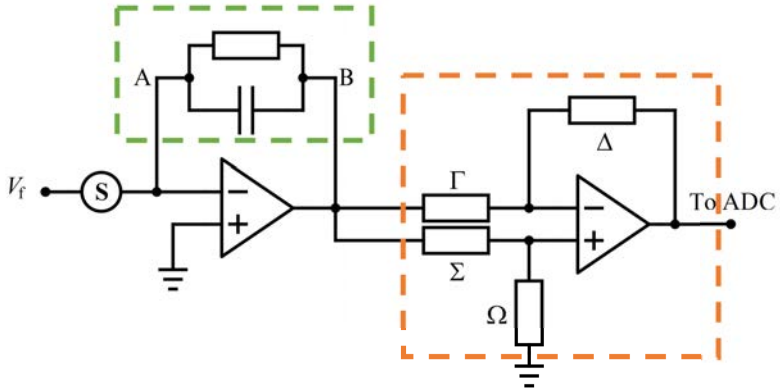

(A)

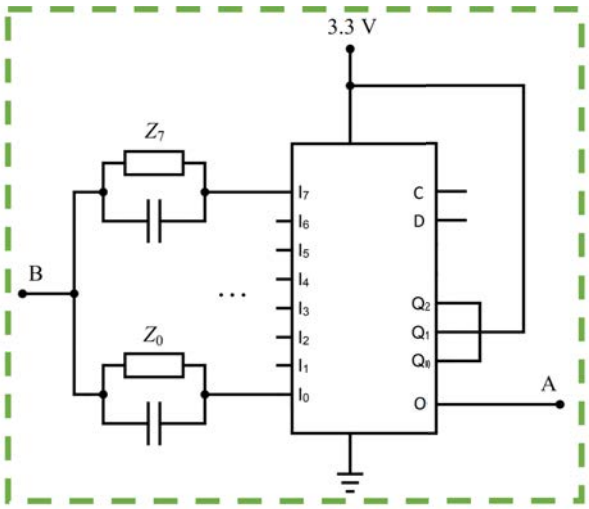

(B)

FIGURE 5.2: Electronic circuitry for amperometric excitation and measurement of a two-lead sensor –S–. (A) A constant voltage (V_f) is applied at the working electrode of the sensor, and the resulting current is turned to a voltage by a feedback impedance (green rectangle, which can be selected digitally out of eight impedances in a multiplexor shown in (B)). The orange rectangle points out a signal conditioning stage outputing a positive response regarding the configuration of the Δ, Γ, Σ and Ω resistors.

5.2.1 Power stage

The power stage consists of a 4000 mA h rechargeable battery with an output voltage of 3.7 V. A swithching regulator (TPS799) placed at the battery output provides a constant DC value of 3.3 V, and another switching regulator (LM2611A) outputs a constant and stable level of −3.3 V. The 3.7 V original signal powers directly the Wi-Fi communication transceiver HUZZAH EPS8266. The 3.3 V line powers the digital parts of the electronics, control and power-on-reset LEDs, and the positive lead to the analogue part. The −3.3 V line powers the negative lead to the analogue part. Moreover, decoupling and bulk capacitors were strategically distributed in order to guarantee a proper power supply along the whole system.

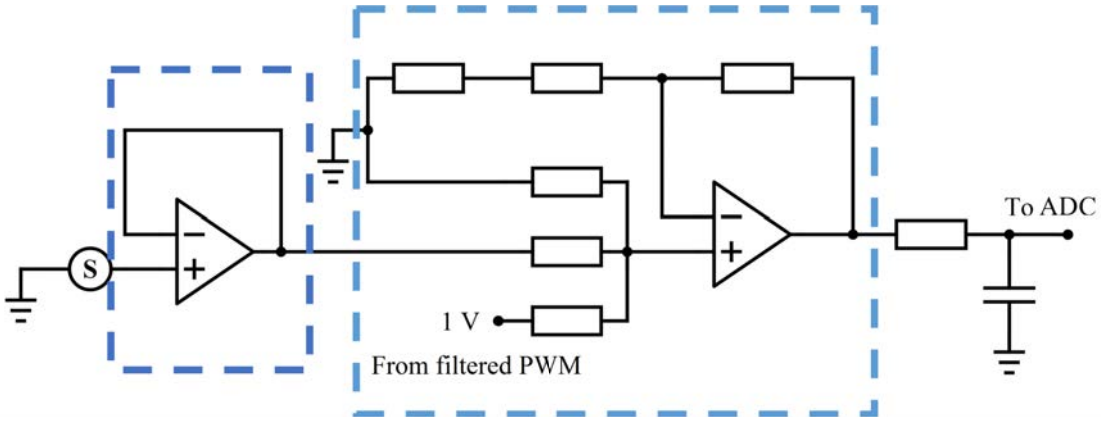

FIGURE 5.3: Electronic circuitry for potentiometric measurement of open-source voltage between the two leads of a sensor –S–. The dark blue rectangle is a voltage follower-configured operational amplifier. The measured voltage is shifted 1 V towards positive values by means of an adder configuration (light blue rectangle), and finally filtered before ADC acquisition.

5.2.2 Signal generation for amperometric excitation

The amperometry measurement requires a constant voltage for exciting the sensor. This was generated by means of a pulse modulating system (PWM), consisting in the generation of a squared AC signal with a variable duty cycle provided by the microcontroller, and which must then go through a low-pass filter. This is shown in Figure 5.1. The relationship between the pulse width and the equivalent voltage level can be appreciated in Figure 5.1a. Figure 5.1b shows the second-order low-pass Sallen-Key filter employed in this design for filtering the PWM-generated signal and cancelling all the noise levels that there may be. The operational amplifier of the active low-pass filter can be configured either in the inverter mode or in the voltage follower mode, depending on whether the amperometry experiment requires a negative or a positive voltage level. In the present circuit, the covered range goes from -3 V to 3 V, with a precission of 3.2 mV.

5.2.3 Detection stages for amperometry and potentiometry

The analogue electronics for the detection stages of amperometry (Figure 5.2) and potentiometry (Figure 5.3) are clearly differentiated and still the design is such that both measurements can be conducted simultaneously. To this end, the virtual mass potential used at the positive input lead of the transimpedance amplifier (left-most operational amplifier in Figure 5.2a) must be the same as the reference potential in the potentiometric circuit (on one lead of the sensor in Figure 5.3). This way, the potentiometry measurement does not affect the amperometry measurement and *viceversa*. This approach was inspired by the work of Schelter *et al.* [202], with the difference that we are employing ion sensitive electrodes (ISEs) for the potentiometry measurement and Schelter made use of ion sensitive field effect transistors (ISFETs).

Regarding the electronics for amperometry, Figure 5.2a shows the transimpedance amplifier used for the current measurement and transformation into a measurable voltage by a variable feedback impedance. The variable feedback impedance was implemented by means of a multiplexer (integrated circuit ADG728), with eight different input impedances (composed of the parallel association of a resistor and a capacitor).

This is shown in Figure 5.2b, where the eight input impedances are $\{I_0, ..., I_7\}$ and the output impedance is O. The latter is selected by three selector inputs, $\{Q_0, Q_1, Q_2\}$, and the whole integrated circuit is interfaced by the microcontroller *via* I2C through the C (clock) and D (data) inputs. All this is followed by an inversor stage, which changes the sign of the resulting voltage signal in case this is negative, so that it can be acquired by the microcontroller's analogue-to-digital converter (ADC), for the range of detection of the ADC varies from 0 V to 3.3 V. For this, if the signal is positive at the output of the transimpedance amplifier, then resistors Δ and Σ are 0 and resistors Γ and Ω are not placed (infinitive resistance paths). This would be the voltage follower configuration and the signal would still be positive at the output of the amplifier. On the other hand, if the signal is negative at the output of the first transimpedance amplifier, then the resistor Σ is not placed (path of infinitive resistance) and Ω is zero, and Γ and Δ are resistors of the same value; this is an inverter configuration, and the output signal is positive.

The amperometric sensor is connected to the negative input lead of the operational amplifier, as shown in Figure 5.2a. The system mass potential is connected to the positive input lead; this way, the current flowing through the sensor corresponds to the voltage difference caused by the sensor polarization voltage and the virtual ground value corresponding to the mass at the positive lead of the operational amplifier. As mentioned before, this ground potential is taken as a reference by the potentiometry circuit.

Regarding the electronics for the monitorization of open ciruit potential, Figure 5.3 shows the potentiometric measurement stage. The sensor signal goes through the positive input lead of the operational amplifier configured as a voltage follower. The output of this stage goes through one of the branches entering a voltage adder, which ensures a positive signal at the ADC. This 1 V offset is deleted *via* software to show the actual values.

5.2.4 Signal processing, data transmission and control software

The processing and data transmission stage consists of two devices: the PIC32MX795 microcontroller and the HUZZAH ESP8266 transceiver. The PIC32MX795 microcontroller is a 32 bit RISC architecture-based processor with a serial USB peripheral that permits (1) to load the measurement configuration parameters; (2) the generation of the powering signals for the amperometry measurements; (3) the analogue-to-digital simultaneous conversion of the amperometric and potentiometric sensors by means of the microcontroller's 10 bit ADCs; (4) the configuration of the feedback resistors, by means of the I2C communication with the ADG728 device (the multiplexer); (5) the data processing and (6) the transmission by means of a second I2C port of the data to the Wi-Fi transceiver HUZZAH ESP8266. The HUZZAH transceiver is a device that can be connected to a Wi-Fi network and can transfer the data as if it was a computer. Moreover, this device holds a connector where the power battery can be plugged.

The whole device is integrated in a compact box fabricated by 3D printing for isolation. The sensor leads were implemented with microUSB connectors to electrically isolate them from the environment. The control software was based on open-source Python programming language. A view of the main software front panel is shown in Figure 5.4. First, the user must select, from the top-left panels, the COM ports for configuration of the potentiostatic device and for the data transmitter (which can be either the same potentiostat –the transmission would be done *via* USB cable– or the

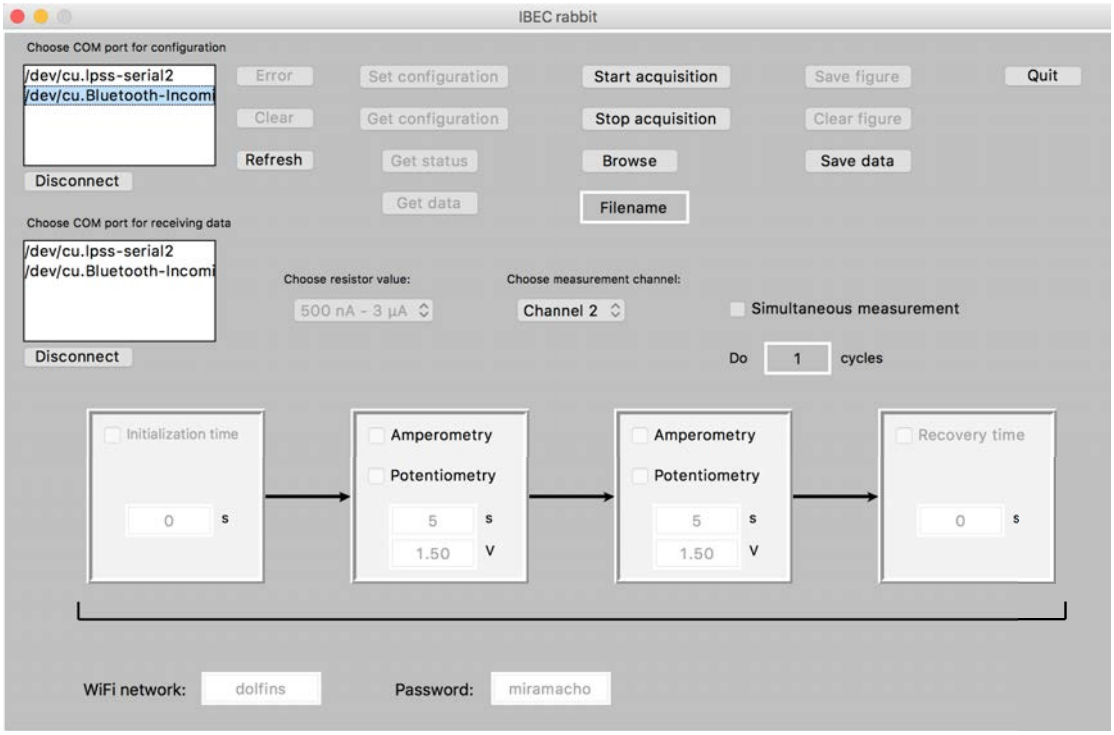

FIGURE 5.4: Front panel of the graphical user interface developed in Python.

ESP8266 module –in this case, the transmission is done *via* Wi-Fi–). Second, the user must choose a value for the feedback resistor (at the transimpedance amplifier in the amperometric circuitry), which depends on the approximate intensity of the current to be measured: the lower the current to be measured, the higher the required feedback resistor. Then, the measurement channel (or both) must be selected (each consisting of one amperometric and two potentiometric modules), and the "simultaneous measurement" checkbox must be ticked in case both potentiometries and the amperometry were to be measured simultaneously. On the contrary, if a specific order of measurement is desired, this is to be indicated in the sequencing boxes, where the time duration and excitation voltage level in the particular case of amperometry must be set. By pressing the "start acquisition" button, the device is configured and the measurement starts; the data is sent back to the computer and plotted in real time. Once the measurement finishes, a filename may be chosen and a directory may be browsed so that the data and plots can be saved.

5.2.5 Proof-of-concept: transparent and nanostructured ITO-based pH electrodes

Henceforth, the text reproduced in this section is partly extracted from a conference paper published in Multidisciplinary Digital Publishing Institute Proceedings, 2(13); R. Pruna, F. Palacio, I. Fuentes, C. Viñas, F. Teixidor, M. López, "A novel transparent pH sensor based on a nanostructured ITO electrode coated with [3,3'-Co(1,2-$C_2B_9H_{11}$)$_2$]-*doped poly (pyrrole)", 869, 2018; with permission from MDPI.*

Commercial-based pH sensors are becoming obsolete in many challenging applications such as biomedical and environmental monitoring, for they are constructed around liquid-filled glass membranes that imply limitations in size and rigidity. To overcome these limitations, solid-state pH sensors based on various organic materials were suggested in the past, which allowed the mass-production and miniaturization of flexible electrodes. Still a challenge in pH sensors is optical transparency, which would allow the simultaneous monitoring of potentiometry and optical features (e.g. fluorescence in some biochemical systems). Indeed, some important biomedical applications [203] have recently been reported in these terms.

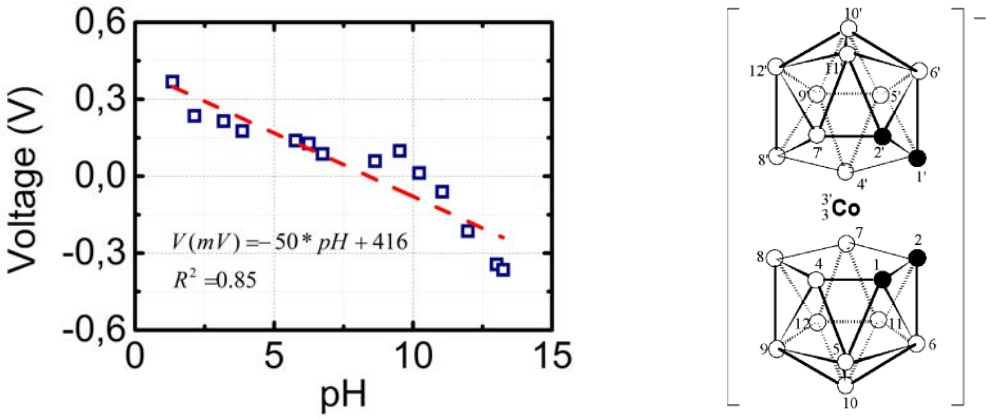

(A) (B)

FIGURE 5.5: (A) Nernstian evolution of the voltage measured by the ion-sensitive electrode with the pH of solution, showing linear behavior along the whole pH range. (B) Chemical structure of the cobaltabis(dicarbollide) [3,3'-Co(1,2-$C_2B_9H_{11})_2$]$^-$ anion.

In this work, the use of transparent nanostructured electrodes based on indium tin oxide (ITO) as a novel electrochemical platform for pH determination is proposed. These were grown by electron beam evaporation at 300 °C at a constant rate of 1 Å s^{-1} during 30 min, and further annealed at 600 °C during 1 h in N_2 atmosphere. The surface was coated with a functional conducting polymer via electrochemical polymerization by cyclic voltammetry (CV). Poly(pyrrole) (PPy) was used in this scope for being one of the most stable intrinsic conducting polymers (ICPs) known [204]. Cobaltabis(dicarbollide) [3,3'-Co(1,2-$C_2B_9H_{11})_2$]$^-$, whose chemical structure is shown in Figure 5.5b, was used as doping structure for its high chemical resistance and major advantages over common dopant anions [205]. A three-electrode system was used to electropolymerize a solution of 100 mM Pyrrole and 50 mM [3,3'-Co(1,2-$C_2B_9H_{11})_2$]$^-$ in acetonitrile by CV between 1.2 V and −0.9 V, at 100 mV s^{-1} for three cycles to keep electrode transparency. The potential response behavior of this novel transparent, conductive and nanostructured film was investigated in aqueous pH buffers prepared from HCl and NaOH solutions. A self-developed low-cost and miniaturized potentiostatic device was used for two-electrode potentiometry measurements, with the modified ITO film as ion-sensitive working electrode with respect to a Ag/AgCl (KCl sat.) reference electrode. A preliminary calibration is shown in Figure 5.5a, where a Nernstian behavior (around 50 mV change per pH unit) is observed in the whole pH range, confirming the quality of the developed electrode.

In summary, the preliminary results presented in this work point towards a new promising transparent ion-sensitive film coupled to a low-cost and miniaturized electronic system to achieve a fully autonomous measurement kit for precise potentiometric measurements in point-of-care medical environments.

Chapter 6

Conclusions

The main conclusions of this doctoral thesis are gathered in the present chapter. First, some general conclusions are drawn concerning an overall vision of the whole project; then, specific conclusions for each specific topic studied in this dissertation are provided.

6.1 General conclusions

(i) Transparent nanostructured indium tin oxide (ITO) electrodes were employed for electrochemical biosensing for the first time to the best of our knowledge. Several derivatization and functionalization methods were explored, and the results showed that nanostructured ITO is still a material with unexplored possibilities in terms of sensing.

(ii) New approaches on the miniaturization of potentiostats with the capability of conducting several electrochemical techniques were provided, resulting in novel, simplified devices at a low cost and very versatile in terms of integration into point of care (POC) systems.

(iii) Still the issue of simultaneous optical and electrochemical detection needs to be addressed in the future, for example by designing innovative electrode holders integrated into transparent electrochemical cells and modifying the electronic devices in order to accomodate adequate optical systems into the already working circuitry.

6.2 Specific conclusions

6.2.1 On the preparation of the functional material

(i) The fabrication process of transparent thin film and nanostructured ITO electrodes can be optimized to obtain a high electrochemical performance. Since these were prepared by electron beam evaporation, substrate temperature during deposition resulted to be a critical parameter, and a value of 300 °C delivered electrodes with optimized surface nanostructuration and optical transparency.

(ii) The electrochemically active surface area of the electrodes was estimated by successive voltammetry cycles at several scan rates and subsequent data analysis. The nanostructured electrodes showed a 40 % increase in electroactive surface area compared to thin ITO films for a projected area lower than 1 cm^2.

(iii) Both thin and nanostructured ITO films were shown suitable for surface chemical modification with several crosslinkers (organosilanes and aryl diazonium salts),

being the latter process a first step towards derivatization and functionalization of electrodes for biosensing.

6.2.2 On the usage of the funcional material as biosensor

(i) The nanostructured ITO surfaces show higher sensitivity for the electrochemical detection of species rather than thin films due to their increased electroactive surface area. This was tested by means of a model molecule labelled with ferrocene, which presents redox activity.

(ii) Nanostructured ITO electrodes were successfully employed as working electrodes for the detection of tumour necrosis factor α (TNF–α) by electrochemical impedance spectroscopy. An adequate surface functionalization was demonstrated by spectroscopic techniques (mainly FTIR) and also by fluorescence microscopy.

(iii) Other relevant immunoassays were performed using both thin and nanostructured ITO films as working electrodes: bovine serum albumin analysis confirmed the increased performance of nanostructured ITO as amperometric sensor due to its increased electroactive surface area, and the biotin-streptavidin assay demonstrated the feasability of creating repeatible and highly specific biosensors using nanostructured ITO as working electrode.

6.2.3 On the integration of biosensor and portable readout electronics

(i) A miniaturized and low-cost potentiostat was developed and successfully employed for the detection of TNF–α by electrochemical impedance spectroscopy analysis on a gold-based micropatterned electrode array. A good repeatability was obtained for concentrations ranging from below 250 pg mL^{-1} up to around 700 ng mL^{-1}.

(ii) A second miniaturized potentiostatic instrument was developed complementary to the first one in order to perform other electrochemical measurements such as potentiometry and amperometry. Besides, some of the electronic designs in the instrument were optimized and the consumption was lowered; a Wi-Fi module for data transmission was used to make the device portable and the graphical user interface was codified in free software to make it available to anybody without the need for expensive licenses.

(iii) The viability of integrating the nanostructured ITO biosensors and the developed potentiostat was also demonstrated, showing a case study in which the ITO working electrode surface was chemically modified with a doped polymer for the detection of pH variations in aqueous media. This sensor showed Nernstian behaviour (50 mV variation per pH unit).

Appendix A

Some notes on semiconductor electronic bands

Band theory

Materials can be classified as metals, semimetals, semiconductors and insulators regarding their conductivity properties. The conductivity of materials can be predicted by studying the distribution of electron orbitals in a set of molecules or atoms forming a crystal structure. As a brief reminder: according to quantum mechanics, atomic orbitals are discrete energetic regions available for electrons in atoms. In other words, electrons inside an atom are organized regarding the energy they possess, and the most external electrons (away from the nucleus) are the most energetic, and have the final say in the properties of the atom. Such atomic orbitals split into a set of sublevels each when atoms are grouped to form molecules. In turn, in a semi-infinite group of atoms or molecules forming a crystal lattice, these molecular sublevels tend to overlap, eventually forming molecular bands. Since all physical systems "try" to minimize the total energy related to that system (in the present case, the total energy in the material), the electrons start "filling up" the band structure from the bottom, and the energy of the last theoretically placed electron is called the "Fermi level". The latter is a thermodynamic concept that is defined as a hypothetical energy state with 50 % chances of being occupied, and its position within the band structure determines the electrical properties of the material, as can be observed in Figure A.1a. In semiconductor theory, the set of filled bands below the Fermi level are called "valence bands", and the set of unfilled bands above the Fermi level are called the "conduction bands". Both sets of bands are separated by the band gap, a forbidden energy region of magnitude E_g depending on the material. In metals and semimetals, the valence and conduction bands are overlapped to some extent, this is the reason why they are electrically conducting at thermodynamic equilibrium.

On the other hand, in the case of an insulator the valence and conduction bands are so much far away that no electron will ever find the chance to promote himself to the conduction band. The case of semiconductors is the most interesting of them all. Intrinsic semiconductors, as explained before, have the valence and conduction bands separated by a bandgap energy more or less small. The Fermi level lies right at the middle of the bandgap. A small external perturbation, such as a temperature increase, light, polarization, etc. can excite valence electrons over the bandgap to the conduction band and trigger electrical conductivity. However, another mechanism to trigger electrical conductivity in semiconductors is doping. Materials can be doped in two ways:

[1]Inspired by Kittel's Introduction to Solid State Physics 7th Edition, chapter 7 [53]. Author: Nanite (own work). Creative Commons CC0 1.0 Universal License. `https://en.wikipedia.org/wiki/Electronic_band_structure$#$/media/File:Band_filling_diagram.svg`.

(1) adding atoms that accept electrons, leaving holes in the valence band that have some degree of freedom and thus allow conductivity; (2) adding atoms that donate free electrons to the conduction band, allowing thus for electrical conductivity. The second case is what happens when doping indium oxide with tin, as can be observed in the band diagram shown in Figure A.1b.

In the case of indium oxide, it is worth observing the effect of doping tin doping in theoretical band structures, which show the distribution of electronic bands along high symmetry lines in the Brillouin zone. In this context, Figure A.2 shows the band diagrams of bare (Figure A.2a) and tin-doped (Figure A.2b) indium oxide as theorized by Mryasov and Freeman [51]. They performed an *ab initio* calculation of the band structure using the full potential linear muffin-tin orbital (FLMTO) method, the description of which is out of the scope of this thesis and can be found elsewhere [207, 208]. Their results showed that the conditions for transparent conducting behaviour with electron

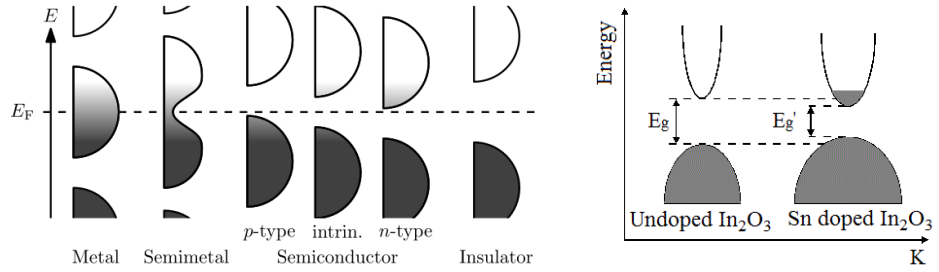

(A) (B)

FIGURE A.1: (A) Several material types electronic states and how they fill at equilibrium. Black means all states filled, whereas white means no state filled, and all intermediate states follow a Fermi-Dirac distribution; y-axis represents density of states available for a certain energy.[1] (B) For the particular case of ITO, comparison of conduction properties for undoped and tin-doped indium oxide. Extracted from [206].

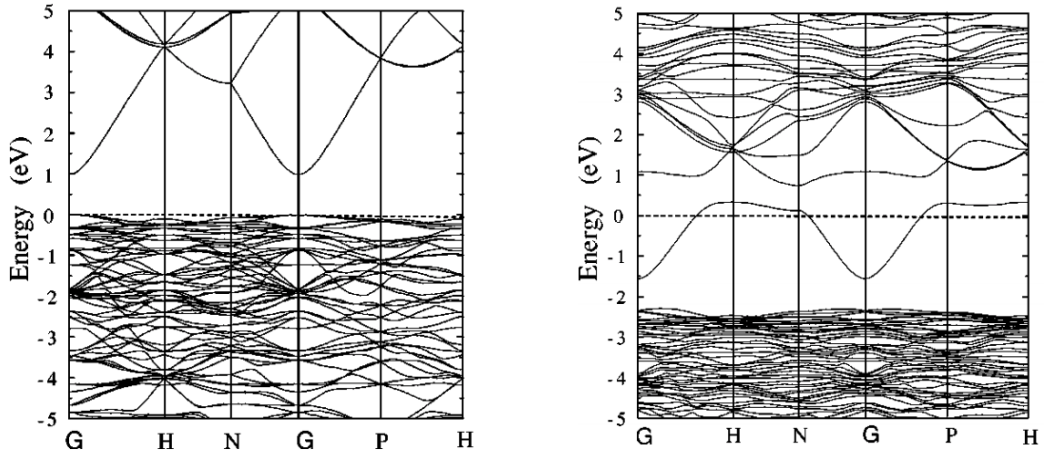

(A) (B)

FIGURE A.2: Electronic band structures of bare (A) and tin-doped (B) indium oxide (the latter at a doping level of 6.5 %), In_2O_3. Extracted from [51].

doping were provided by the position and high dispersion at the bottom of the conduction band, as can be observed in the figures. Anyhow, it must be noted that these calculations predict the existence of a direct band gap of about 1 eV, which indicates an underestimation commited by the local density approxmiation (LDA) model, since the experimentally measured optical band gap is around 3.6 eV [209].

The semiconductor–electrolyte interface

Along the previous section, some concepts on semiconductor band theory were provided, since the main material employed along this thesis is indium tin oxide, a n-type transparent semiconductor. However, the material is not used isolated and on its own, but immersed in an aqueous solution containing a redox couple. For this reason, we will now focus on the behaviour of the electronic bands of the semiconductor–redox couple system.

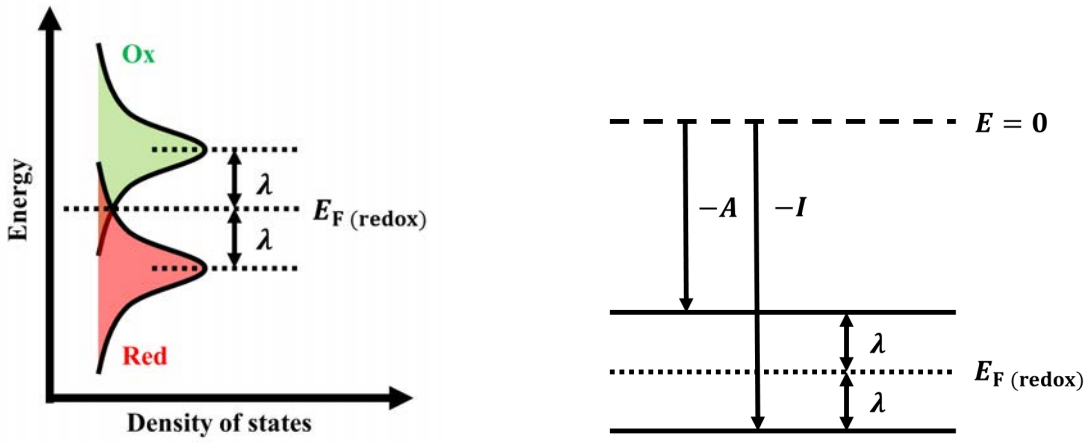

FIGURE A.3: (A) Schematic of the redox states (Red and Ox) in solution, the corresponding Fermi level ($E_{F(redox)}$ and the solvent reorganization energy, λ. Adapted from [145]. (B) Complementary representation of the band energy organization for the redox solution.

The energy levels for the redox-active species contained in the aqueous solution are shown in Figure A.3, and these levels depend on the probabilities of the Red (donors) and Ox (acceptors) being occupied and vacant, respectively. A measure of such probabilities (best described in terms of gaussian distributions) is provided by the solvent-sheath energies (λ) around the redox species: the continuous distributions shown in Figure A.3a arise from the dynamics of the exchange of solvent molecules between the coordination sphere of the redox species and the bulk electrolyte. By all means, the Fermi level is the energy state which has 0.5 probability of being occupied by an electron.

Let us now consider the case of immersing an n-type semiconductor electrode in a redox solution, graphically schematized in Figure A.4. In this case, when considered separately, the Fermi level of the material is higher than the Fermi level of the redox couple in solution; as usual, these levels have to equalize when the phases are brought into physical contact to reach thermodynamical equilibrium. This occurs as a consequence of the transference of electrons from the material to the Ox (acceptors) species. Since the semiconductor carrier densities are usually much lower than the densities of the redox

species in solution, a sheet of negative charge acts as a counterbalance in the electrolyte and the semiconductor energy bands are bent in the depletion zone. Any voltage applied to the semiconductor (through a potentiostat) will cause the Fermi levels to separate, thus changing the band bending [145]. In a complementary way, *p*-type semiconductors (Figure A.5) present a Fermi level lower than that of the redox couple, and thus the equilibrium is achieved through the transfer of electrons from the Red (donor) species to the semiconductor. This charges the semiconductor negatively, resulting in a sheet of positive charge counterbalancing the electrolyte and producing an upwards bending of the semiconductor bands.

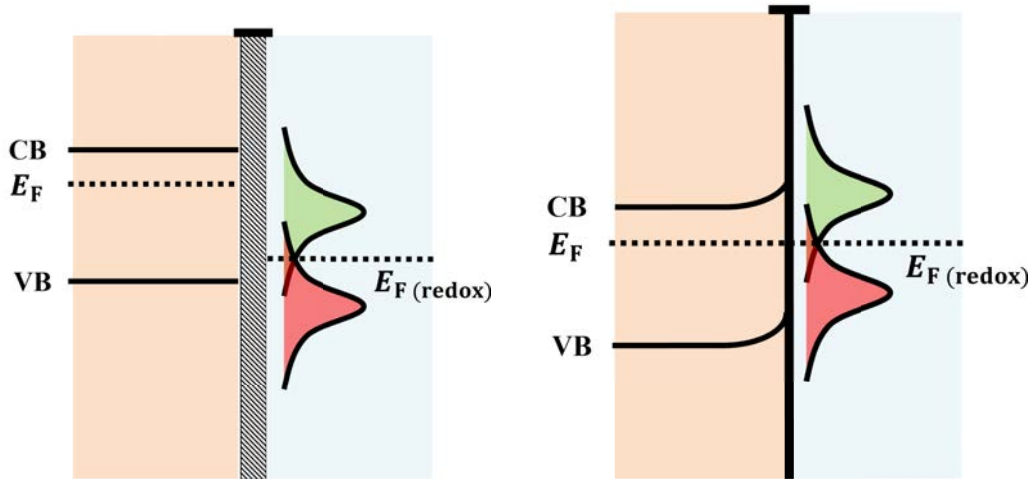

FIGURE A.4: Band diagram of *n*-type semiconductor and redox solution (A) separately and (B) brought to contact. Adapted from [145].

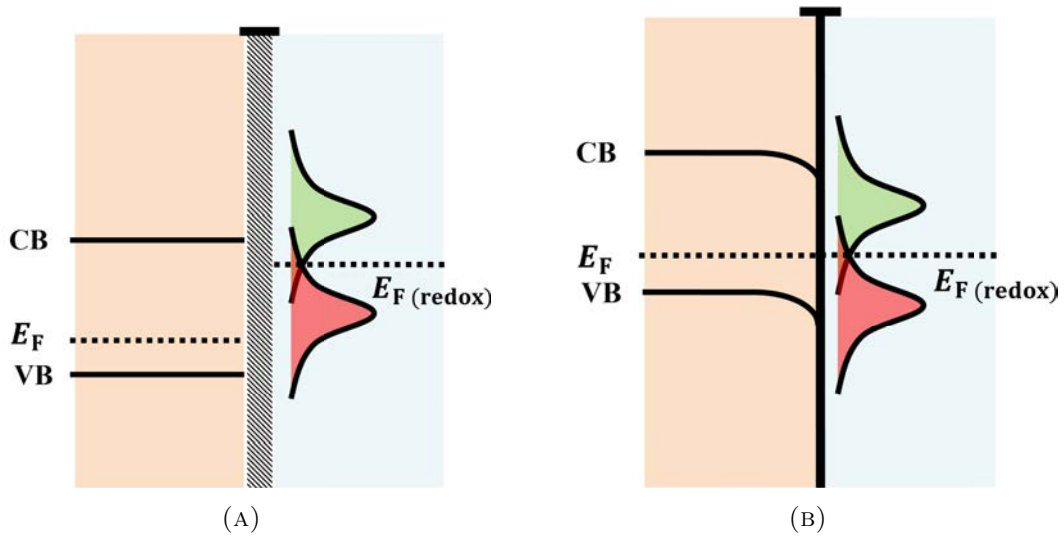

FIGURE A.5: Band diagram of *p*-type semiconductor and redox solution (A) separately and (B) brought to contact.

Appendix B

How does the immune system produce monoclonal antibodies?

The immune system, which responds in a specific way and displays a long-term memory of exposure to pathogens, is composed of (1) the innate or non-specific and (2) the adaptive or specific systems. The innate immune system consists in a first line of defence against infection, with components such as skin, body fluids, etc. When the latter fails to defend the body against pathogens, the adaptive immune system (composed of several cells and molecules such as lymphocytes and antibodies) is activated. Lymphocytes can be classified as B cells, cytotoxic T (TC) cells and helper T (TH) cells. B cells act in the humoral response, when a known pathogen is fought by releasing antibodies specific to that agent. TC cells act in the cell-mediated response, binding to foreing or infected cells and inducing their lysis. These B, TC and TH cells carry surface receptors that bind specifically (one cell – one antigen) to antigens. But how are antibodies produced?

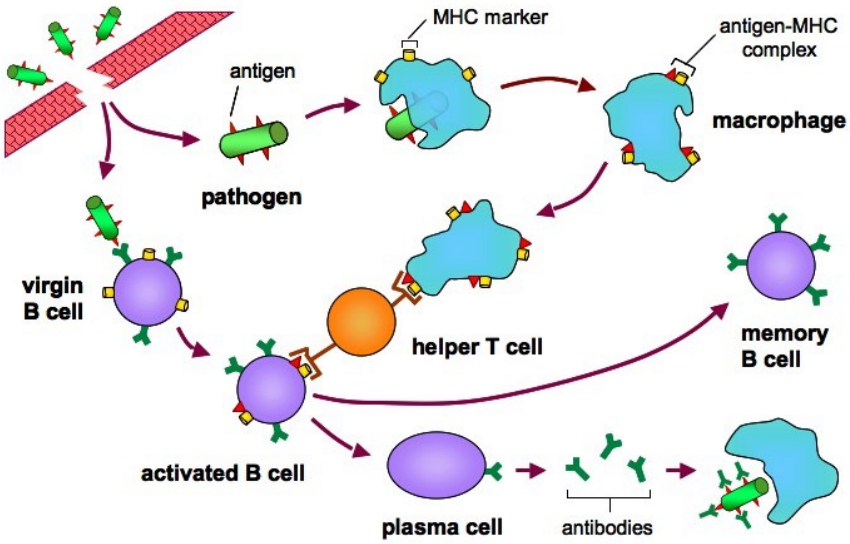

FIGURE B.1: Schematic showing the reaction of the immune system to the break in of foreign pathogens in order to deliver the appropriate antibodies or to generate a stock of them.[1]

The pathogen that succeeds in breaking the primary barriers of the immune system and gets inside the body, immediately faces the response of virgin B cells and macrophages (see Figure B.1). On one hand, macrophages engulf the pathogens, and the

[1] `http://www.old-ib.bioninja.com.au/higher-level/topic-11-human-\health-and/111-defence-against-infecti.html`

major histocompatibility complex (MHC) markers of the macrophages become linked to an antigen of the pathogen. The latter corresponds to the non-specific pathway. These linked MHC – antigen complexes are presented to helper T cells (lymphocytes) as *non-self* invaders. Each B cell has on its surface a specific antibody with affinity for a specific antigen. Of all B cells, only those with the appropriate antigen become activated and cloned at the presence of the MHC – antigen complex macrophage. These B cells differentiate into antibody-producing plasma cells, and a few of them become memory B cells. The latter remain in the bloodstream for years, and provide with a faster immune reaction if a second infection with the same antigen occurred. Parallelly, plasma cells produce high quantities of specific antibody to the infecting antigen.

Regarding the monoclonal antibodies used in diagnosis and treatment (and also in the experiments performed during this thesis), their production is schematized in Figure B.2. An animal, usually a mouse or a rabbit, is injected with an antigen and produces plasma cells by the immune proceure explained before. The plasma cells are retrieved and hybridized with tumour cells capable of keeping on reproducing *ad infinitum*. Large quantities of specific antibody can be synthesized by the resulting hybridoma, which are used in diagnosis and treatment of diseases.

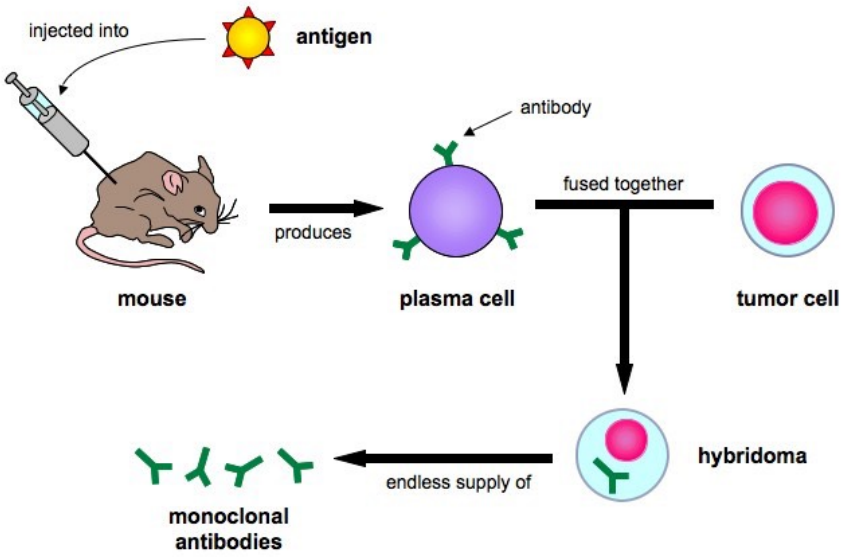

FIGURE B.2: Laboratory protocol for producing monoclonal antibodies for a specific antigen.[2]

[2] `http://www.old-ib.bioninja.com.au/higher-level/topic-11-human-health-\and/111-defence-against-infecti.html`.

Appendix C

Scientific curriculum vitæ

Raquel Pruna Morales

Born in Barcelona (Spain) on June 13th 1992.

Current professional situation

For the past four years I have been working in the preparation, characterization and biofunctionalization of transparent, conducting and nanostructured surfaces and their integration into portable potentiostatic systems for the optimization of lab-on-a-chip devices. This work has led to the realization of my doctoral dissertation in Engineering and Applied Sciences.

Academic formation

PhD in Engineering and Applied Sciences	2016–2019	Department of Electronic and Biomedical Engineering, Universitat de Barcelona
Master in Biomedical Engineering	2014–2016	Universitat de Barcelona and Universitat Politècnica de Catalunya
Degree in Physics	2010–2014	Universitat de Barcelona

Published articles

R. Pruna, M. López, F. Teixidor, *Tuning the deposition parameters for optimizing the faradaic and non-faradaic electrochemical performance of nanowire array-shaped ITO electrodes prepared by electron beam evaporation*, **Nanoscale** 11 (2019), 276-284. doi: 10.1039/c8nr07908k.

R. Pruna, A. Baraket, A. Bonhommé, N. Zine, A. Errachid, M. López, *Novel nanostructured indium tin oxide electrode for electrochemical immunosensors: Suitability for the detection of TNF-α*, **Electrochimica Acta** 283 (2018), 1632-1639. doi: 10.1016/j.electacta.2018.07.066.

R. Pruna, F. Palacio, A. Baraket, N. Zine, A. Streklas, J. Bausells, A. Errachid, M. López, *A low-cost and miniaturized potentiostat for sensing of biomolecular species such as TNF-α by electrochemical impedance spectroscopy*, **Biosensors and Bioelectronics** 100 (2018), 533-540. doi: 10.1016/j.bios.2017.09.049.

A. García-Cruz, F. Nessark, M. Lee, N. Zine, M. Sigaud, R. Pruna, M. López, P. Marote, J. Bausells, N. Jaffrezic-Renault, A. Errachid, *Efficient fabrication of poly(pyrrole)-nanowires through innovative nanocontact printing, using commercial CD as mold, on flexible thermoplastics substrates: application for cytokines immunodetection*, **Sensors and Actuators B** 255 (2018), 2520-2530. doi: 10.1016/j.snb.2017.09.057.

R. Pruna, F. Palacio, M. López, J. Pérez, M. Mir, O. Blázquez, S. Hernández, B. Garrido, *Electrochemical characterization of organosilane-functionalized nanostructured ITO surfaces*, **Applied Physics Letters** 100(6) (2016), 063109. doi: 10.1063/1.4960734.

R. Pruna, F. Palacio, M. Martínez, O. Blázquez, S. Hernández, B. Garrido, M. López, *Organosilane-functionalization of nanostructured indium tin oxide films*, **Interface Focus** 6(6) (2016), 20160056. doi: 10.1098/rsfs.2016.0056.

A. García-Cruz, M. Lee, P. Marote, N. Zine, M. Sigaud, A. Bonhommé, R. Pruna, M. López, J. Bausells, N. Jaffrezic, A. Errachid, *Large area in situ fabrication of poly(pyrrole)-nanowires on flexible thermoplastic films using nanocontact printing*, **Materials Research Express** 3 (8) (2016), 085018. doi: 10.1088/2053-1591/3/8/085018.

Proceedings

R. Pruna, F. Palacio, I. Fuentes, C. Viñas, F. Teixidor, M. López, *A novel transparent pH sensor based on a nanostructured ITO electrode coated with [3,3'- Co(1,2-$C_2B_9H_{11}$)$_2$]-doped poly(pyrrole)*, **MDPI Proceedings** (2018). doi: 10.3390/proceedings2130869

R. Pruna, F. Palacio, M. López, *Towards Nanostructured ITO-Based Electrochemical Sensors: Fabrication, Characterization and Functionalization*, **MDPI Proceedings** (2017). doi: 10.3390/proceedings1040288.

R. Pruna, F. Palacio, A. Baraket, J. Bausells, A. Errachid, M. López, *Low-Cost Impedance Measurements for Lab-on-a-Chip Architectures: Towards Potentiostat Miniaturization*, **MDPI Proceedings** (2017). doi: 10.3390/proceedings1040604.

F. Palacio, J.M. Gómez, J. Burgués, R. Pruna, A. Scorzoni, S. Zampolli, S. Marco, *Evaluation of MOX Sensor Characteristics in Ultra-Low Power Operation Modes: Application to a Semi-Passive RFID Tag for Food Logistics*, **MDPI Proceedings** (2017). doi: 10.3390/proceedings1040459.

Participations in congresses

Oral contributions and invited talks

B. Garrido, O. Blázquez, J. López-Vidrier, A. Huguet, R. Pruna, M. López, J.L. Frieiro, S. Hernández, *Materials and Devices for Integrated Optoelectronics, Biosensing and Human Centric Lighting*, **2nd Workshop on Photonic Integrated Circuits for Telecom** & **Bio/Life Sciences** (2018), Castelldefels, Spain.

R. Pruna, F. Palacio, J.P. Salvador M. Martínez, O. Blázquez, S. Hernández, B. Garrido, M.P. Marco, M. López, *On the potential use of nanostructured ITO electrodes as amperometric biosensors*, **E-MRS 2017 Spring Meeting** (2017), Strasbourg, France.

R. Pruna, F. Palacio, M. Martínez, M. López, *Portable and miniaturized potentiostats in the literature and in the SEA-on-a-CHIP project: a review*, **3rd SEA-on-a-CHIP Progress Workshop** (2017), Olhao, Portugal.

F. Palacio, R. Pruna, M. López, *ong lifetime wireless marine sensor networks based on duty cycle management*, **3rd SEA-on-a-CHIP Progress Workshop** (2017), Olhao, Portugal.

R. Pruna, F. Palacio, M. López, A. Diéguez, M. Mir, J. Pérez, O. Blázquez, S. Hernández, B. Garrido, *Development of DNA biosensors based on nanostructured ITO films*, **E-MRS 2016 Spring Meeting** (2016), Lille, France.

R. Pruna, F. Palacio, M. Martínez, M. López, *Portable acquisition electronic systems for electrochemical biosensors. An electronic approach towards chemistry*, **2nd SEA-on-a-CHIP Progress Workshop** (2016), Ferrara, Italy.

R. Pruna, F. Palacio, M. Martínez, M. López, M. Lee, A. Baraket, A. Errachid, J.P. Salvador, M.P. Marco, *Portable impedance measurements for contaminants in open water fish farms*, **SURFOCAP'15** (2015), Agadir, Morocco.

R. Pruna, F. Palacio, M. Martínez, M. López, M. Lee, A. Baraket, A. Errachid, J.P. Salvador, M.P. Marco, *Irgarol detection based on a new portable impedance measurement device and FFT analysis*, **1st Progress Workshop** & **1st Case Study** (2015), Sivota, Greece.

Poster contributions

R. Pruna, F. Teixidor, M. López, *A transparent indium tin oxide nanowire array for electrochemical biodetection: tuning its properties for optimizing the sensing performance*, **E-MRS 2019 Spring Meeting** (2019), Nice, France.

R. Pruna, F. Palacio, I. Fuentes, C. Viñas, F. Teixidor, M. López, *A novel transparent pH sensor based on a nanostructured ITO electrode coated with [3,3'- Co(1,2-$C_2B_9H_{11}$)$_2$]-doped poly(pyrrole)*, **Eurosensors XXXII** (2018), Graz, Austria.

R. Pruna, F. Palacio, M. López, *Towards nanostructured ITO-based electrochemical sensors: fabrication, characterization and functionalization*, **Eurosensors XXXI** (2017), Paris, France.

R. Pruna, F. Palacio, A. Baraket, J. Bausells, A. Errachid, M. López, *Low-cost impedance measurements for lab-on-a-chip architectures: towards potentiostat miniaturization*, **Eurosensors XXXI** (2017), Paris, France.

R. Pruna, F. Palacio, M. Martínez, O. Blázquez, S. Hernández, B. Garrido, M. López, *Optimizing the electrochemical performance of nanostructured ITO electrodes*, **E-MRS 2017 Spring Meeting** (2017), Strasbourg, France.

R. Pruna, F. Palacio, M. López, J.M. Gómez, M. Mir, J. Pérez, O. Blázquez, S. Hernández, B. Garrido, *Characterization and functionalization of nanostructured ITO films for biosensing applications*, **E-MRS 2016 Spring Meeting** (2016), Lille, France.

R. Pruna, F. Palacio, M. López, M. Martínez, A. Baraket, M. Lee, A. Errachid, *Portable impedance measurements for the detection of contaminants in sea water. Application to Irgarol detection*, **BBMEC 2015** (2015), Regensburg, Germany.

F. Palacio, R. Pruna, J.D. Prades, J.M. Gómez, M. Martínez, A. Errachid, M. López, *Portable impedance measurements for Interleukin-10 detection. Comparison with the standard analysis*, **BITE 2015** (2015), Lisbon, Portugal.

F. Palacio, R. Pruna, J.D. Prades, J.M. Gómez, M. Martínez, A. Errachid, M. López, *A new low-power instrument for impedance measurements in biomedicine based on FFT. Application to Interleukin-10 protein detection*, **Eurosensors XXVIII** (2014), Brescia, Italy.

R. Pruna, A. Gutiérrez-Gálvez, *Odor information segregation information in the olfactory bulb. An application of biological neural networks*, **7th IBEC Symposium** (2014), Barcelona, Spain.

Other collaborations

During my PhD, I have been involved in several collaborations with national and international research groups. I have participated with the Universitat de Barcelona group in the European Seventh Framework Programme project "SEA-on-a-CHIP" (grant agreement no. 614168), developing new potentiostat electronics for a remote sensor platform system to monitor seawater contaminants.

I collaborated with the group *Nanobiotechnology for Diagnosis* at the Institut de Química Avançada de Catalunya (IQAC) – CSIC and with the group *Functional Molecular and Nanostructured Inorganic Materials* at the Institut de Ciència de Materials de Barcelona (ICMAB) – CSIC, both in Spain.

I also stayed at the Institut des Sciences Analytiques (Lyon, France) for three months, collaborating with Professor Abdelhamid Errachid and his team in the *Micro and Nanobiotechnology* Lab. Four publications in top-ranked journals resulted from this collaboration.

Other relevant skills

Basic programming skills in Python, MATLAB, C and Java.

Certificate in Advanced English (CAE) – C1, University of Cambridge.

German A1 certificate from EIM (School of Modern Languages at the Universitat de Barcelona.

Teaching assistant of the subjects "Introduction to computer architecture", "Programming" and "Tools for electrical design" of the Information Technology, Biomedical Engineering and Electronic Engineering degrees from the Universitat de Barcelona.

Appendix D

Resumen en español

Hipótesis y objetivos

La importancia de desarrollar sistemas de punto de cuidado (*point-of-care*, POC por sus siglas en inglés) cualificados en entornos médicos y para la monitorización de parámetros ambientales (por ejemplo calidad del aire y del agua) es de suma importancia, y está llevando a los científicos a investigar (1) la miniaturización y el desarrollo de circuitería electrónica integrada y sensores compactos y integración en dispositivos portables; y (2) nuevos materiales sensores capaces de facilitar la miniaturización e integración de electrónica y biosensores, garantizando niveles de sensibilidad razonables.

En este trabajo, se propone el óxido de indio dopado con estaño (*indium tin oxide*, ITO por sus siglas en inglés) en forma nanoestructurada como material adecuado para el desarrollo de electrodos de trabajo para biosensores electroquímicos. En primer lugar, la combinación de interesantes propiedades como una alta conductividad eléctrica y transmitancia óptica puede hacer del ITO un material adecuado no sólo para el sensado electroquímico, también para biosensores ópticos o para desarrollar sensores basados en la combinación de ambos principios. Además, la nanoestructuración del material puede contribuir a incrementar la sensibilidad del sensor, especialmente cuando se intenta miniaturizar el dispositivo final, puesto que esto comporta una reducción del área geométrica de sensado, y las nanoestructuras contribuirían a aumentar la superficie específica.

Por otro lado, este trabajo incluye también contirbuciones a la electrónica de medida de biosensores electroquímicos. En efecto, se desarrollaron algunos prototipos de potenciostato y se testearon en colaboración con otras instituciones europeas en el marco del proyecto "Real time monitoring of SEA contaminants by an autonomous Lab-on-a-CHIP biosensor" ("SEA-on-a-CHIP", ayuda número 614168) del séptimo programa marco de la Unión Europea. La descripción de estos prototipos, así como los resultados obtenidos con ellos, se presentan en esta tesis. Con todo, los principales objetivos de este proyecto consisten en:

- desarrollar electrodos de ITO nanoestructurado mediante evaporación por haz de electrones y examinar su ejecución en un entorno electroquímico, comparando estos resultados con los obtenidos mediante electrodos de ITO en capa fina;
- optimizar los parámetros de fabricación de los electrodos para obtener ITO nanoestructurado de alta calidad y máxima sensibilidad electroquímica;
- probar que las superficies de los electrodos de ITO nanoestructurado pueden ser adecuadamente modificados con moléculas como silanos o sales de diazonio,

que hacen de puente para posteriormente poder enlazar otras biomoléculas (e.g. proteínas), y caracterizar estos procesos por métodos espectroscópicos como XPS o FTIR;

- desarrollar un immunoensayo completo sobre el ITO nanoestructurado usado como electrodo de trabajo con el objetivo de detectar biomoléculas de interés mediante técnicas electroquímicas con potenciostatos comerciales;
- desarrollar la circuitería electrónica adecuada para la miniaturización de potenciostatos, centrándonos en la medida de espectroscopía de impedancia electroquímica, potenciometría y amperometría;
- diseñar y desarrollar una interfaz gráfica de usuario flexible y en código abierto para facilitar la manipulación de los potenciostatos portables desarrollados, y
- integrar la electrónica, hardware y software en un dispositivo compacto con electrodos comerciales o basados en ITO que pueda ser aplicado en entornos POC.

Resumen de la tesis

Existe una creciente necesidad de desarrollar sistemas de *point-of-care* (punto de cuidado, POC por sus siglas en inglés) innovadores, versátiles y de bajo coste, que sean capaces de buscar y detectar enfermedades antes de que los síntomas se manifiesten, esto es, en estadios de desarrollo tempranos. Los sistemas POC consisten en un biosensor integrado en un sistema electrónico y eventualmente un sistema microfluídico que gestione las posibles muestras de fluidos biológicos [21, 22]. El objetivo general de esta tesis doctoral es investigar distintas posibilidades de mejorar la tecnología POC.

Por un lado, los sistemas biosensores actualmente integrados en sistemas POC son limitados. Pongamos por caso uno de los sistemas POC por excelencia: el detector de glucosa en sangre. Éste está basado en el concepto de inmunoensayo de flujo lateral, tecnología consistente en un sistema de lechos capilares (e.g. papel poroso o polímero microestructurado) capaces de transportar el fluido. Así, éste se desplaza sobre distintos lechos capilares con distintas moléculas destinadas a conjugarse con el analito supuestamente contenido en la muestra inicial. De este modo (la explicación detallada del funcionamiento del inmunoensayo de flujo lateral está recogida en [23–25]), se obtienen indicadores cualitativos muy precisos acerca de la presencia o no de un analito (como la glucosa) en una muestra (de sangre, por ejemplo). De igual modo funcionan los test de embarazo, si bien es cierto que en ambos casos los dispositivos comerciales actuales proporcionan datos cuantitativos precisos [26, 27]. No obstante, existen otros muchos analitos que no pueden ser correctamente detectados y cuantificados mediante un ensayo de flujo lateral, y requieren de métodos basados en potentes sistemas electrónicos que aporten la energía necesaria que desencadene una reacción que pueda ser medida. Para esto, se necesita por un lado de sustratos adecuados que permitan tanto el acoplo de analitos y otras biomoléculas como la detección de reacciones químicas ocurridas en su superficie; por otro lado, es necesaria una potente circuitería electrónica capaz de excitar el sensor y a la vez medir su respuesta y que pueda ser miniaturizada para poder ser integrada en sistemas POC.

Los biosensores electroquímicos y ópticos han tomado mucha relevancia en cuanto a lo que a sistemas POC se refiere. Esto es debido a la versatilidad de los sistemas

de medida basados en transductores electroquímicos y ópticos [28–30], dotando a estos sensores de una alta sensibilidad y especificidad. Concretamente, la sensibilidad puede verse gravemente afectada por la miniaturización de los dispositivos y por tanto de la parte sensora de los mismos. En los últimos años, los materiales más usados en biosensores electroquímicos por ser capaces de proveer alta sensbilidad a los dispositivos han sido el oro [31–33], algunos polímeros [34, 35] y algunos óxidos [36, 37]. No obstante, la necesidad de obtener superficies extremadamente pequeñas con alta sensibilidad ha impulsado el estudio y desarrollo de nanoestructuras como las nanopartículas de oro y superficies nanoestructuradas de oro y algunos óxidos [38–44]. La elevada relación superficie–volumen que presentan las nanoestructuras las hace especialmente interesantes para la biodetección de moléculas, pues el aumento de superficie posibilita la interacción con una mayor cantidad de moléculas de menor tamaño y esto supone un aumento de sensibilidad y la posibilidad de reducción del tamaño del sensor [45].

Sin embargo, la atención prestada a materiales transparentes en el campo de la biodetección es escasa y prácticamente se reduce a biosensores ópticos, con alguna excepción [42, 46]. En esta tesis, se propone el óxido de indio dopado con estaño (*indium tin oxide*, ITO por sus siglas en inglés) en forma nanoestructurada como material de electrodo de trabajo (*working electrode*, WE por sus siglas en inglés) en biosensores electroquímicos. Por un lado, la transparencia que presenta el material a longitudes de onda en el rango óptico e infrarojo hacen de él un buen candidato para sensores ópticos; por otro lado, la conductividad que presenta hace que pueda ser considerado para sensores electroquímicos, y la nanoestructuración permitiría la reducción del tamaño total de los dispositivos para poder así ser integrados en sistemas POC.

Así, en la primera parte de esta tesis se ha estudiado las propiedades del ITO, y se ha caracterizado eléctrica, óptica, electroquímica y estructuralmente tanto en forma de capa fina como nanoestructurado, a partir de muestras preparadas sobre silicio (R. Pruna *et al.*, 2016, Electrochemical characterization of organosilane-functionalized nanostructured ITO surfaces) y sobre vidrio (R. Pruna *et al.*, 2019, Tuning the deposition parameters for optimizing the faradaic and non-faradaic electrochemical performance of nanowire array-shaped ITO electrodes prepared by electron beam evaporation) mediante evaporación por haz de electrones. Así mismo, se ha estudiado la interacción de moléculas conocidas como *crosslinkers*, que permiten la posterior funcionalización de superficies con biomoléculas, con los sustratos de ITO nanoestructurado (R. Pruna *et al.*, 2016, Organosilane-functionalization of nanostructured indium tin oxide films). Finalmente, se han realizado varios inmunoensayos usando el ITO nanoestructurado como sustrato, desde los clásicos para el estudio de la adecuación del material para este tipo de aplicaciones (como los que involucran la albúmina de suero bovino -*bovine serum albumin*, BSA por sus siglas en inglés- o la interacción entre biotina y estreptavidina) hasta la detección de distintas concentraciones de un biomarcador de fallo cardíaco muy estudiado en ámbitos POC: el factor *alfa* de necrosis tumoral (*tumour necrosis factor* α, TNF–α, por sus siglas en inglés) (Pruna *et al.*, 2018, Novel nanostructured indium tin oxide electrode for electrochemical immunosensors: Suitability for the detection of TNF-α).

Por otro lado, en esta tesis se ha prestado también atención a la parte electrónica que integra los sistemas POC y que complementa la parte biosensora. Se ha estudiado distintos mecanismos de medida de sensores electroquímicos basados en distintas formas de atacar eléctricamente el sensor y de procesar la respuesta del mismo, a saber,

potenciometría, amperometría y espectroscopía de impedancia electroquímica. En la primera, se mide la tensión abierta entre dos electrodos sumergidos en un medio acuoso, cosa que dará cuenta de la cantidad de iones libres en el medio, o lo que es lo mismo, su pH. La amperometría consiste en aplicar un nivel de tensión constante al sensor con respecto a un electrodo de referencia, y monitorizar el comportamiento de la corriente. De este modo, si la especie a detectar presenta por ejemplo actividad *redox* a ese nivel de tensión, observaremos sus efectos en el comportamiento de la corriente. Según la aplicación, esta medida puede realizarse con dos o tres electrodos, igual que la espectroscopía de impedancia electroquímica, aunque suele recomendarse el uso de tres terminales. En este último caso, se aplica entre el sensor y el electrodo de referencia una tensión alterna de pequeña amplitud cuya frecuencia se varía con el tiempo, y se monitoriza el nivel y desfase de la corriente resultante medida entre el sensor y el electrodo auxiliar, obteniendo un valor numérico para la impedancia del mismo en cada frecuencia, y pudiendo así ajustar su comportamiento a un modelo electrónico según las especies bioquímicas que interaccionan en su superficie.

En cuanto a lo que a espectroscopía de impedancia electroquímica se refiere, se ha diseñado y desarrollado un dispositivo de bajo coste y miniaturizado para la detección de distintas concentraciones del biomarcador TNF–α mediante un conjunto de ocho microsensores de oro en paralelo (R. Pruna *et al.*, 2018, A low-cost and miniaturized potentiostat for sensing of biomolecular species such as TNF–α by electrochemical impedance spectroscopy). También se ha diseñado la electrónica necesaria para realizar medidas de amperometría con dos electrodos, así como de potenciometría. Este último sistema se ha ensayado con ITO nanoestructurado recubierto con un polímero conductor dopado sensible a cambios de pH en medio acuoso.

En síntesis, esta tesis recoge algunas propuestas para la mejora de los sistemas POC actuales, tanto en la cuestión biosensora como en la parte electrónica, usando para las medidas y pruebas de concepto un biomarcador importante en el ámbito biomédico, y siendo estas medidas extensibles al ámbito medioambiental.

Contribuciones específicas

En primer lugar, se ha determinado la contribución de las nanoestructuras de ITO a la superficie electroquímicamente activa mediante voltametría cíclica, y se ha comparado con el área activa del ITO en capa fina. Esto se ha hecho tanto para las muestras recién preparadas como para electrodos sometidos a un posterior recocido. Se ha detectado un incremento en el área activa gracias a la nanoestructuración de las superficies de ITO independientemente de la cristalinidad del sustrato.

En segundo lugar, la fabricación de electrodos de ITO nanoestructurado por evaporación por haz de electrones se ha optimizado para maximizar el área superficial electroactiva y mejorar así la sensibilidad a reacciones electroquímicas que ocurran en las superficies. Esto se ha logrado mediante el estudio de la influencia de los parámetros de configuración, y concretamente la temperatura del sustrato, durante el proceso de evaporación.

En tercer lugar, se ha propuesto por primera vez un modelo de la formación de nanohilos de ITO sobre silicio cristalino por evaporación por haz de electrones basado

en el crecimiento epitaxial descrito por Stranski-Krastanov. Se ha propuesto este modelo como complemento al mecanismo ámpliamente reportado y conocido como *self-catalyzed vapour-liquid-solid* (VLS). Creemos que esto ayuda a entender la geometría de los nanohilos, así como la apariencia de la visión transversal de los electrodos resultantes.

En cuarto lugar, los electrodos transparentes de ITO nanoestructurado se emplearon por primera vez como electrodos de trabajo para la detección electroquímica de un importante biomarcador cardíaco conocido como factor *alfa* de necrosis tumoral (TNF–α). El proceso de derivatización y funcionalización del ITO nanoestructurado mediante reducción de sales de diazonio y anti–TNF–α, respectivamente, se han verificado mediante técnicas espectroscópicas (FTIR) y también por microscopía de fluorescencia. La detección de varias concentraciones de TNF–α se ha realizado por espectroscopía de impedancia electroquímica con un potenciostato comercial.

En quinto lugar, se ha diseñado y desarrollado un potenciostato miniaturizado y de bajo consumo para el análisis de espectroscopía de impedancia electroquímica, y se ha contactado con un array de electrodos de trabajo de oro con terminales integrados de referencia y auxiliar. Se han detectado concentraciones crecientes de TNF–α y los resultados se han comparado con los obtenidos con un potenciostato comercial, observando una fuerte correlación entre los niveles de señal, así como una buena relación señal-ruido.

Por último, se ha propuesto una arquitectura alternativa de potenciostato para la monitorización de amperometría y potenciometría. Se ha desarrollado una interfaz de usuario gráfica basada en software libre, capaz de interaccionar con el potenciostato miniaturizado. El funcionamiento de este dispositivo se ha verificado con electrodos de trabajo basados en ITO nanoestructurado empleados como sensores potenciométricos.

Organización de la tesis

El capítulo 1 incluye la motivación de esta tesis, con una visión histórica del origen y evolución del diagnóstico médico. El capítulo incluye también un breve apartado sobre el empleo de biosensores a análisis de alimentos y a cuidado medioambiental. También se incluye un resumen de la presente disertación, así como un esquema de las contribuciones específicas de esta tesis.

El capítulo 2 consiste en una revisión exhaustiva de principios teóricos a tener en cuenta al leer esta tesis. Los temas principales que se discuten son tres: (1) descripción del material ITO desde un punto de vista de la física del estado sólido; (2) revisión de principios básicos de electroquímica y conceptos de electrónica aplicada a medidas potenciostáticas, y (3) introducción de generalidades acerca de sistemas biosensores e inmunoquímica, así como descripción de los inmunoensayos estudiados durante esta tesis.

En el capítulo 3 se incluye una descripción minuciosa de la fabricación de electrodos de ITO, así como una caracterización físico-química. Se presenta una comparación entre capas finas y superficies nanoestructuradas en cuanto a área superficial disponible para la biodetección, así como un estudio de la influencia de la temperatura de sustrato durante el depósito del material en las características morfológicas de los electrodos resultantes.

El capítulo 4 incluye los resultados de los experimentos realizados empleando el ITO nanoestructurado como sensor electroquímico. Concretamente, se ha descrito con detalle el proceso de preparación del inmunosensor, y se ha caracterizado cada paso mediante distintas técnicas microscópicas y electroquímicas. Finalmente, se presentan los resultados de la inmunodetección como prueba de concepto.

En el capítulo 5 se presentan dos dispositivos electrónicos miniaturizados y de bajo coste para la medida de biosensores electroquímicos. Se incluye la descripción de la circuitería electrónica y el software, así como un análisis de pros y contras de ambos sistemas. Además, se presentan y analizan los resultados de la inmunodetección realizada con los dispositivos, usando tanto electrodos de oro como electrodos basados en ITO nanoestructurado.

El capítulo 6 concluye esta disertación subrayando los aspectos más relevantes presentados en la tesis.

Lista de publicaciones

Las publicaciones especificadas a continuación están recogidas como el cuerpo principal de esta tesis doctoral. Cada publicación está reproducida en las páginas indicadas con permiso de la correspondiente revista.

Artículo I. R. Pruna, F. Palacio, M. López, J. Pérez, M. Mir, O. Blázquez, S. Hernández and B. Garrido, *Electrochemical characterization of organosilane-functionalized nanostructured ITO surfaces*, Applied Physics Letters 109 (2016) 063109. DOI: 10.1063/1.4960734.
El artículo se reproduce en la **página 69**.

Artículo II. R. Pruna, F. Teixidor and M. López, *Tuning the deposition parameters for optimizing the faradaic and non-faradaic electrochemical performance of nanowire array-shaped ITO electrodes prepared by electron beam evaporation*, Nanoscale 11 (2019) 276 – 284. DOI: 10.1039/C8NR07908K.
El artículo se reproduce en la **página 79**.

Artículo III. R. Pruna, F. Palacio, M. Martínez, O. Blázquez, S. Hernández, B. Garrido and M. López, *Organosilane functionalization of nanostructured indium tin oxide films*, Interface Focus 6.6 (2016) 20160056. DOI: 10.1098/rsfs2016.0056.
El artículo se reproduce en la **página 107**.

Artículo IV. R. Pruna, A. Baraket, A. Bonhommé, N. Zine, A. Errachid and M. López, *Novel nanostructured indium tin oxide electrode for electrochemical immunosensors: Suitability for the detection of TNF-α*, Electrochimica Acta 283 (2018) 1632 – 1639. DOI: 10.1016/j.electacta.2018.07.066.
El artículo se reproduce en la **página 120**.

Artículo V. R. Pruna, F. Palacio, A. Baraket, N. Zine, A. Streklas, J. Bausells, A. Errachid and M. López, *A low-cost and miniaturized potentiostat for sensing of biomolecular species such as TNF-α by electrochemical impedance spectroscopy*, Biosensors and Bioelectronics 100 (2018) 533 – 540. DOI: 10.1016/j.bios.2017.09.049.
El artículo se reproduce en la **página 143**.

References

[1] Alan D McNaught and Alan D McNaught. *Compendium of chemical terminology*, volume 1669. Blackwell Science Oxford, 1997.

[2] J Duffus. Glossary for chemists of terms used in toxicology (iupac recommendations 1993). *Pure and applied chemistry*, 65(9):2003–2122, 1993.

[3] Darlene Berger. A brief history of medical diagnosis and the birth of the clinical laboratory. part 1—ancient times through the 19th century. *MLO Med Lab Obs*, 31(7):28–30, 1999.

[4] James Finlayson. Ancient egyptian medicine:[a bibliographical demonstration 1 in the library of the faculty of physicians and surgeons, glasgow, january 12th, 1893.]. *British Medical Journal*, 1(1684):748, 1893.

[5] Edwin Smith. *The Edwin Smith Surgical Papyrus*. University of Chicago Press, 1930.

[6] Markham J Geller. *Ancient Babylonian medicine: theory and practice*. John Wiley & Sons, 2010.

[7] Nathan Sivin. Science and medicine in imperial china—the state of the field. *The Journal of Asian Studies*, 47(1):41–90, 1988.

[8] Mark D Adams, Jenny M Kelley, Jeannine D Gocayne, Mark Dubnick, Mihael H Polymeropoulos, Hong Xiao, Carl R Merril, Andrew Wu, Bjorn Olde, Ruben F Moreno, et al. Complementary dna sequencing: expressed sequence tags and human genome project. *Science*, 252(5013):1651–1656, 1991.

[9] Sandra Misale, Rona Yaeger, Sebastijan Hobor, Elisa Scala, Manickam Janakiraman, David Liska, Emanuele Valtorta, Roberta Schiavo, Michela Buscarino, Giulia Siravegna, et al. Emergence of kras mutations and acquired resistance to anti-egfr therapy in colorectal cancer. *Nature*, 486(7404):532, 2012.

[10] Anthony V D'amico, Ming-Hui Chen, Kimberly A Roehl, and William J Catalona. Preoperative psa velocity and the risk of death from prostate cancer after radical prostatectomy. *New England Journal of Medicine*, 351(2):125–135, 2004.

[11] Gerard A Schellekens, Hendrik Visser, Ben AW De Jong, Frank HJ Van Den Hoogen, Johanna MW Hazes, Ferdinand C Breedveld, and Walther J Van Venrooij. The diagnostic properties of rheumatoid arthritis antibodies recognizing a cyclic citrullinated peptide. *Arthritis & Rheumatism: Official Journal of the American College of Rheumatology*, 43(1):155–163, 2000.

[12] K Hensley, JM Carney, MP Mattson, M Aksenova, M Harris, JF Wu, RA Floyd, and DA Butterfield. A model for beta-amyloid aggregation and neurotoxicity based on free radical generation by the peptide: relevance to alzheimer disease. *Proceedings of the National Academy of Sciences*, 91(8):3270–3274, 1994.

[13] Daniel R Thévenot, Klara Toth, Richard A Durst, and George S Wilson. Electrochemical biosensors: recommended definitions and classification. *Analytical Letters*, 34(5):635–659, 2001.

[14] Linda Lee, Eric Nordman, Martin Johnson, and Mark Oldham. A low-cost, high-performance system for fluorescence lateral flow assays. *Biosensors*, 3(4):360–373, 2013.

[15] Stephen A Butler, Sarah A Khanlian, and Laurence A Cole. Detection of early pregnancy forms of human chorionic gonadotropin by home pregnancy test devices. *Clinical Chemistry*, 47(12):2131–2136, 2001.

[16] Celine IL Justino, Armando C Duarte, and Teresa AP Rocha-Santos. Recent progress in biosensors for environmental monitoring: A review. *Sensors*, 17(12):2918, 2017.

[17] Jan Dirk Van Elsas, Alexander V Semenov, Rodrigo Costa, and Jack T Trevors. Survival of escherichia coli in the environment: fundamental and public health aspects. *The ISME journal*, 5(2):173, 2011.

[18] Kyung-Min Lee, Mick Runyon, Timothy J Herrman, Robert Phillips, and John Hsieh. Review of salmonella detection and identification methods: aspects of rapid emergency response and food safety. *Food control*, 47:264–276, 2015.

[19] P Elizaquível, JA Gabaldón, and R Aznar. Quantification of salmonella spp., listeria monocytogenes and escherichia coli o157: H7 in non-spiked food products and evaluation of real-time pcr as a diagnostic tool in routine food analysis. *Food Control*, 22(2):158–164, 2011.

[20] Kim R Rogers and Clare L Gerlach. Peer reviewed: environmental biosensors: a status report. *Environmental science & technology*, 30(11):486A–491A, 1996.

[21] Ajeet Kaushik and Mubarak Mujawar. Point of care sensing devices: Better care for everyone, 2018.

[22] Joseph Wang. Electrochemical biosensors: towards point-of-care cancer diagnostics. *Biosensors and Bioelectronics*, 21(10):1887–1892, 2006.

[23] Geertruida A Posthuma-Trumpie, Jakob Korf, and Aart van Amerongen. Lateral flow (immuno) assay: its strengths, weaknesses, opportunities and threats. a literature survey. *Analytical and bioanalytical chemistry*, 393(2):569–582, 2009.

[24] Brendan O'Farrell. Evolution in lateral flow–based immunoassay systems. In *Lateral flow immunoassay*, pages 1–33. Springer, 2009.

[25] Thomas C Tisone and Brendan O'Farrell. Manufacturing the next generation of highly sensitive and reproducible lateral flow immunoassay. In *Lateral Flow Immunoassay*, pages 1–26. Springer, 2009.

[26] Brittany A Rohrman, Veronica Leautaud, Elizabeth Molyneux, and Rebecca R Richards-Kortum. A lateral flow assay for quantitative detection of amplified hiv-1 rna. *PLoS One*, 7(9):e45611, 2012.

[27] John P Campbell, Jennifer LJ Heaney, Meena Shemar, Dene Baldwin, Ann E Griffin, Emma Oldridge, Margaret Goodall, Zaheer Afzal, Tim Plant, Mark Cobbold, et al. Development of a rapid and quantitative lateral flow assay for the simultaneous measurement of serum κ and λ immunoglobulin free light chains (flc): inception of a new near-patient flc screening tool. *Clinical Chemistry and Laboratory Medicine (CCLM)*, 55(3):424–434, 2017.

[28] K Narsaiah, Shyam Narayan Jha, Rishi Bhardwaj, Rajiv Sharma, and Ramesh Kumar. Optical biosensors for food quality and safety assurance—a review. *Journal of food science and technology*, 49(4):383–406, 2012.

[29] Anthony PF Turner. Biosensors: sense and sensibility. *Chemical Society Reviews*, 42(8):3184–3196, 2013.

[30] Niina J Ronkainen, H Brian Halsall, and William R Heineman. Electrochemical biosensors. *Chemical Society Reviews*, 39(5):1747–1763, 2010.

[31] Sheetal Chawla and Chandra Shekhar Pundir. An electrochemical biosensor for fructosyl valine for glycosylated hemoglobin detection based on core–shell magnetic bionanoparticles modified gold electrode. *Biosensors and Bioelectronics*, 26(8):3438–3443, 2011.

[32] Feng Li, Xiaoping Han, and Shufeng Liu. Development of an electrochemical dna biosensor with a high sensitivity of fm by dendritic gold nanostructure modified electrode. *Biosensors and Bioelectronics*, 26(5):2619–2625, 2011.

[33] Thomas Bryan, Xiliang Luo, Paulo R Bueno, and Jason J Davis. An optimised electrochemical biosensor for the label-free detection of c-reactive protein in blood. *Biosensors and Bioelectronics*, 39(1):94–98, 2013.

[34] Madalina M Barsan, M Emilia Ghica, and Christopher MA Brett. Electrochemical sensors and biosensors based on redox polymer/carbon nanotube modified electrodes: a review. *Analytica chimica acta*, 881:1–23, 2015.

[35] Raquel Gracia and David Mecerreyes. Polymers with redox properties: materials for batteries, biosensors and more. *Polymer Chemistry*, 4(7):2206–2214, 2013.

[36] Xiao-Chen Dong, Hang Xu, Xue-Wan Wang, Yin-Xi Huang, Mary B Chan-Park, Hua Zhang, Lian-Hui Wang, Wei Huang, and Peng Chen. 3d graphene–cobalt oxide electrode for high-performance supercapacitor and enzymeless glucose detection. *ACS nano*, 6(4):3206–3213, 2012.

[37] Martin Pumera. Graphene in biosensing. *Materials today*, 14(7-8):308–315, 2011.

[38] Shuwen Zeng, Ken-Tye Yong, Indrajit Roy, Xuan-Quyen Dinh, Xia Yu, and Feng Luan. A review on functionalized gold nanoparticles for biosensing applications. *Plasmonics*, 6(3):491, 2011.

[39] Krishnendu Saha, Sarit S Agasti, Chaekyu Kim, Xiaoning Li, and Vincent M Rotello. Gold nanoparticles in chemical and biological sensing. *Chemical reviews*, 112(5):2739–2779, 2012.

[40] Md Rahman, AJ Ahammad, Joon-Hyung Jin, Sang Jung Ahn, Jae-Joon Lee, et al. A comprehensive review of glucose biosensors based on nanostructured metal-oxides. *Sensors*, 10(5):4855–4886, 2010.

[41] Chengzhou Zhu, Guohai Yang, He Li, Dan Du, and Yuehe Lin. Electrochemical sensors and biosensors based on nanomaterials and nanostructures. *Analytical chemistry*, 87(1):230–249, 2014.

[42] Sunil K Arya, Shibu Saha, Jaime E Ramirez-Vick, Vinay Gupta, Shekhar Bhansali, and Surinder P Singh. Recent advances in zno nanostructures and thin films for biosensor applications. *Analytica chimica acta*, 737:1–21, 2012.

[43] Ying Wang, Sheng Zhang, Dan Du, Yuyan Shao, Zhaohui Li, Jun Wang, Mark H Engelhard, Jinghong Li, and Yuehe Lin. Self assembly of acetylcholinesterase on a gold nanoparticles–graphene nanosheet hybrid for organophosphate pesticide detection using polyelectrolyte as a linker. *Journal of Materials Chemistry*, 21(14):5319–5325, 2011.

[44] Yuanyuang Li, Hermann J Schluesener, and Shunqing Xu. Gold nanoparticle-based biosensors. *Gold Bulletin*, 43(1):29–41, 2010.

[45] José R Siqueira Jr, Luciano Caseli, Frank N Crespilho, Valtencir Zucolotto, and Osvaldo N Oliveira Jr. Immobilization of biomolecules on nanostructured films for biosensing. *Biosensors and Bioelectronics*, 25(6):1254–1263, 2010.

[46] XB Yan, XJ Chen, BK Tay, and Khiam Aik Khor. Transparent and flexible glucose biosensor via layer-by-layer assembly of multi-wall carbon nanotubes and glucose oxidase. *Electrochemistry Communications*, 9(6):1269–1275, 2007.

[47] David S Ginley and Clark Bright. Transparent conducting oxides. *MRS bulletin*, 25(8):15–18, 2000.

[48] Andreas Stadler. Transparent conducting oxides—an up-to-date overview. *Materials*, 5(4):661–683, 2012.

[49] Xinge Yu, Tobin J Marks, and Antonio Facchetti. Metal oxides for optoelectronic applications. *Nature materials*, 15(4):383, 2016.

[50] Yidong Zhang, Gangcheng Jiang, Ka Wai Wong, and Zhi Zheng. Green synthesis of indium oxide hollow spheres with specific sensing activities for flammable organic vapors. *Sensor Letters*, 8(2):355–361, 2010.

[51] ON Mryasov and AJ Freeman. Electronic band structure of indium tin oxide and criteria for transparent conducting behavior. *Physical Review B*, 64(23):233111, 2001.

[52] Hiromi Nakazawa, Yuko Ito, Eiji Matsumoto, Kenji Adachi, Nobuyuki Aoki, and Yuichi Ochiai. The electronic properties of amorphous and crystallized in 2 o 3 films. *Journal of applied physics*, 100(9):093706, 2006.

[53] Charles Kittel, Paul McEuen, and Paul McEuen. *Introduction to solid state physics*, volume 8. Wiley New York, 1996.

[54] Radhouane Bel Hadj Tahar, Takayuki Ban, Yutaka Ohya, and Yasutaka Takahashi. Tin doped indium oxide thin films: Electrical properties. *Journal of Applied Physics*, 83(5):2631–2645, 1998.

[55] N Nadaud, N Lequeux, M Nanot, J Jove, and T Roisnel. Structural studies of tin-doped indium oxide (ito) and in4sn3o12. *Journal of Solid State Chemistry*, 135(1):140–148, 1998.

[56] In2o3 crystal structure: Datasheet from "pauling file multinaries edition – 2012" in springermaterials (https://materials.springer.com/isp/crystallographic/docs/sd_0531025). Copyright 2016 Springer-Verlag Berlin Heidelberg & Material Phases Data System (MPDS), Switzerland & National Institute for Materials Science (NIMS), Japan.

[57] I Elfallal, RD Pilkington, and AE Hill. Formulation of a statistical thermodynamic model for the electron concentration in heavily doped metal oxide semiconductors applied to the tin-doped indium oxide system. *Thin Solid Films*, 223(2):303–310, 1993.

[58] Hans Hartnagel, AL Dawar, AK Jain, and Cand Jagadish. *Semiconducting transparent thin films*. Institute of Physics Bristol, 1995.

[59] SA Agnihotry, KK Saini, TK Saxena, KC Nagpal, and SUBHAS Chandra. Studies on e-beam deposited transparent conductive films of in2o3: Sn at moderate substrate temperatures. *Journal of Physics D: Applied Physics*, 18(10):2087, 1985.

[60] JC Manifacier. Thin metallic oxides as transparent conductors. *Thin Solid Films*, 90(3):297–308, 1982.

[61] Fang Aiping. *Analytical applications of self-assembled biomolecules*. PhD thesis, 2003.

[62] JH Park, C Buurma, S Sivananthan, R Kodama, W Gao, and TA Gessert. The effect of post-annealing on indium tin oxide thin films by magnetron sputtering method. *Applied Surface Science*, 307:388–392, 2014.

[63] Neng Wan, Tao Wang, Hongcheng Sun, Guran Chen, Lei Geng, Xinhui Gan, Sihua Guo, Jun Xu, Ling Xu, and Kunji Chen. Indium tin oxide thin films for silicon-based electro-luminescence devices prepared by electron beam evaporation method. *Journal of Non-Crystalline Solids*, 356(18-19):911–916, 2010.

[64] Carrie Donley, Darren Dunphy, David Paine, Chet Carter, Ken Nebesny, Paul Lee, Dana Alloway, and Neal R Armstrong. Characterization of indium- tin oxide interfaces using x-ray photoelectron spectroscopy and redox processes of a chemisorbed probe molecule: effect of surface pretreatment conditions. *Langmuir*, 18(2):450–457, 2002.

[65] Timothy J Gardner, C Daniel Frisbie, and Mark S Wrighton. Systems for orthogonal self-assembly of electroactive monolayers on au and ito: an approach to molecular electronics. *Journal of the American Chemical Society*, 117(26):6927–6933, 1995.

[66] Gianni Zotti, Gilberto Schiavon, Sandro Zecchin, Anna Berlin, and G Pagani. Adsorption of ferrocene compounds on indium- tin- oxide electrodes. enhancement of adsorption by decomposition of ferrocenium molecules by oxygen. *Langmuir*, 14(7):1728–1733, 1998.

[67] Hyun Cho and Young-Hoon Yun. Characterization of indium tin oxide (ito) thin films prepared by a sol–gel spin coating process. *Ceramics International*, 37(2):615–619, 2011.

[68] Akbar Eshaghi and Alireza Graeli. Optical and electrical properties of indium tin oxide (ito) nanostructured thin films deposited on polycarbonate substrates "thickness effect". *Optik-International Journal for Light and Electron Optics*, 125(3):1478–1481, 2014.

[69] Min Hyung Ahn, Eou-Sik Cho, and Sang Jik Kwon. Effect of the duty ratio on the indium tin oxide (ito) film deposited by in-line pulsed dc magnetron sputtering method for resistive touch panel. *Applied Surface Science*, 258(3):1242–1248, 2011.

[70] R Pruna, F Palacio, M Martínez, O Blázquez, S Hernández, B Garrido, and M López. Organosilane-functionalization of nanostructured indium tin oxide films. *Interface focus*, 6(6):20160056, 2016.

[71] JS Kim, PKH Ho, DS Thomas, RH Friend, F Cacialli, G-W Bao, and SFY Li. X-ray photoelectron spectroscopy of surface-treated indium-tin oxide thin films. *Chemical Physics Letters*, 315(5-6):307–312, 1999.

[72] Takahiro Daido and Toshihiro Akaike. Electrochemistry of cytochrome c: influence of coulombic attraction with indium tin oxide electrode. *Journal of Electroanalytical Chemistry*, 344(1-2):91–106, 1993.

[73] CH Chiu, Peichen Yu, CH Chang, CS Yang, MH Hsu, HC Kuo, and MA Tsai. Oblique electron-beam evaporation of distinctive indium-tin-oxide nanorods for enhanced light extraction from ingan/gan light emitting diodes. *Optics express*, 17(23):21250–21256, 2009.

[74] MK Fung, YC Sun, AMC Ng, XY Chen, KK Wong, AB Djurišić, and WK Chan. Indium tin oxide nanowires growth by dc sputtering. *Applied Physics A*, 104(4):1075–1080, 2011.

[75] Jae Hyoung Park, Hoo Keun Park, Jinhoo Jeong, Woong Kim, Byoung Koun Min, and Young Rag Do. Wafer-scale growth of ito nanorods by radio frequency magnetron sputtering deposition. *Journal of The Electrochemical Society*, 158(5):K131–K135, 2011.

[76] Neng Wan, Jun Xu, Guran Chen, Xinhui Gan, Sihua Guo, Ling Xu, and Kunji Chen. Broadband anti-reflection and enhanced field emission from catalyst-free grown small-sized ito nanowires at a low temperature. *Acta Materialia*, 58(8):3068–3072, 2010.

[77] AL Beaudry, RT Tucker, JM LaForge, MT Taschuk, and MJ Brett. Indium tin oxide nanowhisker morphology control by vapour–liquid–solid glancing angle deposition. *Nanotechnology*, 23(10):105608, 2012.

[78] Thian-Khok Yong, Sek-Sean Tan, Chen-Hon Nee, Seong-Shan Yap, Yeh-Yee Kee, György Sáfrán, Zsolt Endre Horváth, Jason Moscatello, Yoke-Khin Yap, and Teck-Yong Tou. Pulsed laser deposition of indium tin oxide nanowires in argon and helium. *Materials Letters*, 66(1):280–281, 2012.

[79] Jaron G Van Dijken and Michael J Brett. Nanopillar ito electrodes via argon plasma etching. *Journal of Vacuum Science & Technology A: Vacuum, Surfaces, and Films*, 30(4):040606, 2012.

[80] Colm O'Dwyer, Marta Szachowicz, Giuseppe Visimberga, Vladimir Lavayen, Simon B Newcomb, and CM Sotomayor Torres. Bottom-up growth of fully transparent contact layers of indium tin oxide nanowires for light-emitting devices. *Nature nanotechnology*, 4(4):239, 2009.

[81] Hoon Sik Jang, Do-Hyung Kim, Hyeong-Rag Lee, and Sung-Youp Lee. Field emission from cone-like single crystalline indium tin oxide nanorods. *Materials Letters*, 59(12):1526–1529, 2005.

[82] KP Kalyanikutty, Gautam Gundiah, Christopher Edem, A Govindaraj, and CNR Rao. Doped and undoped ito nanowires. *Chemical physics letters*, 408(4-6):389–394, 2005.

[83] Toshiro Maruyama and Kunihiro Fukui. Indium-tin oxide thin films prepared by chemical vapor deposition. *Journal of applied physics*, 70(7):3848–3851, 1991.

[84] LA Ryabova, VS Salun, and IA Serbinov. Transparent conductive films of in2o3: Sn prepared by the pyrolysis method. *Thin Solid Films*, 92(4):327–332, 1982.

[85] R Pommier, C Gril, and J Marucchi. Sprayed films of indium tin oxide and fluorine-doped tin oxide of large surface area. *Thin Solid Films*, 77(1-3):91–98, 1981.

[86] J-C Manifacier, L Szepessy, JF Bresse, M Perotin, and R Stuck. In2o3:(sn) and sno2:(f) films-application to solar energy conversion part ii—electrical and optical properties. *Materials Research Bulletin*, 14(2):163–175, 1979.

[87] AK Saxena, SP Singh, R Thangaraj, and OP Agnihotri. Thickness dependence of the electrical and structural properties of in2o3: Sn films. *Thin Solid Films*, 117(2):95–100, 1984.

[88] KDJ Christian and SR Shatynski. Thin film passive solar windows produced by reactive evaporation of in-sn. *Thin Solid Films*, 108(3):319–324, 1983.

[89] P Thilakan, C Minarini, S Loreti, and E Terzini. Investigations on the crystallisation properties of rf magnetron sputtered indium tin oxide thin films. *Thin Solid Films*, 388(1-2):34–40, 2001.

[90] M Fujinaka and AA Berezin. Tin-doped in2o3 films deposited by rf sputtering. *Thin Solid Films*, 101(1):7–10, 1983.

[91] Yuzo Shigesato, Yasuo Hayashi, Akio Masui, and Takeshi Haranou. The structural changes of indium-tin oxide and a-wo3 films by introducing water to the deposition processes. *Japanese journal of applied physics*, 30(4R):814, 1991.

[92] A Kawada. Indium-tin oxide deposition by dc reactive sputtering on a low softening point material. *Thin Solid Films*, 191(2):297–303, 1990.

[93] Esko Ahvenniemi, Andrew R Akbashev, Saima Ali, Mikhael Bechelany, Maria Berdova, Stefan Boyadjiev, David C Cameron, Rong Chen, Mikhail Chubarov, Veronique Cremers, et al. Recommended reading list of early publications on atomic layer deposition—outcome of the "virtual project on the history of ald". *Journal of Vacuum Science & Technology A: Vacuum, Surfaces, and Films*, 35(1):010801, 2017.

[94] Paddy French, Gijs Krijnen, and Fred Roozeboom. Precision in harsh environments. *Microsystems & nanoengineering*, 2:16048, 2016.

[95] RP Goyal, D Raviendra, and BRK Gupta. Electroless deposition of in2o3 and in2o3: Sn (ito). *physica status solidi (a)*, 87(1):79–83, 1985.

[96] Osamu Yamamoto, Tadashi Sasamoto, and Michio Inagaki. Indium tin oxide thin films prepared by thermal decomposition of ethylene glycol solution. *Journal of materials research*, 7(9):2488–2491, 1992.

[97] John CC Fan. Preparation of sn-doped in2o3 (ito) films at low deposition temperatures by ion-beam sputtering. *Applied Physics Letters*, 34(8):515–517, 1979.

[98] John CC Fan. Sputtered films for wavelength-selective applications. *Thin Solid Films*, 80(1-3):125–136, 1981.

[99] AJ Nelson and H Aharoni. X-ray photoelectron spectroscopy investigation of ion beam sputtered indium tin oxide films as a function of oxygen pressure during deposition. *Journal of Vacuum Science & Technology A: Vacuum, Surfaces, and Films*, 5(2):231–233, 1987.

[100] Sung Kyu Park, Jeong In Han, Dae Gyu Moon, and Won Keun Kim. Mechanical stability of externally deformed indium–tin–oxide films on polymer substrates. *Japanese journal of applied physics*, 42(2R):623, 2003.

[101] J-M Park, J-S Hong, J-Y Yang, J-J Kim, S-H Park, H-M Kim, and J-S Ahn. Bending effects of indium-zinc oxide thin films deposited on polyethylene terephthalate substrate by radio frequency magnetron sputtering. *Journal of the Korean Physical Society*, 48(6):1530–1533, 2006.

[102] David S Hecht, Liangbing Hu, and Glen Irvin. Emerging transparent electrodes based on thin films of carbon nanotubes, graphene, and metallic nanostructures. *Advanced materials*, 23(13):1482–1513, 2011.

[103] Michael W Rowell, Mark A Topinka, Michael D McGehee, Hans-Jürgen Prall, Gilles Dennler, Niyazi Serdar Sariciftci, Liangbing Hu, and George Gruner. Organic solar cells with carbon nanotube network electrodes. *Applied Physics Letters*, 88(23):233506, 2006.

[104] Peichen Yu, Chia-Hua Chang, Ching-Hua Chiu, Chin-Sheng Yang, Jue-Chin Yu, Hao-Chung Kuo, Shih-Hsin Hsu, and Yia-Chung Chang. Efficiency enhancement of gaas photovoltaics employing antireflective indium tin oxide nanocolumns. *Advanced materials*, 21(16):1618–1621, 2009.

[105] SI Castaneda, Fernando Rueda, R Dıaz, José María Ripalda, and Isabel Montero. Whiskers in indium tin oxide films obtained by electron beam evaporation. *Journal of applied physics*, 83(4):1995–2002, 1998.

[106] J Gao, R Chen, DH Li, L Jiang, JC Ye, XC Ma, XD Chen, QH Xiong, HD Sun, and T Wu. Uv light emitting transparent conducting tin-doped indium oxide (ito) nanowires. *Nanotechnology*, 22(19):195706, 2011.

[107] RS Wagner and WC Ellis. Vapor-liquid-solid mechanism of single crystal growth. *Applied Physics Letters*, 4(5):89–90, 1964.

[108] R Rakesh Kumar, K Narasimha Rao, K Rajanna, and AR Phani. Low temperature and self catalytic growth of ultrafine ito nanowires by electron beam evaporation method and their optical and electrical properties. *Materials Research Bulletin*, 52:167–176, 2014.

[109] WF Gale and TC Totemeier. Smithells metals reference book" eight edition, amsterdam, boston, heidelberg, london, new york, 2004.

[110] Brent A Wacaser, Kimberly A Dick, Jonas Johansson, Magnus T Borgström, Knut Deppert, and Lars Samuelson. Preferential interface nucleation: an expansion of the vls growth mechanism for nanowires. *Advanced Materials*, 21(2):153–165, 2009.

[111] Sen-Tsun Jean and Yung-Chiun Her. Growth mechanism and photoluminescence properties of in2o3 nanotowers. *Crystal Growth & Design*, 10(5):2104–2110, 2010.

[112] Changjung Kim and Youngsoo Park. Touch panel including nanowire, June5 2012. US Patent 8,194,053.

[113] Jen-Hsien Huang, Min-Hsiang Hsu, Yu-Sheng Hsiao, Peilin Chen, Peichen Yu, and Chih-Wei Chu. Performance of chromophore-type electrochromic devices employing indium tin oxide nanorod optical amplification. *Solar Energy Materials and Solar Cells*, 98:191–197, 2012.

[114] Yeh Yee Kee, Sek Sean Tan, Thian Khok Yong, Chen Hon Nee, Seong Shan Yap, Teck Yong Tou, György Sáfrán, Zsolt Endre Horváth, Jason P Moscatello, and Yoke Khin Yap. Low-temperature synthesis of indium tin oxide nanowires as the transparent electrodes for organic light emitting devices. *Nanotechnology*, 23(2):025706, 2011.

[115] Arunandan Kumar, Ritu Srivastava, MN Kamalasanan, and Dalip Singh Mehta. Enhancement of light extraction efficiency of organic light emitting diodes using nanostructured indium tin oxide. *Optics letters*, 37(4):575–577, 2012.

[116] Alberto Vomiero, Sebastiano Bianchi, Elisabetta Comini, Guido Faglia, Matteo Ferroni, and Giorgio Sberveglieri. Controlled growth and sensing properties of in2o3 nanowires. *Crystal Growth and Design*, 7(12):2500–2504, 2007.

[117] Dick van Dam, Niels JJ van Hoof, Yingchao Cui, Peter J van Veldhoven, Erik PAM Bakkers, Jaime Goómez Rivas, and Jos EM Haverkort. High-efficiency nanowire solar cells with omnidirectionally enhanced absorption due to self-aligned indium–tin–oxide mie scatterers. *ACS nano*, 10(12):11414–11419, 2016.

[118] Xingwang Song, Guobo Dong, Fangyuan Gao, Yu Xiao, Qirong Liu, and Xungang Diao. Properties of niox and its influence upon all-thin-film ito/niox/litao3/wo3/ito electrochromic devices prepared by magnetron sputtering. *Vacuum*, 111:48–54, 2015.

[119] Dongmei Dong, Wenwen Wang, Aline Rougier, GuoBo Dong, Mathias Da Rocha, Lionel Presmanes, Khawla Zrikem, Giljoo Song, Xungang Diao, and Antoine Barnabé. Life-cycling and uncovering cation-trapping evidence of monolithic inorganic electrochromic device: Glass/ito/wo3/litao3/nio/ito. *Nanoscale*, 2018.

[120] Chien-Jen Tang, Jia-Ming Ye, Yueh-Ting Yang, and Ju-Liang He. Large-area flexible monolithic ito/wo3/nb2o5/nivoχ/ito electrochromic devices prepared by using magnetron sputter deposition. *Optical Materials*, 55:83–89, 2016.

[121] I Hamberg, A Hjortsberg, and CG Granqvist. High quality transparent heat reflectors of reactively evaporated indium tin oxide. *Applied Physics Letters*, 40(5):362–364, 1982.

[122] NG Patel, KK Makhija, and CJ Panchal. Fabrication of carbon dioxide gas sensor and its alarm system using indium tin oxide (ito) thin films. *Sensors and Actuators B: Chemical*, 21(3):193–197, 1994.

[123] NG Patel, KK Makhija, CJ Panchal, DB Dave, and VS Vaishnav. Fabrication of carbon tetrachloride gas sensors using indium tin oxide thin films. *Sensors and Actuators B: Chemical*, 23(1):49–53, 1995.

[124] J Zhang, JQ Hu, FR Zhu, H Gong, and SJ O'shea. Ito thin films coated quartz crystal microbalance as gas sensor for no detection. *Sensors and Actuators B: Chemical*, 87(1):159–167, 2002.

[125] NG Patel, PD Patel, and VS Vaishnav. Indium tin oxide (ito) thin film gas sensor for detection of methanol at room temperature. *Sensors and Actuators B: Chemical*, 96(1-2):180–189, 2003.

[126] Cheng-Wei Lin, Huey-Ing Chen, Tai-You Chen, Chien-Chang Huang, Chi-Shiang Hsu, Rong-Chau Liu, and Wen-Chau Liu. On an indium–tin-oxide thin film based ammonia gas sensor. *Sensors and Actuators B: Chemical*, 160(1):1481–1484, 2011.

[127] Satyendra K Mishra and Banshi D Gupta. Surface plasmon resonance-based fiber-optic hydrogen gas sensor utilizing indium–tin oxide (ito) thin films. *Plasmonics*, 7(4):627–632, 2012.

[128] Takuya Kawashima, Tetsuya Ezure, Kenichi Okada, Hiroshi Matsui, Kenji Goto, and Nobuo Tanabe. Fto/ito double-layered transparent conductive oxide for dye-sensitized solar cells. *Journal of Photochemistry and Photobiology A: Chemistry*, 164(1-3):199–202, 2004.

[129] Jin-A Jeong and Han-Ki Kim. Low resistance and highly transparent ito–ag–ito multilayer electrode using surface plasmon resonance of ag layer for bulk-heterojunction organic solar cells. *Solar Energy Materials and Solar Cells*, 93(10):1801–1809, 2009.

[130] Johannes Krantz, Moses Richter, Stefanie Spallek, Erdmann Spiecker, and Christoph J Brabec. Solution-processed metallic nanowire electrodes as indium tin oxide replacement for thin-film solar cells. *Advanced Functional Materials*, 21(24):4784–4787, 2011.

[131] Frederik C Krebs. Roll-to-roll fabrication of monolithic large-area polymer solar cells free from indium-tin-oxide. *Solar Energy Materials and Solar Cells*, 93(9):1636–1641, 2009.

[132] J Meiss, MK Riede, and K Leo. Towards efficient tin-doped indium oxide (ito)-free inverted organic solar cells using metal cathodes. *Applied Physics Letters*, 94(1):3, 2009.

[133] Allen J Bard, Larry R Faulkner, Johna Leddy, and Cynthia G Zoski. *Electrochemical methods: fundamentals and applications*, volume 2. wiley New York, 1980.

[134] Francis Weston Sears. *Thermodynamics, kinetic theory, and statistical thermodynamics*. Addison-Wesley, 1975.

[135] John Thomas Stock, Mary Virginia Orna, et al. *Electrochemistry, past and present*, volume 390. ACS Publications, 1989.

[136] George J Janz and David JD Ives. *Reference electrodes theory and practice*. Academic Press, 1961.

[137] Donald T Sawyer, Andrzej Sobkowiak, and Julian L Roberts. *Electrochemistry for chemists*. Wiley, 1995.

[138] Hainan Wang and Laurent Pilon. Accurate simulations of electric double layer capacitance of ultramicroelectrodes. *The Journal of Physical Chemistry C*, 115(33):16711–16719, 2011.

[139] Keith B Oldham. A gouy–chapman–stern model of the double layer at a (metal)/(ionic liquid) interface. *Journal of Electroanalytical Chemistry*, 613(2):131–138, 2008.

[140] Ryan Burt, Greg Birkett, and XS Zhao. A review of molecular modelling of electric double layer capacitors. *Physical Chemistry Chemical Physics*, 16(14):6519–6538, 2014.

[141] Vincent Gau, Shu-Ching Ma, Hua Wang, Joni Tsukuda, John Kibler, and David A Haake. Electrochemical molecular analysis without nucleic acid amplification. *Methods*, 37(1):73–83, 2005.

[142] Janice C Myland and Keith B Oldham. An analytical expression for the current-voltage relationship during reversible cyclic voltammetry. *Journal of Electroanalytical Chemistry and Interfacial Electrochemistry*, 153(1-2):43–54, 1983.

[143] R Pruna, F Palacio, M López, J Pérez, M Mir, O Blázquez, S Hernández, and B Garrido. Electrochemical characterization of organosilane-functionalized nanostructured ito surfaces. *Applied Physics Letters*, 109(6):063109, 2016.

[144] Anis Allagui, Todd J Freeborn, Ahmed S Elwakil, and Brent J Maundy. Reevaluation of performance of electric double-layer capacitors from constant-current charge/discharge and cyclic voltammetry. *Scientific reports*, 6:38568, 2016.

[145] K Gelderman, L Lee, and SW Donne. Flat-band potential of a semiconductor: using the mott–schottky equation. *Journal of chemical education*, 84(4):685, 2007.

[146] Krishnan Rajeshwar. Fundamentals of semiconductor electrochemistry and photoelectrochemistry. *Encyclopedia of electrochemistry*, 6:1–53, 2007.

[147] Nandhinee Radha Shanmugam, Sriram Muthukumar, Anjan Panneer Selvam, and Shalini Prasad. Electrochemical nanostructured zno biosensor for ultrasensitive detection of cardiac troponin-t. *Nanomedicine*, 11(11):1345–1358, 2016.

[148] WH Reinmuth. Three-dimensional representation of voltammetric processes. *Analytical Chemistry*, 32(11):1509–1512, 1960.

[149] M Sluyters-Rehbach and JH Sluyters. On the impedance of galvanic cells: Xxix. the potential dependence of the faradaic parameters for electrode processes with coupled homogeneous chemical reactions. *Journal of Electroanalytical Chemistry and Interfacial Electrochemistry*, 26(2-3):237–257, 1970.

[150] Claude Gabrielli. Identification of electrochemical processes by frequency response analysis. Technical Report Ref. 004/83, Solartron Instrument Group, 1980.

[151] F Mansfeld and WJ Lorenz. *Techniques for characterization of electrodes and electrochemical processes*, chapter 12. John Wiley & Sons, New York, 1991.

[152] DD Macdonald. *Techniques for characterization of electrodes and electrochemical processes*, chapter 11. John Wiley & Sons, New York, 1991.

[153] C Gabrielli. *Physical Electrochemistry*, chapter 6. Marcel Dekker, New York, 1995.

[154] Richard P Buck and E Lindner. Recommendations for nomenclature of ionselective electrodes (iupac recommendations 1994). *Pure and Applied Chemistry*, 66(12):2527–2536, 1994.

[155] Rastislav Monošík, Miroslav Streďanskỳ, and Ernest Šturdík. Biosensors-classification, characterization and new trends. *Acta Chimica Slovaca*, 5(1):109–120, 2012.

[156] Gary W Litman, Jonathan P Rast, Michael J Shamblott, Robert N Haire, Michele Hulst, William Roess, Ronda T Litman, Kristin R Hinds-Frey, Anna Zilch, and Chris T Amemiya. Phylogenetic diversification of immunoglobulin genes and the antibody repertoire. *Molecular biology and evolution*, 10(1):60–72, 1993.

[157] Jianwen Wang, Liping Wang, Junwei Di, and Yifeng Tu. Electrodeposition of gold nanoparticles on indium/tin oxide electrode for fabrication of a disposable hydrogen peroxide biosensor. *Talanta*, 77(4):1454–1459, 2009.

[158] Jiehua Lin, Wei Qu, and Shusheng Zhang. Disposable biosensor based on enzyme immobilized on au–chitosan-modified indium tin oxide electrode with flow injection amperometric analysis. *Analytical biochemistry*, 360(2):288–293, 2007.

[159] Liping Wang, Wei Mao, Dandan Ni, Junwei Di, Ying Wu, and Yifeng Tu. Direct electrodeposition of gold nanoparticles onto indium/tin oxide film coated glass and its application for electrochemical biosensor. *Electrochemistry Communications*, 10(4):673–676, 2008.

[160] Yanling Hu, Yan Song, Yuan Wang, and Junwei Di. Electrochemical synthesis of gold nanoparticles onto indium tin oxide glass and application in biosensors. *Thin Solid Films*, 519(19):6605–6609, 2011.

[161] Jianbo Jia, Bingquan Wang, Aiguo Wu, Guangjin Cheng, Zhuang Li, and Shaojun Dong. A method to construct a third-generation horseradish peroxidase biosensor: self-assembling gold nanoparticles to three-dimensional sol- gel network. *Analytical Chemistry*, 74(9):2217–2223, 2002.

[162] Li Wang and Erkang Wang. A novel hydrogen peroxide sensor based on horseradish peroxidase immobilized on colloidal au modified ito electrode. *Electrochemistry Communications*, 6(2):225–229, 2004.

[163] Huifeng Tian, Mingzhe Jia, Mingxing Zhang, and Jingbo Hu. Nonenzymatic glucose sensor based on nickel ion implanted-modified indium tin oxide electrode. *Electrochimica Acta*, 96:285–290, 2013.

[164] Aiping Fang, Hou Tee Ng, and Sam Fong Yau Li. A high-performance glucose biosensor based on monomolecular layer of glucose oxidase covalently immobilised on indium–tin oxide surface. *Biosensors and bioelectronics*, 19(1):43–49, 2003.

[165] E Moore, D O'Connell, and P Galvin. Surface characterisation of indium-tin oxide thin electrode films for use as a conducting substrate in dna sensor development. *Thin Solid Films*, 515(4):2612–2617, 2006.

[166] Liju Yang and Yanbin Li. Afm and impedance spectroscopy characterization of the immobilization of antibodies on indium–tin oxide electrode through self-assembled monolayer of epoxysilane and their capture of escherichia coli o157: H7. *Biosensors and Bioelectronics*, 20(7):1407–1416, 2005.

[167] Shiyou Xu and Yong Shi. Low temperature high sensor response nano gas sensor using ito nanofibers. *Sensors and Actuators B: Chemical*, 143(1):71–75, 2009.

[168] Maziar Afshar, Elisabeth M Preiß, Tilman Sauerwald, Marius Rodner, Dara Feili, Martin Straub, Karsten König, Andreas Schütze, and Helmut Seidel. Indium-tin-oxide single-nanowire gas sensor fabricated via laser writing and subsequent etching. *Sensors and Actuators B: Chemical*, 215:525–535, 2015.

[169] Mohsen Shariati. The field effect transistor dna biosensor based on ito nanowires in label-free hepatitis b virus detecting compatible with cmos technology. *Biosensors and Bioelectronics*, 105:58–64, 2018.

[170] Greg T Hermanson. *Bioconjugate techniques*. Academic press, 2013.

[171] Edwin P Plueddemann. Chemistry of silane coupling agents. In *Silane coupling agents*, pages 31–54. Springer, 1991.

[172] P Van Der Voort and EF Vansant. Silylation of the silica surface a review. *Journal of liquid chromatography & related technologies*, 19(17-18):2723–2752, 1996.

[173] Bruno Fabre. Ferrocene-terminated monolayers covalently bound to hydrogen-terminated silicon surfaces. toward the development of charge storage and communication devices. *Accounts of chemical research*, 43(12):1509–1518, 2010.

[174] Jun Wang, Jinhua Li, Alfred J Baca, Jingbo Hu, Feimeng Zhou, Wei Yan, and Dai-Wen Pang. Amplified voltammetric detection of dna hybridization via oxidation of ferrocene caps on gold nanoparticle/streptavidin conjugates. *Analytical chemistry*, 75(15):3941–3945, 2003.

[175] AM Bond, EA McLennan, RS Stojanovic, and FG Thomas. Assessment of conditions under which the oxidation of ferrocene can be used as a standard voltammetric reference process in aqueous media. *Analytical Chemistry*, 59(24):2853–2860, 1987.

[176] Jose Hodak, Roberto Etchenique, Ernesto J Calvo, Kavita Singhal, and Philip N Bartlett. Layer-by-layer self-assembly of glucose oxidase with a poly (allylamine) ferrocene redox mediator. *Langmuir*, 13(10):2708–2716, 1997.

[177] Chalermpol Innuphata and Pipat Chootoa. Determination of trace levels of cd (ii) in tap water samples by anodic stripping voltammetry with an electrografted boron-doped diamond electrode. *SCIENCEASIA*, 43(1):33–41, 2017.

[178] Evangelina Pensa, Emiliano Cortes, Gaston Corthey, Pilar Carro, Carolina Vericat, Mariano H Fonticelli, Guillermo Benitez, Aldo A Rubert, and Roberto C Salvarezza. The chemistry of the sulfur–gold interface: in search of a unified model. *Accounts of chemical research*, 45(8):1183–1192, 2012.

[179] C Vericat, ME Vela, G Benitez, P Carro, and RC Salvarezza. Self-assembled monolayers of thiols and dithiols on gold: new challenges for a well-known system. *Chemical Society Reviews*, 39(5):1805–1834, 2010.

[180] Gerd H Woehrle, Leif O Brown, and James E Hutchison. Thiol-functionalized, 1.5-nm gold nanoparticles through ligand exchange reactions: Scope and mechanism of ligand exchange. *Journal of the American Chemical Society*, 127(7):2172–2183, 2005.

[181] Melissa R Dewi, Geoffry Laufersky, and Thomas Nann. A highly efficient ligand exchange reaction on gold nanoparticles: preserving their size, shape and colloidal stability. *RSC Advances*, 4(64):34217–34220, 2014.

[182] Anshika Kapur, Fadi Aldeek, Xin Ji, Malak Safi, Wentao Wang, Ada Del Cid, Oliver Steinbock, and Hedi Mattoussi. Self-assembled gold nanoparticle–fluorescent protein conjugates as platforms for sensing thiolate compounds via modulation of energy transfer quenching. *Bioconjugate chemistry*, 28(2):678–687, 2017.

[183] Brent M DeVetter, Prabuddha Mukherjee, Catherine J Murphy, and Rohit Bhargava. Measuring binding kinetics of aromatic thiolated molecules with nanoparticles via surface-enhanced raman spectroscopy. *Nanoscale*, 7(19):8766–8775, 2015.

[184] Zhishuo Zheng, Deyu Qi, and Lei Shi. Copper-catalyzed thiolation of imidazo [1, 2-a] pyridines with (hetero) aryl thiols using molecular oxygen. *Catalysis Communications*, 66:83–86, 2015.

[185] Qijin Chi, Michael J Ford, Arnab Halder, Noel S Hush, Jeffrey R Reimers, and Jens Ulstrup. Sulfur ligand mediated electrochemistry of gold surfaces and nanoparticles: What, how, and why. *Current Opinion in Electrochemistry*, 1(1):7–15, 2017.

[186] Diming Zhang, Yanli Lu, Qian Zhang, Lei Liu, Shuang Li, Yao Yao, Jing Jiang, Gang Logan Liu, and Qingjun Liu. Protein detecting with smartphone-controlled electrochemical impedance spectroscopy for point-of-care applications. *Sensors and Actuators B: Chemical*, 222:994–1002, 2016.

[187] Lassaad Barhoumi, Abdoullatif Baraket, Francesca G Bellagambi, Georgia S Karanasiou, Mounir Ben Ali, Dimitrios I Fotiadis, Joan Bausells, Nadia Zine, Monique Sigaud, and Abdelhamid Errachid. A novel chronoamperometric immunosensor for rapid detection of tnf-α in human saliva. *Sensors and Actuators B: Chemical*, 266:477–484, 2018.

[188] Rui Ma, Hong Pan, Tao Shen, Peng Li, Yanan Chen, Zhenyu Li, Xiaxia Di, and Shuqi Wang. Interaction of flavonoids from woodwardia unigemmata with bovine serum albumin (bsa): Application of spectroscopic techniques and molecular modeling methods. *Molecules*, 22(8):1317, 2017.

[189] N Michael Green. Avidin. In *Advances in protein chemistry*, volume 29, pages 85–133. Elsevier, 1975.

[190] OH Laitinen, VP Hytönen, HR Nordlund, and MS Kulomaa. Genetically engineered avidins and streptavidins. *Cellular and Molecular Life Sciences CMLS*, 63(24):2992–3017, 2006.

[191] Zhida Xu, Xinhao Wang, Kevin Han, Shuo Li, and G Logan Liu. Elastomeric 2d grating and hemispherical optofluidic chamber for multifunctional fluidic sensing. *JOSA A*, 30(12):2466–2472, 2013.

[192] Zhida Xu, Jing Jiang, Xinhao Wang, Kevin Han, Abid Ameen, Ibrahim Khan, Te-Wei Chang, and Gang Logan Liu. Large-area, uniform and low-cost dual-mode plasmonic naked-eye colorimetry and sers sensor with handheld raman spectrometer. *Nanoscale*, 8(11):6162–6172, 2016.

[193] Gordana N Ostojic and Mark C Hersam. Biomolecule-directed assembly of self-supported, nanoporous, conductive, and luminescent single-walled carbon nanotube scaffolds. *Small*, 8(12):1840–1845, 2012.

[194] Chuan Zhang, Cheng Tian, Fei Guo, Zheng Liu, Wen Jiang, and Chengde Mao. Dna-directed three-dimensional protein organization. *Angewandte Chemie International Edition*, 51(14):3382–3385, 2012.

[195] Maciej B Olszewski, Arjan J Groot, Jaroslaw Dastych, and Edward F Knol. Tnf trafficking to human mast cell granules: mature chain-dependent endocytosis. *The Journal of Immunology*, 178(9):5701–5709, 2007.

[196] Walter Swardfager, Krista Lanctôt, Lana Rothenburg, Amy Wong, Jaclyn Cappell, and Nathan Herrmann. A meta-analysis of cytokines in alzheimer's disease. *Biological psychiatry*, 68(10):930–941, 2010.

[197] Richard M Locksley, Nigel Killeen, and Michael J Lenardo. The tnf and tnf receptor superfamilies: integrating mammalian biology. *Cell*, 104(4):487–501, 2001.

[198] Yekta Dowlati, Nathan Herrmann, Walter Swardfager, Helena Liu, Lauren Sham, Elyse K Reim, and Krista L Lanctôt. A meta-analysis of cytokines in major depression. *Biological psychiatry*, 67(5):446–457, 2010.

[199] FC Victor and AB Gottlieb. Tnf-alpha and apoptosis: implications for the pathogenesis and treatment of psoriasis. *Journal of drugs in dermatology: JDD*, 1(3):264–275, 2002.

[200] H Kim, a CM Gilmore, A Pique, JS Horwitz, H Mattoussi, H Murata, ZH Kafafi, and DB Chrisey. Electrical, optical, and structural properties of indium–tin–oxide thin films for organic light-emitting devices. *Journal of Applied Physics*, 86(11):6451–6461, 1999.

[201] CJ Huang, Yan-Kuin Su, and Shi-Lun Wu. The effect of solvent on the etching of ito electrode. *Materials Chemistry and Physics*, 84(1):146–150, 2004.

[202] W Schelter, Wea Gumbrecht, B Montag, U Sykora, and W Erhardt. Combination of amperometric and potentiometric sensor principles for on-line blood monitoring. *Sensors and Actuators B: Chemical*, 6(1-3):91–95, 1992.

[203] Rahim Rahimi, Uriel Brener, Shirisha Chittiboyina, Tahereh Soleimani, David A Detwiler, Sophie A Lelièvre, and Babak Ziaie. Laser-enabled fabrication of flexible and transparent ph sensor with near-field communication for in-situ monitoring of wound infection. *Sensors and Actuators B: Chemical*, 267:198–207, 2018.

[204] C Masalles, S Borros, C Vinas, and F Teixidor. Simple pvc–ppy electrode for ph measurement and titrations. *Analytical and bioanalytical chemistry*, 372(4):513–518, 2002.

[205] Carlos Masalles, Salvador Borrós, C Viñas, and Francesc Teixidor. Are low-coordinating anions of interest as doping agents in organic conducting polymers? *Advanced Materials*, 12(16):1199–1202, 2000.

[206] Lata Gupta, Abhai Mansingh, and PK Srivastava. Band gap narrowing and the band structure of tin-doped indium oxide films. *Thin solid films*, 176(1):33–44, 1989.

[207] M Methfessel. Elastic constants and phonon frequencies of si calculated by a fast full-potential linear-muffin-tin-orbital method. *Physical Review B*, 38(2):1537, 1988.

[208] M Methfessel, CO Rodriguez, and OK Andersen. Fast full-potential calculations with a converged basis of atom-centered linear muffin-tin orbitals: Structural and dynamic properties of silicon. *Physical Review B*, 40(3):2009, 1989.

[209] Ivar Hamberg, Claes Göran Granqvist, K-F Berggren, Bo E Sernelius, and L Engström. Band-gap widening in heavily sn-doped in 2 o 3. *physical Review B*, 30(6):3240, 1984.